RP TU Rheinland-Pfälzische Technische Universität Kaiserslautern Landau

Analysis of mitotic sister chromatid junctions in response to replication stress

vom Fachbereich Biologie

der Rheinland-Pfälzischen Technischen Universität Kaiserslautern-Landau

zur Verleihung des akademischen Grades Dr. rer. nat. genehmigte

Dissertation

von

Angela Wieland, M.Sc., geb. in Filderstadt

Mündliche Prüfung:	26.09.2025
Dekan:	Prof. Dr. Stefan Kins
Promotionskommisionsvorsitzender:	Prof. Dr. Tanja Maritzen
Berichterstattende:	Prof. Dr. Zuzana Storchová
	Prof. Dr. Jörg Fahrer

D 386

Eidesstattliche Erklärung

Ich erkläre hiermit, dass die eingereichte Dissertation von mir, Angela Wieland, selbständig angefertigt wurde. Alle Hilfsmittel und Hilfestellungen in der Arbeit habe ich angegeben.

Die Dissertation oder Teile daraus wurden nicht als Prüfungsarbeit für eine staatliche oder andere wissenschaftliche Prüfung eingereicht.

Die gleiche oder eine andere Abhandlung der Dissertation wurde nicht bei einem anderen Fachbereich oder einer anderen Universität eingereicht.

_____

Datum, Unterschrift Doktorandin

Darlegung des Eigenanteils

Name der Doktorandin: Angela Wieland

Thema der Dissertation: “Analysis of mitotic sister chromatid junctions in response to replication stress”

Anteil Dritter an der Dissertation:

Konzeption/Planung: Prof. Dr. Zuzana Storchová, Dr. Markus Räschle (in Teilen)

Literaturrecherche:

Versuchsdesign: Prof. Dr. Zuzana Storchová, Dr. Markus Räschle (in Teilen)

Methodenentwicklung: Prof. Dr. Zuzana Storchová, Dr. Markus Räschle (in Teilen)

Datenerhebung: Betreute Studenten (Divya Reddy, Farbod Mohseni, Nidhi Preman, Tamara Hamann) sowie Andrea Tijhuis und das Labor von Prof. Dr. Floris Foijer (scWGS Daten), wie unten stehend im Detail und in den jeweiligen Abbildungsbeschriftungen angegeben (in Teilen)

Datenanalyse: Betreute Studenten (Divya Reddy, Farbod Mohseni, Nidhi Preman, Tamara Hamann), Andrea Tijhuis und das Labor von Prof. Dr. Floris Foijer (scWGS Daten), Dr. Markus Räschle, Paul Menges und Jan-Eric Boekenkamp (MS Daten) wie unten stehend im Detail und in den jeweiligen Abbildungsbeschriftungen angegeben (in Teilen)

Programmierung: Dr. Markus Räschle, Paul Menges und Jan-Eric Boekenkamp (von R und Perseus) (in Teilen)

Interpretation und Diskussion der Ergebnisse: Zuzana Storchová, Markus Räschle, FOR2800 Forschungsgruppe (in Teilen)

Anteil Dritter an dem Manuskript „Mitotic BLM functions are required to maintain genomic stability“: Konzeption/Planung: Dr. Markus Räschle und Prof. Dr. Zuzana Storchová (vollständig), Methodenentwicklung: Dr. Markus Räschle und Prof. Dr. Zuzana Storchová (vollständig), Datenerhebung: Tamara Hamann (zu gleichen Teilen), Andrea Tirincsi, Kruno Vukusic, Farbod Mohseni, Rene Wardenaar, Marialucrezia Losito, Ipek Gönenc und Floris Foijer (in Teilen), Original Entwurf: Dr. Markus Räschle und Prof. Dr. Zuzana Storchová (vollständig), Schreiben des Manuskripts sowie Überprüfung und Bearbeitung: Dr. Markus Räschle und Prof. Dr. Zuzana Storchová (überwiegend),Tamara Hamann, Andrea Tirincsi, Kruno Vukusic, Farbod Mohseni, Rene Wardenaar, Marialucrezia Losito, Ipek Gönenc, Bernd Wollnik, Floris Foijer, Iva Tolic (in Teilen), Akquisition: Dr. Markus Räschle und Prof. Dr. Zuzana Storchová (mehrheitlich), Bernd Wollnik (in Teilen), Floris Foijer (in Teilen) und Iva Tolic (in Teilen).

Eigenanteil der Dissertation am Manuskript „Mitotic BLM functions are required to maintain genomic stability“: Datenerhebung (zu gleichen Teilen), Schreiben des Manuskripts sowie Überprüfung und Bearbeitung (in Teilen).

Die Abbildung 17b,c,e,f, Abbildung 18b-e, g, h, Abbildung 19b,c und Abbildung 20b,d zeigt Daten von IVT und IVC Messungen, Klonierungen von pX330 und Homology Donor

Konstrukten die ich in Zusammenarbeit mit Divya Reddy, RPTU Kaiserslautern-Landau, durchgeführt habe.

Abbildung 28 zeigt Daten von Zellsynchronisierungen, die ich in Zusammenarbeit mit Divya Reddy, RPTU Kaiserslautern-Landau, durchgeführt habe.

Abbildung 43b zeigt Daten von Metaphase Chromosomenbrüchen, die ich in Zusammenarbeit mit Tamara Hamann, RPTU Kaiserslautern-Landau, durchgeführt habe.

Abbildung 45 zeigt Daten von 53BP1 Analysen, die ich in Zusammenarbeit mit Farbod Mohseni und Nidhi Preman, RPTU Kaiserslautern-Landau, durchgeführt habe.

Abbildung 47 zeigt Daten von scWGS Analysen, die von Andrea Tijhuis und dem Labor von Prof. Dr. Floris Foijer, UMCG/ERIBA Groningen, durchgeführt wurden.

Abbildung 49 zeigt Daten von ChIP-MS Messungen, die ich in Abbildung 49a, b in Zusammenarbeit mit Divya Reddy, RPTU Kaiserslautern-Landau und in Abbildung 49c, e, f in Zusammenarbeit mit Farbod Mohseni, RPTU Kaiserslautern-Landau durchgeführt habe.

Die vorliegende Einschätzung über die erbrachte Leistung von Dritten wurde mit den genannten Personen einvernehmlich abgestimmt.

_____ _____

Datum, Unterschrift Doktorandin Datum, Unterschrift Betreuerin

Darlegung aller benutzen Hilfsmittel und Hilfestellungen

Name der Doktorandin: Angela Wieland

Thema der Dissertation: “Analysis of mitotic sister chromatid junctions in response to replication stress”

Die Analyse der Daten erfolgte mit Hilfe von Microsoft Office, Cell Profiler, FIJI und SnapGene Viewer, die von der RPTU Kaiserslautern-Landau, sowie Slidebook, FlowJo, BioRender, Adobe Illustrator und GraphPad Prism, die von Prof. Dr. Zuzana Storchová, RPTU Kaiserslautern-Landau bereit gestellt wurden und Benchling.com, OligoEvaluator.com, ImageJ, MaxQuant, Perseus, RStudio und R language, welche frei zugänglich sind. Dr. Markus Räschle, RPTU Kaiserslautern-Landau, Paul Menges, RPTU Kaiserslautern-Landau, Jan-Eric Boekenkamp, RPTU Kaiserslautern-Landau sowie Andrea Tijhuis und das Labor von Floris Foijer, UMCG/ERIBA Groningen haben mich bei der statistischen Analyse der Daten unterstützt. Ich habe ChatGPT.com und DeepL.com für den Text der Einleitung, Methoden, Ergebnisse und Zusammenfassung zur Grammatiküberprüfung sowie Stilverbesserung genutzt.

_____

Datum, Unterschrift Doktorandin

Table of Contents

Publications during PhD enrolment

Boekenkamp, J.-E., Keuper, K., Redel, S., Barthel, K., Johnson, L., Becker, A., **Wieland, A.**, Räschle, M., Storchová, Z. Proteogenomic analysis reveals adaptive strategies for alleviating the consequences of aneuploidy in cancer. EMBO J. 2025 Mar;44(6):1829-1865. doi: 10.1038/s44318-025-00372-w. PMID: 39930267

Pudelko, K., **Wieland, A.**, Hennecke, M., Räschle, M., Bastians, H. Increased microtubule growth triggered by microvesicle-mediated paracrine signaling is required for melanoma cancer cell invasion. Cancer Res Commun. 2022 May 18;2(5):366-379. doi: 10.1158/2767-9764.CRC-22-0010. eCollection 2022 May. PMID: 36875714

Chunduri, N.K., Menges, P., Zhang, X., **Wieland, A.**, Gotsmann, V.L., Mardin, B.R., Buccitelli, C., Korbel, J.O., Willmund, F., Kschischo, M., Raeschle, M., Storchová, Z. Systems approaches identify the consequences of monosomy in somatic human cells. Nat Commun. 2021 Sep 22;12(1):5576. doi: 10.1038/s41467-021-25288-x. PMID: 34552071

Lukow, D.A., Sausville, E.L., Suri, P., Chunduri, N.K., **Wieland, A.**, Leu, J., Smith, J.C., Girish, V., Kumar, A.A., Kendall, J., Wang, Z., Storchová, Z., Sheltzer, J.M. Chromosomal instability accelerates the evolution of resistance to anti-cancer therapies. Dev Cell. 2021 Sep 13;56(17):2427-2439.e4. doi: 10.1016/j.devcel.2021.07.009. Epub 2021 Aug 4. PMID: 34352222

Review articles

Keuper, K., **Wieland, A.**, Räschle, M., Storchová, Z. Processes shaping cancer genomes – From mitotic defects to chromosomal rearrangements. DNA Repair (Amst). 2021 Nov;107:103207. doi: 10.1016/j.dnarep.2021.103207. Epub 2021 Aug 10. PMID: 34425515

Preprint, not peer-reviewed:

Hamann, T.E.*, **Wieland, A.***, Tirincsi, A., Vukušić, K., Mohseni, F., Wardenaar, R., Losito, M., Gönenc, I.I., Wollnik, B., Foijer, F., Tolić, I.M., Storchová, Z., Räschle, M. Mitotic BLM functions are required to maintain genomic stability. bioRxiv 2025.06.16.659902; doi: https://doi.org/10.1101/2025.06.16.659902. *(in submission)*

*equal contribution

Gönenc, I.I., Wolff, A., Busley, A.V., **Wieland, A.**, Tijhuis, A., Müller, C., Wardenaar, R., Argyriou, L., Kaulfuß, S., Räschle, M., Spierings, D.C.J., Foijer, F., Bastians, H., Yigit, G., Zibat, A., Cyganek, L., Wollnik, B. BTRR complex deficiency is a driver for genomic instability in Bloom syndrome. bioRxiv 2025.04.17.649287; doi: https://doi.org/10.1101/2025.04.17.649287 *(in submission)*

Summary

Replication stress has been extensively studied in the context of DNA synthesis defects and downstream consequences such as genomic instability and tumorigenesis. However, the specific mechanisms linking replication stress to mitotic errors, particularly the formation of persistent sister chromatid connections such as ultrafine anaphase bridges, remain insufficiently defined. Many proteins and regulatory pathways have been identified to manage these chromosome junctions throughout the cell cycle, either by preventing their formation or facilitating their resolution. While proteins such as BLM, PICH, and FANCD2 have been identified as ultrafine anaphase bridge-associated factors, their precise role in genome maintenance is not yet fully understood.

Considering the detrimental impact of mitotic errors on cell fate and their potential role in cancer development, it is essential to investigate further the roles of ultrafine anaphase bridge-associated proteins, their molecular interactions, and the mechanisms through which they preserve genomic integrity.

Using CRISPR/Cas9 technology, the generation of cell lines with controllable auxin-induced protein degradation provides a powerful tool for dissecting the functions of anaphase bridge-binding proteins, enabling precise investigation of their roles at specific cell cycle stages. Additionally, fluorescent tagging of target proteins facilitates protein detection and allows for real-time visualization.

This work provides a fundamental basis for the establishment of such degradation system-based cell lines via a modular cloning strategy as well as the successful generation of a cell line for the anaphase bridge-binding protein BLM for rapid and targeted research in specific contexts. Loss of functional BLM led to increased sister chromatid exchange, reduced proliferative capacity, and, especially under replication stress, a pronounced decline in colony-forming ability accompanied by elevated DNA damage, mitotic aberrations, and micronuclei formation. These observations highlight the critical role of BLM in preserving genomic integrity and sustaining cell viability, particularly under conditions that challenge the stability of the genome.

Additionally, it was observed, for the first time to our knowledge, that BLM's association with ultrafine anaphase bridges during mitosis represents a function that is independent of its roles in other phases of the cell cycle. Using the AID system, this finding suggests that BLM operates through stage-specific mechanisms that are not necessarily interconnected. In particular, the exclusive role of BLM during mitosis is shown to be critical for attenuating the development of mitotic aberrations and anaphase bridges, thereby preventing deleterious consequences such as genomic instability.

Zusammenfassung

Replikationsstress ist im Zusammenhang mit DNA-Synthesedefekten und den sich daraus ergebenden Folgen wie genomische Instabilität und Tumorentstehung eingehend untersucht worden. Die spezifischen Mechanismen, die Replikationsstress mit mitotischen Fehlern verbinden, insbesondere die Bildung persistenter Schwesterchromatidenverbindungen wie ultrafeine Anaphase-Brücken, sind jedoch noch unzureichend definiert. Es wurden zahlreiche Proteine und Regulationswege identifiziert, die diese Chromosomenverbindungen während des Zellzyklus steuern, indem sie entweder ihre Bildung verhindern oder ihre Auflösung erleichtern. Während Proteine wie BLM, PICH und FANCD2 als ultrafeine Anaphase-Brücken-assoziierte Faktoren identifiziert wurden, ist ihre genaue Rolle bei der Erhaltung des Genoms noch nicht vollständig geklärt.

In Anbetracht der schädlichen Auswirkungen mitotischer Fehler auf das Zellschicksal und ihrer potenziellen Rolle bei der Krebsentstehung ist es von entscheidender Bedeutung, die Rolle der ultrafeinen Anaphase-Brücken-assoziierten Proteine, ihre molekularen Interaktionen und die Mechanismen, durch die sie die genomische Integrität bewahren, weiter zu untersuchen.

Mit Hilfe der CRISPR/Cas9-Technologie können Zelllinien mit kontrollierbarem Auxin-induziertem Proteinabbau generiert werden, was ein wirkungsvolles Mittel zur Untersuchung der Funktionen von Anaphase-Brückenbindungsproteinen darstellt und eine präzise Untersuchung ihrer Rolle in bestimmten Zellzyklusphasen ermöglicht. Darüber hinaus erleichtert die Fluoreszenzmarkierung der Zielproteine den Nachweis der Proteine und ermöglicht eine Visualisierung in Echtzeit.

Diese Arbeit liefert eine grundlegende Basis für die Etablierung solcher auf dem Auxin-induziertem Proteinabbau basierender Zelllinien durch eine modulare Klonierungsstrategie. Zudem wurde für die schnelle und gezielte Forschung in spezifischen Kontexten erfolgreich eine Zelllinie für das Anaphase-Brückenbindungsprotein BLM generiert. Der Verlust des funktionellen BLM führte zu einem erhöhten Austausch von Schwesterchromatiden, einer verringerten Proliferationsfähigkeit und, insbesondere unter Replikationsstress, zu einem deutlichen Rückgang der Fähigkeit zur Koloniebildung, begleitet von erhöhten DNA-Schäden, mitotischen Aberrationen und der Bildung von Mikronuklei. Diese Beobachtungen unterstreichen die entscheidende Rolle von BLM bei der Erhaltung der genomischen Integrität und der Lebensfähigkeit der Zellen, insbesondere unter Bedingungen, die die Stabilität des Genoms in Frage stellen.

Darüber hinaus wurde zum ersten Mal unseres Wissens nach festgestellt, dass die Assoziation von BLM mit ultrafeinen Anaphase-Brücken während der Mitose eine Funktion darstellt, die unabhängig von seiner Rolle in anderen Phasen des Zellzyklus ist. Unter Verwendung des AID-Systems deutet diese Erkenntnis darauf hin, dass BLM durch zellzyklusspezifische Mechanismen wirkt, die nicht unbedingt miteinander verbunden sind. Insbesondere die ausschließliche Rolle von BLM während der Mitose erweist sich als wesentlich für die Abschwächung der Entwicklung von mitotischen Aberrationen und Anaphase-Brücken, wodurch schädliche Folgen wie genomische Instabilität verhindert werden.

List of abbreviations

Table 1|List of abbreviations

Abbreviation	Name
3‘	3-prime
5‘	5-prime
53BP1	p53-binding protein 1
aEJ	Alternative NHEJ
APC/C	Anaphase-promoting complex/cyclosome
APS	Ammonium persulfate
ATM	Ataxia telangiectasia mutated
ATR	Ataxia telangiectasia and Rad3 related
BER	Base excision repair
BFB-cycle	Breakage-fusion-bridge cycle
BIR	Break-induced replication
BLM	Bloom syndrome helicase
Bp	Base pair(s)
BrdU	5-bromo-2’-deoxyuridine
BS	Bloom syndrome
BSA	Albumin Bovine Serum
Cas9	CRISPR-associated protein 9
CDK	Cyclin-dependent kinase
cDNA	Complementary DNA
CFS	Common fragile sites
Chk1	Checkpoint kinase 1
Chk2	Checkpoint kinase 2
CIN	Chromosomal instability
CKI	CDK inhibitor
CN	Copy number
CO_2	Carbon dioxide
CRISPR	Clustered Regularly Interspaced Short Palindromic Repeats
crRNA	CRISPR RNA
C-UFB	Centromeric ultrafine bridge
DAPI	4’,6-diamidino-2-phenylindole
DDAOG	DDAO-galactoside substrate
DDR	DNA damage response
dHJ	Double Holliday junction
D-loop	Displacement loop
DMEM	Dulbecco's Modified Eagle Medium
DMSO	Dimethylsulfoxide
DNA	Deoxyribonucleic acid
Dox	Doxycycline
Doxo	Doxorubicin
DSB	Double-strand break
DSBR	Double-strand break repair pathway
dsDNA	Double-stranded DNA
DTT	Dithiothreitol
ECL	Enhanced chemiluminescence
EDTA	Ethylenediaminetetraacetic acid
eGFP	Enhanced green fluorescence protein
Escherichia coli	*E. coli*

EtOH	Ethanol
FACS	Fluorescence-activated cell sorting
FBS	Fetal bovine serum
FoSTeS	Fork Stalling and Template Switching
FSC	Forward scatter
FS-UFB	Fragile site ultrafine bridge
Fw	Forward
G	Guanine
G1 phase	Gap phase 1
G2 phase	Gap phase 2
GFP	Green fluorescence protein
gRNA	Guide RNA
H_2O	Water
HCl	Hydrochloric acid
HCT116	Human colon cancer cell line 116
HEPES	4-(2-hydroxyethyl)-1-piperazineethanesulfonic acid
HR	Homologous recombination
HR-UFB	Homologous recombination ultrafine bridge
Hygro	Hygromycin
IAA	Indole-3-acetic acid
ICL	Interstrand crosslinks
IF	Immunofluorescence
IVC	*In vitro* cleavage
IVT	*In vitro* transcription
kb	Kilobase(s)
KCl	Potassium chloride
kDa	Kilo dalton
KH_2PO_4	Dipotassium phosphate
LB	Lysogeny broth
LOH	Loss of heterozygosity
M phase	Mitosis
MCM	Minichromosome maintenance protein
MEM	Minimal Essential Medium
$MgCl_2$	Magnesium chloride
MiDAS	Mitotic DNA synthesis
mmBIR	Microhomology-mediated BIR
MN	Micronucleus
MRN complex	Mre11-Rad50-Nbs1 complex
Na_2HPO_4	Disodium hydrogen phosphate
NaCl	Sodium chloride
NaN_3	Sodium azide
Neo	Neomycin
NER	Nucleotide excision repair
NH_4Cl	Ammonium chloride
NHEJ	Non-homologous end joining
Nonidet P40	NP-40
nt	Nucleotide(s)
OD	Optical density
PAM	Protospacer adjacent motif
PBS	Phosphate-buffered saline
PBST	PBS with Tween-20
PCR	Polymerase chain reaction
PEG	Polyethylene glycol
PEI	Polyethylenimine

Pen/Strep	Penicillin/Streptomycin
PFA	Paraformaldehyde
PH	potentia hydrogenii
PI	Propidium iodide
PICH	Plk1-interacting checkpoint helicase
PML-NB	Promyelocytic leukemia nuclear bodies
Pre-RC	Pre-replication complex
Puro	Puromycin
RB	Retinoblastoma protein
RD	Restriction digestion
rDNA	Ribosomal DNA
Rev	Reverse
RIPA	Radioimmunoprecipitation assay
RNA	Ribonucleic acid
RNP	Ribonucleoprotein
RPA	Replication protein A
rpm	Revolutions per minute
RT	Room temperature
R-UFB	Ribosomal ultrafine bridge
S phase	Synthesis phase
SAC	Spindle assembly checkpoint
SA-β-Gal	Senescence-associated beta-galactosidase
SCE	Sister chromatid exchange
S-CIN	Structural chromosomal instability
SD	Standard deviation
SDS	Sodium dodecyl sulfate
SDSA	Synthesis dependent strand annealing
SDS-PAGE	Sodium dodecyl sulfate polyacrylamide gel electrophoresis
SEM	Standard error of mean
sgRNA	Single guide RNA
SpCas9	Streptococcus pyogenes Cas9
SPRI	Solid-phase reversible immobilization
SSA	Single-strand annealing
SSB	Single-strand break
SSC buffer	Salt sodium citrate buffer
SSC	Side scatter
ssDNA	Single-stranded DNA
TBS	Tris-buffered saline
TBST	TBS with Tween-20
TFA	Tri-fluoracetic acid
TOP2A	Topoisomerase II alpha
TOP3A	Topoisomerase III alpha
tracrRNA	Trans-activating CRISPR RNA
T-UFB	Telomeric ultrafine bridge
UFB	Ultra-fine anaphase bridge
UV	Ultraviolet
W-CIN	Whole chromosome chromosomal instability
WGD	Whole genome doubling
WT	Wild-type

1. Introduction

1.1 The human cell cycle: a complex process to maintain genomic stability

All human being starts with one single cell, serving as the basic unit of life. An adult body consists of trillions of cells and a variety of distinct cell types[1]. Throughout life, cells have to preserve viability and distinct cell types are still dividing under controlled conditions and by that have to maintain genomic stability. The fate of a human cell and the guarantee of faithful cell division and viability lie in the hands of the very sophisticated and finely coordinated process during each individual cell division: the cell cycle[2].

During that event, it is critical that the genetic material of each cell is identically duplicated and then divided into two daughter cells. The human cell cycle is structured into four distinct phases: gap phase 1 (G1 phase), synthesis phase (S phase), gap phase 2 (G2 phase), all three collectively known as interphase, and M phase[3] (Fig. 1). At the G1 phase, each new cell will here almost double in size by increasing the volume of cytoplasm and the number of organelles. Also, ribonucleic acid (RNA) and protein synthesis take place in that phase as well as a number of preparations for the following deoxyribonucleic acid (DNA) synthesis during S phase. However, non-dividing cells or the ones limited in resources required will enter the resting phase G0 from this point, where they temporarily exit the cell cycle and remain quiescent until stimulated to re-enter G1. By the increasing levels of DNA damage, cells can also irreversibly exit the cell cycle by entering the non-dividing phase of senescence or undergo programmed cell death by apoptosis. Dividing cells that pass the G1/S checkpoint are now allowed to enter S-phase, which is characterized by DNA replication, in which the replication machinery is assembled, the DNA double helices are separated, and genomic material is identically duplicated. At the end of S phase, each chromosome consists of two sister chromatids, held together by cohesion. The following G2 phase acts in addition to the G1 phase as another gap phase to ensure further cell growth, protein synthesis, preparation of the cell for subsequent cell division, as well as the repair of DNA damage that may have occurred during S phase. Cells that pass the G2/M checkpoint, ensuring that DNA replication is complete and DNA damage has been repaired, are finally entering the last phase of the cell cycle: the M-phase, also known as mitosis. During that phase, the DNA gets tightly packed as condensed chromosomes to facilitate chromosome segregation. Finally, all cell components are equally divided into two identical daughter cells[2].

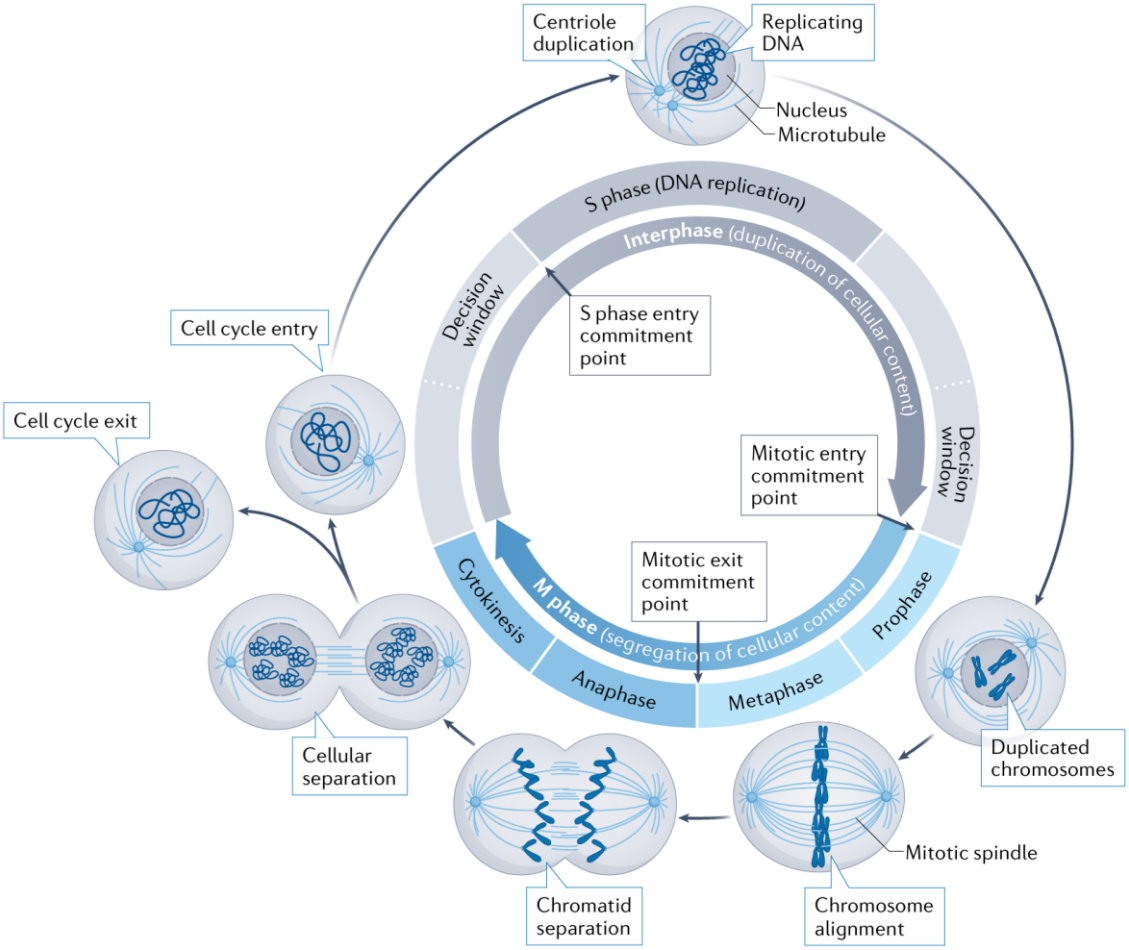

Figure 1|The human cell cycle. The human cell cycle is a precisely regulated process through which cells duplicate their contents and divide. During interphase, the cell grows and replicates its DNA in preparation for division. Entry into S phase, where DNA synthesis occurs, is tightly controlled by a checkpoint ensuring the cell is ready for replication. Similarly, progression out of S phase and into M phase is governed by additional checkpoint mechanisms. Upon commitment to mitosis, cells proceed through a series of distinct stages: the initial condensation of chromatin starts at prophase, chromosomes align at the center of the cell during metaphase, followed by anaphase, characterized by the separation of sister chromatids toward opposite poles, and finally, at the end of each cell cycle, cell division occurs, during which cytokinesis separates the cytoplasm and two daughter cells are formed. After mitosis, a cell may either re-enter the cycle for another round of division or exit the cell cycle (adapted from Matthews et al., 2022[2]).

These very complex processes are regulated by cyclins and their cyclin-dependent kinases (CDKs), among many other proteins involved in cell cycle control, such as checkpoint proteins and tumor suppressors (Fig. 2).

Cyclins are proteins that play a key role in controlling the cell cycle progression[4,5]. Different cyclins are synthesized and degraded at specific stages of the cell cycle, and their abundance and activity fluctuate in a coordinated manner. Cyclins function as regulatory subunits that bind to and activate CDKs by forming cyclin-CDK complexes, thereby modulating their kinase activity and substrate specificity. CDKs belong to a family of serine/threonine protein kinases that function as key regulators of the cell cycle. Their activity is tightly regulated by cyclin binding, phosphorylation, and association with CDK inhibitors (CKIs). CDKs phosphorylate target proteins involved in cell cycle progression, including proteins regulating DNA replication, chromosome segregation, and cell division. Cyclin-CDK complexes play a critical role in regulating the cell cycle checkpoints, which monitor the integrity of DNA replication and chromosome segregation. Checkpoint activation leads to the inhibition of cyclin-CDK

complexes, halting cell cycle progression until DNA damage is repaired or other cellular abnormalities are resolved[2]. CKIs, such as the p21 and p27 proteins, act as negative regulators of cyclin-CDK complexes[6,7]. While cyclin D and the associated CDK4/6 assemble gradually from the beginning of G1 phase to S phase and degrade towards the middle of mitosis, it further creates a decision window in which the cell cycle entry and replication initiation decision takes place. E2F-dependent transcription leads to increasing levels of cyclin E-CDK2 as well as cyclin A-CDK2 complexes, which play a major role in the G1/S phase transition by inhibition of the retinoblastoma protein (RB) and therefore further initiates the E2F-dependent transcription. High concentrations of cyclin A-CDK2 complexes also support replication initiation by inhibition of the anaphase-promoting complex/cyclosome (APC/C) and are found mainly during S phase through G2, whereby, towards the onset of mitosis, CDK2 is replaced by CDK1, regulating the entry into mitosis. The G2/M-phase checkpoint is further controlled by the formation of the cyclin B-CDK1 complex and APC/C activation, promoting entry into and progression through mitosis by phosphorylating proteins involved in chromosome condensation, spindle assembly, and mitotic progression, while cyclin B can be found in decreasing concentration continuously until mid-mitosis. In addition, a variety of repair mechanisms are involved in the correct cell cycle processes to ensure their accuracy. All these complex mechanisms ultimately maintain genomic stability[2].

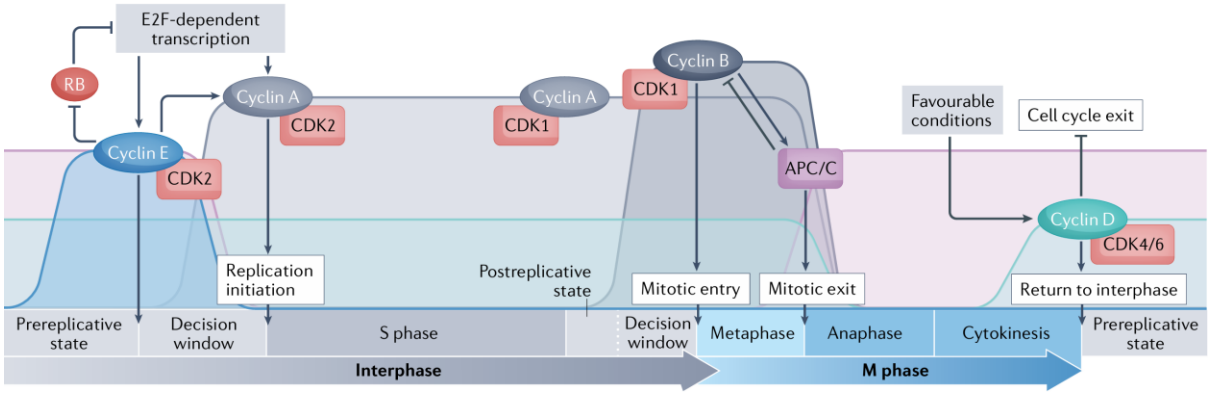

Figure 2|Cell Cycle Regulation by cyclin-CDK complexes. Cyclin E–CDK2 and cyclin A–CDK2 form key regulatory complexes that define the decision window for S phase entry, with cyclin E–CDK2 promoting the activation of E2F-dependent transcription required for DNA replication. Increasing levels of cyclin A/B–CDK1 complexes provide another second decision point that drives mitotic entry, eventually triggering APC/C activation required for progression through and exit from mitosis. Activation of cyclin D–CDK4/6 is important to return to interphase for a new cell cycle round (adapted from Matthews et al., 2022[2]).

1.1.1 S phase: safeguarding DNA replication for accurate DNA duplication

The S phase of the cell cycle is a highly orchestrated process essential for the faithful duplication of the genome. This pivotal phase involves the coordinated action of numerous molecular players to ensure accurate synthesis of DNA strands and preservation of genomic integrity. It is characterized by DNA replication, a critical event that ensures the duplication of genetic material prior to cell division. S phase DNA replication is tightly regulated to prevent errors and safeguard against mutations that could compromise cellular viability and function. Initiation begins at specific sites within the genome known as origins of replication. The initiation process is governed by a multiprotein complex called the pre-replication complex

(pre-RC), which assembles at origins during the G1 phase of the cell cycle. Activation of the pre-RC during S phase triggers the recruitment and activation of the minichromosome maintenance protein (MCM) complex, serving as a DNA helicase to initiate the unwinding of the DNA double helix and the formation of replication forks[8,9]. Once replication forks are established, DNA synthesis proceeds bidirectionally along the template strands[10]. DNA polymerases catalyze the addition of nucleotides to the growing daughter strands, consisting of a leading and a lagging strand, in a highly coordinated manner. Leading and lagging strand synthesis differ in their mechanisms, with continuous synthesis occurring on the leading strand and discontinuous synthesis generating Okazaki fragments on the lagging strand. RNA primers are synthesized by primase to initiate Okazaki fragment synthesis, which is subsequently elongated by the DNA polymerase[11]. DNA polymerases also possess proofreading activity that allows for the detection and correction of errors in nucleotide incorporation that can occur during each single DNA synthesis process. Mismatch repair mechanisms further contribute to the fidelity of DNA replication by identifying and repairing mispaired bases. As DNA replication proceeds, replication forks converge, eventually leading to the termination of DNA synthesis. Termination of replication forks involves the resolution of daughter DNA strands and the disassembly of replication complexes. Specialized proteins mediate the completion of DNA replication and ensure the faithful duplication of the entire genome[12].

1.1.2 DNA replication stress and repair: maintaining genomic integrity

The tightly controlled process of DNA replication is critical to ensure accurate duplication of the approximately 3 billion base pairs[13]. However, the replication machinery frequently encounters various obstacles that threaten the smooth progression of replication forks, collectively leading to a phenomenon termed replication stress[14]. Replication stress can be induced by both endogenous and exogenous factors. Intrinsic challenges include DNA secondary structures such as G-quadruplexes, repetitive elements, R-loops, spontaneous DNA lesions, and limited nucleotide pools, all of which can impede fork progression or stability[15]. Exogenously, genotoxic insults such as ultraviolet (UV) light and ionizing radiation and agents like hydroxyurea, leading to limited nucleotide availability or aphidicolin that inhibits DNA polymerases, can also interfere with DNA replication and induce DNA damage[15–17]. The human cell has evolved a sophisticated network, termed the replication stress response, to detect replication-associated damage, stabilize replication forks, and initiate repair pathways. Particularly, the Ataxia telangiectasia and Rad3 related (ATR) kinase is important to recognize abnormal replication intermediates, especially regions of single-stranded DNA (ssDNA) coated with replication protein A (RPA) and to coordinate checkpoint activation, fork stabilization, and repair processes[18–20].

When a replication fork encounters an obstacle, it can lead to fork stalling with various outcomes that can arise. These include fork reversal, translesion synthesis repair, or ssDNA gaps that occur, which are repaired by template switching. In severe cases, fork collapse can arise, for example, induced by single-strand breaks (SSBs)[14]. Fork collapse, DNA lesions that lead to replication stress or fork stalling due to telomere attrition may then generate single-ended DNA double-strand breaks (DSBs)[14,21]. Cells can restart replication after single-ended DSB through mechanisms such as break-induced replication (BIR) and microhomology-mediated BIR (mmBIR) (Fig. 3a) or the Fork Stalling and Template Switching (FoSTeS)

mechanism (Fig. 3b), whereby the nascent leading strand invades a nearby fork and resumes synthesis through a recombination-dependent process[22]. However, this template switching mechanism relies on short regions of micro-homologies and can, similarly to BIR, produce chromosomal rearrangements, which are frequently found in cancer genomes[23–25].

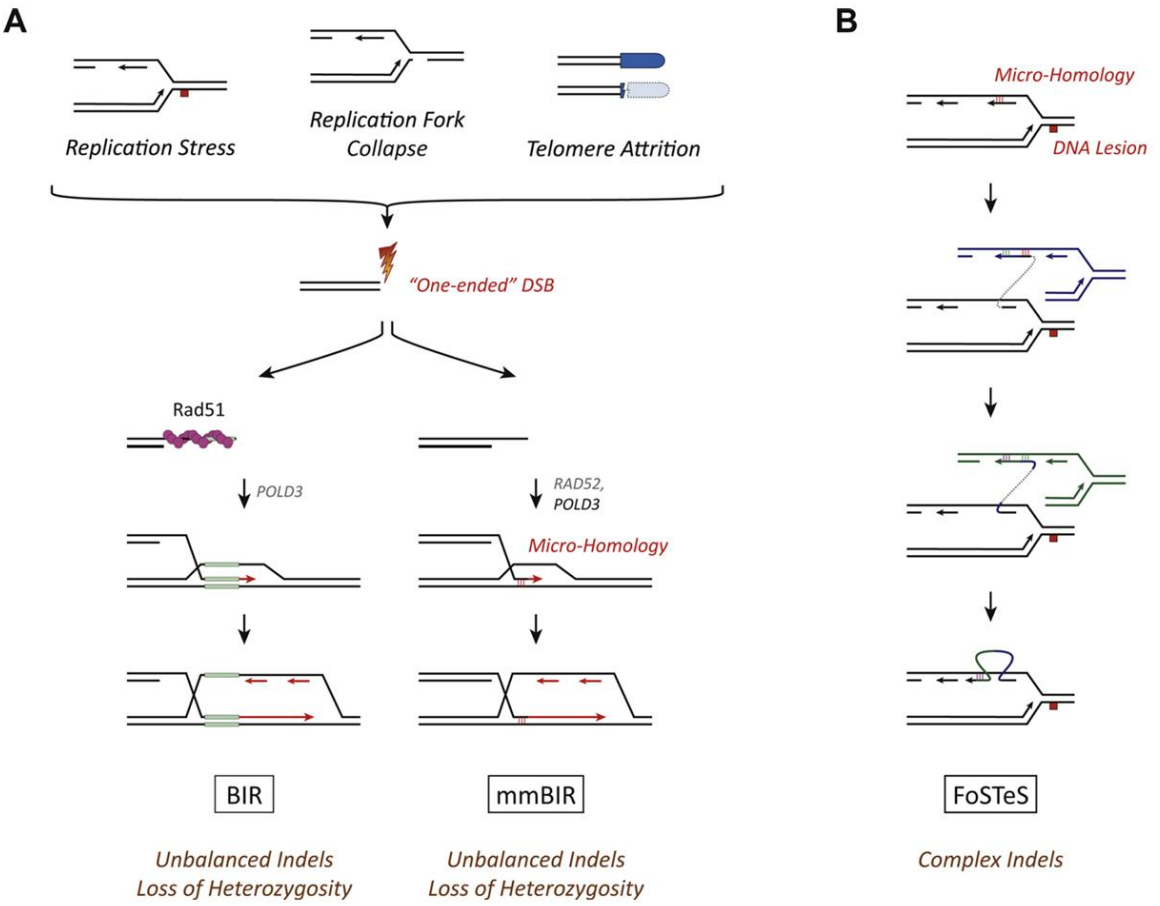

Figure 3|DNA repair mechanisms associated with stalled replication forks. a, Replication fork collapse, telomere shortening, or replication stress, arising from factors such as DNA lesions, can lead to the formation of one-ended double-strand breaks (DSBs), which are typically repaired through break-induced replication (BIR). In the RAD51-dependent BIR pathway, repair can occur, but invasion at repetitive sequences can cause structural abnormalities such as insertions, deletions, or loss of heterozygosity. Alternatively, a RAD51-independent form of BIR, known as microhomology-mediated BIR (mmBIR), utilizes short or long homologous sequences for strand annealing with increased risk of structural variations. **b,** The Fork Stalling and Template Switching (FoSTeS) mechanism is another pathway that may operate under replication stress and has been proposed to account for complex chromosomal rearrangements (adapted from Keuper et al., 2021[22]).

If replication stress is not properly resolved, stalled replication forks can result in under-replicated DNA that can be carried over into mitosis[26,27]. A lack of origin licensing can exacerbate the problem by reducing the cell's ability to rescue stalled forks, leading to replication gaps or under-replicated regions[27]. Such deficiencies can cause mutations, chromosomal breaks, or catastrophic mitotic events, resulting in chromosome mis-segregation and ultimately genomic instability. Obstacles such as interstrand crosslinks (ICLs), unresolved R-loops, and replication across difficult-to-replicate sequences, such as common fragile sites (CFS), further threaten fork progression and genomic integrity[14]. In addition, genotoxic agents such as aphidicolin have been shown to impede fork progression by inducing breaks and gaps

at CFS[14,28]. The interplay between fork stabilization, DNA repair, and chromatin remodeling is thus critical to avoid mutagenesis and transformation.

In summary, DNA replication stress is a central challenge to genome stability. The capacity of a cell to detect and resolve replication-associated disturbances determines whether DNA replication is successfully completed or whether errors persist, potentially leading to genetic aberrations that are transferred to subsequent cell cycles.

1.1.3 Mitotic DNA synthesis: completing DNA replication outside of S phase

During normal cell division, DNA replication is expected to be completed within S-phase. However, under certain conditions, such as replication stress, particularly at CFS, telomeres and other difficult-to-replicate genomic regions, some DNA segments may remain under-replicated or persist as incomplete recombination intermediates by the time the cell enters mitosis. The fragility of these CFS regions, potentially inducing chromosome breakage, is thought to arise from their tendency to replicate late in the cell cycle[29] and their frequent location within very large genes, which may lead to conflicts between replication and transcription[30]. To resolve under-replicated regions, cells can activate a specialized process known as mitotic DNA synthesis (MiDAS)[31].

MiDAS occurs during mitosis and is distinct from classical S-phase replication. While the exact mechanism is not fully understood yet, it is proposed to depend on factors such as POLD3 and RAD52 by utilizing BIR-like mechanisms to complete DNA repair synthesis[31]. Furthermore, endonucleases such as MUS81-EME1 and SLX4 are found to resolve late replication intermediates at CFSs during early mitosis[32–35]. However, other, BIR-independent pathways have also been proposed, including the DNA cleavage by MUS81-EME1 and re-annealing of stalled replication forks at R-loops by DNA ligase IV[36,37], as well as the hypothetical unwinding of replication intermediates by helicases such as BLM[37]. Nonetheless, further investigation is required to clarify the underlying mechanisms.

MiDAS represents a crucial process that ensures the completion of DNA replication in difficult-to-replicate regions, which may remain under-replicated as cells transition into mitosis. It therefore serves as a last chance to resolve replication challenges prior to chromosome segregation and prevents genomic instability[38].

1.1.4 M-phase: faithful chromosome segregation into identical daughter cells

Mitosis represents a fundamental process during each cell cycle, ensuring the accurate distribution of duplicated genetic material into two genetically identical daughter cells. It is the final stage of the cell cycle where the cell orchestrates the precise segregation of its replicated chromosomes. The process begins with prophase, where the previously diffuse chromatin condenses into clearly defined chromosomes, each consisting of two identically duplicated

sister chromatids[39]. As prophase progresses, the cohesin proteins that tightly link these chromatids begin to partially loosen, allowing the resolution of intertwined DNA regions known as catenations[40]. These entanglements of DNA regions arise naturally during DNA replication, particularly at sites where replication forks converge. At this stage, the cell initiates structural preparations for division. The centrosomes, which are specialized organelles acting as the primary microtubule organizing centers, duplicate and begin to migrate toward opposite poles of the nucleus. These centrosomes play a critical role in forming the mitotic spindle, a dynamic framework of microtubules that guides chromosome movement during mitosis. Prometaphase marks the disassembly of the nuclear envelope, enabling spindle microtubules to interact with the chromosomes[39]. Specialized protein complexes called kinetochores assemble at the centromere, a constricted region often located near the center of each chromosome[41]. The regions flanking the centromere are referred to as the p-arm (shorter arm) and the q-arm (longer arm), based on their relative lengths[42]. The kinetochores serve as anchor points for spindle fibers, facilitating the capture and alignment of chromosomes. As microtubules extend from the centrosomes and attach to kinetochores, the chromosomes begin moving toward the equatorial region of a cell. During metaphase, the chromosomes align along the equatorial region, forming what is known as the metaphase plate. A control system called the spindle assembly checkpoint (SAC) regulates this phase, ensuring that all chromosomes are properly attached to spindle fibers and are correctly aligned in a bioriented manner before the cell proceeds[43,44]. The onset of anaphase is triggered by the activation of the APC/C, which leads to the removal of cohesins and suppresses SAC activity. This permits the separation of sister chromatids, which are pulled toward opposite spindle poles. This step is essential for maintaining genomic stability, as it guarantees that each daughter cell will receive one complete set of chromosomes. In the final phase, telophase, the spindle apparatus disassembles, and new nuclear envelopes form around the separated sets of chromosomes at each pole. The chromosomes gradually decondense, returning to a less compact state suitable for gene expression and cell function. Cytokinesis, the physical division of the cytoplasm, then occurs to complete cell division, resulting in two daughter cells ready to enter the next interphase[39].

1.1.5 Chromosome mis-segregation: detrimental effects on the fate of a cell

Precise chromosome segregation during mitosis is essential for maintaining genomic stability across cell generations. However, disruptions to this tightly regulated process can lead to errors in chromosome segregation that are strongly associated with genomic instability and cancer progression. Several cellular components and regulatory pathways that coordinate mitosis can malfunction, resulting in inaccurate chromosome distribution[45].

One of the main causes of segregation errors is a defect in the mitotic spindle apparatus. For instance, centrosome amplification can give rise to multipolar spindles, causing chromosomes to be pulled in more than two directions, increasing the risk of inaccurate segregation[46–48]. An increased number of centrosomes can arise as a consequence of polyploidy, frequently arising from cytokinesis failure and defined as a state in which cells acquire an abnormal number of entire chromosome sets[49]. Similarly, inaccurate kinetochore-microtubule orientations, particularly merotelic attachments, where a single kinetochore is connected to microtubules from both poles, can hinder proper chromosomal movement during anaphase[50,51]. Additionally,

defective cohesion between sister chromatids can lead to their premature disconnection[52], and an abnormal SAC signaling may fail to detect or delay mitotic progression[53]. Telomere fusions can give rise to unstable anaphase bridges, which are prone to breakage during chromosome segregation. These breakage events can generate chromosome fragments that are improperly segregated[54].

One of the most common contributors to chromosome mis-segregation is the persistence of lagging chromosomes during anaphase, resulting from merotelic kinetochore-microtubule attachments[51]. As a consequence, these chromosomes stay behind the main chromosomal masses that are moving toward opposite spindle poles (Fig. 4, red chromosome). Depending on whether they contain a centromere, lagging chromosomes are classified as either centric or acentric, whereby the detection of a lagging chromosome lacking a centromere suggests that laggards may also arise from defects before entering mitosis and are considered to have a higher risk of mis-segregation[55]. Lagging chromosomes are especially vulnerable to being excluded from the newly formed primary nuclei in the following cell cycle and are instead surrounded by separate structures known as micronuclei (MN)[56]. These extranuclear bodies differ from the main nucleus in terms of DNA replication timing, repair efficiency, and nuclear envelope integrity. As a result, the DNA within MN is prone to extensive damage and genomic rearrangements, sometimes even undergo catastrophic events such as chromothripsis, where a chromosome shatters and is reassembled in a disordered fashion[57,58]. Interestingly, some studies suggest that lagging chromosomes, despite frequently becoming enclosed in micronuclei, often end up in the correct daughter cell after division[56]. In contrast, chromosomes that are misaligned during metaphase appear to have a higher risk for mis-segregation. These misaligned chromosomes, which fail to position correctly at the metaphase plate, can become surrounded with several layers of endomembranes, a phenomenon known as "ensheathing", which interferes with their incorporation into the correct daughter nucleus and become enclosed in an MN with disrupted nuclear envelopes in the following cell cycle (Fig. 4, blue chromosome)[59–61].

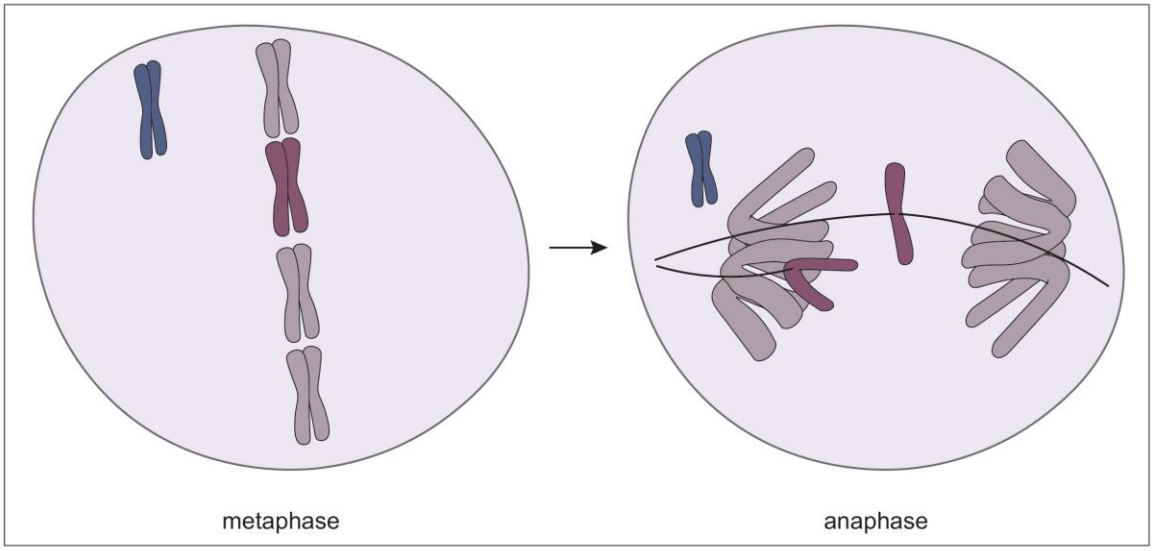

Figure 4|Causes of chromosome mis-segregation by lagging and misaligned chromosomes. Misaligned chromosomes (depicted in blue) are positioned away from the metaphase plate due to improper congression during metaphase, but typically segregate with the main chromatin mass during anaphase. In contrast, lagging chromosomes in anaphase (centered chromosome shown in red) frequently result from erroneous kinetochore-microtubule interactions (black lines). These chromosomes often lag behind the separating chromatin masses during anaphase. Failure of accurate re-integration of misaligned and lagging chromosomes can lead to chromosome mis-segregation.

1.1.6 Ends in sight: Dealing with DNA double-strand breaks

The stability of the genome is essential for normal cellular function, development, and survival. To maintain this stability, cells rely on tightly regulated surveillance systems that monitor DNA integrity throughout the cell cycle. Despite these controls, DNA is frequently exposed to damage from both internal sources, such as reactive oxygen species and replication stress, and external factors like radiation or chemical agents. The nature of the repair pathway activated depends on the type of DNA lesion. For example, nucleotide excision repair (NER) targets bulky adducts and crosslinks, while base excision repair (BER) deals with small, non-helix-deforming lesions such as oxidized bases[62]. Among the various types of DNA lesions that can arise, DSBs are especially harmful because they sever both strands of the DNA helix, posing a high risk for mutations, chromosomal rearrangements, or cell death if not accurately repaired. Besides replication stress-associated single-ended DSBs, other factors frequently lead to two-ended DSBs[63].

To detect and respond to such damage, cells activate a complex signaling network called the DNA damage response (DDR)[62]. Two phosphoinositide 3-kinase-related kinases, ATR and ATM (ataxia telangiectasia mutated), are key regulators of this response, each responding to distinct forms of DNA stress and activating downstream proteins such as the checkpoint kinases 1 and 2 (Chk1 and Chk2)[20,64]. ATM is primarily activated by DSBs following the initial recruitment of the p53-binding protein 1 (53BP1), which contributes to chromatin protection and stabilization at the damage site, thereby also mediating ATR signaling[65]. ATM activation is further supported by the binding of the Mre11-Rad50-Nbs1 (MRN) complex to the broken double-strand DNA (dsDNA) ends[66]. ATM then initiates signaling cascades that can pause the cell cycle, promote DNA repair, or lead to programmed cell death depending on the context and severity of damage. It phosphorylates a range of proteins involved in cell cycle checkpoints and repair, such as Chk2, p53, and H2AX, to coordinate a cellular response[67,68]. ATR, on the other hand, is mostly involved in replication-related damage response or when single-stranded DNA accumulates at stalled replication forks. Its activation depends on the binding of RPA-coated ssDNA, which recruits ATR through its partner protein ATRIP[69]. ATR primarily phosphorylates Chk1, leading to cell cycle arrest and facilitating repair in response to DNA damage[70].

Once DNA damage is detected, cells must choose from several repair strategies. For DSBs, the selection of the repair pathway is influenced by the cell cycle phase and the nature of the break. Two main DSB repair mechanisms exist, non-homologous end joining (NHEJ) and homologous recombination (HR)[63]. Collectively, both main DSB repair strategies are important for the cell. While HR typically ensures high-fidelity restoration of the original DNA sequence, NHEJ provides a rapid, though rather error-prone, repair[71] (Fig. 5).

NHEJ is active throughout the cell cycle and is the preferred pathway during G1 phase in the absence of an identical sister chromatid template[62,72]. Thereby, broken DNA ends are ligated without using a template. The Ku70/Ku80 complex recognizes the break and recruits other components, such as DNA-PKcs and ligase IV, to rejoin the ends. Although fast, this pathway is prone to small insertions or deletions, making it relatively error-prone. A variation called alternative NHEJ (aEJ) relies on microhomology-mediated end joining using short homologous sequences and often results in larger deletions and other chromosomal rearrangements[73,74].

In contrast, HR is a more accurate repair pathway and is active mainly in the S and G2 phases when a sister chromatid template is available[75]. The process starts with recognition of the

break by the MRN complex, which initiates resection of the 5' DNA ends to generate 3' overhangs. These are coated by RPA and then replaced by RAD51, facilitated by proteins such as BRCA1 and BRCA2. RAD51 mediates strand invasion into the homologous DNA template to initiate DNA synthesis, called synthesis dependent strand annealing (SDSA) repair (Fig. 5). This mechanism avoids crossover events[63,76].

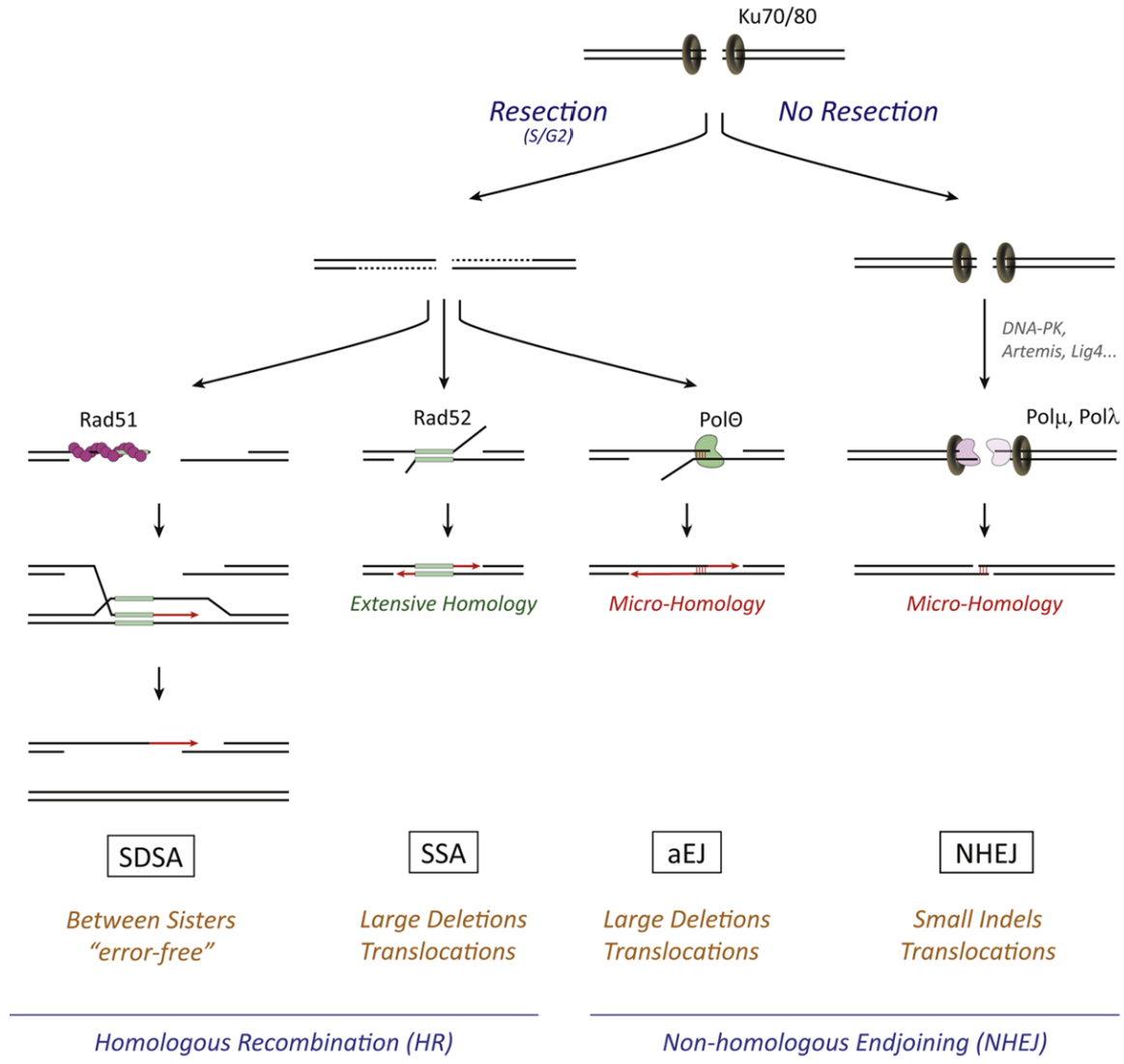

Figure 5|DNA double-strand break repair pathway choice. Broken DNA ends are recognized by the heterodimer Ku70/80, among other factors such as the MRN complex and ATM. DNA end resection mainly occurs during S and G2 phase. While the synthesis-dependent strand annealing (SDS) pathway requires Rad51 and leads to error-free repair, single-strand annealing (SSA) and alternative non-homologous end joining (aEJ) need extensive homologies or micro-homologies, resulting in detrimental consequences for the genome, such as large deletions and translocations. In contrast to SDSA and SSA, which belong to the homologous recombination (HR) repair pathways, the non-homologous end joining (NHEJ) pathway does not depend on the presence of a homologous sister chromatid and can therefore operate throughout all phases of the cell cycle. The canonical NHEJ pathway is capable of ligating DNA ends that are not directly compatible, often requiring modification of few nucleotides at the broken ends before rejoining. This process involves a coordinated action of key factors, including DNA-PK, Artemis, Ligase IV, and the polymerases Polμ and Polλ, which modify and align the DNA ends to facilitate repair. This can lead to the loss of few nucleotides, resulting in small indels and translocations (adapted from Keuper et al., 2021[22]).

Another HR-associated mechanism is the double-strand break repair (DSBR) pathway, which also begins with resection and strand invasion but proceeds to form a double Holliday junction (dHJ)[77]. This intermediate can be resolved in two ways. The dissolution pathway is mediated by the BLM and its complex members and exclusively avoids crossover events[78,79]. On the other hand, resolution of dHJ, performed by endonucleases such as MUS81-EME1 and others, results in either crossover or non-crossover products[80]. While crossover events are important during meiosis to ensure genetic diversity, recent studies have also suggested that dHJ arise during mitotic-cycling cells, whereby avoiding crossover events is preferred[79,81].

A more error-prone variant of HR is the single-strand annealing (SSA) pathway, that occurs between repetitive DNA sequences flanking a DSB[22,82] (Fig. 5). After extensive end resection, homologous sequences on either side of the break are aligned and annealed, leading to consequences such as large deletions and translocations and therefore compromises genomic integrity[83].

1.2 Genomic instability: A process shaping cancer genomes

In each cell cycle, healthy cells rely on finely tuned DNA surveillance and repair mechanisms to safeguard the genome from damage that can constantly arise from endogenous and exogenous stress. Several types of damage can occur to the DNA, such as DNA base mismatching, SSBs, DSBs, and others, which can lead to changes in the DNA sequence if not properly repaired. The accumulation of genetic alterations at an elevated rate is defined as genomic instability, a condition strongly associated with cancer development and progression[22,84]. The genome becomes less stable and the risk increases for mutations that affect key regulators of cell growth and division. Such instability can drive malignant transformation through the loss of tumor suppressor function or by the amplification or activation of oncogenes[84]. One of the most striking features of tumor cells is their highly altered genomic landscape, which includes both numerical changes, such as the loss or gain of entire chromosomes, and structural abnormalities, like deletions, duplications, translocations, or chromosomal rearrangements[73,85] (Fig. 6). Indeed, advances in cancer genome sequencing have uncovered the remarkable complexity of these alterations, revealing that structural variants can range in size from small disruptions involving at least 50 nucleotides to large-scale alterations affecting entire chromosomes or megabase-size regions[86]. When cells possess an abnormal set of chromosomes, this state is referred to as aneuploidy[87]. Aneuploidy can be subclassified into numerical aneuploidy, which involves the gain or loss of entire chromosomes or alterations affecting whole chromosome arms, and structural aneuploidy, defined as changes at subchromosomal scales. Many cancer genomes exhibit both types, sometimes in the same cell, contributing to an extremely heterogeneous and unstable genome[88]. Such complexity is frequently driven by persistent chromosomal instability (CIN), characterized by the recurrent gain or loss of entire chromosomes (W-CIN) or structural chromosome fragments (S-CIN) across successive cell divisions[89].

Numerical aneuploidy results in deviations from the normal chromosome copy number (CN), manifesting as losses, including monosomy or as gains, such as trisomy, tetrasomy, or polyploidy[89] (Fig. 6). Although aneuploidy is exceptionally rare in somatic cells, affecting less than 1%[90], it is remarkably prevalent in cancer[91], observed in approximately 88% of tumor genomes[92]. This presents a paradox, as aneuploidy typically leads to impaired fitness and is often lethal during embryonic development, with only a few exceptions such as trisomy 21

(Down syndrome), trisomy 18 (Edwards syndrome), and monosomy X in females (Turner syndrome)[93]. In contrast, cancer cells may acquire adaptations that allow them to tolerate or even benefit from aneuploidy, such as selective growth advantages induced by the loss of tumor suppressor genes or amplification of oncogenes, particularly under stressful environmental conditions[94]. The primary cause of numerical aneuploidy is believed to be a mitotic error, which disrupts the accurate segregation of chromosomes[95]. These errors may stem from incorrect spindle-chromosome attachments, cohesion defects between sister chromatids and cytokinesis failure, as discussed in chapter 1.1.5. Failure in proper cell division can result in detrimental consequences such as whole genome doubling (WGD), leading to a tetraploid state with genetic instability[96]. When chromosome mis-segregation occurs, it typically produces two daughter cells with unequal chromosomal content: one cell lacking a whole chromosome or chromosome fragment, and the other carrying an excess.

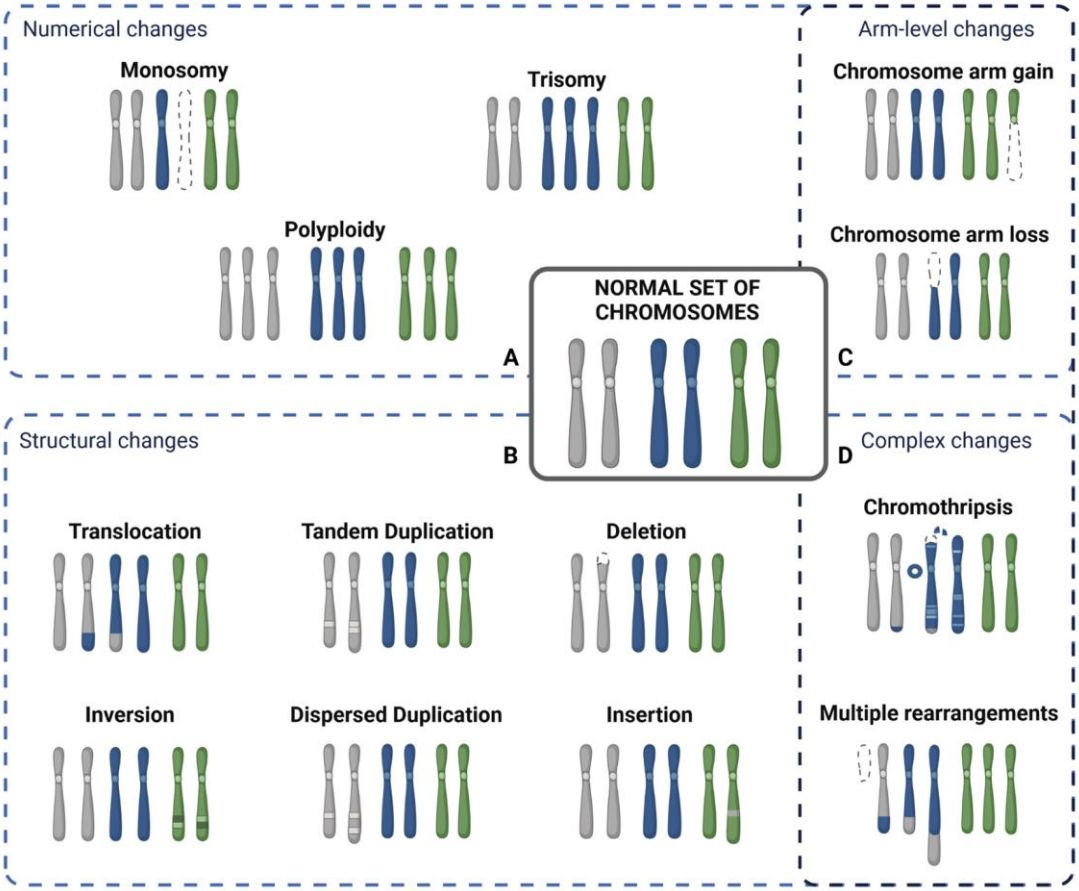

Figure 6|Structural and chromosomal changes of the genome. Chromosomal abnormalities can involve numerical deviations, such as the loss (monosomy) or gain (trisomy) of individual chromosomes, or the duplication of the entire chromosome set (polyploidy). Gains or losses at the level of chromosome arms may be classified as both numerical and structural forms of aneuploidy. Structural alterations include balanced rearrangements, such as inversions and balanced translocations, that preserve gene copy number, as well as unbalanced alterations. These include tandem duplications, where duplicated segments remain linked together), dispersed duplications, where duplicated segments are relocated, deletions, resulting in loss of DNA segments, and insertions, resulting in gain of DNA regions. Complex structural variants may span multiple chromosomes and include phenomena grouped under chromoanagenesis. One notable example is chromothripsis, characterized by extensive fragmentation and random reassembly of one or a few chromosomes, producing complex structural variants and sometimes leading to the formation of circular extrachromosomal DNA elements called double-minute chromosomes (adapted from Keuper et al., 2021[22]).

Structural aneuploidy encompasses subchromosomal alterations that may present as either balanced karyotype changes, such as translocations or inversions that preserve overall DNA content, or unbalanced karyotype changes, including duplications, deletions, or insertions that disrupt chromosomal integrity and have been found in 95% of investigated tumor genomes[73] (Fig. 6). While traditionally considered distinct from numerical abnormalities, structural variants can also arise as a consequence of mitotic errors. Defective chromosome segregation during mitosis may cause breakage of chromosomes, implicating aberrant mitosis as a contributor to structural abnormalities in cancer cells. In addition, defects in DNA repair and damage response pathways are key driver of structural rearrangements. Mutations in genes such as those associated with Fanconi anaemia or Ataxia telangiectasia compromise the cell's ability to correctly repair damaged DNA[97]. Disruption of HR, particularly through dysfunction of the BTRR complex required for HR associated dHJ dissoluation, as observed in Bloom syndrome (BS) and BS-like disorders, further impairs high-fidelity DNA repair[78,98–100]. Besides the HR repair, cells can chose more error-prone pathways such as SSA, aEJ or cNHEJ[74,82,101]. These mechanisms frequently result in deletions, translocations, or complex rearrangements, as discussed in chapter 1.1.6 (Fig. 5). Replication-associated errors represent another possibility for structural variation, as discussed in chapter 1.1.2 (Fig. 3). Persistent ssDNA, particularly at stalled replication forks, can give rise to one-ended DSBs, which, in the absence of external mutagens, are thought to be a primary source of DNA damage[25]. Indeed, replication stress has been frequently detected in early stages of tumorigenesis[102], further leading to the accumulation of DSBs, thereby reinforcing the strong mechanistic link between replication dysfunction and the emergence of structural chromosomal aberrations in cancer. BRCA1, frequently observed in ovarian and breast cancers, plays a central role in protecting stalled replication forks and facilitating high-fidelity HR repair. Its loss promotes tandem duplications, thought to arise through a “replication restart-bypass” mechanism followed by error-prone end joining or microhomology-mediated template switching[103]. In addition to HR, BRCA1 is also involved in mismatch repair processes, highlighting its broad role in preserving genome stability[104,105].

Structural chromosomal aberrations can have profound consequences for cellular homeostasis by disrupting key regulatory genes involved in cell cycle control, checkpoint activation, and DNA repair. Such disruptions often enhance genomic instability and contribute to cancer progression. For instance, in certain lymphomas, the *BCL-2* gene is placed under the control of the immunoglobulin heavy chain promoter by translocation t(14;18), leading to its overexpression and the inhibition of apoptosis[106]. Another example involves deletions at chromosome 13q in the retinoblastoma tumor suppressor gene *RB1*, leading to uncontrolled cell cycle progression[107]. Through a balanced translocation t (9; 22), the *BCR::ABL1* fusion gene or the so-called Philadelphia chromosome is formed, which leads to oncogene activation and promotes uncontrolled proliferation of immature white blood cells[108].

In addition to classical chromosomal alterations such as translocations and deletions, cancer genomes often exhibit highly complex structural rearrangements[109]. Chromoplexy, chromoanasynthesis, and chromothripsis, collectively defined as chromoanagenesis, have been described as major classes of such complex events[110] (Fig. 7). Chromoplexy is defined by a series of interconnected rearrangements that typically affect more than one chromosome and are likely initiated by a single event[111]. In contrast, chromoanasynthesis involves extensive rearrangements driven by various template-switching events during DNA replication. These are typically mediated by error-prone mechanisms such as mmBIR or FoSTeS[110,112]. Chromothripsis involves the shattering of a chromosome or chromosome fragment into many pieces, followed by haphazard and random reassembly, mostly via NHEJ[109,113]. This results in a rearrangement of genomic segments with alternating CN states. The catastrophic DNA breakage leading to chromothripsis is thought to occur in a single cellular event. One of its

oncogenic consequences is the loss of tumor suppressors, as observed in the *TP53* gene or by amplification of oncogenes, such as through the formation of extrachromosomal circular DNA fragments known as double-minute chromosomes, as described for members of the *MYC* oncogene family[109,114].

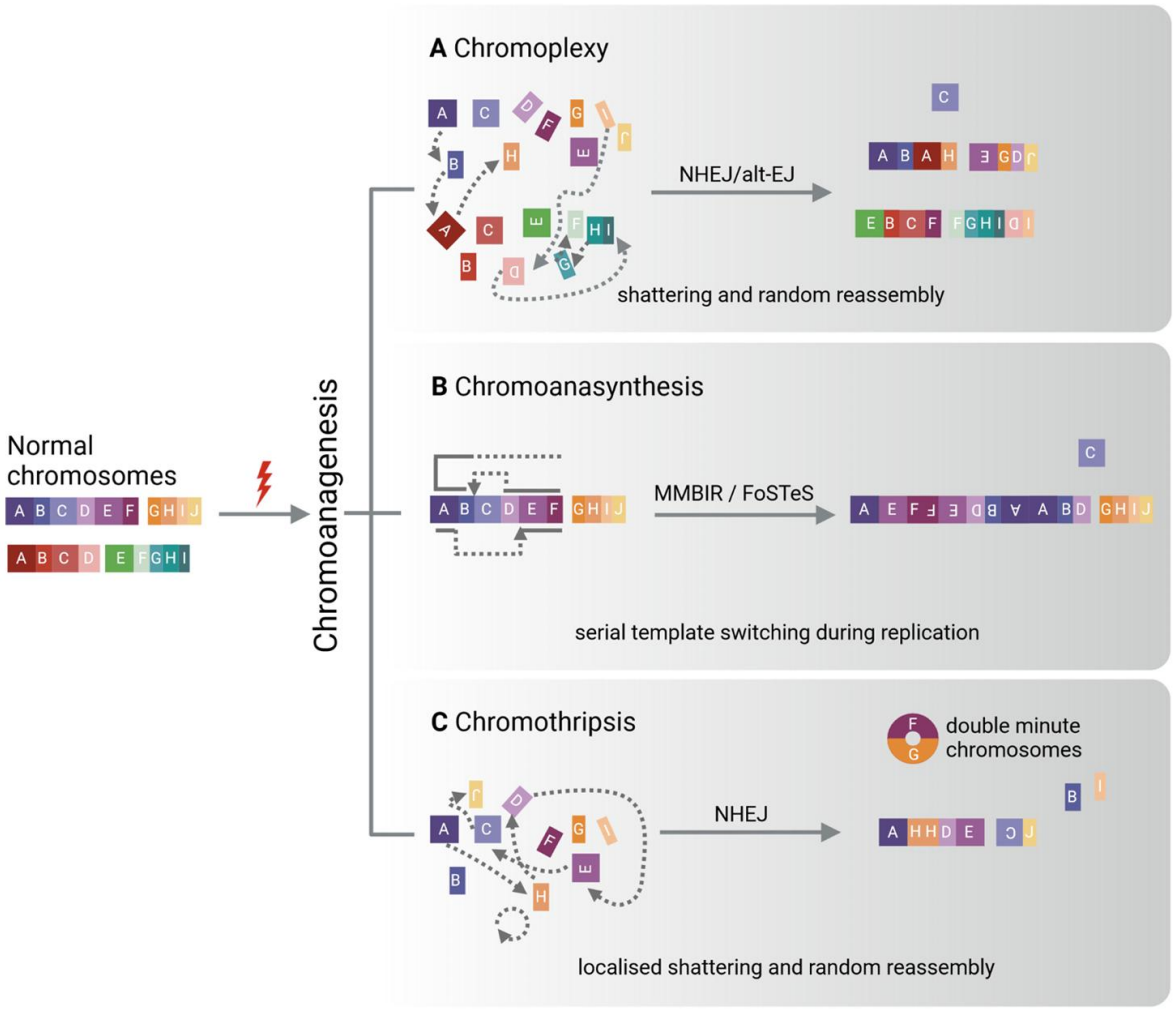

Figure 7|Complex genome rearrangements under the collective term chromoanagenesis. a, Chromoplexy involves a series of interdependent DNA rearrangements affecting multiple chromosomes, often occurring in a single catastrophic event. The rejoining of fragmented DNA is typically mediated by error-prone repair mechanisms such as non-homologous end joining (NHEJ) and alternative end joining (aEJ). **b,** Chromoanasynthesis is characterized by replication-based errors involving multiple template-switching events. This process is primarily driven by mechanisms such as microhomology-mediated break-induced replication (mmBIR) and fork stalling and template switching (FoSTeS). **c,** Chromothripsis results from the fragmentation of one or a few chromosomes or chromosomal regions, followed by random reassembly. This process is also largely dependent on NHEJ and can lead to the formation of circular extrachromosomal DNA elements, such as double-minute chromosomes (adapted from Keuper et al., 2021[22]).

Notably, a mechanistic link has been established between chromothripsis and the formation of MN, which often arise following mis-segregation of lagging chromosomes during aberrant mitosis and thus function as a marker for DNA damage[57,115] (Fig. 8). Chromosomes or fragments encapsulated in MN undergo delayed DNA replication, rendering them particularly vulnerable to replication stress and premature chromosome condensation, both of which can induce several DSBs[57]. These breaks are frequently repaired by NHEJ, leading to complex

reassembly and loss of genomic information, which is also frequently observed in chromothripsis[115]. MN are also functionally compromised due to frequent rupture of the nuclear envelope, which disrupts nuclear-cytoplasmic transport and permits access of cytosolic nucleases such as TREX1[116]. This can result in the accumulation of ssDNA and activation of the innate immune response.

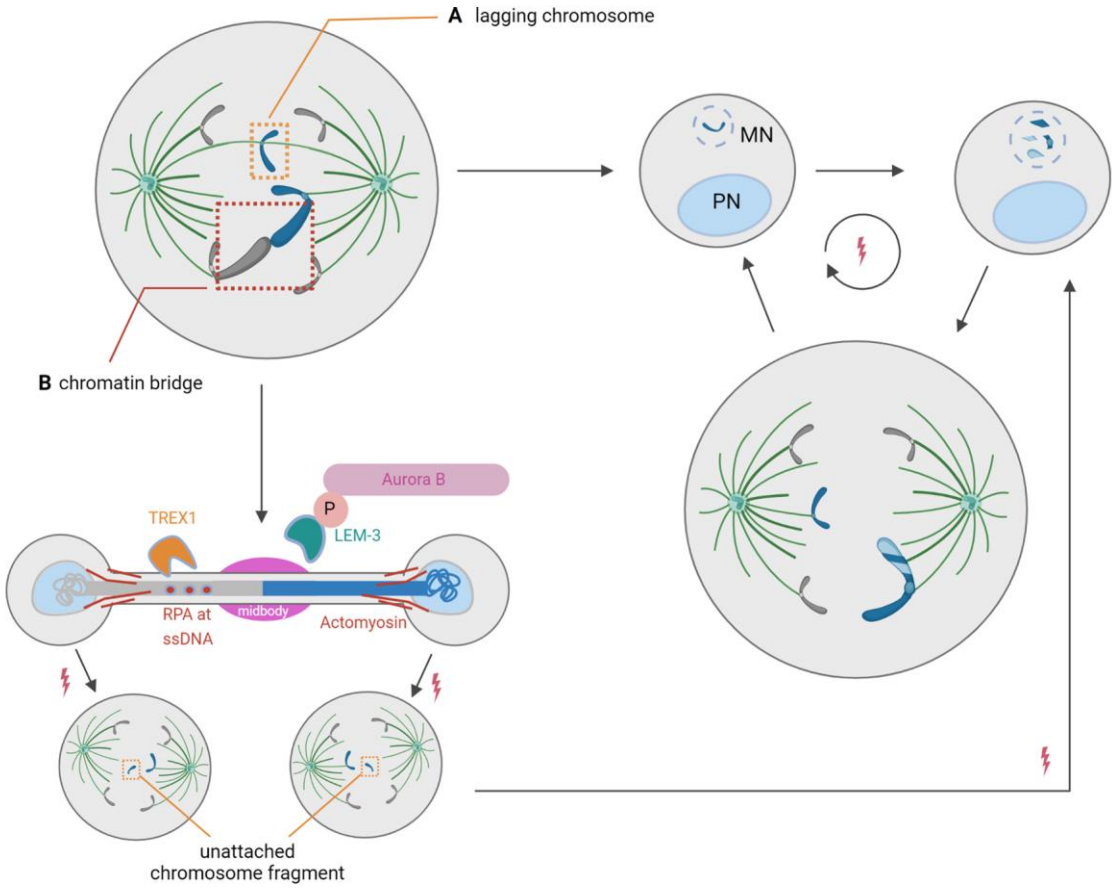

Figure 8|Contribution of lagging chromosomes and chromatin anaphase bridges to chromothripsis. a, Lagging chromosomes that fail to properly re-integrate and segregate during mitosis often become enclosed in micronuclei (MN), which are extranuclear compartments formed in daughter cells, separate from the primary nucleus (PN). **b,** Chromatin bridges, which can result from telomere-to-telomere chromosome fusions, may be cleaved by nucleases such as TREX1, generating RPA-coated single-stranded DNA (ssDNA) or disrupted during cytokinesis by actomyosin-mediated forces. These events can produce chromosome breaks at random sites and potentially lead to unattached chromosome fragments that are not incorporated into the main nucleus and may instead become sequestered in MN during the following cell cycle. Repeated cycles of fragment fusion and breakage, termed the breakage-fusion-bridge (BFB) cycle, can amplify genome instability and contribute to chromothripsis, a catastrophic rearrangement event. MN are structurally fragile and prone to nuclear envelope rupture and delayed or defective DNA replication. Erroneous replication gives rise to further fragmentation and random reassembly of chromosomal material, contributing to chromothripsis. DNA damage is indicated by red lightning symbols (adapted from Keuper et al., 2021[22]).

In addition to lagging chromosomes, anaphase bridges represent another cause of chromothripsis[54,58] (Fig. 8). These bridges are highly unstable and prone to mechanical breakage during cell division, often generating MN[58,117,118]. They can arise through the fusion of two chromosome ends, unresolved replication intermediates, or defects in chromosome condensation or decatenation. Dicentric chromosomes, generated by end-to-end fusions of broken chromosomes, such as those occurring during telomere crisis, are particularly prone

to forming such bridges and are associated with promoting genomic instability[54]. Telomere shortening exposes chromosome ends and activates DSB repair pathways, triggering fusion and initiating a cascade known as the breakage–fusion–bridge (BFB) cycle[119,120]. Repeated cycles of breakage and fusion can produce a cascade of structural rearrangements. Persistent anaphase bridges during cell division are often enclosed by the nuclear envelope during cytokinesis. However, excessive stretching can cause this membrane to rupture, allowing the cytosolic exonuclease TREX1 to access and degrade the DNA. This process results in the excessive generation of RPA-coated ssDNA and fragmented DNA, which can persist and subsequently become encapsulated into MN[54,116]. Extensive ssDNA formation also serves as a major substrate for antiviral cytidine deaminases, which can induce kataegis, a phenomenon characterized by clustered, localized hypermutations, such as cytosine-to-thymine substitutions. This mutational signature is frequently observed in cancer genomes and contributes to tumor heterogeneity and evolution[121]. In addition to TREX1-mediated degradation, two other mechanisms have been proposed to explain how persistent anaphase bridges can lead to chromothripsis. One mechanism involves the physical stretching of DNA during cytokinesis, where actomyosin-generated mechanical forces induce breakage of the DNA bridge. These breaks are often repaired through error-prone rejoining of the DNA fragments, leading to extensive genomic rearrangements as observed in chromothripsis. The mis-segregation of these fragmented chromosomes further promotes their encapsulation into MN, where additional DNA damage and fragmentation can occur, ultimately producing the characteristic pattern of chromothripsis[58]. Recent studies further suggest that the nuclease ANKLE1, similar to its ortholog LEM-3 in *Caenorhabditis elegans*, may contribute to chromatin bridge cleavage at the midbody. This activity appears to be regulated, at least in part, by phosphorylation via Aurora B kinase[122–124].

1.3 Ultrafine anaphase bridges: an underestimated origin of genomic instability

In addition to DAPI-positive chromatin anaphase bridges, which, if not properly resolved, contribute to genomic instability as discussed in Chapter 1.2, a distinct class of DNA structures known as ultra-fine anaphase bridges (UFBs) has been identified[125,126]. These extremely thin DNA threads, which represent persistent sister chromatid junctions, lack histone-containing nucleosomes and escape detection by conventional DNA dyes such as DAPI or Hoechst. UFBs were only discovered in 2007, due to their visualization through proteins such as the Bloom syndrome helicase (BLM) and Plk1-interacting checkpoint helicase (PICH), which specifically bind to and decorate these bridges[125,126]. Remarkably, UFBs are more common than chromatin bridges, appearing in nearly all cells during early anaphase, even under unperturbed conditions.[125]. However, their number decreases rapidly as cells progress through anaphase and are largely absent by telophase, suggesting that they are normally resolved during mitosis to prevent chromosomal rearrangements and genomic instability by chromosomal breakage and MN formation, as described for chromatin bridges[58,125] (Fig.8).

However, UFB persistence has been observed into late anaphase and telophase under certain conditions, such as replication stress or inhibition of chromosome decatenation. For instance, treatment with topoisomerase II inhibitors increases UFB frequency, while DNA polymerase inhibitors like aphidicolin also elevate UFB numbers and reveal the association of UFBs with DNA repair proteins such as FANCD2 and its heterodimer partner FANCI[125–127]. These proteins

are components of the Fanconi anemia pathway and are specifically enriched at CFSs, suggesting a mechanistic link to replication stress[127]. Notably, FANCD2/FANCI-positive UFBs are not observed following topoisomerase II inhibition, implying the existence of multiple UFB subtypes[127]. To date, five distinct classes of UFBs have been described, categorized by their chromosomal region from which they were formed and the underlying mechanisms by which they arise[117,126–130] (Fig. 9).

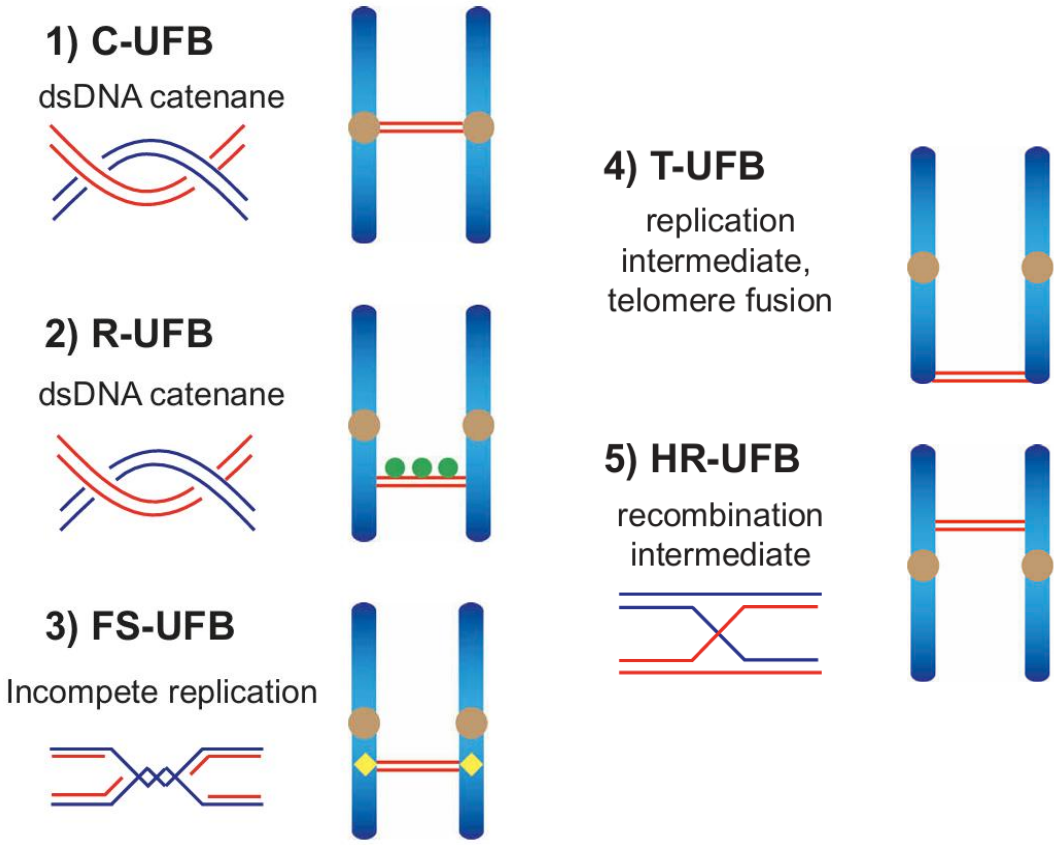

Figure 9|Proposed classification of five distinct types of ultrafine bridges (UFBs) observed during anaphase. 1) Centromeric UFBs (C-UFBs) arise from centromeric regions and contain DNA catenanes; they can be triggered by topoisomerase II alpha inhibition using ICRF-193. **2)** Ribosomal UFBs (R-UFBs) originate from catenated ribosomal DNA loci, containing catenanes, and are marked by the ribosomal DNA binding protein UBF (green dots). **3)** Fragile Site UFBs (FS-UFBs) are linked to under-replicated common fragile sites and are typically flanked by FANCD2/FANCI sister-foci (yellow diamonds). Replication stress induction, such as by the treatment with aphidicolin, triggers the formation of FS-UFBs. **4)** Telomeric UFBs (T-UFBs) stem from telomere regions, which are hard to replicate and often result from replication stress or TRF2 overexpression, which may promote telomeric fusions. **5)** Homologous Recombination UFBs (HR-UFBs) develop from unresolved recombination intermediates. A lack of Holliday junction-resolving enzymes such as GEN1 or MUS81, or the loss of 53BP1, can promote the formation of HR-UFBs (adapted and modified from Chan et al., 2018[130]).

Centromeric UFBs (C-UFBs) represent the most frequently observed subtype of UFBs and are commonly detected in unperturbed, normally dividing cells[125]. These structures originate from the centromeric regions of chromosomes, which are composed of highly repetitive DNA sequences and serve as the attachment site for spindle microtubules[131]. During mitosis, sister chromatids are held together by cohesin complexes, which are progressively removed from chromosome arms starting in prophase. However, at centromeres, cohesins are protected until the onset of anaphase, when the SAC is silenced[44] (see Chapter 1.1.4). Despite this

tightly regulated process, errors can arise, particularly due to incomplete resolution of intertwined centromeric DNA. This often results from defects in DNA decatenation, a process mediated by topoisomerase II alpha (TOP2A). TOP2A is highly enriched at centromeres and is essential for disentangling sister chromatids at the metaphase-anaphase transition[132]. When TOP2A activity is inhibited, such as by the inhibitor ICRF-193, the frequency of C-UFBs increases strongly[125]. In contrast, treatments that induce replication stress, like hydroxyurea or aphidicolin, do not significantly elevate C-UFB levels, suggesting a mechanism independent of replication completion[132–134]. Additionally, unresolved recombination events may contribute to the formation of C-UFBs, since homologous recombination within the repetitive elements of centromeric DNA can result in looped DNA intermediates[131,135].

In contrast to C-UFBs, which remain largely unaffected by replication stress, fragile site-UFBs (FS-UFBs) become markedly more prevalent upon treatment with replication inhibitors such as aphidicolin and hydroxyurea. These bridges are closely associated with CFSs, genomic regions that are particularly prone to replication challenges, and are characterized by the presence of the DNA repair proteins FANCD2 and its heterodimeric partner FANCI. These proteins typically localize to the origins of the bridges, forming what are referred to as “sister foci” [127,136]. The activity of FANCD2 and FANCI is regulated by monoubiquitination, a post-translational modification essential for their recruitment to stalled replication forks and subsequent formation of repair foci, thereby supporting the hypothesis that FS-UFBs arise primarily from segments of under-replicated DNA that persist into mitosis due to replication stress[127,137].

Another class of UFBs originates from unresolved intermediates formed during HR, a critical pathway for repairing DSBs. HR proceeds by utilizing a homologous template, forming a displacement loop (D-loop) that initiates DNA synthesis[138]. This repair process can generate dHJs[77], as discussed in chapter 1.1.6, which must be resolved before cell division. In mitotic cells, it is proposed that the primary mechanism for resolving dHJs is through dissolution mediated by the BTRR complex, composed of BLM, topoisomerase III alpha (TOP3A), RMI1, and RMI2, which promotes non-crossover outcomes[139,140]. In situations where the BTRR complex is dysfunctional or in the presence of excessive DNA damage, an alternative resolution pathway becomes active. This backup pathway involves structure-specific endonucleases such as SLX1-SLX4, MUS81-EME1 and GEN1, which can process dHJs and lead to either crossover or non-crossover products. The use of this pathway is associated with increased levels of sister chromatid exchange (SCE), particularly in the absence of BTRR activity[139,141,142]. These backup mechanisms by endonucleases are mainly active in mitosis, once the nuclear envelope disassembles, allowing their access to chromosomal DNA, typically in prometaphase[143]. Deficiencies in these resolvases result in the persistence of unresolved recombination intermediates, leading to a higher incidence of UFBs during anaphase. These structures are frequently coated with markers such as PICH, BLM, and RPA and are categorized as HR-UFBs. HR-UFBs are also more frequent in cells deficient in RAD51 or BRCA2, proteins central to the initiation and stabilization of HR[117]. Moreover, depletion of 53BP1, primarily known for accumulation at DSB sites and promoting NHEJ in G1, has been shown to impair HR during the S/G2 phases, suggesting that HR-UFBs may originate from replication-associated lesions that are inappropriately resulting in HR, indicating a link between late replication intermediates and recombination intermediates[144,145].. Notably, homologous recombination-UFBs (HR-UFBs) do not contain FANCD2 foci, distinguishing them from FS-UFBs, and unlike C-UFBs, they are thought to arise outside of centromeric regions, particularly in the context of intact 53BP1 function[117].. However, the exact chromosomal locations prone to HR-UFB formation remain to be further investigated.

Another class of UFBs has been described as ribosomal UFBs (R-UFBs), defining DNA catenanes that persist at ribosomal DNA (rDNA) loci. These bridges colocalise with the ribosomal RNA transcription factor UBF[128]. PICH foci were found to be present at rDNA loci in early mitosis and suggesting that R-UFBs are positive for PICH and TOP2A[146]. R-UFBs can be increased by the TOP2A inhibitor ICRF-193, suggesting that these regions also arise from decatenation defects similar to C-UFBs, which might be explained by the fact that the rDNA locus is transcriptionally active even in early mitosis[147], which could interfere with condensation[148,149].

Finally, UFBs have been identified at telomeric regions, referred to as T-UFBs. These structures are notably more frequent in cells treated with aphidicolin or lacking functional WRN protein, a member of the RecQ helicase family similar to BLM. T-UFBs are frequently associated with colocalization of both PICH and BLM along their entire length[129,150]. Although BLM plays a known role in telomere maintenance, particularly in WRN-deficient backgrounds, its presence throughout UFBs makes it challenging to assess its specific contribution at telomeric regions[127,129]. Telomeres are composed of long stretches of repetitive sequences, hardly to replicate and prone to forming G-quadruplex structures[151]. These features are similar to CFSs, making them susceptible to under-replication and structural instability. The shelterin complex, which binds and protects telomeric repeats, is thought to contribute to the regulation of replication at these sites[152]. T-UFBs do not appear to form under normal, unperturbed conditions but are induced under stress, such as overexpression of TRF2, a component of the shelterin complex involved in telomere protection, which once overexpressed induces telomere deletion and chromosome end-to-end fusion[150]. This finding suggests that T-UFBs may also originate from chromatin bridges formed by chromosome end-to-end fusions, as supported by the observation that these bridges often lack histones, likely due to their extensive stretching[54,153]. This can trigger mechanisms such as TREX1-mediated cleavage, generating excessive RPA-coated ssDNA regions[54], as described for chromatin bridges in chapter 1.2. Strikingly, this mechanism is commonly associated with complex genome rearrangements such as chromothripsis[121] and therefore might link particularly unresolved T-UFBs with genomic instability. Another potential contributor is ANKLE-1, a nuclease proposed to cleave anaphase bridges, although its specific role in T-UFB formation in human remains to be clarified[123,124,154].

Although the various classes of UFBs arise from distinct mechanisms and genomic regions, it is suggested that they share a common DNA processing mechanism[117]. The helicase PICH, along with BLM and RPA, has consistently been observed on multiple UFB types[130]. It is proposed that PICH is the first to be recruited, likely in response to the mechanical tension generated by separating sister chromatids at the onset of anaphase. Interestingly, PICH foci are already detectable in prometaphase on mitotic chromatin, particularly at sites of kinetochores[126,155]. Once bound, PICH facilitates the recruitment of BLM, which leads to the resolution of the DNA structures, subsequently generating stretches of ssDNA that are coated by RPA. However, notable exceptions to this canonical pathway have been described. For instance, as previously described for T-UFBs, RPA-coated ssDNA regions might form without the involvement of PICH and BLM, as observed in cases of TREX1 activity[121]. Moreover, two alternative C-UFB resolution pathways have been proposed, both lacking RPA-coated ssDNA. One includes the scaffold protein TOPBP1, which has been shown to play a critical role by recruiting TOP2A to centromeric UFBs, facilitating DNA decatenation in a BLM- and PICH-independent manner[156]. An additional mechanism has been recently proposed involving RIF1, which operates in a PICH-dependent but BLM-independent manner to resolve C-UFBs. RIF1 appears to prevent the formation of RPA-bound ssDNA while promoting the decatenation of dsDNA[157,158]. According to this model, PICH recruits both the BTRR complex and RIF1 to the

UFB, while the BTRR complex gets dissociated and rather acting as a backup pathway (Fig. 10). This mechanism may directly promote dsDNA decatenation without generating ssDNA.

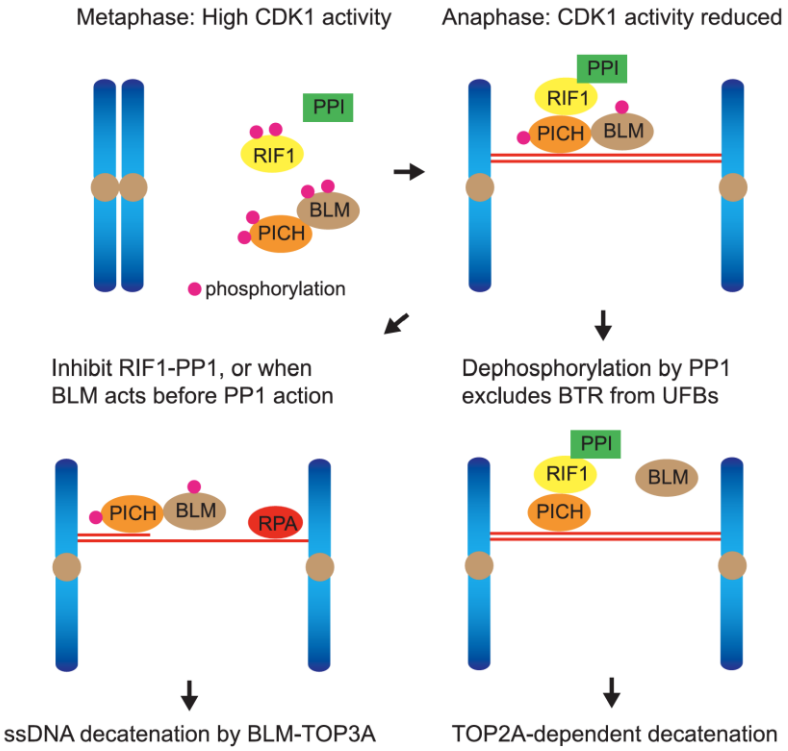

Figure 10|Proposed pathway choice between RIF1- and BLM-mediated C-UFB resolution. Prior to chromosome segregation, both RIF1 and BLM undergo phosphorylation. Dephosphorylation of RIF1 by PP1 promotes its activation, favoring a decatenation pathway mediated by topoisomerase II alpha (TOP2A) that proceeds without the formation of single-stranded DNA (ssDNA). As a backup pathway, potentially in case of a delay or dysfunctional RIF1 activation, BLM, together with its BTRR complex partners, facilitates decatenation through the generation of RPA-coated ssDNA as an intermediate (adapted from Kong et al., 2023[158]).

Further investigation is needed to understand the underlying mechanisms, including the identification of specific genomic loci where distinct classes originate, as well as additional interacting proteins that may help clarify the regulatory pathways involved.

1.4 Bloom syndrome helicase: a key player in DNA damage response

The Bloom syndrome protein BLM, encoded by the *BLM* gene located on chromosome 15q26.1, belongs to the highly conserved RecQ family of DNA helicases[159]. This family plays a vital role in preserving genome integrity across species. The gene comprises 21 coding exons, and the resulting protein functions as an ATP-dependent DNA helicase, translocating in the 3′ to 5′ direction to unwind duplex DNA structures[160,161].

Under normal cellular conditions, BLM predominantly localizes to promyelocytic leukemia nuclear bodies (PML-NBs), and to a lesser extent to the nucleolus and telomeres[162,163]. Upon DNA damage, BLM is dynamically redistributed to sites of repair and replication stress, where

it interacts with numerous key proteins and is phosphorylated in response to DSBs by ATM at Thr-99[164] and by ATR in an replication stress-associated manner at Thr-99 and Thr-122[165]. Further, it has also been shown that BLM is phosphorylated at multiple sites during mitosis by the kinases Cdc2, MPS1, and PLK1[166–168]. Although the exact functional consequences remain to be fully elucidated, it is suggested that mitotic phosphorylation may promote BLM dissociation from centromeres in early mitosis, thereby protecting these regions from unwanted entanglements[169,170].

Among its major functional partners is the BTRR complex, composed of TOP3A, RMI1, and RMI2, which is essential for resolving homologous recombination intermediates[171–173]. BLM also cooperates with the MRN complex (MRE11-RAD50-NBS1), ATM kinase and others together with BRCA1 within the BASC complex[174], as well as with RAD51 in response to DSBs[175]. Additional interactions include topoisomerase I and TOP2a[176,177], ubiquitinated FANCD2 at stalled forks[178], 53BP1[179], telomere-binding proteins TRF1 and TRF2[180], and the PICH helicase, a marker of UFBs[125]. The expression of BLM is dynamically regulated throughout the cell cycle, with minimal levels observed in the G1 phase, followed by a marked increase during S phase, which continues through G2 and mitosis[181].

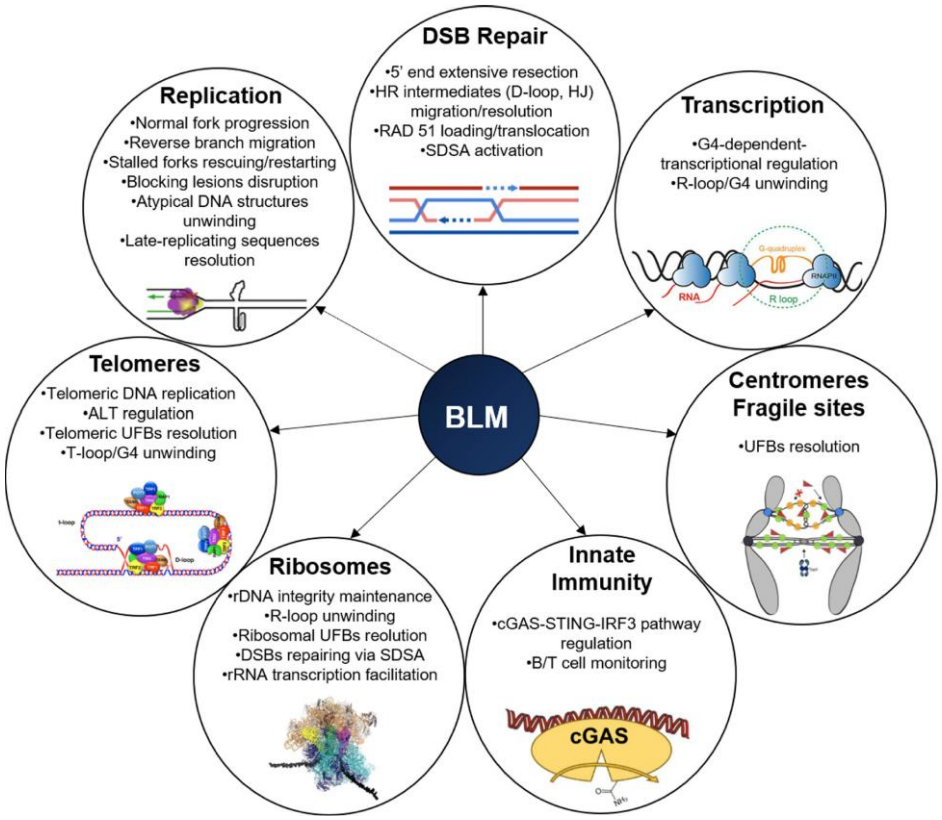

Figure 11|Schematic representation of BLM helicase functions across various cellular processes and locations. BLM contributes to multiple aspects of DNA metabolism, such as during DNA replication, where it facilitates fork progression, restart, reverse branch migration, and the resolution of interfering DNA structures. It also unwinds DNA and RNA structures such as G-quadruplexes (G4) and R-loops, which may hinder transcription. In the context of DNA repair, BLM plays a key role in homologous recombination (HR) by processing intermediates such as displacement loops (D-loops) and Holliday junctions (HJ). Additionally, BLM supports telomere replication, especially in cells that rely on the alternative lengthening of telomeres (ALT) pathway. Its activity at ribosomal DNA (rDNA) regions helps maintain rDNA stability, where R-loops are also commonly found. BLM is also proposed to be essential for resolving ultrafine anaphase bridges (UFBs) originating from centromeres, under-replicated regions, recombination intermediates, telomeres, and rDNA. Emerging evidence also suggests a role for BLM in modulating innate immune responses through the cGAS–STING–IRF3 signaling pathway (adapted from Ababou et al., 2021[161]).

BLM shows high affinity for a range of specialized DNA structures, including replication forks, D-loops, dHJs, G-quadruplexes, R-loops, and UFBs[161,182–184] (Fig. 11). Through its activity on these structures, BLM plays a key role in restarting stalled replication forks[185] and in HR, especially by facilitating DNA end resection in conjunction with EXO1, DNA2, the MRN complex, and ATM[186,187]. In response to HR-associated repair, BLM also promotes the SDSA pathway[188,189] and is instrumental in resolving dHJs through non-crossover-producing dissolution, thereby limiting SCE[79], which would otherwise strongly increase via backup resolvase pathways, as described in chapter 1.1.6 and 1.3. In addition, BLM has been implicated in telomere replication and maintenance, especially during alternative lengthening of telomeres[129,180,190] and helps to suppress genome instability by resolving R-loops and G-quadruplexes, both of which affect transcription[184]. The identification of BLM binding on UFBs, along with its co-localization with PICH and the observed increase in anaphase bridges, lagging chromosomes, and MN in BLM deficient cells, underscores its essential role during mitosis[125]. Specifically, BLM is proposed to facilitate resolution of persistent UFBs caused by incomplete replication, recombination intermediates, or topological entanglements[117], as discussed in Chapter 1.3. Recent findings also suggest that BLM contributes to the maintenance of rDNA, as it has been shown to localize at rDNA repeat regions[191]. This further supports a potential role for BLM in resolving R-UFBs. Additionally, BLM may influence the innate immune response, as MN observed in BLM-deficient cells have been found to be positive for cGAS, a critical DNA sensor that activates immune signaling pathways[192].

1.4.1 Defects in the BLM gene: a high predisposition to cancer development

Mutations in the BLM gene that result in a dysfunctional BLM protein are not necessarily embryonically lethal, but when inherited in a homozygous manner, they cause the Bloom syndrome (BS) disorder[193]. BS is a rare autosomal recessive disorder characterized by growth retardation, photosensitivity with facial rashes, microcephaly, moderate immune deficiencies and genomic instability[194]. The most severe consequence of BS is a marked predisposition to early-onset cancer, with an average age of diagnosis around 15 years for hematologic malignancies, around 29 years for solid tumors, and a median survival age of approximately 36 years[195]. Notably, there is no restriction to a specific cancer type and multiple distinct primary tumors are often observed[196].

A hallmark feature of BS is the strongly elevated rate of SCE, distinguishing it from other disorders impairing DNA repair and can therefore be utilized as a clinical diagnostic marker for BS[161,197–199]. Interestingly, mutations in other components of the BTRR complex can lead to BS-like syndromes, which share similar phenotypes, including growth defects and elevated SCE levels, though these cases often show a less severe phenotype compared to mutations in the *BLM* gene[99,100,200].

The high frequency of SCE has been widely proposed to be the major driver of genomic instability in BS, potentially due to the loss of heterozygosity (LOH)[197,201,202]. In addition, BS cells display an increased number of MN, further highlighting the genome destabilizing effects of BLM deficiency[203]. Together, the various features of BLM collectively emphasize the critical role of BLM in maintaining genomic integrity and preventing tumorigenesis, as further proven by genomic alterations found in BLM-deficient cells by the activation of alternative, error-prone

pathways[204,205]. However, the precise mechanisms by which BLM contributes to genomic stability remain incompletely understood. Dissecting its distinct roles at specific stages of the cell cycle may provide further insight into its genome maintenance functions.

1.5 The AID-system: controlled protein degradation

The ability to modulate protein levels with high temporal precision is of enormous value for dissecting complex biological processes. One effective approach is the auxin-inducible degron (AID) system, which was originally characterized in plants and later adapted for use in mammalian systems[206,207] (Fig. 12). The AID system allows the study of protein function by enabling rapid and reversible depletion of target proteins[208]. Its ability to tightly control protein levels is particularly advantageous when studying the separation of cell cycle-specific functions or investigating essential proteins, where permanent gene knockout would interfere with critical cellular functions or compromise cell survival.

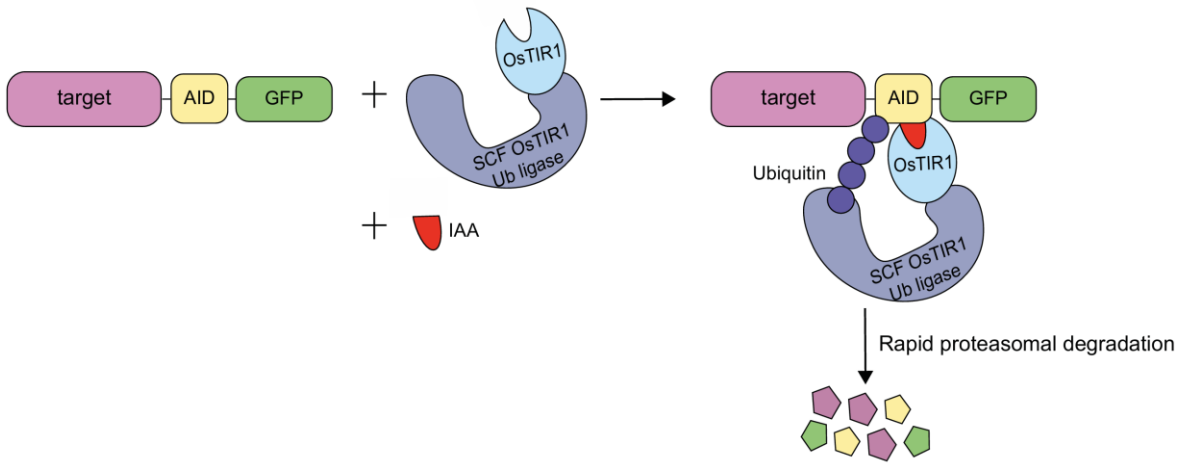

Figure 12|Schematic illustrating auxin-inducible degradation of a target protein via the proteasome. The protein of interest, is endogenously tagged with an auxin-inducible degron (AID) domain, optionally combined with a fluorescent marker such as the green fluorescence protein (GFP). Co-expression of the plant-derived TIR1 protein enables the assembly of the SCF E3 ubiquitin ligase complex. Upon the addition of the plant hormone auxin (indole-3-acetic acid, IAA), TIR1 binds to the AID domain, promoting the ubiquitination and subsequent rapid degradation of the AID-tagged protein by the proteasome.

The AID system relies on the fusion of the protein of interest with an AID tag, comprising the plant protein IAA17 of *Arabidopsis thaliana*[207]. This tagging can be achieved using genome editing tools such as CRISPR/Cas9, allowing for precise, endogenous modification. Upon the addition of the plant hormone auxin, such as indole-3-acetic acid (IAA) and the presence of the plant F-box protein TIR1, the tagged protein is recognized by the SCF E3 ubiquitin ligase complex. This leads to its ubiquitination and subsequent degradation via the proteasome. Importantly, this process is reversible upon removal of auxin, enabling controlled, time-sensitive manipulation of protein levels in living cells[206].

1.6 Aim of the study

To maintain genomic stability throughout the cell cycle, cells depend on a complex network of mechanisms to detect and repair DNA damage caused by both endogenous and exogenous stressors. Failure to correctly repair DNA lesions can result in their transmission to daughter cells, potentially leading to the accumulation of mutations, genomic instability, and ultimately, tumorigenesis. A less widely appreciated yet significant contributor to genomic instability is the presence of sister chromatid junctions, particularly UFBs. If persisting unresolved during mitosis, these junctions can give rise to anaphase bridges, physical connections between sister chromatids that should separate toward the opposite poles during anaphase. Failure to resolve these bridges before cell division can have detrimental consequences. They can either cause cytokinesis failure, resulting in whole genome doubling (WGD) and polyploidy if they are sustained, or breakage can occur that generates chromosome fragments, potentially leading to chromosome mis-segregation. These fragments may then become encapsulated into MN in the next G1 phase, where they are at increased risk of further fragmentation and chromothripsis, events with severe consequences for genomic integrity.

This study focuses on the investigation of cell cycle–specific functions of proteins associated with preventing persistent sister chromatid junctions, especially under mild replication stress. These proteins may act either by suppressing the formation of such connections or by actively resolving them during mitosis. Some may also serve primarily as markers that recruit other factors directly responsible for resolving these bridges. Besides well-known UFB binding proteins such as PICH and FANCD2, another key player in this process might be the BLM helicase, a central DNA repair protein that localizes to anaphase bridges. Although their association with UFBs is well known, the underlying mechanisms remain poorly understood.

To examine the role of these proteins, this study aims to take advantage of the AID system by combining CRISPR/Cas9-based genome editing and a modular cloning strategy to endogenously tag proteins of interest. This approach facilitates the dissection of protein function at specific stages of the cell cycle and allows integration with additional tags, such as fluorescent proteins, facilitating live-cell imaging or biochemical analyses like protein pulldown.

BLM is of particular interest due to its broad involvement in various DNA repair and replication processes across the cell cycle. However, the individual contributions of its distinct functions remain difficult to untangle. By selectively manipulating BLM levels using the AID system, this study aims to reveal how its activity during specific cell cycle stages contributes to the maintenance of genomic stability.

2. Materials

2.1 Equipment

Table 2|List of equipment

Equipment	Manufacturer
Agarose gel documentation system	Intas Science Imaging Instruments GmbH, Göttingen, Germany
Agarose gel electrophoresis system	Nippon genetics EUROPE GmbH, Düren, Germany
Automated microscope stage MS-2000 XYZ	Applied Scientific Instrumentation, Eugene, USA
Blotting paper Whatman 3 mm	A. Hartenstein GmbH, Würzburg, Germany
C18 extraction disks silica Empore™ 47 mm	CDS Analytical LLC, Oxford, USA
Cell counter Countess™ II automated	Thermo Fisher Scientific, Inc., Waltham, USA
Cell counting chamber slides Countess™	Thermo Fisher Scientific, Inc., Waltham, USA
Cell culture black glass-bottom 10-well CELLview plate	Greiner Bio-One, Kremsmünster, Austria
Cell culture black glass-bottom 96-well plate	Greiner Bio-One, Kremsmünster, Austria
Cell culture dish (all sizes)	Sarstedt AG & CO, Nürmbrecht, Germany
Cell culture flask (all sizes)	Sarstedt AG & CO, Nürmbrecht, Germany
Cell culture multiwell plates	Sarstedt AG & CO, Nürmbrecht, Germany
Centrifuge Rotina 420R	Andreas Hettich GmbH & Co. KG, Tuttlingen, Germany
Cloning discs sterile ø3.2 mm	Sigma-Aldrich, St.Louis, USA
CO_2 incubator Heracell™	Thermo Fisher Scientific, Inc., Waltham, USA
Confocal Scanner CSU-X1	Rota Yokogawa GmbH & Co. KG, Wehr, Germany
Confocal spinning disk microscope CSU-W1 Sora	Nikon Corporation, Tokyo, Japan
CoolSNAP HQ2 monochrome camera	Teledyne Photometrics, Tucson, USA
Coverslips 0.17 mm, 1.5H, round, ø12 mm	Carl Roth GmbH + Co. KG, Karlsruhe, Germany
EASY-nLC™ 1200 system	Thermo Fischer Scientific, Inc., Waltham, USA
Electrophoresis power supply PowerPac™ HC	Bio-Rad Laboratories, Inc., Hercules, USA
Epifluorescence microscope Zeiss Axio Observer Z1	Carl Zeiss AG, Oberkochen, Germany
Epifluorescence microscope Eclipse Ti2-E with Spectra III	Nikon Corporation, Tokyo, Japan
Flow Cytometer Attune™ NxT	Thermo Fisher Scientific, Inc., Waltham, USA
Gel imaging system Azure c500	Azure Biosystems, Inc., Dublin, USA
Heat Block	Störk Tronic, Stuttgart, Germany
Homogenizer Bandelin HD 2200	Bandelin electronic GmbH & Co. KG, Berlin, Germany

HPLC column PicoTip Emitter™	New Objective, Inc., Littleton, USA
Inverse-Microscope AE 2000-Trino	Motic®, Vacnouver, Canada
LaserStack (473 nm, 561 nm, 640 nm)	Intelligent Imaging Innovations, Denver, USA
Magnetic separation rack	Thermo Fisher Scientific, Inc., Waltham, USA
Mass spectrometer Q Exactive™ HF	Thermo Fischer Scientific, Inc., Waltham, USA
Mass spectrometry Nanospray Flex™ Ion Source	Thermo Fisher Scientific Inc., Waltham, USA
Microcentrifuge Eppendorf 5415R refrigerated	Eppendorf SE, Hamburg, Germany
Microscope slide SuperFrost Plus™ 25x75 mm	Thermo Fisher Scientific, Inc., Waltham, USA
Multiwell plate Microtiter™ transparent 96-well	Thermo Fisher Scientific, Inc., Waltham, USA
Nitrocellulose blotting membrane Amersham™ Protran® (0.45 µm)	GE HealthCare Technologies, Inc., Chicago, USA
Objectives 20x air, 40x air, 60x oil	Carl Zeiss AG, Oberkochen, Germany
PH meter inoLab® pH7110	Xylem Analytics Germany Sales GmbH & Co. KG, Weilheim, Germany
Plate reader GloMax® Explorer	Promega Corporation, Madison, USA
Polyacrylamid electrophoresis system Mini-PROTEAN®	Bio-Rad Laboratories, Inc., Hercules, USA
Polyacrylamid Mini-PROTEAN® short plates	Bio-Rad Laboratories, Inc., Hercules, USA
Polyacrylamid Mini-PROTEAN® spacer plates (1.0 mm)	Bio-Rad Laboratories, Inc., Hercules, USA
Precision Scale PCB	KERN & SOHN, Balingen, Germany
Real-Time PCR Detection System CFX96 Touch	Bio-Rad Laboratories, Inc., Hercules, USA
Rotator SB3 Stuart	Cole-Parmer, Vernon Hills, USA
Safety bench hood Hersafe™	Thermo Fisher Scientific, Inc., Waltham, USA
Sonication device Bioruptor® Pico	Diagenode LLC., Denville, USA
Spectrophotometer DS-11	DeNovix Inc., Wilmington, USA
Thermal Cycler C1000 Touch	Bio-Rad Laboratories, Inc., Hercules, USA
Tube roller LLG-uniRoller 10	Lab Logistics Group, Meckenheim, Germany
UHPLC silica media ReproSil-Pur C18-AQ	Dr. Maisch, Ammerbuch, Germany
Ultrapure lab water Elga Purelab® flex 4 Typ 1	Veolia Water Technologies Deutschland GmbH, Celle, Germany
Ultrasonic bath SONOREX	Bandelin electronic GmbH & Co. KG, Berlin, Germany
UV-Transilluminator 312 nm	Bachofer GmbH & Co. KG, Reutlingen, Germany
Vacuum pump Integra Vacusafe	Integra Bioscience GmbH, Biebertal, Germany
Vortex Genie 2	Scientific Industries, Inc., Bohemia, USA
Water bath Typ1008	GFL GmbH, Burgwedel, Germany

2.2 Chemicals

Table 3|List of chemicals

Chemical	Manufacturer
2-Chloroacetamide	Sigma-Aldrich, St. Louis, USA
4-(2-hydroxyethyl)-1-piperazineethanesulfonic acid (HEPES)	VWR International, Darmstadt, Germany
Acetic acid	Sigma-Aldrich, St.Louis, USA
Agarose	Carl Roth GmbH + Co. KG, Karlsruhe, Germany
Albumin Bovine Serum (BSA)	BWR Life Sciences, Leuven, Belgium
Ammonium chloride (NH_4Cl)	Sigma-Aldrich, St. Louis, USA
Ammonium persulfate (APS)	Sigma-Aldrich, St.Louis, USA
Bromophenol blue	Sigma-Aldrich, St.Louis, USA
Dimethylsulfoxide (DMSO)	Carl Roth GmbH + Co. KG, Karlsruhe, Germany
Dipotassium phosphate (KH_2PO_4)	Carl Roth GmbH + Co. KG, Karlsruhe, Germany
Disodium hydrogen phosphate (Na_2HPO_4)	Carl Roth GmbH + Co. KG, Karlsruhe, Germany
Dithiothreitol (DTT)	Carl Roth GmbH + Co. KG, Karlsruhe, Germany
Ethanol (EtOH)	Sigma-Aldrich, St.Louis, USA
Ethylenediaminetetraacetic acid (EDTA)	Sigma-Aldrich, St.Louis, USA
Glycerol	Sigma-Aldrich, St.Louis, USA
Glycine	AppliChem, Darmstadt, Germany
H_2O nuclease-free	Sigma-Aldrich, St.Louis, USA
Hydrochloric acid (HCl)	Thermo Fisher Scientific, Inc., Waltham, USA
Isopropanol	Thermo Fisher Scientific, Inc., Waltham, USA
LB Agar	Carl Roth GmbH + Co. KG, Karlsruhe, Germany
Magnesium chloride ($MgCl_2$)	Sigma-Aldrich, St.Louis, USA
Methanol analytical reagent grade	Thermo Fisher Scientific, Inc., Waltham, USA
Nonidet P40 (NP-40) 10%	BioVision, In., Milpitas, USA
Paraformaldehyde (PFA)	Sigma-Aldrich, St.Louis, USA
Polyethylene glycol (PEG)	Sigma-Aldrich, St.Louis, USA
Ponceau S	Sigma-Aldrich, St.Louis, USA
Potassium chloride (KCl)	Carl Roth GmbH + Co. KG, Karlsruhe, Germany
Skim milk powder	SERVA Electrophoresis, Heidelberg, Germany
Sodium azide (NaN_3)	Sigma-Aldrich, St.Louis, USA
Sodium chloride (NaCl)	Sigma-Aldrich, St.Louis, USA
Sodium citrate	Sigma-Aldrich, St.Louis, USA
Sodium deoxycholate	Carl Roth GmbH + Co. KG, Karlsruhe, Germany
Sodium dodecyl sulfate (SDS)	Carl Roth GmbH + Co. KG, Karlsruhe, Germany
Tetramethylethylenediamine (TEMED)	AppliChem, Darmstadt, Germany

Tris	Carl Roth GmbH + Co. KG, Karlsruhe, Germany
Triton X-100	Carl Roth GmbH + Co. KG, Karlsruhe, Germany
Trypan blue	Thermo Fisher Scientific, Inc., Waltham, USA
Tween® 20	Sigma-Aldrich, St.Louis, USA
Urea	AppliChem, Darmstadt, Germany
β-Mercaptoethanol	AppliChem, Darmstadt, Germany

2.3 Buffers and Solutions

Table 4| List of prepared buffers and solutions

Name	**Composition**
General	
Phosphate-buffered saline (PBS) 10x	1.37 M NaCl, 27 mM KCl, 100 mM Na_2HPO_4, 18 mM KH_2PO_4 in H_2O
Phosphate-buffered saline with Tween-20 (PBST) 1x	0.1 % Tween-20 in 1x PBS
TAE 50x	2 M Tris, 0.05 M EDTA (pH 8.0), 1 M acetic acid
TE buffer 1x (pH 8.0)	10 mM Tris, 1 mM EDTA in H_2O
Tris-buffered saline (TBS) 10x (pH 7.5)	500 mM Tris, 1.5 M NaCl
Tris-buffered saline with Tween-20 (TBST 1x)	0.1 % Tween-20 in 1x TBS
Molecular biology	
IVC reaction buffer 5x	100 mM HEPES pH 7.5, 750 mM KCl, 25 mM $MgCl_2$, 2.5 mM DTT, 0.5 mM EDTA in H_2O
Gibson mix 2x	5x ISO buffer (500 mM Tris-HCl (pH 7.5), 50 mM $MgCl_2$, 50 mM DTT, 5 mM NAD, 1 mM/dNTP, 25 % Polyethylene glycol (PEG)-8000 in H_2O), 0.008 U/µl T5 exonuclease, 0.04 U/µl Phusion DNA polymerase, 8 U/µl Taq DNA ligase in H_2O
Precipitation buffer for solid-phase reversible immobilization (SPRI) beads	18 % PEG-8000, 1 M NaCl, 0.055 % Tween-20, 10 mM Tris-HCl (pH 8.0), 1 mM EDTA in nuclease-free H_2O
Cell culture	
Freezing mix	10% DMSO in fetal bovine serum (FBS)
Chromosome spreads	
Hypotonic solution	75 mM KCl in H_2O
Fixative solution	25% acetic acid, 75 % methanol
Sorensen phosphate buffer (pH 6.8) 1x	50 % 0.1 M Na_2HPO_4, 50 % 0.1 M KH_2PO_4
Salt sodium citrate (SSC) buffer (pH 7.0) 20x	3 M NaCl, 300 mM sodium citrate
Colony formation assay	
Crystal violet fixative	20 % methanol, 0.5 % w/v crystal violet in H_2O
Cell lysis	

Radioimmunoprecipitation assay (RIPA) buffer (pH 7.5)	10 % NP-40, 10 % sodium deoxycholate, 5 M NaCl, 0.5 M EDTA, 1 M Tris-HCl (pH 7.5), 1x protease inhibitor cOmplete Mini EDTA-free and 1x phosSTOP phosphatase inhibitor
SDS-polyacrylamide gel electrophoresis (SDS-Page) and Western blotting	
Blocking solution	5 % skim milk/3 % BSA in 1x TBST
Bradford solution	20 % Bradford reagent in H_2O
Laemmli buffer (pH 6.8) 1x	62.5 mM Tris-HCl (pH 6.8), 2 % SDS, 10 % glycerol, 0.01 % bromphenol blue, 1 % β-mercaptoethanol in H_2O
Ponceau solution	0.2 % Ponceau S, 1 % acetic acid in H_2O
Resolving gels (pH 8.8) 2x 7.5 %	3.75 ml 30 % acrylamide; 3.75 ml resolving gel SDS-buffer (pH 8.8); 7.5 ml H_2O, 300 µl 10% APS, 15 µl TEMED
Resolving gel SDS-buffer (pH 8.8)	1.5 M Tris-HCl (pH 8.8), 0.4% (w/v) SDS in H_2O
Running buffer (pH 8.3) 1x	25 mM Tris-HCl (pH 8.3); 190 mM glycine; 0.1 % SDS in H_2O
Stacking gels (pH 6.8) 2x 5 %	0.8 ml 30% acrylamide, 1.2 ml stacking gel SDS-buffer pH 6.8, 3 ml H_2O, 50 µl 10% APS, 5 µl TEMED
Stacking gel SDS-buffer (pH 6.8)	0.5 M Tris-HCl (pH 6.8), 0.4 % (w/v) SDS in H_2O
Wet-Transfer buffer 1x	25 mM Tris, 192 mM glycine, 20 % (v/v) methanol, in H_2O

Microscopy	
Aldehyde deactivation buffer	50 mM NH_4Cl in 1x PBS
Blocking solution for methanol-fixation	5 % FBS, 3 % Triton X-100, 1 % NaN_3 in 1x PBS
Blocking solution for PFA-fixation	3% BSA, 1% NaN_3 in 1x PBST
Fixation solution with methanol	100 % ice-cold methanol
Fixation solution with PFA	3% PFA, 0.1% Triton X-100 in 1x PBS
Permeabilization buffer for PFA-fixation	0.5% Triton X-100 in 1x PBS
Staining solution with DAPI	10 µg/ml RNase, DAPI 0.1 µg/ml in 1x PBS
Staining solution with Sytox™ green	10 µg/ml RNase, 167 nM Sytox™ green in 1x PBS
Pull downs	
Elution buffer I	2 M Urea, 50 mM Tris (pH 7.5), 2 mM DTT, 20 µg/ml trypsin in H_2O
Elution buffer II	2 M Urea, 50 mM Tris (pH 7.5), 10 mM chloroacetamide in H_2O
Fast-IP buffer	150 mM NaCl, 5 mM EDTA (pH 7.5), 5 mM Tris (pH 7.5), 1 % Triton X-100, 0.5 % NP-40, 1x protease inhibitor cOmplete Mini EDTA-free and 1x phosSTOP phosphatase inhibitor, in H_2O
High salt wash buffer	50 mM HEPES (pH 7.5), 500 mM NaCl, 1 % Triton X-100 in H_2O
Low salt wash buffer	50 mM HEPES (pH 7.5), 140 mM NaCl, 1 % Triton X-100 in H_2O
Shearing buffer	1 % SDS, 10 µM EDTA (pH 8.0), 50 mM Tris (pH 8.0) in H_2O

IP RIPA buffer	10 mM Tris-HCl (pH 7.5), 150 mM NaCl, 0.5 mM EDTA, 0.1 % SDS, 1 % Triton X-100, 1 % deoxycholate, 2.5 mM $MgCl_2$, 1 mM PMSF, 1x protease inhibitor cOmplete Mini EDTA-free and 1x phosSTOP phosphatase inhibitor, in H_2O, pH adjusted at 4°C
Wash buffer I	10 mM TRIS pH 7.5, 150 mM NaCl, 0.25% NP-40 in H_2O
Wash buffer II	10 mM TRIS pH 7.5, 150 mM NaCl in H_2O
Mass spectrometry	
Buffer A	0.1 formic acid
Buffer B	80 % acetonitrile, 0.1 % formic acid
Buffer A*	2 % acetonitrile, 0.1 % TFA pH 2

2.4 Molecular biology

Table 5| List of molecular biological reagents and cloning buffers

Reagents and buffers	**Manufacturer**
DMSO	New England Biolabs, Ipswich, USA
dNTPs 10 mM	New England Biolabs, Ipswich, USA
Ethidium bromide	Thermo Fisher Scientific Inc., Waltham, USA
FastDigest buffer 10x	Thermo Fisher Scientific, Inc., Waltham, USA
Gel loading dye, purple 6x	New England Biolabs, Ipswich, USA
rNTP each 100 mM	New England Biolabs, Ipswich, USA
$MgCl_2$	New England Biolabs, Ipswich, USA
Pfu buffer 10x	Agilent Technologies, Inc., Santa Clara, USA
Phusion GC buffer 5x	New England Biolabs, Ipswich, USA
Phusion HF buffer 5x	New England Biolabs, Ipswich, USA
Quick ligation reaction buffer 2x	New England Biolabs, Ipswich, USA
Quick-Load 1 kilobase (kb) DNA ladder	New England Biolabs, Ipswich, USA
Quick-Load 100 base pairs (bp) DNA ladder	New England Biolabs, Ipswich, USA
rCutSmart™ buffer	Thermo Fisher Scientific, Inc., Waltham, USA
Sera-Mag SpeedBeads carboxylate-modified	GE HealthCare Technologies, Inc., Chicago, USA
T4 ligase buffer 10x	New England Biolabs, Ipswich, USA
T7 reaction buffer 10x	New England Biolabs, Ipswich, USA
ThermoPol buffer 10x	New England Biolabs, Ipswich, USA
Plasmid-Safe™ buffer 10x	Biozym Scientific GmbH, Hessisch Oldendorf, Germany
ATP 10 mM	Biozym Scientific GmbH, Hessisch Oldendorf, Germany

Table 6| List of general enzymes

Enzyme	Manufacturer
Pfu Turbo DNA polymerase	Agilent Technologies, Inc., Santa Clara, USA
Phusion DNA polymerase	New England Biolabs, Ipswich, USA
Plasmid-Safe™ DNase	Biozym Scientific GmbH, Hessisch Oldendorf, Germany
Proteinase K	Carl Roth GmbH + Co. KG, Karlsruhe, Germany
Quick ligase	New England Biolabs, Ipswich, USA
RNase A	Macherey-Nagel, Düren, Germany
T4 DNA ligase	New England Biolabs, Ipswich, USA
Taq DNA polymerase	New England Biolabs, Ipswich, USA
Cas9	New England Biolabs, Ipswich, USA
Turbo™ DNase	Thermo Fisher Scientific, Inc., Waltham, USA
T7 RNA polymerase mix	New England Biolabs, Ipswich, USA
FastAP	Thermo Fisher Scientific, Inc., Waltham, USA

Table 7|List of restriction enzymes

Enzyme	Manufacturer
BbsI FastDigest	Thermo Fisher Scientific, Inc., Waltham, USA
BsaI-HFv2	New England Biolabs, Ipswich, USA
DpnI	New England Biolabs, Ipswich, USA
PstI	New England Biolabs, Ipswich, USA
SspI-HF	New England Biolabs, Ipswich, USA

2.5 Plasmids

Table 8|List of plasmids

Name	Used for	Size (bp)	Bacterial resistance	Manufacturer
pIDC	Linear Gibson Assembly backbone vector	1832	Chloramphenicol	Kind gift of Michael Taschner
pMK292 (mAID-mCherry2-NeoR)	Origin for Neomycin resistance cassette	6108	Ampicillin	Addgene, Watertown, USA (#72830)
pMK293 (mAID-mCherry2-Hygro)	Origin for Hygromycin resistance cassette	6377	Ampicillin	Addgene, Watertown, USA (#72831)
pSG3651 pLIBT7_A	Golden Gate backbone vector	5159	Ampicillin	Kind gift of Michael Taschner

pX330-U6-Chimeric_BB-CBh-hSpCas9	Cas9/sgRNA vector	8484	Ampicillin	Addgene, Watertown, USA (#42230)

2.6 Oligonucleotides and primers

Table 9| List of general primers

Description	Direction	Region	Sequence (5' – 3')
Primer 1_Fw	Forward (fw)	pSG2651 vector left side of insertion region	CGAAGCTCTTCCCGATAATACGAC
Primer 2_Rv	Reverse (rev)	GFP start	CCGTAGGTGGCATCGCCCTC
Primer 3_Fw	Fw	SMC5 HL	CAAACACATGGAATTTAAAGGCTTTCC
Primer 3_Fw	Fw	AID	TAAAGATCCAGCCAAACCTCC
Primer 4_Rv	Rev	PGK promoter of Hygro	GTGTAGCGCCAAGTGCCCAG
Primer 4_Rv_Neo	Rev	Neo SV40 promoter	CCTGGGGACTTTCCACACCCTAAC
Primer 5_Fw	Fw	GFP	CCAGTCCGCCCTGAGCAAAG
Primer 6_Rv	Rev	Hygro middle	GTTCGGTTTCAGGCAGGTCTTGCAAC
Primer 6_Rv_Neo	Rev	Neo middle	CTCTTCGTCCAGATCATCCTG
Primer 7_Fw	Fw	Hygro start	CTCACCGCGACGTCTGTCG
Primer 7_Fw_Neo	Fw	Neo start	GCTATTGGGCGAAGTGCCGGG
Primer 8_Fw_Neo	Fw	Neo ende	CCTTCTTGACGAGTTCTTCTGAG
Primer new	Rev	GFP start	GCAGATGAACTTCAGGGT
Primer 8_Rv	Rev	Hygro termination	CCCGGGGATCTGATATCATC
Primer 9_Fw	Fw	Hygro middle	CGTACACAAATCGCCCGC
Primer 10_Rv new	Rev	pSG2651 vector right side of insertion region	GGCAAGTGTAGCGGTCAC
pIDC sequ_Fw	Fw	85 bp before insert	CGCGGTACCATAACTTCGTATAGC
pIDC sequ_Rv	Rev	81 bp after insert	GGGGTTATGATAGTTATTGCTCAGCGG
P HL start_Fw	Fw	Start of PICH HL gblock	CTCCGGAATATTAGGTCTCACCATCTGCAC
P HL end Rev	Rev	End of PICH HL gblock	GGCTCAAGCAGTGGGTCTCCTGATATTGTT
PICH HL mutag_Fw	Fw	For substitution in PICH HL gblock	GAAGATCTCTGGCTTCTAGGAGATCTCTTATTAATATGGTTTTAGA
PICH HL mutag Rev	Rev	For substitution in PICH HL gblock	TCTAAAACCATATTAATAAGAGATCTCCTAGAAGCCAGAGATCTTC

BLM HL two GG	Fw	After BLM HL gblcok	GCCTTCATATGCATTCTCAGGATCACCTAAAGATCCAGCC
BLM HL two GG	Rev	After BLM HL gblcok	GGCTGGATCTTTAGGTGATCCTGAGAATGCATATGAAGGC
PICH HL two GG	Fw	After PICH HL gblcok	CTTTAAGTTTGTATAAGCAACTTAATAACAATGGATCACCTAAAGATCCAGC
PICH HL two GG	Rev	After PICH HL gblcok	GCTGGATCTTTAGGTGATCCATTGTTATTAAGTTGCTTATACAAACTTAAAG
FANCD2 HL two GG	Fw	After FANCD2 HL gblcok	CCATTTCCATTCCCTCCAGGATCACCTAAAGATCCAGC
FANCD2 HL two GG	Rev	After FANCD2 HL gblcok	GCTGGATCTTTAGGTGATCCTGGAGGGAATGGAAATGG

Table 10| List of primers to generate dsDNA templates for IVT

Primer	Direction	Region	Sequence (5' - 3')
ML557	Fw	T7 Promoter	TAATACGACTCACTATAG
ML558	Rev	End of tracRNA	AAAAAAAGCACCGACTCGGTGC
ML611	Rev	tracRNA	AAAAAAAGCACCGACTCGGTGCCACTTTTTCAAGTTGATAACGGACTAGCCTTATTTAAACTTGCTATGCTG TTTCCAGCATAGCTCTTAAAC
Gene-specific	Fw	T7+crRNA+part of tracRNA	TAATACGACTCACTATAGNNNNNNNNNNNNNNNNNN NNGTTTAAGAGCTATGCTGGAA

Table 11| List of primers to generate dsDNA templates for IVC

Gene	Direction	Sequence (5' – 3')	Length [bp]	Expected fragments [bp]
SMC5	Fw Rev	CCTTAGGCCAGGCTACAGGTATGCTAATTTAGGTAAGGAT CCAGCTGCTATTTTGGAAAGGTCATTATAGTTTCC	810	602 + 208
BLM	Fw Rev	CCTTGCTCTGGACTGTGCAA CGGCAGCAAAACATGCTTATTC	822	601 + 221
BLM (new)	Fw Rev	CAAGTCCAGTCATTCCGG CACCCCCCAGCATTTATTTAA	805	594 + 155
PICH	Fw Rev	TCAGATGGCGAAGATGAAGATGAT GTTGCAGGGCAGAAGTTGC	811	615 + 196
FANCD2	Fw Rev	atactgtcCTTTAGCCTCCGC CAGAAAATACTTCGATGACTTCTCCC	807	615 + 192

Table 12| List of oligos for pX300 cloning

Description	Direction	Sequence (5' – 3')
BLM (oligo 1)	Fw	CACCGTGTTATGAGAATGCATATGA
BLM (oligo 2)	Rev	AAACTCATATGCATTCTCATAACAC
PICH (oligo 1)	Fw	CACCGAAAGTCAAGAGCATAACTTC
PICH (oligo 2)	Rev	AAACGAAGTTATGCTCTTGACTTTC
FANCD2 (oligo 1)	Fw	CACCGAAGCACAGAAGCTGTTATGG
FANCD2 (oligo 2)	Rev	AAACCCATAACAGCTTCTGTGCTTC

Table 13| Oligonucleotides (gblocks) for DNA inserts

Overhangs in italic, *BsaI* restriction site in underscore, Golden Gate overhang in bold, stop codon three nt in red, silent mutation in bold, italic and red, PAM sequence in grey square

Description	Sequence (5' – 3')
AID	*CTCCGGAATATTA*GGTCTCA**atca**CCTAAAGATCCAGCCAAACCTCCGG CCAAGGCACAAGTTGTGGGATGGCCACCGGTGAGATCATACCGGAAG AACGTGATGGTTTCCTGCCAAAAATCAAGCGGTGGCCCGGAGGCGG CGGCGTTCGTGAAG**atgg**GGAGACC*CACTGCTTGAGCC*
GFP	*CTCCGGAATATTA*GGTCTCA**ATGG**TGAGCAAGGGCGAGGAGCTGTTC ACCGGGGTGGTGCCCATCCTGGTCGAGCTGGACGGCGACGTAAACG GCCACAAGTTCAGCGTGTCCGGCGAGGGCGAGGGCGATGCCACCTA CGGCAAGCTGACCCTGAAGTTCATCTGCACCACCGGCAAGCTGCCC GTGCCCTGGCCCACCCTCGTGACCACCCTGACCTACGGCGTGCAGT GCTTCAGCCGCTACCCCGACCACATGAAGCAGCACGACTTCTTCAAG TCCGCCATGCCCGAAGGCTACGTCCAGGAGCGCACCATCTTCTTCAA GGACGACGGCAACTACAAGACCCGCGCCGAGGTGAAGTTCGAGGGC GACACCCTGGTGAACCGCATCGAGCTGAAGGGCATCGACTTCAAGGA GGACGGCAACATCCTGGGGCACAAGCTGGAGTACAACTACAACAGCC ACAACGTCTATATCATGGCCGACAAGCAGAAGAACGGCATCAAGGTGA ACTTCAAGATCCGCCACAACATCGAGGACGGCAGCGTGCAGCTCGCC GACCACTACCAGCAGAACACCCCCATCGGCGACGGCCCCGTGCTGC TGCCCGACAACCACTACCTGAGCACCCAGTCCGCCCTGAGCAAAGAC CCCAACGAGAAGCGCGATCACATGGTCCTGCTGGAGTTCGTGACCGC CGCCGGGATCACTCTCGGCATGGACGAGCTGTACAAGTAAAACTTGT TTATTGCAGCTTATAATGGTTACAAATAAAGCAATAGCATCACAAATTTC ACAAATAAAGCATTTTTTTCACTGCATTCTAGTTGTGGTTTGTCCAAACT CATCAATGTAT**CTTA**GGAGACC*CACTGCTTGAGCC*
SMC5 HL	*CTCCGGAATATTA*GGTCTCA**ccat**AGGCTATCAAAGAAGTTGCTTGAGA AGTGTTTATAAATAAAAAGTGAAAGTATCTACCCTAGGAAAATTGTGGA GGACATACTCTTTTCCAAGGTCTGCCAAGGAAGTTGAATAATCCCAGT TATCCTGTGAATCTAGAGGGCTGGATTATTCCTTATTTTGATTGTTCCTT AGGCCAGGCTACAGGTATGCTAATTTAGGTAAGGATTACAGTCTGGCA AGGTTTATATTGAGGTGTTTAAGAGCTTCTTAAGAGTCTTATTggctgggga cagtggctcacacctgtaatctcagcactttgggaagccaaggcgggcagatcacctgaggtcagga gttcga*t*accagcctggccaacatggtgaaaccctgtctgtactaaaaatacaaaaagttagctgggc ctgatggtgcatgcctgtaatcccagctactctggaggctggctgaggcacgagaatctcttgaatctgg gtggtggaggttgcactgagctgagatcgcacctctgtactccggcctgagcagcagagtgggaaaa aaaaaGTTTTATTAATATTGCAAATAAAATAATACATTTGACTGTACACATG TAAGGTTGGAAAACTATACTTCTCAGTATATAGCTTATATGACAATTTGTT

	TTAATACTTACAGCTCCTGCAAAATCTTCCTTATTCTGAAAAGATGACAG TTTTGTTTGTCTACAATGGCCCTCATATGCTGGAACCAAACACATGGAA TTTAAAGGCTTTCCAAAGGCGGCGGCG***T***CGTATTACATTCACTCAACC TTCTGG**atca**GGAGACC*CACTGCTTGAGCC*
SMC5 HR	*CTCCGGAATATTA*GGTCTCA**tggt**TAAAAGTAAAGAGAGGGAACTTGGG AAttttttttGTTAAATTCTGTTTATAAGTATGGCTCAACTGAATAAAAGGAGA TTCACTAAAACGAAAAGCAGTTATTTTTGGAAACCTGCTTTTAAATACAA ATAGGTTGATAATGGAAACTATAATGACCTTTCCAAAATAGCAGCTGGT AGTAAAAGTTAAGTCTTCTTCAGTCTTGGTTGAACTTGAGTTCTTGGCA CTCTGACCATGAGTCATTCAGTTCTCATGTTAAAATGTACTTAATATTAC AAATCAAAGGTACAGTGGAAGAAGGGTTAATCACAAGAAGTTACTTATA TGGTAGCCCTGAGCTTTAATTGCAGAGTAACTTTAATTACTTTTAGAGC CTAAAGATGACTCTAGAGCCTAAGTCCTAGTTTCTCCCAATGTTATATTT AATTTTAAAAAATTGATATGAAAATGTCTAATGTATAGTAATAATTTATGAC AGATCTAGTCATTTCTTCCTATTAAAAAAGATTACCTTATCTCCAGTAGG AAATGGAATTTTATGGGCCTTTAAAAGAAAGTTTTATGAAACTTGATGCT ATAATTTTATTGGTATTTCAAGGGGAAAAAAGCACTGGGGTTCAAAAAT GGTAGCAGAACTGCTTTGAAATGCTGCAAGGTGGCCACTAGATGATG CAAAATACAACCAAAAGATTGACTGAGAATAAAATTAGGTGACAAGGGT TTTTAAAGAATAACCTTTTAAAGTGTGGGGGCAGGGGTTGCttttttttattttatt tAAAGTCAATTATATTTTACA**ggat**GGAGACC*CACTGCTTGAGCC*
BLM HL	*CTCCGGAATATTA*GGTCTCA**ccat**GGAGAGCTGGCAGATCTCTGGGTGT AGGCAGGTGAGCCAGGGAGCTGCTGGACACGGTCCTAACAGAAGGC CGCATCTGCAGCCTTCCTGGGGCTTCCTGGGGCTGGCCAGGAAGAC GCCCAGCTTTGCCACTCCTGGCCACCCAGCTCCACCCCATGCATGCT CACCCCACAGCTGCCTTGCTCTGGACTGTGCAAGTCCAGTCATTCCG GGGTGCCTGTCAGCAGGGAGCTGGGGCCTTACAGCAAGGTGTTTCA CTTCTTTTATTTGGTCAGAATAGATGAGGACATGTGGACCTCAGCTCCT CTTGCAGGCTCTGGTTGTAGGCTGCCGAAGGTGTGGGTGGAGAGAG GGGCGGTGGGTTGGTCACAAGTCAGAAAATTAAGAAACAGTCCTGCA CATTTCAGAAAGACAAATCCAGAACAAATTTATATGAAGGGCCGCGGT CCTTTATTCCATAAGTAGTAAAGGAAACTTACCTTACCTAGGGGGCTCG TAGGCAGAAAATGCACAAGGACACATTAGGCCCAGGGAAGTGGTATT GTAGCTCTGTGCAGGTTGAGAGGAAGGTCATTcatttttggtttcatttaacattttgat ttttttCTTTGTCACATTTCAGGGGGTCTGCCACATGTAGAAAGATATCTTC CAAAACGAAATCCTCCAGCATCATTGGATCCAGTTCAGCCTCACATAC TTCTCAAGCGACATCAGGAGCCAATAGCAAATTGGGGATTATGGCTCC ACCGAAGCCTATAAATAGACCGTTTCTTAAGCCTTCATATGCATTCTCA GG**atca**GGAGACC*CACTGCTTGAGCC*
BLM HR	*CTCCGGAATATTA*GGTCTCA**tggt**CAACCGAATCTCAATGTACATAGACC CTCTTTCTTGTTTGTCAGCATCTGACCATCTGTGACTATAAAGCTGTTA TTCTTGTTATACCATTTGAAGTTTTTACTCGTCTCTATTAATATTTAAATAA ATGCTGGGGGGTGATAGTTCTTCTTTTTAAAATAAACATTTTCTTTTGAA TAAGCATGTTTTGCTGCCGCTGCAAGTGTTGTGGCCGTTGTTTCTCAG AACGTCTGAGGCAGCAGCTGAATCATCTCAGTGCAAGAGCTTCTGAG CATAACACGAAACCCAGAAGCCAAAGGAAGAGCCACGCGTGGGCCC TTGTGAAACTAAAGCTTTTCGTGTAAGACAACACAAACAAAATTTAAAG ACAAATGACGGGGAAAAGAGGAGAAAATATATTACAAAGGATTAGTATC CATCATACCAAATACCCGTGAACCAGTCAGAaacatcccaggggcaggtggac caaggatgtgaacaggctagtctcagaagaagaaatacacatgctcatggcccggcactgtggctca cgcctgggatcccagcactttgggaggccgaggcaggtggatcacgaggtcaggagtttg***a***acca gcctgcccaacatggtgaaaccccgtctctactaaaaatacaaaaattagccaggcgtggtgtacag gcacgcctgtagtcccagctactcaggaggctgaggcaagagaatcgcttgaacccaggaggcgg aggttgcagtgagccgagatcgtgccactgcactccagcctgggtgacagagcaagactccgtct**gg** **at**GGAGACC*CACTGCTTGAGCC*

PICH HL	*CTCCGGAATATTA*GGTCTCA**ccat**CTGCACCTAATTCCAGAGCAGGGTT TGTGCATAGCAAAACATGTCTCAGTTGGGAGTTTTCTGAGAAAGACGA TGAACCAGAAGAAGTAGTAGTTAAAGCAAAAATCAGAAGTAAAGCTAG AAGGATTGTTTCAGATGGCGAAGATGAAGATGATTCTTTTAAAGATACC TCAAGCATAAATCCATTCAACACATCTCTCTTTCAATTCTCATCTGTGAA ACAATTTGATGCTTCAACTCCCAAAAATGACATCAGTCCACCAGGAAG GTTCTTTTCATCTCAAATACCCAGTAGTGTAAATAAGTCTATGAACTCTA GAAGATCTCTGGCTTCTAGGAG***A***TCTCTTATTAATATGGTTTTAGACCA CGTGGAGGACATGGAGGAAAGACTTGACGACAGCAGTGAAGCAAAG GGTCCTGAAGATTATCCAGAAGAAGGGGTGGAGGAAAGCAGTGGCG AAGCCTCCAAGTATACAGAAGAGGATCCTTCCGGAGAAACACTGTCTT CAGAAAACAAGTCCAGCTGGTTAATGACGTCTAAGCCTAGTGCTCTAG CTCAAGA***A***ACCTCTCTTGGTGCCCCTGAGCCTTTGTCTGGTGAACAG TTGGTTGGTTCTCCCCAGGATAAGGCGGCAGAGGCTACAAATGACTAT GAGACTCTTGTAAAGCGTGGAAAAGAACTAAAAGAGTGTGGAAAAATC CAGGAGGCCCTAAACTGCTTAGTTAAAGCGCTTGACATAAAAAGTGCA GATCCTGAAGTTATGCTCTTGACTTTAAGTTTGTATAAGCAACTTAATAA CAATGG**atca**GGAGACC*CACTGCTTGAGCC*
PICH HR	*CTCCGGAATATTA*GGTCTCA**tggt**GAATGTAACCTGTTTATTGTATTTTAA AGTGAAACTGAATATGAGGGAATTTTTGTTCCCATAATTGGATTCTTTG GGAACATGAAGCATTCAGGCTTAAGGCAAGAAAGATCTCAAAAAGCAA CTTCTGCCCTGCAACGCCCCCCACTCCATAGTCTGGTATTCTGAGCAC TAGCTTAATATTTCTTCACTTGAATATTCTTATATTTTAGGCATATTCTATA AATTTAACTGTGTTGTTTCTTGGAAAGTTTTGTAAAATTATTCTGGTCAT TCTTAATTTTACTCTGAAAGTGATCATCTTTGTATATAACAGTTCAGATAA GAAAATTAAAGTTACTTTTCTCAAGTGTTTTCCATCCACTTTGTTTCACT GAGATGATACTGGCAGATCTTAAGATATGCTTGTGAACATGCTGTTTCA TGCTTTCAGCTTAATACAGGTTGAGCATCCCTAATCCAATCCAAAATGG GGAAAATTTCTGAGTGCTGACATGATGCCACAAGTGAGGAAAGTTCCA TACCTGATGTCATGTGACATGTCACAGTCAAAATGAAGGTGTATAACAC ACTGTTTACTCAGCATCCCCAAGAGAAAAGAGATTCTGTTAGACCCCT TCAGCTACTATATATCCTTTCCACACAGGCCCAGATTCTCCCATGCAAG CCTGCCTACAAAGGGTAATAAAATGGTTCAACATACACAAACTTTGTTT CATGCACAAAATCGTTAAAAGTAATTATAAAATTACCTTCAGACTATGTAT ATAATGTGTGTATGAAACATAAATGGATTTCAT**ggat**GGAGACC*CACTGC TTGAGCC*
FANCD2 HL	*CTCCGGAATATTA*GGTCTCA**ccat**acagagaattagcttccttttcttcacatcaaccttatga ggcagatactattgtttctgcataaaaattgaagctcagagaagttaagtaatttacctaatgtcattcaac agtgagtgggtggagccggagtttgagtccaaacagtcccaaatccagagctgatgttctgaaaccac ctcaccatactgtcCTTTAGCCTCCGCATGGCCATTCGTGCTTGGTGTGATAG TGCTTAGATACCTTAAGGTATTTGGGAAATTTTAGAACCATGTTCAGCAT CGACTTAGAGTCACCAATACAGTCTAGCCTTTTAAAATGTAGTGTGATA CTAGCATACTAAGATGAACCTTTCGTTACATTACTTATTGTATCAGGGCC ACAGACATCTCAGAAACCTGGAGTTGAGTATCCCTCCTCTAGATGCTG AATCACAAGTTGGTATCCATGTTTGCTGTGTTTTGAATGGCTAAAATATC TTCCTTTGTATTGCCTGTAAACTCAACCTTCTCCCCTATTACCCTAAATG TGATCATTATAACCCACCATTTTCTTGGTCCATTCACATTTAGGGTGAA GAGATTAAGTCCCAAAATTCCCAGGAGAGCACAGCAGATGAGAGTGA GGATGACATGTCATCCCAGGCCTCCAAGAGCAAAGCCACTGAGGTAT CTCTACAAAACCCACCAGAGTCTGGCACTGATGGTTGCATTTTGTTAAT TGTTCTAAGTTGGTGGAGCAGAACTTTGCCTACTTATGTTTATTGTCAA ATGCTTCTATGCCCATTTCCATTCCCTCCAGG**atca**GGAGACC*CACTGC TTGAGCC*
FANCD2 HR	*CTCCGGAATATTA*GGTCTCA**tggt**CAGCTTCTGTGCTTATATAATTTTTGG GACCCAGAAGAAACAACGACACAATCTTAGAATCACTCCTGAGTATCT

CGAGTTGTGGCATTTGTTATAGAGTTGACAATTTTCTGCATTATAGCCT
CTCATTTTCCATGAATTCATATCTGAAACCATTTTAGAAGGGAGAAGTC
ATCGAAGTATTTTCTGAGTGTTGAGAAGAATGAGTTAAACCATTTAAAC
ACATTTGAAACATACAAAAATAGAAATGTGAAAGCATTTGGTGAAAGCC
AAAGCACAGAGTCAGAAGCTGCCACCTTAGAGAACTGAAATAAAAATA
GAAGTTCTTACGCTTTTTTGTGGTACAGATGCTTTCGACAATTTAAAGA
AAGCTAAATaaaaatgtagacatggctggcgcagtggctcatgcttgtaatcctagcacttttgag
gccaaggtaggaggattgcttgagtccgggagctcaaggcaaagctgcacaacataacaagaccct
atctccacaaaaaaaatgaaaaaTAAACctgggtgcggtggctcacacctgtaatcccagcacttt
gggaggccgatgtgggcagatcacaaggtcaggagttcaagaccagcctggccaacatagtgaaa
ccccatctctactgaaaatacaaaaattagctgggtgtggtggcacgtgcctgttatctcagctacttggg
aggctgaggcaggagaatcacttgaacctgggaggtggaggttgtggtgagccgagatcatgctact
gcactccagcctgggcaacagagtgagact**ggat**GGAGACC*CACTGCTTGAGCC*

Table 14| List of primers to isolate resistance genes

Overhangs in italic, *BsaI* restriction site in underscore, Golden Gate overhang in bold

Description	**Direction**	**Region**	**Sequence (5' – 3')**
Hygromycin_ fw	Fw	First 20 nt	TTATAGGTACC*CTCCGGAATATTA*GGTCTCA**C TTA**GGGTAGGGGAGGCGCTTTTC
Hygromycin_ rv	Rev	Last 24 nt	TTTATACCTAGG*GGCTCAAGCAGTG*GGTCTC C**ACCA**TAAAGAGCAGGCATTTATCTAATC
Neomycin_fw	Fw	First 20 nt	TTATAGGTACC*CTCCGGAATATTA*GGTCTCA**C TTA**CTGAGGCGGAAAGAACCAGC
Neomycin_rv	Rev	Last 24 nt	TTTATACCTAGG*GGCTCAAGCAGTG*GGTCTC C**ACCA**GAACAAAAGCTGGGTACCGGATCC

Table 15| List of primers to amplify linear pIDC vector

Description	**Direction**	**Sequence (5' – 3')**
pIDC_linear_fw	Fw	GGAGACC*CACTGCTTGAGCC*TAGAAGATCCG
pIDC_linear_rev	Rev	TGAGACCTAATATTCCGGAGTAGGTCGCG

Table 16| List of primers for genotypic screen of cell clones

Description	**Direction**	**Target**	**Sequence (5' – 3')**
BLM Fw geno	Fw	Upstream of BLM HL	GAAGGACTTGGTAATCGGCTC
BLM Rv geno	Rev	downstream of BLM HR	ctttttcacatatttgcagagcatgt
FANCD2 Fw geno	Fw	Upstream FANCD2 HL	GGAGTTACAACATTTTTCAGAT AGGGT
FANCD2 RV geno	Rev	Downstream FANCD2 HR	CAGGGGTTCTTAAATCTGAGCT
PICH geno Fw	Fw	Downstream PICH HL	AGTGAGGCCAAGTTGGAAGA
PICH geno Rv	Rev	Inside PICH 800 bp HR	CAAAACTTTCCAAGAAACAACA CAG

Primer B_genotypes_Rev	Rev	Inside GFP	TTCTCGTTGGGGTCTTTGCT
Primer C_genotypes_Rev	Rev	SMC5 HR	AATTCCATTTCCTACTGGAGAT AAGGTA

2.7 Pull-down

Table 17|List of pull-down specific reagents

Reagents	Manufacturer
GFP-Trap® agarose	ChromoTek GmbH, Planegg, Germany
RFP-Trap® agarose	ChromoTek GmbH, Planegg, Germany
ChIP Grade Protein G Agarose Beads	CellSignaling Technology, Inc., Danvers, USA

2.8 Bacteria culture

Table 18|List of bacteria strains

Name	Description	Provider
pirHC chemically competent cells	*Escherichia coli* (*E. coli)*	Kind gift of Michael Taschner
One Shot™ TOP10 chemically competent cells	*E. coli*	Thermo Fisher Scientific, Inc., Waltham, USA
DH5alpha chemically competent cells	*E. coli*	Thermo Fisher Scientific, Inc., Waltham, USA

Table 19|List of bacteria culture specific reagents

Reagents	Manufacturer
Lysogeny broth (LB) medium	Carl Roth GmbH + Co. KG, Karlsruhe, Germany
Ampicillin sodium salt	Sigma-Aldrich, St.Louis, USA
Chloramphenicol	Sigma-Aldrich, St.Louis, USA

2.9 Cell culture

Table 20|List of human cell lines

Name	Cell type	origin	Description	Provider
HCT116	Colorectal carcinoma	Colon	Mutation in codon 13 of the ras proto-oncogene	ATCC, Manassas, USA
HCT116 Tet-OsTIR1 WT	Colorectal carcinoma	Colon	Mutation of ras proto-oncogene, OsTIR1 expression from AAVS1 locus	Kind gift of Holger Bastian laboratory, Göttingen, Germany

			under the control of a conditional Tet-promoter	
HCT116 Tet-OsTIR1 $BLM^{AID/AID}$ clone B1	Colorectal carcinoma	Colon	Mutation of ras proto-oncogene, OsTIR1 expression, homozygous BLM-AID/GFP expression	Generated during this study by CRISPR/Cas9 in HCT116 Tet-OsTIR1 WT cells (Angela Wieland)
HCT116 Tet-OsTIR1 $BLM^{WT/AID}$ clone B5	Colorectal carcinoma	Colon	Mutation of ras proto-oncogene, OsTIR1 expression, heterozygous BLM-AID/GFP expression	Generated during this study by CRISPR/Cas9 in HCT116 Tet-OsTIR1 WT cells (Angela Wieland)
HCT116 Tet-OsTIR1 $BLM^{WT/AID}$ clone B6	Colorectal carcinoma	Colon	Mutation of ras proto-oncogene, OsTIR1 expression, heterozygous BLM-AID/GFP expression	Generated during this study by CRISPR/Cas9 in HCT116 Tet-OsTIR1 WT cells (Angela Wieland)
PSNF5 (GM08505 + BLM plasmid)	Fibroblasts SV40-transformed	BS patient	BLM positive	Kind gift of Ian Hickson laboratory, Kopenhagen, Denmark
PSNG13 (GM08505 + vector control)	Fibroblasts SV40-transformed	BS patient	BLM negative	Kind gift of Ian Hickson laboratory, Kopenhagen, Denmark

Table 21|List of cell culture specific reagents

Reagents	**Manufacturer**
3-Indole-acetic acid (IAA)	Sigma-Aldrich, St.Louis, USA
Aphidicolin	Sigma-Aldrich, St.Louis, USA
Colchicine solution 10 µg/ml	SERVA Electrophoresis, Heidelberg, Germany
Doxorubicin (Doxo)	Sigma-Aldrich, St.Louis, USA
Doxycycline (Dox)	Sigma-Aldrich, St.Louis, USA
Dulbecco's Modified Eagle Medium (DMEM), high glucose, GlutaMAX™	Thermo Fisher Scientific, Inc., Waltham, USA
Dulbecco's Modified Eagle Medium (DMEM), high glucose, no glutamine, no phenol red	Thermo Fisher Scientific, Inc., Waltham, USA
Fetal bovine serum (FBS)	Thermo Fisher Scientific, Inc., Waltham, USA
G418 for Neomycin (Neo) selection	InvivoGen, San Diego, USA
Hydroxyurea (HU)	Sigma-Aldrich, St.Louis, USA
Hygromycin (Hygro) B Gold	InvivoGen, San Diego, USA
L-Glutamine 200 mM	Thermo Fisher Scientific, Inc., Waltham, USA
Minimal Essential Medium (MEM) alpha	Thermo Fisher Scientific, Inc., Waltham, USA
Penicillin/Streptomycin (Pen/Strep)	Thermo Fisher Scientific, Inc., Waltham, USA
Polyethyleneimine (PEI)	Polysciences, Inc., Warrington, USA
Puromycin (Puro)	Thermo Fisher Scientific, Inc., Waltham, USA

Thymidine	Sigma-Aldrich, St.Louis, USA
Trypsin-EDTA 0.25 %	Thermo Fisher Scientific, Inc., Waltham, USA

Table 22|List of cell line specific medium

Cell line	Medium	Supplements
HCT116 WT	DMEM, high glucose, GlutaMAX™	10 % FBS, 1 % Pen/Strep
HCT116 Tet-OsTIR1 WT	DMEM, high glucose, GlutaMAX™	10 % FBS, 1 % Pen/Strep, 1 µg/ml Puro
HCT116 Tet-OsTIR1 BLM clones	DMEM, high glucose, GlutaMAX™	10 % FBS, 1 % Pen/Strep, 1 µg/ml Puro, 100 µg/ml Hygro
PSNF5	MEMalpha	10% FBS, 2 mM L-Glutamine, 1 % Pen/Strep, 0.35 mg/ml G418
PSNG13	MEMalpha	10% FBS, 2 mM L-Glutamine, 1 % Pen/Strep, 0.35 mg/ml G418

2.10 SDS-PAGE and Western blotting

Table 23|List of immunoblotting reagents

Reagents	Manufacturer
Acrylamide/Bis Solution 37.5:1, 30% w/v	SERVA Electrophoresis, Heidelberg, Germany
Bradford dye reagent concentrate 5x	Bio-Rad Laboratories, Inc., Hercules, USA
Clarity™ Western enhanced chemiluminescence (ECL) Substrate	Bio Rad Laboratories, Hercules, USA
cOmplete™ Mini, EDTA-free protease inhibitors	Roche Diagnostics, Mannheim, Germany
Lumigen ECL Ultra (TMA-100) Solution	Lumigen, Southfield, USA
PhosSTOP™ EASYpack phosphatase inhibitors	Roche Diagnostics, Mannheim, Germany
Precision Plus Protein™ All Blue Standards	Bio Rad Laboratories, Hercules, USA
Color Prestained Protein Standard	New England Biolabs, Ipswich, USA

2.11 Microscopy

2.11.1 Immunofluorescence

Table 24|List of immunofluorescence specific reagents

Reagents	Manufacturer
5-bromo-2'-deoxyuridine (BrdU)	Thermo Fisher Scientific, Inc., Waltham, USA
Antifade Mounting Medium with DAPI, VECTASHIELD	Biozol Diagnostica Vertrieb GmvH, Eching, Germany
Antifade Mounting Medium, VECTASHIELD	Biozol Diagnostica Vertrieb GmvH, Eching, Germany
DAPI	Carl Roth GmbH + Co. KG, Karlsruhe, Germany
Giemsa	Sigma-Aldrich, St.Louis, USA
Hoechst 33258	Thermo Fisher Scientific, Inc., Waltham, USA
Sytox™ Green	Thermo Fisher Scientific, Inc., Waltham, USA

2.11.2Live-cell imaging

Table 25|List of live-cell imaging-specific reagents

Reagents	Manufacturer
NucSpot® Live 650	Biotium, Inc., Fremont, USA
FluoroBrite™ DMEM	Thermo Fisher Scientific, Inc., Waltham, USA

2.12 Flow cytometry

Table 26|List of flow cytometry-specific reagents

Reagents	Manufacturer
Bafilomycin	Sigma-Aldrich, St.Louis, USA
DDAO galactoside	Thermo Fisher Scientific, Inc., Waltham, USA
FxCycle™ propidium iodide (PI)/RNase staining solution	Thermo Fisher Scientific, Inc., Waltham, USA

2.13 Mass spectrometry

Table 27|List of mass spectrometry specific chemicals and reagents

Reagents	Manufacturer
Acetonitrile 80%, H_2O 20%, formic acid 0.1 %	Thermo Fisher Scientific, Inc., Waltham, USA
Acetonitrile anhydrous	Sigma-Aldrich, St. Louis, USA
Acetonitrile LC-MS grad	Honeywell, Charlotte, USA
Formaldehyde (Methanol-free) 16%	Thermo Fisher Scientific, Inc., Waltham, USA
Formic acid	Honeywell, Charlotte, USA
H_2O LC-MS grade	Thermo Fisher Scientific, Inc., Waltham, USA
H_2O with formic acid 0.1%	Thermo Fisher Scientific, Inc., Waltham, USA
Methanol LC-MS grade	Honeywell, Charlotte, USA
Tri-fluoracetic acid (TFA)	Carl Roth GmbH + Co. KG, Karlsruhe, Germany
Trypsin proteomics grade	Sigma-Aldrich, St. Louis, USA

2.14 List of antibodies

Table 28|List of primary antibodies

Name	Dilution	Host	Molecular weight [kDa]	Manufacturer	Reference
53BP1	IF: 1:500	Mouse	214	Merck KGAA, Darmstadt, Germany	MAB3802
Alpha-Actinin	WB: 1:1000	mouse	100	Santa Cruz Biotechnology Inc., Dallas, USA	sc-17829
BLM	WB: 1:250	Mouse	180	Santa Cruz Biotechnology Inc., Dallas, USA	Sc-365753
Cyclin A2	IF: 1:500	rabbit	49	Abcam, Cambridge, UK	Ab181591
Cyclin B1	WB. 1:1000	Mouse	55	Cell Signaling Technology, Inc., Danvers, USA	4135
FANCD2	IP: 2 µg/IP	Rabbit	164.1	Novus Biologicals, LLC, Centennial, USA	NB100-182
GFP	WB: 1:250	rat	27	ChromoTek GmbH, Planegg, Germany	3H9
MPM-2 Anti-phospho-Ser/Thr-Pro	Flow: 1:1000	Mouse	Varies	Merck KGAA, Darmstadt, Germany	05-368

Normal mouse IgG	IP: 1:1000	Mouse	150	Santa Cruz Biotechnology Inc., Dallas, USA	Sc-2025
OsTIR1	WB: 1:1000	rabbit	67	MBL Life Science, Sunnyvale, USA	PD048
Phospho RPA2 (S33)	IF/Flow: 1:500	rabbit	32	Fortis Life Sciences, Waltham, USA	A300-246A
Phospho gamma H2AX (S139)	IF/Flow: 1:500	rabbit	15	Abcam, Cambridge, UK	Ab2893
PICH	IF: 1:150	Rabbit	140	Abnova GmbH, Taipei, Taiwan	H00054821-D01
RMI1	WB: 1:500	Rabbit	75	Proteintech Group, Inc., Rosemont, USA	14630-1-AP
RPA32/RPA2	IF: 1:1000	Mouse	32	Abcam, Cambridge, UK	ab2175

Table 29|List of secondary antibodies

Name	**Dilution**	**Host**	**Manufacturer**	**Reference**
Anti-mouse HRP	WB: 1:5000	Goat	R&D Systems, Inc., Minneapolis, USA	HAF007
Anti-mouse, Alexa Fluor® 594	IF/Flow: 1:500	Donkey	Jackson ImmunoResearch, West Grove, USA	715-585-150
Anti-mouse, Alexa Fluor® 488	IF/Flow: 1:500	Goat	Jackson ImmunoResearch, West Grove, USA	115-545-003
Anti-rabbit HRP	WB: 1:5000	Goat	R&D Systems, Inc., Minneapolis, USA	HAF008
Anti-rabbit, Alexa Fluor® 594	IF/Flow: 1:500	goat	Jackson ImmunoResearch, West Grove, USA	711-586-152
Anti-rabbit, Alexa Fluor® 647	IF/Flow: 1:500	Donkey	Jackson ImmunoResearch, West Grove, USA	JIM-711-605-152
Anti-rabbit, Alexa-Fluor® 488	IF/Flow: 1:500	Goat	Jackson ImmunoResearch, West Grove, USA	111-545-003
Anti-rat HRP	WB: 1:5000	Chicken	R&D Systems, Inc., Minneapolis, USA	HAF005

2.15 Kits

Table 30|List of kits

Kit	Manufacturer
CellTiter-Glo® Luminescent Cell Viability Assay	Promega, Fitchburg, USA
DNeasy® Blood & Tissue kit	Qiagen, Venlo, Netherlands
FxCycle™ PI/RNase Staining Solution	Thermo Fisher Scientific, Inc., Waltham, USA
HiScribe® T7 High Yield RNA Synthesis kit	New England Biolabs, Ipswich, USA
MycoStrip® Mycoplasma Detection kit	InvivoGen, San Diego, USA
Pierce™ BCA Protein Assay Kit	Thermo Fisher Scientific, Inc., Waltham, USA
PureLink™ HiPure plasmid midiprep kit	Thermo Fisher Scientific, Inc., Waltham, USA
QIAprep® Spin Miniprep kit	Qiagen, Venlo, Netherlands
QIAquick® PCR Purification kit	Qiagen, Venlo, Netherlands
Quick Ligation™ kit	New England Biolabs, Ipswich, USA

2.16 Software

Table 31|List of software

Sofware	Manufacturer
Adobe Illustrator CC 2018	Adobe Inc., San José, USA
Agilent platform	Agilent Technologies, Inc., Santa Clara, USA
Benchling platform	Benchling, Inc., San Francisco, USA
BioRender	BioRender, Toronto, Canada
CellProfiler 4.2.1	Broad Institute
Cytoscape v3.9.0	National Human Genome Research Institute, Rockville Pike, USA
FlowJo™ V10	Becton, Dickinson and Company, New Jersey, USA
ImageJ/FIJI 1.52i	ImageJ, National Institutes of Health, Bethesda, USA
GraphPad Prism 5 and 9	GraphPad Software Inc.
ImageJ	National Institutes of Health, Bethesda, USA
MaxQuant 1.6.17	Max Planck institute of biochemistry, Martinsried, Germany
Microsoft 365 Apps 2105	Microsoft Corporation, Redmond, USA
OligoEvaluator™ platform	Sigma-Aldrich, St. Louis, USA
Perseus 1.6.10.43 and 1.6.15.0	Max Planck institute of biochemistry, Martinsried, Germany
RStudio 1.1.463 and R language 3.5.3	Posit PBC, Boston, USA
SlideBook 6.0	Intelligent Imaging Innovations Inc., Denver, USA
SnapGene® Viewer 5.0.7	GSL Biotech LLC, San Diego, USA

3. Methods

3.1 Molecular biology techniques

All reactions and solutions were prepared with nuclease-free H_2O unless otherwise specified. The SnapGene® Viewer software was used to examine DNA sequences of plasmids, identify restriction enzyme sites, and select appropriate restriction enzymes for digestion. It was also employed to design primers by providing essential information, including primer length, GC content, and melting temperature. Additionally, the oligonucleotide calculator web tool OligoEvaluator™ was used to assess the self-complementarity of primers and to check for potential secondary structures, such as hairpin formation and primer-dimers, to ensure efficient and specific primer binding during PCR amplification. All procedures involving bacteria were conducted under sterile conditions near an open flame to prevent contamination by maintaining an aseptic environment.

3.1.1 Bacterial transformation

To produce multiple copies of plasmid DNA, chemically competent *E. coli* cells were transformed with the plasmid DNA, leveraging their bacterial replication machinery for autonomous replication of the plasmid. If not otherwise specified, for the amplification of desired DNA plasmids, 2 µl of plasmid DNA reaction was added to 50 µl of chemically competent TOP10 *E. coli* cells. The mixture was incubated on ice for 15 min. Afterward, the cells were subjected to a heat shock at 42°C for 45 sec to facilitate the uptake of the plasmid DNA into the bacterial cells. Subsequently, the bacteria are placed back on ice for 2 min to stabilize the cells. 250 µl pre-warmed LB medium was added, and bacteria were recovered at 37°C with shaking at 230 revolutions per minute (rpm) for 60 min. Cells were centrifuged at 13,000 rpm for 1 min, most of the supernatant was discarded, and around 50 µl of cell suspension was plated onto an agar plate containing an antibiotic that corresponds to the resistance gene on the plasmid (Table 8). After overnight incubation at 37°C, individual colonies growing on the selective media can be picked for further analysis, such as plasmid extraction and screening to confirm successful transformation, as described below. A negative control plate was set up by carrying out the same transformation procedure without adding plasmid DNA.

3.1.2 Plasmid mini-preparation

Mini-preparation was performed to extract plasmid DNA on an analytical scale. Following bacterial transformation overnight, several colonies were picked separately with a sterile pipette tip, briefly touched onto a backup plate and inoculated into 5 mL of LB medium containing the appropriate antibiotic. The cultures were incubated at 37°C with shaking overnight at 230 rpm. After incubation, the cultures were centrifuged at 4,000 x g for 10 min at 4°C, and the supernatant was discarded. Following the manufacturer's instructions of the

QIAprep® Spin Miniprep kit, the bacterial pellet was resuspended, lysed, and neutralized to precipitate proteins and other cellular debris in the provided buffers. After subsequent centrifugation, the plasmid DNA was bound to the purification columns, washed, and eluted in 50 µL of elution buffer. The purified plasmid DNA was stored at -20°C. Before further use, the quality of the plasmid DNA was assessed by determining its concentration and purity, performing restriction digestion and sequencing as described below.

3.1.3 DNA and RNA concentration determination

DNA and RNA concentrations were estimated by adding 1 µL of the sample to a spectrometer to measure the optical density (OD), specifically by assessing the absorbance at a wavelength of 260 nanometers (nm), at which nucleic acids absorb light at a maximum. The concentration is calculated based on the premise that an OD of 1 at 260 nm corresponds to a DNA concentration of 50 µg/ml and to a RNA concentration of 40 µg/ml. The purity of the nucleic acids was assessed by considering the absorbance at a wavelength of 280 nm, with the ideal OD_{260}/OD_{280} ratio being around 1.8 indicating high-purity DNA and around 2.0 indicating pure RNA. A ratio below 1.6 may indicate contamination with proteins. Additionally, the OD_{260}/OD_{230} ratio is used to analyze potential contamination with substances such as lipids or salts, with the ideal ratio between 2.0 – 2.2. The background absorbance was measured using the elution solution of the DNA or RNA, such as nuclease-free H_2O or elution buffer, as a blank.

3.1.4 Restriction digestion

Restriction digestion was utilized to characterize plasmid DNA from each colony picked after bacterial transformation by analyzing the resulting characteristic DNA fragments. Using SnapGene® Viewer software, restriction sites for various enzymes were identified, and the appropriate restriction enzyme was selected to cleave the plasmid DNA at specific loci, resulting in one or more linear DNA fragments of predicted lengths. A 50 µl digestion reaction was set up containing the plasmid DNA, the selected restriction enzyme, and the enzyme's recommended buffer. The reaction was carried out according to the manufacturer's instructions, typically incubating the mixture at 37°C for 1 h. The enzyme's optimal conditions were followed to ensure complete digestion of the plasmid DNA. After digestion, a loading dye was added to the mixture. The samples were loaded onto an agarose gel to analyze the results of the restriction digestion using gel electrophoresis. The fragment sizes were then compared to a negative control that omitted the restriction enzyme and assessed to confirm the presence of specific DNA sequences in a construct.

3.1.5 Agarose gel electrophoresis

Agarose gels of the appropriate percentage, based on the main fragment sizes to be detected, were freshly prepared by dissolving agarose powder in 1x TAE buffer in a glass flask. The solution was heated in a microwave at approximately 20-second intervals and swirled until fully dissolved. After the solution was allowed to cool for some seconds, 2 drops of ethidium bromide (at a dilution of approximately 1:10,000) were added per 100 ml of agarose solution to allow the ethidium bromide to intercalate with nucleic acids, facilitating their visualization under UV light. After swirling the flask to ensure proper dissolution of ethidium bromide, the solution was poured into a gel chamber equipped with a comb to create loading wells. Once the gel solidified and cooled, the gel tray was placed into the electrophoresis tank, which was filled with 1x TAE buffer. The nucleic acid samples were loaded into the wells of the gel. Additionally, 2 µL of 1 kb or 100 bp DNA ladder mix was loaded at the beginning and end of the sample lanes for reference. The gels were run at 90 V in 1x TAE buffer for approximately 1 h until sufficient separation of the ladder bands was reached. The DNA or RNA bands were then visualized under UV light using the gel documentation system.

3.1.6 Sanger sequencing analysis

All DNA sequences used for experiments in this thesis were, after successful restriction digestion, finally analyzed by Sanger sequencing for potential nucleotide mutations. DNA samples were sent along with the appropriate primers (Table 9) according to company guidelines. Primers were designed using the SnapGene® Viewer software. To ensure comprehensive coverage, primers were designed to target both the leading and lagging DNA strands with overlapping regions between them, allowing for complete sequencing of the DNA fragment. The sequencing results were aligned with the reference sequences to verify the accuracy and confirm the presence of the correct sequences.

3.1.7 Plasmid midi-preparation

To prepare plasmid DNA on a preparative scale, positive bacterial colonies selected for expansion were picked from backup plates and inoculated into 50 ml of LB medium containing the appropriate antibiotic. After overnight incubation at 37°C with shaking at 230 rpm, the bacterial culture was transferred to fresh tubes, and 500 µl of the culture was saved as a bacterial stock by diluting it 1:2 in 50% glycerol and storing it at -80°C for long-term storage. The remaining bacterial culture was centrifuged at 4,000 x g for 10 min, and the supernatant was discarded. The plasmid DNA was then prepared using the PureLink™ HiPure Plasmid Midiprep kit, following the manufacturer's protocol. After purification, the plasmid DNA was eluted in nuclease-free H_2O. The DNA concentration was subsequently determined (as described in chapter 3.1.3), and the samples were stored at -20°C until further use.

3.1.8 The CRISPR/Cas9 system

CRISPR/Cas9 (Clustered Regularly Interspaced Short Palindromic Repeats/CRISPR associated protein 9) is a revolutionary genome-editing technology that allows precise and efficient modification of DNA within living organisms[209] (Fig. 13). The method leverages the natural defense mechanisms of bacteria against viruses and has been adapted for use in various biological systems. The endonuclease Cas9 introduces DSBs in the DNA at specific locations, guided by a small RNA molecule. Therefore, the Cas9 enzyme forms a complex with the guide RNA (gRNA), which consists of a CRISPR RNA (crRNA) and a trans-activating CRISPR RNA (tracrRNA). In engineered systems, these are often fused into a single guide RNA (sgRNA). Cas9 requires a short DNA sequence adjacent to the target site, known as the protospacer adjacent motif (PAM), to bind and cleave the DNA. The PAM sequence varies between different Cas9 variants. For the commonly used *Streptococcus pyogenes* Cas9 (SpCas9), which was also used in this project, the PAM sequence is N-guanine-guanine (NGG) in the 5-prime (5') to 3-prime (3') direction. In this sequence, "N" represents any nucleotide, followed by two guanines. The sgRNA consists of the crRNA with 20 nucleotides (nt) upstream (in the 5' direction) of a PAM sequence and the following tracrRNA. This method was employed to introduce the AID domain and other tags into the genome of a gene of interest for use with the auxin-inducible degradation system. There are several strategies for delivering the Cas9 and sgRNA into mammalian cells, including plasmid DNA transfection and the direct delivery of Cas9 protein and sgRNA forming ribonucleoprotein (RNP) complexes.

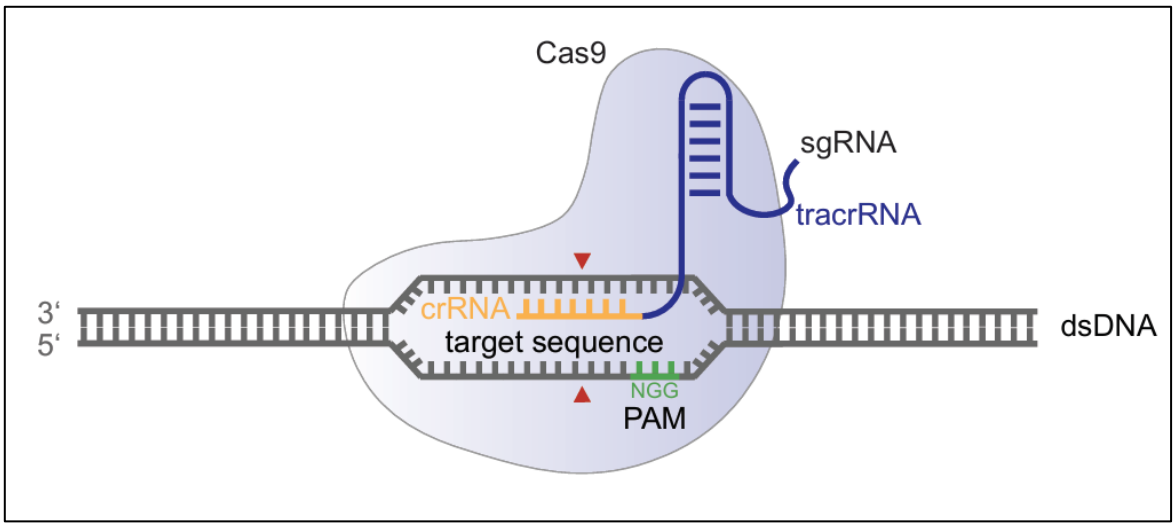

Figure 13|The CRISPR/Cas9 strategy. The Cas9 enzyme binds to a specific RNA sequence known as tracrRNA, which interacts with another RNA sequence called crRNA. The crRNA guides the complex to a complementary DNA sequence. Upon binding of the Cas9/RNA complex to the target DNA sequence and recognition of a nearby PAM sequence, Cas9 induces a double-strand break in the DNA, occurring three nucleotides upstream of the PAM sequence. Red arrows indicate the DNA cutting sites.

3.1.8.1 Design of sgRNA oligonucleotide sequences

Using the “CRISPR guide RNA design tool” on the Benchling.com platform, all potential target DNA sequences for the sgRNA within the coding exons of a desired gene were displayed, along with their off-target and on-target scores. Based on prediction algorithms[210,211], both scores are between 0 and 100, with the higher the better. On-target scores represent the cutting efficiency, while off-target scores indicate the inverse probability of Cas9 off-target binding to sequences in the rest of the genome. According to the platform, it should be noted that the scoring system is not linear and only 5% of the gRNAs achieve a score of 60 or higher. To design the sgRNA, a target DNA sequence of 20 nt was selected being the most proximal to the stop codon for c-terminal genome editing with optimal on- and off-target scores (Table 32).

Table 32|List of the 20 nt target sequence

Gene	DNA strand	PAM	On-/Off-target score	20 nt target sequence (5’ – 3’)
SMC5	Lagging	CGG	18/58	AAGGTTGAGTGAATGTAATA
BLM	Lagging	AGG	16/52	TGTTATGAGAATGCATATGA
PICH	Lagging	AGG	21/37	AAAGTCAAGAGCATAACTTC
FANCD2	Lagging	AGG	22/61	AAGCACAGAAGCTGTTATGG

3.1.8.2 Generation of sgRNA by in vitro transcription

In vitro transcription (IVT) was performed following a modified protocol from Li et al. 2019[212], to generate a target-specific sgRNA required to assemble with a Cas9 protein to form an RNP complex (Fig. 14). The sgRNA was transcribed from a 131 bp dsDNA template with the following sequence: 5’-TAATACGACTCACTATAGNNNNNNNNNNNNNNNNNNNGTTTAAGAGCTATGCTGGAAA CAGCATAGCAAGTTTAAATAAGGCTAGTCCGTTATCAACTTGAAAAAGTGGCACCGAGTC GGTGCTTTTTTT-3’. This sequence includes a T7 promoter region (TAATACGACTCACTATA), a gene-specific 20 nt crRNA sequence starting with an additional G for optimal T7 transcription (GNNNNNNNNNNNNNNNNNNN), and a common tracrRNA region. The dsDNA template was generated via polymerase chain reaction (PCR). The reaction was performed using four primers (Table 10), specifically primer ML557 for the T7 promoter, primer ML558 with a part of the tracrRNA, primer ML611 with the full-length tracrRNA, and a gene-specific primer containing the crRNA sequence and overlapping regions. A 40 µl PCR reaction mixture (Table 33) was amplified using the following thermocycler steps: 95°C for 3 min, 20 cycles of (98°C for 20 s, 57°C for 15 s, 72°C for 5 s), 72°C for 1 min, and 4 °C final.

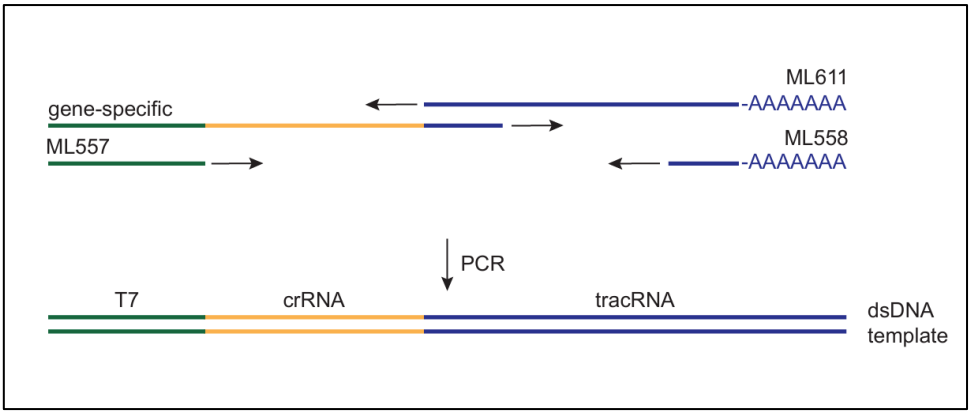

Figure 14|Primer design to generate a dsDNA template for *in vitro* transcription (IVT). By combining four primers, ML557 (targeting the T7 promoter), ML558 (targeting the end of the tracrRNA region), ML611 (targeting the tracrRNA region), and a gene-specific primer containing the crRNA sequence and overlapping regions, a dsDNA template was generated. This dsDNA template was subsequently used for *in vitro* transcription.

For magnetic purification of the PCR product, 60 µL of 100% EtOH and 100 µL of home-brew SPRI magnetic beads in precipitation solution were added to the reaction mixture, followed by 10 min incubation at room temperature (RT). Subsequently, the reaction was incubated on a magnetic isolation rack for 5 min to isolate the beads. While on the magnets, the supernatant was discarded, and the beads were washed twice with nuclease-free 70% EtOH, allowing each wash to sit for 30 s before removing the EtOH. The beads were then air-dried by leaving them on the magnets for 10 min at RT. Next, PCR products were eluted in 12 µl of nuclease-free H_2O, incubated for 3 min at RT, placed back on magnets, and supernatant was transferred into a fresh tube and stored at -20°C. The presence of the dsDNA product was verified by agarose gel electrophoresis, as described in 3.1.5.

Table 33| PCR reaction for IVT specific dsDNA template

Reagent	**Volume [µl]**
5x Phusion HF buffer	8
10 mM dNTPs mix	0.8
0.8 pmol gene-specific sgRNA	0.8
0.8 ML611	0.8
40 pmol ML557	0.4
40 pmol ML558	0.4
Phusion DNA Polymerase	0.4
H_2O	Fill up to 40

To perform T7 IVT of sgRNA from the complementary DNA sequence, 4 µl of purified PCR products were added in a 40 µl reaction (Table 34) using the reagents provided with the HiScribe® T7 High Yield RNA Synthesis kit and incubated for 3 h at 37°C in a thermocycler. Subsequently, 1 µl of Turbo™ DNase was added to the reaction and incubated for 15 min at 37°C. For RNA purification, 80 µl of 100% EtOH and 100 µl of magnetic beads in precipitation solution were added to the reaction. After magnetic purification as described above, the single-stranded sgRNA products with a length of 112 nt omitting the T7 promoter were eluted in 20 µl of RNase-free H_2O and the RNA concentration was determined as described in 3.1.3. The concentration was further adjusted to 130 µM and stored at -80°C, ready for transfection. The

presence of the sgRNA product was verified by agarose gel electrophoresis, as described in 3.1.5.

Table 34|IVT reaction

Reagent	Volume [µl]
PCR product	4
10x T7 reaction buffer	4
100 mM rNTP each	4 each
T7 RNA Polymerase Mix	4
H_2O	Fill up to 40

3.1.8.3 RNP formation and cleavage efficiency assay

To analyze the *in vitro* cleavage (IVC) efficiency of the RNP complex, a target DNA template corresponding to the genomic region where Cas9 introduces a DSB was amplified by PCR. This DNA template of approximately 800 bp in length included the sgRNA target site and was designed to produce two distinct fragments, approximately 600 bp and 200 bp, after successful Cas9-mediated cleavage. Human DNA was extracted from an HCT116 cell line using the DNeasy® Blood & Tissue kit following manufacturer's instructions. A 25 µL PCR reaction mixture (Table 35) with specific primers (Table 11) was prepared and amplified with the following thermocycler steps: 94°C for 1 min, 35 cycles of (94°C for 30 s, 55°C for 1 min, 72°C for 1 min), 72°C for 3 min and 4° final. The PCR product was purified using the QIAquick® PCR Purification kit following manufacturer's instructions. DNA concentration was determined as described in chapter 3.1.3, and samples were stored at -20°C until further use.

Table 35|PCR reaction for IVC target DNA template

Reagent	Volume [µl]
10 x ThermoPol buffer	2.5
10 mM dNTPs	0.5
10 µM Primer forward	0.5
10 µM Primer reverse	0.5
5 U/µl Taq Polymerase	0.5
20 ng/µl DNA	5
H_2O	*Fill up to 25*

For the IVC efficiency assay, the purified PCR fragment was combined with the *in vitro* transcribed sgRNA and the purified recombinant Cas9 protein at a ratio of 1:10:10 (Table 36). The Cas9 and sgRNA reaction was first incubated together in a thermocycler at 37°C for 10 min to allow RNP complex formation. Following this, the RNP complex was combined with the target DNA template and incubated for 90 min at 37°C to allow cleavage of the target DNA. The PCR product was purified using the QIAquick® PCR Purification kit according to the manufacturer's instructions. The cleavage reaction was analyzed by agarose gel electrophoresis, as described in chapter 3.1.5.

Table 36|PCR reaction for IVC assay

Reagent	Volume [µl]
5x IVC reaction buffer	6
150 nM Cas9	1.5
150 nM sgRNA	1.5
H_2O	Fill up to 27
Incubate 10 min at 37°C	
15 nM target DNA	3
Incubate 90 min at 37°C	

3.1.8.4 Cas9/sgRNA plasmid cloning

The Cas9/sgRNA plasmid, used as another approach for Cas9 and sgRNA delivery, was constructed using the px330-U6-Chimeric_BB-CBh_hSPCas9 plasmid by Feng Zhang (Table 8)[213]. Two oligonucleotides, each containing a crRNA sequence of 20 nt and required overhangs (Table 12), were cloned into the px330-based plasmid in accordance with the established target sequence cloning protocol[214].

First, 1 µg of the pX330 plasmid was digested with *BbsI* for 30 min at 37°C (Table 37). The product was purified using the QIAquick® PCR Purification kit according to manufacturer's instructions. Next, each pair of oligos was phosphorylated and annealed (Table 38) in a thermocycler: 37°C for 30 min, 95°C for 5 min, then ramped down to 25°C at 5°C/min. A ligation reaction was prepared (Table 39) and incubated at RT for 10 min. To prevent unwanted recombination products, the ligation reaction was treated with the Plasmid-Safe™ exonuclease reaction (Table 40) and incubated at 37°C for 30 min. To produce multiple copies of the plasmid DNA, chemically competent *E.coli* cells were transformed as described in chapter 3.1.1, and the cell suspension was plated on LB-agar plates containing 100 µg/ml ampicillin.

Table 37| PX330 plasmid digestion reaction

Reagent	Volume [µl]
1 µg Plasmid	x
FastDigest *BbsI*	1
FastAP	1
10x FastDigest buffer	2
H_2O	Fill up to 20

Table 38| Oligo phosphorylation and annealing reaction

Reagent	Volume [µl]
100 µM oligo 1	1
100 µM oligo 1	1
10x T4 ligation buffer	1
H_2O	Fill up to 9.5
T4 PNK	0.5

Table 39| Ligation reaction

Reagent	Volume [µl]
50 ng *BbsI* digested plasmid	x
1:200 diluted oligo duplex phosphorylated and annealed	1
2x Quick ligation reaction buffer	5
H_2O	Fill up to 10
Quick Ligase	1

Table 40| PlasmidSafe exonuclease reaction

Reagent	Volume [µl]
Ligation reaction	11
10x Plasmid-Safe™ buffer	1.5
10 mM ATP	1.5
Plasmid-Safe™ DNase	1

3.1.8.5 Homology donor generation

Homology donor plasmids containing the desired DNA insertion sequence were generated through a multi-step cloning process. Initially, various elements, including target-specific homology arms, fluorescence markers, the AID degron, and resistance genes, were individually cloned into backbone plasmids to generate a library of entry clones using the Gibson assembly cloning strategy. Subsequently, the final homology donor plasmids were assembled by combining these modules into an acceptor vector via the Golden Gate cloning method.

3.1.8.5.1 DNA insert design

Homology arms, AID domain, GFP

The DNA insert sequences from the individual homology arms, the AID domain, and the fluorescence marker green fluorescence protein (GFP) were ordered as gblocks from Integrated DNA Technologies, Inc., Coralville, USA (Table 13). The homology arm sequences, each of a length of 800 bp, were chosen complementary to the left and the right site surrounding the cutting site of the Cas9, whereby the missing nucleotides until the stop codon were included in the left homology arm, omitting the stop codon itself. The right homology arm started with the first base pairs after the endogenous stop codon of the gene of interest. A minimal working sequence of the AID domain was chosen with a length of 132 bp, spanning from the amino acids 71-114 of the original IAA17 sequence[215]. For the green fluorescence protein marker, the sequence of the enhanced GFP (eGFP) with a length of 842 bp was chosen. Due to the length and repetitive regions within the sequence, the hygromycin (1830 bp) and neomycin (1485 np) resistance genes could not be ordered as gblocks.

Resistance genes

The hygromycin and neomycin resistance genes were not possible to order as gblocks and therefore isolated and amplified from commercial plasmids by PCR (Table 41), using the pMK292 plasmid for neomycin and pMK293 for hygromycin (Table 8) and appropriate primers (Table 14). Due to the high GC content, the PCR reaction for the hygromycin resistance gene was performed with the 5x Phusion GC buffer and the addition of DMSO (Table 42). The reaction was incubated in a thermocycler: 98°C for 30 s, 35 cycles of (98°C for 5 s, 58°C for 20 s, 72°C for 1 min), 72°C for 2 min, and 4 °C final. The PCR product was purified using the QIAquick® PCR Purification kit following manufacturer's instructions and stored at -20°C.

Table 41| PCR reaction for neomycin resistance gene isolation

Reagent	Volume [µl]
5x Phusion HF buffer	10
10 mM dNTPs	1.0
10 µM Primer forward	0.5
10 µM Primer reverse	0.5
1400 ng/µl Plasmid DNA	0.5
2 U/µl Phusion DNA Polymerase	0.5
H_2O	Fill up to 50

Table 42| PCR reaction for hygromycin resistance gene isolation

Reagent	Volume [µl]
5x Phusion GC buffer	10
10 mM dNTPs	1.0
10 µM Primer forward	0.5
10 µM Primer reverse	0.5
Plasmid DNA	0.5
2 U/µl Phusion DNA Polymerase	0.5
DMSO	1.5
H_2O	Fill up to 50

3.1.8.5.2 Gibson assembly

Using the Gibson assembly cloning technique[216], entry vectors were generated, each harbouring one tag such as a homology arm, the AID domain, a fluorescence marker, or a resistance gene, as part of the final homology donor used for following CRISPR/Cas9-based genome editing. First, the linear pIDC backbone vector was mixed thoroughly with the DNA insert oligonucleotide and then combined with the 2x Gibson mix (kind gift of Michael Taschner) containing a T5 exonuclease, DNA polymerase, as well as a DNA ligase (Table 43). The Gibson reaction was incubated for 60 min at 50°C. This single-tube reaction allowed the exonuclease to chew back the 5' ends of the DNA strands and to anneal the DNA insert and linear plasmid fragment, followed by the polymerase extending the annealed fragments, and a DNA ligase sealing the nicks. This technique is advantageous as it minimizes errors and biases that often occur during PCR, particularly when dealing with very long DNA sequences. To produce multiple copies of the plasmid DNA, chemically competent pirHC cells were transformed, as described in chapter 3.1.1 with the following changes: the Gibson reaction

was incubated for 1 h at 50°C, then 5 µl of the reaction was added to 50 µl of cells and incubated for 10 min on ice. After heatshock for 1 min at 42°C, the reaction was placed back on ice for 2 min. Cell suspension was plated on LB-agar plates containing 30 µg/ml chloramphenicol. After overnight incubation, several colonies were picked and inoculated in a 5 ml chloramphenicol-LB medium. Plasmid DNA was isolated and verified as described in chapters 3.1.2 to 3.1.7.

Table 43|Gibson reaction

Reagent	**Volume [µl]**
50 ng/µl linear pIDC vector	0.5
DNA insert	0.5
H_2O	Fill up to 5
2x Gibson mix	5

3.1.8.5.3 Golden Gate Assembly

Homology donors ready for transfection in human cells were generated by the Golden Gate assembly cloning technique by allowing several DNA fragments from different entry clones to assemble in the correct order[217]. A 20 µl Golden Gate reaction (Table 44) was incubated in a thermocycler: 30 cycles of (37°C for 2 min, 16 °C for 5 min), 50°C for 10 min, 80°C for 5 min, and 4°C final. Chemically competent DH5alpha *E.coli* cells were transformed as described in chapter 3.1.1. The cell suspension was plated on LB-agar plates containing 100 µg/ml ampicillin. After overnight incubation, several colonies were picked and inoculated in a 5 ml ampicillin-LB medium. Plasmid DNA was isolated and verified as described in chapters 3.1.2 to 3.1.7.

Table 44|Golden Gate reaction

Reagent	**Volume [µl]**
100 ng of each plasmid	100 ng/each
10x T4 ligase buffer	2
BsaI-HFv2	0.25
T4 DNA Ligase	0.3
H_2O	Fill up to 20

3.1.8.6 Site-directed mutagenesis

Site-directed mutagenesis was used to introduce specific changes to a DNA sequence by substituting, deleting, or inserting one or more nucleotides within a DNA sequence. According to the “QuikChange site-directed mutagenesis” tool of the Agilent.com platform, oligonucleotide sequences were designed and ordered.

Site-directed mutagenesis of plasmids

Site-directed mutagenesis of plasmid DNA using the “Quikchange” method[218] was performed, for example, to insert two additional nucleotides inside the homology donor to ensure in-frame expression of all tags or to introduce silent mutations of the PAM sequence within the homology arm left if occurring in-frame (Table 9). First, reaction 1 (Table 45) was mixed with reaction 2 (Table 46) and amplified following the thermocycler program: 95°C for 2 min, 30 times (95°C for 30 s, 55 °C for 30 s, 72°C for 10 min), 72°C for 10 min and 4°C final. After amplification, 2 µl *DpnI* restriction enzyme was added and incubated at 37°C for 2 h, cleaving only the methylated, parental plasmid DNA. The plasmid was further transformed into chemically competent *E. coli* cells as described in chapter 3.1.1. Plasmid DNA was isolated and verified as described in chapters 3.1.2 to 3.1.7.

Table 45|Site-directed mutagenesis reaction 1

Reagent	**Volume [µl]**
20 µM Primer forward	0.63
20 µM Primer reverse	0.63
50 ng/µl Template plasmid DNA	1.0
H_2O	Fill up to 2.26

Table 46|Site-directed mutagenesis reaction 2

Reagent	**Volume [µl]**
10x Pfu buffer	2.5
10 mM dNTP’s	0.7
DMSO	1.0
Pfu Turbo DNA Polymerase	1.0
H_2O	Fill up to 22.8

Site-directed mutagenesis of linear DNA sequences

Site-directed mutagenesis of linear DNA sequences was performed by overlapping primer extension utilizing mutagenic primers in two separate PCR reactions. Two tubes were prepared (tube 1 and 2), one for the left and the right site of the entire DNA sequence, and one for the surrounding region of the desired change (Table 47). Both reactions were then combined in a third reaction (Table 48) to generate the final sequence with the desired sequence changes. All reactions were amplified by PCR following the thermocycler program: 98°C for 30 s, 30 times (98°C for 5 s, 71°C for 20 s, 72°C for 30 min), 72°C for 5 min, and 4°C final. The PCR product was purified using the QIAquick® PCR Purification kit following manufacturer’s instructions and stored at -20°C. This was performed for the substitution of the *BsaI* recognition sequence 5’-GGTCTC-3’ to 5’-AGTCTC-3’ inside the linear PICH HL sequence, ready for subsequent Gibson assembly to generate pIDC entry clones (see chapter 3.1.8.5.2).

Table 47|Tube 1 and tube 2 for site-directed mutagenesis of linear sequence

Reagent	Volume [µl]
5x Phusion HF buffer	10
10 mM dNTP's	1
10 µM Primer forward	2.5
10 µM Primer reverse	2.5
Template DNA ~ 5 ng/µl	2
2 U/µl Phusion Polymerase	0.5
H_2O	Fill up to 50

Table 48|Tube 3 for site-directed mutagenesis of linear sequences

Reagent	Volume [µl]
5x Phusion HF buffer	10
10 mM dNTP's	1
10 µM Primer forward	2.5
10 µM Primer reverse	2.5
Template DNA 10 µl tube 1 + 10 µl tube 2	20
Phusion Polymerase	0.5
H_2O	Fill up to 50

3.1.8.7 Genomic PCR

Genomic DNA was isolated from human cells using the Qiagen DNeasy® Blood & Tissue kit following manufacturer's instructions. In brief, a maximum of $5x10^6$ cells were collected and lysed, DNA was precipitated and eluted in 200 µl of nuclease-free H_2O. DNA concentration was determined by a spectrometer according to chapter 3.1.3. The verification of human cell clones consisting of edited DNA was assessed by performing a three-primer PCR reaction (Table 49) using gene-specific primers, two outside of the homology donor and one inside the GFP region (Table 9). The reaction was amplified by PCR following the thermocycler program: 98°C for 30 s, 30 times (98°C for 5 s, 72°C for 20 s, 72°C for 30 min), 72°C for 5 min, and 4°C final. The PCR product was purified using the QIAquick® PCR Purification kit following manufacturer's instructions and stored at -20°C.

Table 49| Three-primer PCR reaction for human cell clones

Reagent	Volume [µl]
5x Phusion HF buffer	10
10 mM dNTP's	1
10 µM Primer forward	2.5
10 µM Primer reverse	2.5
125 ng/µl Template DNA	2
2 U/µl Phusion Polymerase	0.5
H_2O	Fill up to 50

3.2 Cell culture techniques

All cell culture experiments served as the basis of this research project and were performed precisely, requiring a sterile workplace under a laminar flow hood to keep cells free from any contamination with microorganisms. Each device needed was used under the flow hood after being sterilized with 70% ethanol. Cell density and health were routinely monitored by light microscopy. Additionally, cells were regularly screened for mycoplasma contamination using the MycoStrip® Mycoplasma Detection kit, following manufacturer's instructions. All experiments described in this thesis were conducted using mycoplasma-free cells.

3.2.1 Cell line maintenance

All human cell lines used in this project were adherent cells and cultured in a 2D monolayer at 37°C in a humidified incubator with 5% carbon dioxide (CO_2).

The original HCT116 colorectal carcinoma cells were derived from an adult male and harbour a mutation in codon 13 of the Ras proto-oncogene. The cells are nearly diploid and, due to the frequent loss of the Y chromosome, usually have a chromosome number of 45. HCT116 Tet-OsTIR1 cancer cells from the Kanemaki laboratory[206] (see list of cell lines, Table 20) carry additionally a homozygous insertion of the auxin-responsive F-box protein TIR1 derived from the plant *Oryza sativa*, OsTIR1, under the control of the conditional Tet promoter as well as a puromycin resistance cassette at the safe harbor AAVS1 locus.

The fibroblastic cell lines PSNF5 (BLM-proficient) and PSNG13 (BLM-deficient) from the Hickson laboratory originate from the SV40-transformed BS fibroblast cell line GM08505. PSNF5 is stably transfected with a plasmid expressing Flag-tagged BLM ($BLM^{+/+}$), whereas PSNG13 carries an empty vector ($BLM^{-/-}$)[219].

Cells were cultured in 10 ml of their specific growth medium (table 22) in a 75 cm² culture flask and were splitted every 2-3 days as soon as they had reached about 70% confluence. After aspirating the medium from the culture flask, cells were washed once with pre-warmed 1x PBS to remove the remaining medium. For this purpose, about 5 ml of 1xPBS was carefully added to the flask and the flask was rotated to cover and wash the cells adhering to the bottom. After removing the PBS, cells were detached from the surface by trypsinization with 1 ml of pre-warmed trypsin, incubation for 5 min at 37°C, and gently tapping the flask to allow full detachment of the cells. Cells were resuspended in fresh medium to inactivate trypsin and subsequently transferred at a dilution of 1:10 to a new flask containing a total of 10 ml of pre-warmed fresh growth medium. The cells were evenly distributed by moving the flask crosswise and placed back into the 37°C incubator. Newly splitted cells were assigned a new passage number.

3.2.2 Freezing and thawing

Freezing of human cell lines

Trypsinized and detached cells, as described in 3.2.1, from one culture flask with approximately 60% confluence were collected in a 15 ml tube, centrifuged at 1,300 rpm for 3 min at RT, the supernatant was removed, and the cell pellet was resuspended in 1 ml of freezing mix. The cell suspension was transferred to a cryotube, the cap was closed and loosened one full turn. Cells were slowly frozen in a freezing box containing isopropanol at -80°C overnight. The next day, the cryotubes were transferred to liquid nitrogen for long-term storage.

Thawing of human cell lines

Frozen cells were thawed by quickly placing the cryotubes that were stored in liquid nitrogen in a 37°C water bath until the medium began to defrost. Subsequently, the cell suspension was then transferred step by step with pre-warmed fresh growth medium to a new tube containing 10 ml of pre-warmed fresh growth medium and centrifuged at 1,300 rpm for 3 min at RT. After removing the supernatant, the cell pellet was resuspended in 10 ml of fresh growth medium to remove DMSO containing freezing mix. Cells were transferred to a new 75 cm² culture flask and stored at a 37 °C incubator after moving the flask cross-wise to ensure evenly spread cells. The next day, the medium was replaced to remove dead cells. Further passaging of the cells was performed as described in chapter 3.2.1.

3.2.3 Cell counting

For each subsequent experiment, a defined number of cells were seeded per condition. The cell count was determined using the Countess™ II automatic cell counter. By mixing 10 µl cell suspension with Trypan Blue at a dilution of 1:2 and applying it to a counting chamber provided the cell number per ml was specified.

3.2.4 AID-cell line generation by transient transfection and clone isolation

HCT116 Tet-OsTIR1 cells were used as the parental cell line to generate AID mutants by inserting an AID domain at the endogenous locus of genes of interest. 0.3 x 10^6 cells/well were seeded in 6-well plates 24 h prior to transfection. For transfection, 350 µl of serum-free medium containing 2 µg of pX300-based CRISPR/Cas9 plasmid DNA and 2 µg of Hygro donor plasmid DNA per well was prepared. Additionally, 350 µl of serum-free medium containing 6 µg of PEI transfection reagent (pH 7.5) per well was added to the plasmid reaction while forming bubbles. The transfection mixture was incubated for 30 min at RT to allow complex formation and then added dropwise to the cells. Cells were incubated at 37°C and after 6 h, the medium was refreshed to remove the transfection reagent and provide fresh nutrition. 48

hours after transfection, the cells were collected, thoroughly resuspended, and distributed across 2-4 culture dishes (15 cm), each containing 20 ml of medium with 100 µg/ml hygromycin. This allowed for the selection of successfully transfected cells carrying the resistance marker. The cells were plated in a way that ensured each individual cell grew separately to form distinct colonies. The selection medium was replaced every 2 d. After approximately 14 d until no longer strong cell dying, the individual colonies were washed once in 1x PBS, picked up using sterile cloning disks with a diameter of 3.2 mm soaked for 5 min in trypsin and then transferred to 96-well plates using a sterilized forceps. After one day, cells were attached to the wells and cloning disks were removed. Upon outgrowth of the wells, clones were transferred to 6-well plates for further validation by genomic DNA isolation used for genotype analysis and for protein analysis by western blotting, microscopy, and flow cytometry. Positive homozygous clones for insertions at the BLM locus were further referred to as HCT116 Tet-OsTIR1 $BLM^{AID/AID,}$ and heterozygous ones as HCT116 Tet-OsTIR1 $BLM^{AID/WT}$.

3.2.5 Cell synchronization

To synchronize cells, HCT116 Tet-OsTIR1 $BLM^{AID/AID}$ cells were grown for 24 h either on sterilized coverslips embedded in 6-well plates for microscopic purposes or in 6-well plates for protein detection and flow cytometric analysis. After a preincubation with 1 µg/ml Dox for 24 h to activate the tet promoter to express *OsTIR1*, cells were additionally treated with 2 mM thymidine for another 24 h to induce a single-thymidine block at the G1/S boundary. After careful washing of the cells twice with pre-warmed 1xPBS and twice with pre-warmed medium, cells were released into the cell cycle. To induce mild replication stress, cells were additionally treated with 100 nM aphidicolin from the timepoint of cell release.

3.2.6 Cell cycle-specific depletion of BLM

Cell cycle-specific functions of BLM were addressed by depleting BLM either during S-phase, during M-phase or during S- and M-phase together. Cells were synchronized according to chapter 3.2.5. To evoke BLM depletion during S- and M-phase (S+M) as well as S-phase alone (S), cells were at the timepoint of the treatment with thymidine additionally incubated with 500 µM IAA. After cell release into the cell cycle, IAA was supplemented again. BLM depletion only during S-phase was induced by growing cells in the presence of 500 µM IAA until 6 h after cell release. After 6 h, cells were washed twice with pre-warmed 1x PBS and twice with pre-warmed medium and cultured furthermore in fresh medium until collection. Depletion only during M phase (M) was induced by growing the cells with the addition of IAA only from the time point of 6 h after cell release from thymidine block until collection.

3.3 Colony formation assay

After seeding 500 cells/well of thoroughly distributed HCT116 Tet-OsTIR1 $BLM^{AID/AID}$ cells in 6-well plates, medium was replaced 24 h later with medium containing 1 µg/ml Dox. After 24 h, cells were additionally grown in the absence or presence of 500 µM IAA and/or 100 nM aphidicolin, respectively. Medium and treatments were replaced every 24 h. After 10 d of treatments, colonies were washed twice with pre-warmed 1x PBS and fixed in crystal violet fixative for 20 min at RT. The crystal violet fixative was removed and kept for reuse. After washing once with 1x PBS and 1-2 times with H_2O, colonies were dried in the plate with open lid under the fume hood for two days and analysed using FIJI software.

3.4 Proliferation assay

Cell proliferation assay was performed by seeding $1.5x10^3$ cells/well in triplicates into 96-well plates. In total 4 plates, one for each day, were prepared per cell line. After 24 h, asynchronous cells were treated with 1 µg/ml Dox. After another 24 h, cells were additionally treated either with 500 µM IAA, 100 nM APH or in combination for 24 h. ATP was quantified using the CellTiter-Glo® Luminescent Cell Viability Assay kit following manufacturer´s instructions. Every 24 h 50 µl of the CellTiter-Glo® reagent/well was added, cells were further incubated for 2 min and shaked at RT for 10 min right before luminescence measurement using the GloMax Explorer multimode microplate reader. All measurements were normalized to day 0. The experiments were performed in triplicates.

3.5 Senescence x-gal assay

$0.3x10^6$ cells/well were seeded into 6-well plates. After 24 h, the medium was replaced with fresh medium containing 1 µg/ml Dox. 24 h later, cells were treated with either 500 µM IAA, 100 nM APH, or both. 1 µM Doxo was used as a positive control. The medium was replaced after 24 h to induce recovery for 4 days with medium exchange every day. For those conditions with 4 days of treatment, medium with Dox and substances was exchanged every day. Senescence-associated beta-galactosidase (SA-β-Gal) assays were performed by chromogenic substrate x-gal staining on fixed cells as well as flow cytometric detection of the fluorescent SA-β-Gal substrate DDAO-galactoside (DDAOG; see chapter 3.6.3). For x-gal detection[220], medium was removed, cells were washed twice with 1x PBS and incubated in 2 ml/ well x-gal fixation solution for 5 min at RT. After removing fixation solution, cells were washed twice with 1x PBS and incubated in 2 ml/well of x-gal staining solution overnight at 37°C. After removing the staining solution, cells were washed twice with 1x PBS, once with 1 ml of 100% methanol per well and were allowed to air dry. Cellular senescence was indicated by the presence of dark cytoplasmic staining resulting from β-galactosidase substrate activity.

3.6 Flow Cytometry

Flow cytometry analysis was performed by excluding cell debris and dead cells, and identifying single-cell populations based on forward scatter (FSC) and side scatter (SSC) parameters, which reflect cell size and granularity. Doublets, typically resulting from cell clumps, were excluded based on their increased FSC signal.

3.6.1 GFP signal analysis by flow cytometry

$0.3x10^6$ cells/well were seeded into 6-well plates. After 24 h, cells were harvested by trypsinization, followed by centrifugation at 1300 rpm for 3 min. To assess GFP signal dynamics following BLM depletion, asynchronous cells were additionally treated with 500 µM auxin and collected at defined time points for analysis. The cell pellet was resuspended in 200 µL of 1x PBS and analyzed on an Attune™ NxT Flow Cytometer using a 488 nm blue excitation laser and a 530/30 bandpass filter to detect GFP fluorescence. FlowJo software was used for data acquisition and analysis. The GFP signal intensity was quantified to assess BLM depletion efficiency over time by applying gates to the GFP histogram plot.

3.6.2 Cell cycle analysis by flow cytometry

$0.3x10^6$ cells/well were seeded into 6-well plates for 24 h and synchronized according to the synchronization procedure as described in chapter 3.2.5. Every 2 h after thymidine wash out, cells were harvested by trypsinization followed by centrifugation at 1300 rpm for 3 min. Immunostaining was performed as described in chapter 3.6.4. The 574/26 bandpass filter for used for the DNA stain propidium iodide (PI) detection. Analysis was conducted with FlowJo software. Each cell cycle phase (G1, S, G2 and M) were quantified by applying gates to the PI and MPM-2 histogram plot.

3.6.3 Senescence assay by flow cytometry

Cells were treated as described in chapter 3.5. Culture medium was exchanged to penol red-free medium. Cells were pre-treated with 100 nM bafilomycin A1 for 1 h, followed by 2 h of DDAOG staining. Cells were gently washed twice with pre-warmed 1x PBS to remove staining and harvested by trypsinization, followed by centrifugation of 300 x g for 5 min. Cells were resuspend in 200 µl 1x PBS. Subsequent measurements were taken using the Attune™ NxT Flow Cytometer with 638 nm red excitation and a 670/14 bandpass filter to detect DDAOG. FlowJo software was used for data acquisition and analysis. The DDAOG signal intensity was quantified by applying gates to the DDAOG histogram plot.

3.6.4 Immunostaining for flow cytometry analysis

Cells were harvested by trypsinization and washed with 1x PBS at 2000 rpm for 2 min. Cells were fixed by adding 500 µl of 70% ice-cold ethanol dropwise while vortexing and incubated at 4 °C overnight. The following day, cells were washed once with 1x PBS containing 0.25 % Triton-X-100 and centrifuged at 2000 rpm for 5 min, to remove residual ethanol. The pellet was then resuspended in 100 µl of PBS containing 1% BSA and primary antibody, incubating for 1 h at RT. After washing, cells were resuspended in secondary antibody diluted 1:300 in 100 µl PBS with 1% BSA, incubating for 30 min at RT in the dark. DNA staining and RNA degradation was induced by staining the cells with 500 µl of FxCycle™ PI/RNase staining solution for 30 min at RT in the dark. Measurements were taken using the Attune™ NxT Flow Cytometer with appropriate excitation wavelength and bandpass filter for emission. 574/26 bandpass filter was used for the DNA stain propidium iodide (PI) detection. Analysis was conducted with FlowJo software.

3.7 Microscopy

3.7.1 Mitotic aberration analysis in anaphase by microscopy

Microscopic detection of mitotic aberrations in HCT116 Tet-OsTIR1 $BLM^{AID/AID}$ cells was performed after seeding approximately 0.25 x 10^6 cells per well in 6-well plates to reach 60-70% confluency after 24 h after placing dry and sterile coverslips of ø12 mm and a thickness of 0.17 mm in each well. Cells were treated according to the cell synchronization protocol (chapter 3.2.5). At 10.5 h after cell release (T10.5), cells were gently washed once with 1x PBS and incubated with PFA-containing fixation buffer for 30 min at RT. After careful removing of fixation buffer and keeping a leftover of approximately 200 µl, cells were washed three times with 1x PBS by slowly reducing the left-over of fixation buffer after each washing step. After permeabilization for 20 min, cells were washed three times with 1x PBS and incubated with blocking buffer for PFA-fixation for 1 h at RT. Afterwards, cells were incubated in primary antibodies diluted in blocking buffer at 4°C overnight in a humidified chamber. After washing three times with 1x PBS, secondary antibodies diluted in blocking buffer were added for 1 h at RT and incubated in a humidified chamber. Secondary antibodies were removed by washing three times with 1x PBS. Staining solution was added for 3 min at RT in the dark and removed by washing once with PBS and once with H_2O. Coverslips were mounted at dry glass slides stored at -20°C in 70% ethanol, sealed with nail polish and stored at 4°C in the dark until microscopic detection. 25 anaphases per replicate were captured with a 63x oil immersion objective lens and 10x eyepiece. Captures were taken, using the Nikon Ti2-E epifluorescence microscope, with 500 ms exposure time for DAPI combined with 20% laser power and every other channel 500 ms exposure time and 60% laser power. Relative offsets for z stacks were chosen with 25 steps and a size of 0.3 µm, range 7.2 µm. Mitotic aberrations in anaphases, such as chromatin bridges as well as lagging or misaligned chromatin, require only DAPI staining and no antibody incubation but were analyzed in the same anaphases stained for ultrafine bridge marker, thus all images include antibody staining. Images were analysed using

ImageJ/FIJI program. Co-localization analysis was performed using the JACOP plugin of ImageJ to analyse Pearson's coefficient (r)[221]. BLM intensity was measured by intensity measurement in ImageJ and subtracting the background.

3.7.2 Metaphase spread analysis by microscopy

HCT116 Tet-OsTIR1 BLM$^{AID/AID}$ cells were seeded at approximately 0.25 x 10^6 cells per well in 6-well plates to reach 60-70% confluency after 24 h. Cells were synchronized according to the synchronization protocol (chapter 3.2.5). At 10.5 h after thymidine release, cells were gently washed once with 1x PBS. Medium and PBS containing detached mitotic cells were collected in tubes together with trypsinized cell suspension. Cells were centrifuged at 1,200 rpm for 3 min at RT, then the pellet was washed once with 1x PBS and centrifuged again. After aspiration of most of the medium and leaving 500 µl behind, pellet was resuspended carefully in the remaining medium. 7 ml of hypotonic solution was added to each sample while gently tapping the tube. After incubation at 37˚C for about 20 min, cells were swollen, which can be observed by taking 10 µl cell suspension under the microscope. Cells were centrifuged at 1,000 rpm for 5 min at RT. After removing the supernatant, cells were resuspended in remaining 500 µl. Cells were fixed by adding 7 ml of fixative solution slowly to each sample. Cells were centrifuged at 1,200 rpm for 3 min at RT, supernatant was aspirated, and cells were resuspended in 500 µl leaving behind. Fixation with fixative solution and centrifugation was repeated two additional times and afterwards supernatant was removed completely. After adding fresh 500 µl fixative solution tubes were stored at -20°C until metaphase spreading. Metaphase chromosomes were spread on dry glass slides that were stored at -20°C in 70% ethanol from a height of approximately 100 cm. Coverslips of 0.17 mm thickness were mounted with mounting medium containing DAPI solution and sealed with nail polish. 25 metaphases per replicate were captured with a 63x oil immersion objective lens and 10x eyepiece. Captures were taken, using the Nikon Ti2-E epifluorescence microscope, with 500 ms exposure time for DAPI combined with 20% laser power without z stacks. Images were analysed using ImageJ/FIJI program. Gaps and breaks were not distinguished due to difficulties in making clear demarcations.

3.7.3 Sister chromatid exchange analysis by microscopy

Per experimental condition, 0.4 x 10^6 cells were cultured in a 10 cm culture dish. After a preincubation with 1 µg/ml Dox for 24 h, BLM depletion was induced by treating the cells with 500 µM IAA. Additionally, 20 µM of BrdU was added to the cells and incubated for 40 h to allow two rounds of cell division, while BrdU was incorporated into replicating and newly synthesized DNA by substituting thymidine. 5 h before harvesting, 400 ng/ml colchicine was added. The polymerisation of microtubules by binding to tubulin is inhibited by colchicine, therefore preventing the spindle assembly during mitosis and cells cannot complete cell cycle. Cells were trypsinized and collected in tubes. 7 ml of pre-warmed hypotonic solution was added dropwise to the cell pellet, mixed gently by inversion of the tube, and placed at 37°C for 15 min. After addition of 2 ml ice-cold freshly prepared fixative solution dropwise to the cells, the

tubes were inverted to mix and resuspend cells. After centrifugation for 5 min at 200 x g, supernatant was removed, and 5 ml of fixative solution was added again and cell pellet resuspended. Repeat for a total of three cycles. Afterwards, cells were stored in fixative solution at 4°C indefinitely if required, otherwise protocol was immediately continued. Cells were dropwise, approximately 20 µl, added from a height of an arm length to dried microscopic slides that have been stored at 4°C in H_2O after immersing them in 100% ethanol and H_2O. Cells were allowed to dry overnight in the open air at RT. The next day, slides were immersed in 10 µg/ml Hoechst 33258 for 20 min in a dark slide container. After rinsing slides in Sorensen phosphate buffer, coverslips were added carefully on top of each spread that was mounted with few drops of Sorensen phosphate buffer to prevent slides from drying out. By using the advantage of BrdU incorporated DNA preferentially is more damaged from UV light exposure than without BrdU in the presence of the intercalating UV light-absorbing Hoechst 33258 dye and therefore less stained by Giemsa later, slides were exposed to long wavelength UV light (here 312 nm) for 30 min. After carefully removing of the coverslips, slides were immersed with 1x SSC buffer and incubated in 1x SSC buffer for 1 h at 50°C. Slides were removed and immersed in 4% Giemsa stain for 30 min at RT in the dark. Slides were washed subsequently in H_2O twice and dried overnight at RT in the dark. After mounting with vectashield containing DAPI staining and embedding in cover slips, metaphases spreads were analysed. Captures were taken, using the Zeiss Axio Z1 epifluorescence microscope with 1000 ms exposure time for DNA without z stacks. Images were acquired using SlideBook software.

3.7.4 Consequences in next G1 analysis my microscopy

Microscopic detection of consequences in next G1 in HCT116 Tet-OsTIR1 $BLM^{AID/AID}$ cells was performed after seeding approximately 0.25 x 10^6 cells per well in 6-well plates to reach around 60-70% confluency after 24 h after placing dry and sterile coverslips of ∅12 mm and a thickness of 0.17 mm in each well. Cells were treated according to the cell synchronization protocol (chapter 3.2.5). At 15 h after cell release (T15 h), cells were gently washed once with 1x PBS and incubated with 100% ice-cold methanol for 10 min on ice. Cells were washed by gently removing methanol and leaving around 200 µl behind. Further, cells were washed 3x with ice-cold 1x PBS and blocked for 1 h at RT with blocking buffer for methanol fixation. After adding approximately 30 µl of primary antibody solution diluted in blocking buffer on top of cover slips, cells were incubated with primary antibodies at 4°C overnight in a humidified chamber. After washing three times with 1x PBS, cells were incubated with secondary antibodies diluted in blocking buffer for 1 h at RT in the dark in a humidified chamber. Cells were washed three times with 1x PBS and stained in staining solution for 3 min at RT in the dark and removed by washing once with PBS and once with H_2O. Coverslips were mounted at dry glass slides that were stored at -20°C in 70% ethanol, sealed with nail polish and stored at 4°C until microscopic detection. At least 600 cells were captured per replicate with a 40x objective lens and 10x eyepiece. Captures were taken, using the Nikon Ti2-E epifluorescence microscope, with 500 ms exposure time for DAPI combined with 20% laser power, every other channel with 500 ms exposure time and 60% laser power without z stacks. Images were analysed using ImageJ/FIJI program.

3.7.5 Live-cell imaging by time-lapse microscopy

$0.3x10^5$ cells/well were seeded into 8-well glass-bottom plates with black walls. After 24 h, the medium was replaced with medium containing 1 µg/ml Dox. 24 h later, cells were synchronized by single-thymidine block, as described in chapter 3.2.5. After thymidine wash.out, medium was replaced with phenol red-free FluoroBrite™ medium and treated with 500 µM IAA, 100 nM APH or both. 10 min prior live-cell imaging, DNA was stained with NucSpot® Live 650 dye. Captures were taken, using the Nikon CSU-W1 Confocal spinning disk microscope, beginning at 8 h post-release, with images captured every hour until 10 h. From 10 to 11 h post-release, images were taken every 5 min, followed by hourly imaging from 11 to 24 h post-release. Each condition was captured at 4 different locations. Images were analysed using ImageJ/FIJI program.

3.8 Protein detection

3.8.1 Cell lysis

Cells were harvested by trypsinization as described in chapter 3.2.1, the pellet was washed once with ice-cold 1x PBS and lysed in 50-200 µl ice-cold RIPA lysis buffer supplemented with protease and phosphatase inhibitors. Lysates were sonicated in a water bath at 4°C for 20 min. To collect cell debris, the lysate was centrifuged at 13,000 rpm for 30 min at 4°C and supernatant was transferred to a fresh tube. The protein concentration of the samples was estimated using the Pierce™ BCA protein assay kit or Bradford solution in case of less amount of lysate. The samples were diluted to a final stock concentration of 1 µg/µl in β-mercaptoethanol containing Laemmli buffer and denatured by boiling the samples at 95°C for 5 min.

3.8.2 SDS-PAGE and Western Blotting

Using SDS-PAGE, proteins were separated according to their molecular weight. 20 µg protein per sample was loaded mostly on a polyacrylamide gel. As molecular weight marker, the precision plus protein all blue standard was used. Protein separation was carried out in 1x running buffer at a voltage of 100 V for around 90 min until samples reaching the end of the gels. Subsequently, proteins were transferred onto a nitrocellulose membrane at a voltage of 100 V for 60 min at 4°C in 1x wet-transfer buffer. To validate successful and equal protein transfer, the membranes were stained in ponceau solution for 5 min, washed with H_2O and imaged. Next, the membranes were blocked using 5 % skim milk or 3% BSA blocking solution for 1 h at RT while shaking. The membranes were incubated in primary antibodies (table 28) overnight at 4°C, washed three times each 5 min in TBST and incubated in secondary antibodies (Table 29) coupled to horseradish peroxidase for 1 h at RT. After another washing period of three times each 5 min in TBST, membranes were incubated for 5 min in Clarity™

Western ECL substrate ECL or stronger Lumigen ECL solution, depending on the detection level required and target protein's abundance. Protein bands were detected using the Azure c500 gel imaging system. Density intensity of immunodetected protein bands were recorded in data using ImageJ software.

3.9 Chromatin-immunoprecipitation-mass spectrometry (ChIP-MS)

3.9.1 Cross-linking and harvesting

For the cell synchronization experiments using HCT116 cells, the following seeding densities were applied for each replicate: single-thymidine block synchronization with 4 x 10^6 HCT116 cells and 4.5 x 10^6 HCT116 Tet-OsTIR1 $BLM^{AID/AID}$ per 15 cm dish. The experiments were set up as described in chapter 3.2.5. At the timepoint of cross-linking, each plate should reach approximately 80-90% confluency. For the cross-linking of mitotic cells, the supernatants were saved to prevent the loss of loosened and rounded-up mitotic cells, which tend to detach easily. Medium from each plate was collected separately before trypsinization to retain any mitotic cells that had already detached. Cells were trypsinized as described in 3.2.1 and centrifuged at 1,300 rpm for 3 minutes at RT and the supernatant containing mitotic cells was saved. Cells were cross-linked using 1% methanol-free formaldehyde and incubated for 10 min at RT while rolling. For mitotic cells, formaldehyde was added to the trypsinized cell suspension in a tube while rolling. For non-mitotic cells, formaldehyde was added directly to the growth medium in the culture dish. To stop the cross-linking reaction, 125 mM glycine was added, and the mixture was incubated for an additional 5 minutes at RT. Cells were washed twice with ice-cold 1x PBS. Mitotic cells were collected by centrifugation, non-mitotic cells were scraped carefully from the culture dishes and then collected by centrifugation. The supernatant was discarded, and the resulting cell pellet was snap-frozen in liquid nitrogen. The frozen pellet was stored at -80°C until further use. This process preserves cellular structures for further analysis, such as chromatin immunoprecipitation (ChIP).

3.9.2 Cell lysis

Antibody-based immunoprecipitation

Samples were lysed by resuspending the frozen cell pellet in 2 ml of ice-cold Fast-IP buffer. The cell suspension was then transferred to a fresh tube and incubated on ice for 10 minutes. Afterward, the samples were centrifuged at 12,000 rpm for 1 minute at 4°C. Depending on the experimental needs, the supernatant was either discarded or retained as the soluble fraction for SDS-PAGE analysis, if applicable. The pellet was resuspended in 1 ml of ice-cold Fast-IP buffer and incubated again on ice for 10 minutes. After a second centrifugation, the pellet was resuspended in 1 ml of ice-cold shearing buffer, transferred to a fresh tube, ready for sonication.

GFP- trap immunoprecipitation

Samples were lysed by vigorously resuspending the frozen cell pellet twice with 1 ml of ice-cold IP RIPA buffer, incubating each time for 10 minutes on ice. After each incubation, the samples were centrifuged at 12,000 rpm for 1 minute at 4°C. Following the final spin, the cell pellet was resuspended in 1.8 ml of ice-cold shearing buffer.

3.9.3 Chromatin preparation by sonication

Sonication with a homogenizer

For sonication using the Bandelin homogenizer, each tube containing chromatin from the same condition was pooled into 5 ml tubes to minimize foaming during the process. The chromatin was then sonicated with the Bandelin HD 2200 homogenizer equipped with an MS73 probe. If sonication was performed in 1.5 ml tubes, the MS72 probe was used. To prevent overheating, the tubes were placed on a metal rack, with the bottom of the tube submerged in ice-cold water, and the remaining space was filled with ice. The sonication was conducted at 20% power with a 50% cycle setting, applying 20-second bursts for a total of 30 cycles. After each burst, there was a 20-second break, and after every 10 cycles, a 5-minute break was introduced to maintain optimal conditions for achieving chromatin fragments of approximately 200-500 bp. Once sonication was complete, the sheared chromatin lysate was stored at 4°C until further analysis of chromatin fragmentation.

Sonication with a Bioruptor

Cells, resuspended in 1.8 ml of ice-cold shearing buffer, were evenly distributed into six Diagenode 1.5 ml tubes. This step ensured efficient sonication using the Bioruptor® Pico sonication device, adhering to the recommended cell count of 3-9 x 10^6 cells per 100-300 µl of shearing buffer per tube. The samples were placed in the tube holder, which was immersed in a water bath maintained at 4°C and sonicated at 4°C for 15 cycles (30 seconds on, 30 seconds off) to achieve chromatin fragments of approximately 200-500 bp in size. After sonication, the samples were centrifuged for 20 minutes at 12,000 rpm and 4°C. The supernatant containing the sheared chromatin was carefully transferred to a new tube and stored at 4°C until further analysis of chromatin fragmentation.

3.9.4 Determination of chromatin fragmentation

50 µl of sheared chromatin were incubated with 2 µl of 5 M NaCl at 99°C for 15 min, followed by cooling on ice for 5 min. Samples were then incubated with 2 µl of 10 mg/ml RNase at 37°C for 20 min. 11 µl of Proteinase K solution was added to each tube and the mixture was incubated at 56°C for 20 min to digest proteins. The chromatin was subsequently purified using the Qiagen PCR-purification kit according to the manufacturer's instructions and the DNA was

eluted in 50 µl of nuclease-free H_2O. DNA concentration was measured (as described in chapter 3.1.3) and 800 ng of DNA was loaded onto a 1% agarose gel for electrophoresis (as described in 3.1.5) to analyze the fragment sizes.

3.9.5 Chromatin-immunoprecipitation mass spectrometry

IP with protein G agarose beads

25 µg of chromatin, corresponding to approximately 1000 µg protein, per replicate was filled up to a final volume of 500 µl with Fast-IP buffer. was incubated with the 2 µg of antibody overnight at 4°C while tubes were sealed with parafilm and placed on an overhead rotator. Remaining chromatin was stored at -80°C.

30 µl of ChIP-grade protein G agarose beads per IP were washed in total 10 ml of 1x TBS by centrifuging at 3,000 rpm for 2 min at 4°C. The supernatant was discarded. The beads were resuspended in 500 µl per IP of 1x TBS, each replicate distributed to a fresh tube and centrifuged at 3,000 rpm for 2 min at 4°C. The supernatant was discarded. The immunoprecipitated chromatin was added to the beads and incubated for 2 h on the overhead rotator at 4°C. The antibody/agarose G beads mixtures were washed three times with low salt wash buffer, once with high salt wash buffer and once with 1x TBS by centrifuging at 3,000 rpm for 2 min at 4°C and discarding the supernatant each time. 1 ml of 1x TBS was added to the mixture again, resuspended with a cutted tip and transferred to a fresh tube and centrifuged at 3,000 rpm for 2 min at 4°C. Proteins were eluted by incubating the beads for 30 min with elution buffer I, containing 20 µg/ml trypsin, at 37°C and centrifugation at 1,300 rpm for 2 min at RT. The supernatant was collected. A second elution was performed by adding 50 µl of elution buffer II to the beads and incubation for 5 min at 37°C. Both eluates were combined and further incubated overnight at 25°C for trypsin digestion.

IP with GFP and RFP trap nanobody beads

The GFP nanobody beads & RFP nanobody beads (control) needed to be activated by resuspending a 25 µl bead slurry per replicate with 500 µl ice-cold wash buffer I. (Centrifuge at 2,500 rcf for 2 min at +4°C). The supernatant needed to be discarded, and the samples must be rewashed. For each replicate, 25 µg of chromatin (fill up to a final volume of 500 µl with RIPA buffer) was incubated with the 25 µl nanobody beads for one hour at +4°C, where the tubes were sealed and placed on a Microtube rotator. GFP/RFP beads were washed twice with 500 ml ice-cold wash buffer I to reduce unspecific binding for each replicate. Afterward, the GFP/RFP beads are washed with 500 µl ice-cold wash buffer II for 4-times. Precipitated proteins were eluted by incubating the beads for 30 min with 50 µl of elution buffer I, containing 20 µg/ml trypsin, followed by another elution with 50 µl of elution buffer II for 5 min at 37 °C. Both eluates were combined and further incubated overnight at 25 °C.

3.9.6 MS

MS sample preparation

The trypsin-digested peptides were acidified by adding 10% Trifluoroacetic acid (TFA) to reach a pH of 2 and 1 % TFA final. Then, samples were purified with three-layered C18 membrane stage tips[222]. The C18 extraction disks silica Empore™ 47 mm were attached to a syringe and placed into a 200 µl pipette tip. The membrane needs to be activated first by washing the tips with 100 µl of 100% methanol followed by 100 µl of buffer A two times. The acidified samples were added to the stage tips and washed with 100 µl of buffer A. Samples were eluted with 60 µl of buffer B in PCR tubes. Each centrifugation step was performed at 500 x g for 5 min at RT. After centrifugation at high speed in a speed vac (vacuum pressure machine) for around 1h to evaporate the acetonitrile in the samples, the peptides were resuspended with 9 µl of buffer A/A* ready to be analysed by mass spectrometry or covered with hard-cover lids and stored at -20C until further use.

3.9.7 LC-MS/MS analysis

Peptide samples were analyzed via nanoflow liquid chromatography coupled with tandem mass spectrometry (LC-MS/MS) on an EASY-nano-LC 1200 system connected to a Q Exactive HF quadrupole Orbitrap mass spectrometer through a nanospray Flex Ion source. 3 µl of each peptide sample were injected in 5 % buffer A onto a heated reversed-phase high-pressure liquid chromatography (HPLC) column with a 75 µm inner diameter, which was packed in-house with 1.9 µm ReproSil-Pur C18-AQ beads. The peptides were eluted using a 3-hour gradient from 5 to 95 % buffer B at a constant flow rate of 0.25 µl/min. Mass spectra were acquired in data-dependent acquisition (DDA) mode, alternating between MS and MS/MS (MS2) scans. For each cycle, a full scan was recorded over a mass-to-charge (m/z) range of 300 to 1,650 with a resolution of 60,000 at m/z 200, a maximum injection time of 20 ms, and an ion target of 3E6. The 15 most abundant ions, with a charge state between 2 and 7, were selected for fragmentation using high-energy collision dissociation (HCD), following the protocol described by Olsen et al. (2007). HCD settings included a normalized collision energy of 28, a 1.4 m/z isolation window, a resolution of 15,000 at m/z 200, a maximum injection time of 80 ms, an automatic gain control (AGC) target of 1.6E3, and dynamic exclusion set to 20 seconds to reduce repeated sampling of the same ions. No fixed first mass was applied during MS2 acquisition.

Sample processing

Raw mass spectrometry data were processed using MaxQuant (version 1.6.17) for the identification and label-free quantification of peptides and proteins. Data were searched against the human reference proteome database (UniProtKB FASTA UP000005640), applying a false discovery rate (FDR) threshold of 1% for both peptides and proteins. Cysteine carbamidomethylation was specified as a fixed modification, while N-terminal acetylation and methionine oxidation were set as variable modifications, with a maximum of five modifications per peptide allowed. Trypsin/P was set as protease, allowing for up to two missed cleavages. Peptides were filtered with a minimum length of seven amino acids.

Analysis of proteome data

For further analysis, Perseus (v1.6.10.43 and v1.6.15.0) was used to evaluate the statistical significance of protein abundance differences across experimental conditions. Initial filtering was conducted on identified protein groups to exclude potential contaminants, reverse hits, and proteins identified only by site. LFQ intensity values were then transformed using log2(x), and a minimum of one valid value per row was required. Subsequently, annotations, including Gene Ontology (Biological Process (GOBP), Molecular Function (GOMF), and Cellular Component (GOCC)), KEGG pathways, and CORUM protein complexes, were added. Missing values were imputed based on a normal distribution with a width of 0.3 and a downshift of 1.8 separately for each column. Filtering continued to retain rows with at least three valid values in total across the dataset. For generating volcano plots and performing comparative analysis in Perseus, a permutation-based Student's t-test was used, setting a false discovery rate (FDR) threshold of 0.05 and the significance line s0 to 0.1. This approach was applied to triplicate or quadruplicate chromatin immunoprecipitation mass spectrometry (ChIP-MS) samples per condition, ensuring robust statistical evaluation of protein abundance differences. The use of permutation-based t-tests minimizes false positives and enhances the reliability of differential protein expression findings, which are then visualized effectively in the volcano plot, highlighting significant changes in protein levels between experimental conditions.

3.10 Single-cell whole genome sequencing

Cells were synchronized and treated for BLM depletion as described in Chapter 3.2.5-3.2.6. Following collection at 0 and 12 h post-release, cells were frozen at –80 °C and sent for sequencing to the laboratory of Prof. Dr. Floris Foijer. Sequencing was performed by Andrea Tijhuis, using the Illumina NextSeq 500 platform. Data were demultiplexed using sample-specific barcodes and converted into FASTQ files with *bcl2fastq* (Illumina v1.8.4). Reads were aligned to the human reference genome (GRCh38/hg38) using Bowtie2 (v2.2.4). The resulting BAM files were analyzed using AneuFinder algorithm[223]. After applying GC correction and excluding artifact-prone regions through blacklisting, the libraries were evaluated for heterogeneity, aneuploidy, and structural variants according to AneuFinder's analysis pipeline.

3.11 Statistical analysis

Each dataset is composed of at least three independent experiments unless differently stated in the figure legend. Statistical significance was assessed by unpaired Student's *t*-test, and with Welch's correction for Fig. 24, 25, 43, 4, 45 an 46, using GraphPad Prism. Each test used for individual experiments as well as number of cells quantified, number of independent biological replicates and *p*-values are indicated in the figure or figure legends.

4. Results

Genomic instability, characterized by a substantial rate of alterations in the genome, is a well-known characteristic of cancer cells[84]. One potential mechanism contributing to genomic instability is the presence of UFBs arising from linked sister chromatids by the time cells enter anaphase caused by late replication intermediates, DNA catenanes and recombination intermediates. Resolution of these bridges is essential for faithful chromosome segregation. Defects in proteins known to bind to or participate in the resolution of UFBs have been shown to promote genomic instability and cancer development. However, the underlying mechanisms remain largely unknown. Therefore, several proteins and their contribution to UFB resolution and other cellular functions in maintaining genomic stability were investigated.

4.1 CRISPR/Cas9-based gene editing enables generation of knock-in cell lines

BLM, PICH, and FANCD2 are frequently found at UFBs[125–127], suggesting that they play a role in the resolution of sister chromatid linkages. Similarly, loss of members of the SMC5/6 complex has also been shown to cause increased levels of UFBs, but have so far not been observed to co-localize with mitotic sister chromatid bridges[224]. To investigate how BLM, PICH, FANCD2, and SMC5 contribute to the resolution of UFBs and genome stability, CRISPR/Cas9-based gene editing was chosen to modify their endogenous genes to express them as fusion proteins linked to an AID tag and the fluorescent protein GFP. While the AID tag facilitates rapid degradation of the target proteins, the GFP tag allows to monitor protein localization by live-cell fluorescence microscopy and can be exploited as an affinity tag for the enrichment of protein complexes. In the initial step, sgRNAs were designed to direct the Cas9 endonuclease to the genomic locus of interest, generating a DSB. In the subsequent step, a donor sequence encoding a C-terminal AID/GFP tag was introduced at the break site via homology-directed repair (HDR) (Fig. 15).

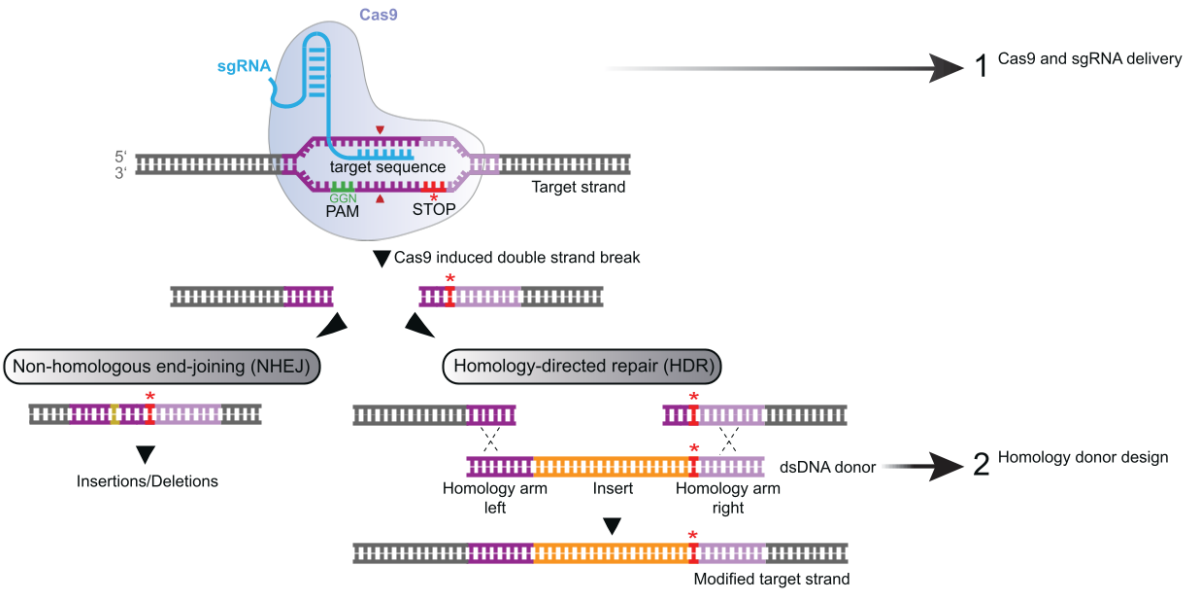

Figure 15| Principle of CRISPR/Cas9-based gene editing. Endogenous gene tagging at the 3'-end to cut near the stop codon depicted as example for generating knock-in cell lines by providing 1) a Cas9 enzyme together with a sgRNA and 2) a homology dsDNA donor. The target-specific sgRNA as well as an enzyme-specific protospacer adjacent motif (PAM) comprising the nucleotide sequence NGG (shown in green) present at the genomic locus guides the Cas9 enzyme to cleave the target DNA near the stop codon (red asterisk). The resulting double-strand breaks can be repaired by the error-prone non-homologous end joining (NHEJ) and often introduces insertions or deletions of a few nucleotides at the break site, leading to out-of-frame mutations. Alternatively, a homologous double-strand DNA (dsDNA) donor can serve as a new repair template repairing the double-strand break by HDR to enable purposeful modification, deletion, or insertion of a target. For the insertion of foreign DNA, the homology donor harbours the insertion sequence (shown in orange) flanked by homology arms (shown in purple) complementary to the genomic sequence on either side of the DNA break.

4.1.1 Comparison of different strategies of Cas9 and sgRNA delivery

To induce a DSB that allows further gene editing, target-specific sgRNAs and Cas9 must be delivered to the cell. To maximize transfection, two delivery strategies were compared: 1) Transfection of cells with RNPs together with the homology donor plasmid and 2) Co-transfection of cells with the pX330 plasmid harbouring expression cassettes for Cas9 and the sgRNA together with the homology donor plasmid (Fig. 16).

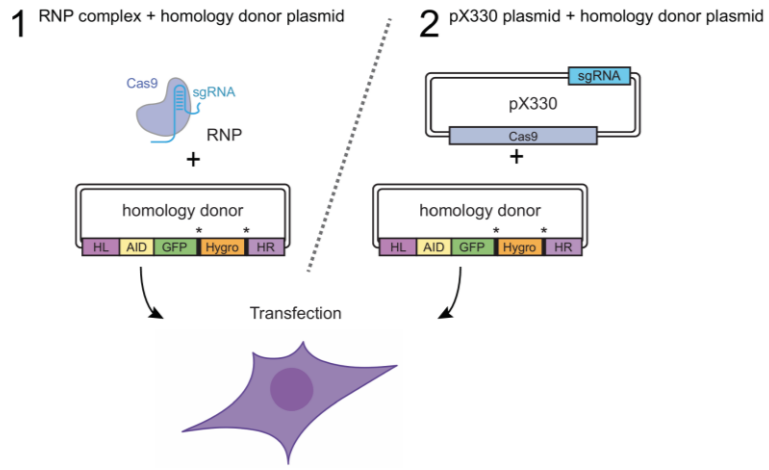

Figure 16|Cas9 and sgRNA delivery strategies. For CRISPR/Cas9 based gene editing a Cas9 enzyme as well as a target-specific sgRNA has to be introduced into cells by transfection. Two different delivery approaches were tested: 1) Co-transfection of cells with an assembled ribonucleoprotein (RNP) complex consisting of sgRNA and the Cas9 protein together with the homology donor plasmid, and 2) Co-transfection of cells with the pX300 plasmid, harbouring the expression cassette for Cas9 as well as the sgRNA, together with the homology donor plasmid.

The first strategy comprised the direct delivery of an RNP complex provided by assembling a purchased Cas9 enzyme together with a target-specific sgRNA, generated by IVT (Fig. 17). A 20-nt target-specific crRNA sequence for *SMC5*, *PICH*, *FANCD2* and *BLM* were selected using the webtool benchling.com (see Material and Method section) and amplified as oligonucleotides using PCR together with a T7 promoter sequence and the tracrRNA sequence (data not shown). By PCR, the dsDNA template for the sgRNA with a length of 130 bp was amplified (Fig. 17a). The dsDNA templates of 130 bp were efficiently generated for *SMC5*, *BLM*, *PICH* and *FANCD2* (Fig. 17b, c). After subsequent T7 transcription initiated by addition of T7 RNA polymerase, the single-stranded sequence of the desired sgRNA with a length of 112 nt omitting the T7 promoter (Fig. 17d) was successfully transcribed for *SMC5*, *BLM*, *PICH* and *FANCD2* (Fig. 17e, f).

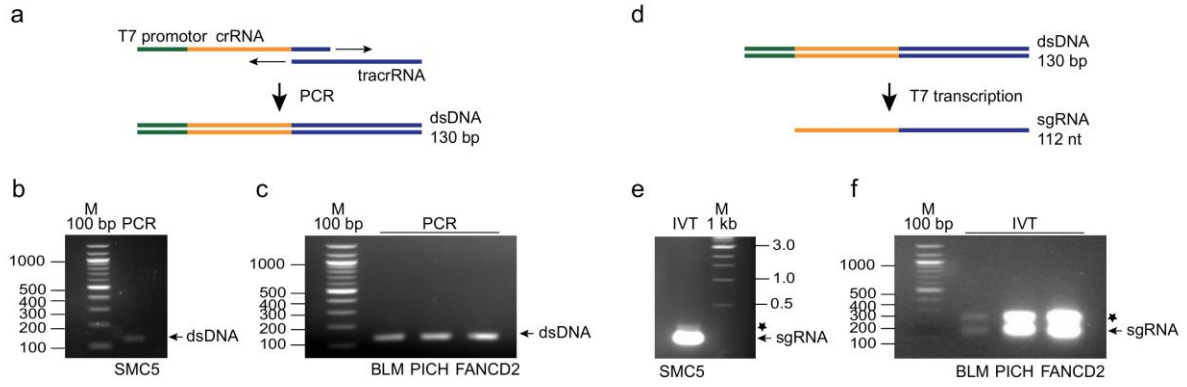

Figure 17|Delivery of Cas9 and sgRNA as RNP complex after sgRNA *in vitro* transcription. a, *in vitro* transcription requires the generation of a dsDNA template of 130 bp by comprising a T7 promoter region, the target-specific CRISPR RNA (crRNA) sequence followed by a trans-activating crRNA (tracrRNA) sequence. **b-c**, The dsDNA templates of SMC5 **(b)** and BLM, PICH and FANCD2 **(c)** were analyzed by gel electrophoresis. **d**, Following T7 transcription, the template is transcribed into the single-stranded RNA sequence of 112 nt. **e-f**, The sgRNA product of SMC5 **(e)** and BLM, PICH and FANCD2 **(f)** were analyzed by gel electrophoresis. The asterisk indicates the secondary structure of the sgRNA. Data acquisition was performed together with Divya Reddy.

Cleavage efficiency of the RNP complex was subsequently assessed by an IVC assay (Fig. 18). To provide substrates for the IVC assays, an approximately 800 bp long segment of the target gene locus harbouring the predicted cleavage site was amplified from genomic DNA isolated from the parental HCT116 Tet-OsTIR1 cell line (Fig. 18a). While most substrates for the cleavage assay (*SMC5*, *PICH* and *FANCD2*) could be readily amplified (Fig. 18b, c), for *BLM*, the PCR conditions had to be optimized (Fig. 18c-e). Following analysis of two additional amplicons of target DNA for *BLM* either did not reveal an 800 bp fragment at all (first lane) or it was observed, but both fragments contained primer dimers that concentrate at the end of the gel (second lane) (Fig. 18d). To avoid dimer formation, new primer sequences were designed and analyzed by a web tool to predict secondary structures, primer dimer formation and physical characteristics. Investigation by gradient PCR using six different annealing temperatures confirmed no primer dimer formation except for the annealing temperatures of 58.1°C and 54.1°C (Fig. 18e). The fragment annealed at 63.2°C was chosen for further IVC of *BLM*. After addition of the sgRNA and Cas9 assembled as an RNP complex, two cleavage products of approximately 600 and 200 bp were generated (Fig. 18f). Successful IVC was performed for *SMC5* and *BLM* (Fig. 18g), as well as for *PICH* and *FANCD2* (Fig. 18h).

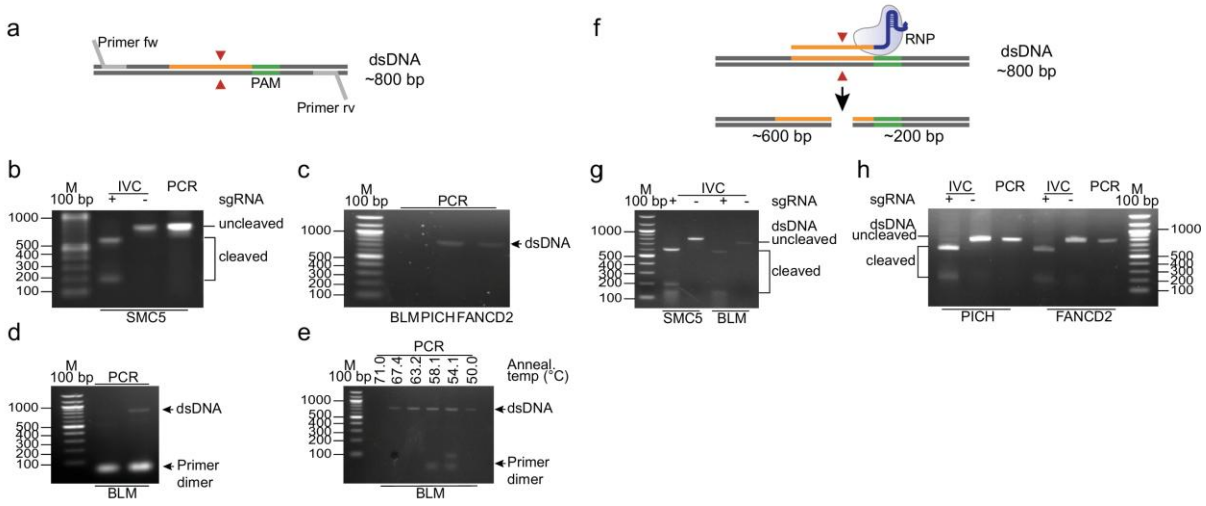

Figure 18|Cleavage efficiency analysis. a, Schematic depiction of the generation of a double-strand DNA (dsDNA) target sequence of 800 bp by PCR including the cutting region. **b-e**, PCR fragments for SMC5 **(b)**, BLM, PICH and FANCD2 **(c)** were analyzed by gel electrophoresis. Following unsuccessful PCR product of BLM in the first round **(c)** and new amplicons with a strong appearance of primer dimer **(d)**, gradient PCR with new dsDNA fragments was performed **(e)**. **f**, Following RNP complex formation by incubating the Cas9 enzyme with the designed sgRNA and its addition to the ds DNA target, cleavage resulted in two fragments of approximately 600 bp and 200 bp. **g-h**, Cleavage efficiency was analysed by gel electrophoresis for SMC5, BLM **(g)**, PICH and FANCD2 **(h)**. Cas9-induced double-strand breaks are shown as red arrows. Data acquisition was performed together with Divya Reddy.

To follow the alternative approach for Cas9 and sgRNA delivery, pX330 plasmid derivatives were generated for the vector-based expression of sgRNA directed against the target sites at the gene locus of *BLM*, *PICH*, and *FANCD2* (Fig. 19). Short dsDNA fragments encoding the target-specific crRNA part of the sgRNA were cloned into the *BbsI* restriction site of pX330 (Fig. 19a). Successful insertion was verified by the loss of the *BbsI* restriction site. While the undigested parental plasmid pX330 migrated as multiple bands through the agarose gel, addition of the *BbsI* enzyme converted the supercoiled plasmid completely into linearized

plasmid that run as a single band at the expected size 8.484 kb (Fig. 19b). Upon insertion of the crRNA of *BLM*, *PICH*, and *FANCD2*, the isolated plasmid DNA became resistant to *BbsI* (Figure 19c).

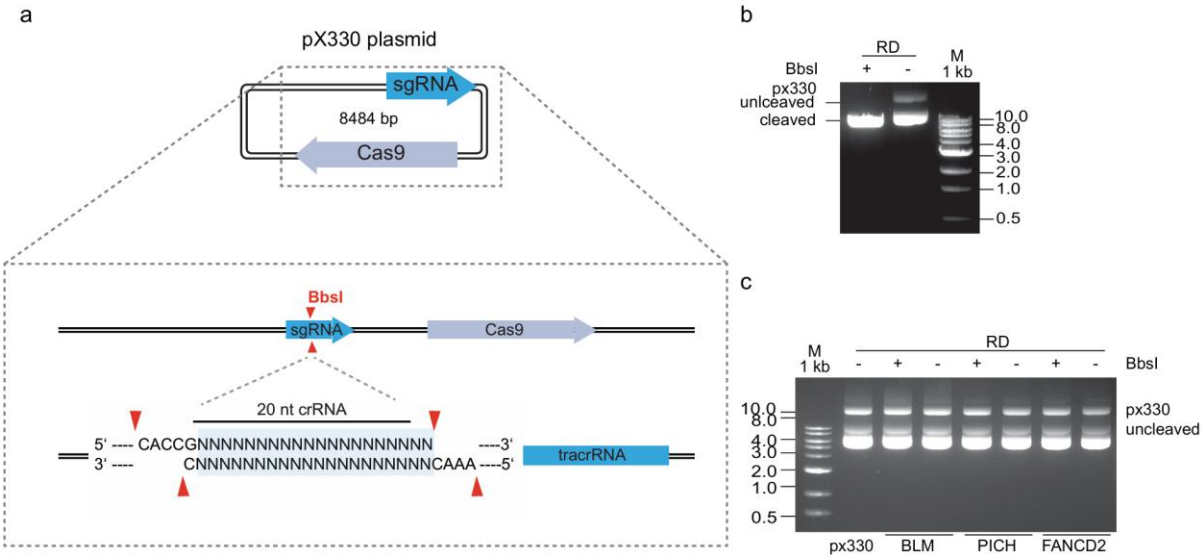

Figure 19| pX330-derived plasmids for the expression of Cas9 and sgRNA. a, Schematic depicting the pX330 cloning strategy. The pX330 plasmids contain two cassettes for the expression of target-specific sgRNA and the Cas9 enzyme. Fragments encoding the target-specific crRNA are inserted into a *BbsI* restriction site. Upon transfection, composite gRNAs are expressed, consisting of individual crRNAs fused to the constant tracrRNA segment encoded downstream of the *BbsI* site. Cutting sites of restriction enzymes are marked as red arrows. **b-c**, Restriction digestion (RD) analysis of pX330 **(b)** and of pX330 derivatives harbouring inserts for the expression of sgRNAs directed against *BLM*, *PICH*, and *FANCD2* **(c)**. Data acquisition was performed together with Divya Reddy.

4.1.2 Combination of Gibson and Golden Gate cloning facilitates the assembly of large, modular homology donor plasmids

Endogenous gene tagging by CRISPR/Cas9 requires homology donors for the insertion of foreign DNA sequences at the Cas9 cleavage site (see Fig. 15). To facilitate selection, such donor plasmids often combine resistance genes with sequences encoding various tags such as the sequences encoding fluorescent proteins or the AID degron, resulting in large homology donor sequences. Efficient integration of such large inserts is mediated by two long, target-specific homology arms. Since the goal was to tag several proteins within the same cell with different fluorescent proteins, with the help of Michael Taschner from the EPFL Lausanne, a modular cloning strategy was established. This strategy combined Gibson and Golden Gate cloning methods to ensure simultaneous assembly of multiple DNA fragments into a single vector (Fig. 20). The modular design allows to freely combine homology arms targeting different genes with a variety of different degrons, fluorescent proteins and resistance genes.

In the first cloning step, each fragment encoding a tag was cloned into the entry vector pIDC using Gibson assembly, resulting in a library of entry clones (Fig. 20a, see Material and Methods for details). These entry clones included pIDC vectors containing each an individual

homology arm left-sided and right-sided (HL and HR) for modification of the endogenous *BLM*, *PICH*, *FANCD2* or *SMC5* gene loci (Fig. 20b-e). Furthermore, entry vectors with sequences encoding the AID domain, GFP or a gene for either neomycin or hygromycin resistance were generated (data not shown). Finally, all entry clones were verified by DNA sequencing.

Assembly of the modules into the acceptor vector pSG3651 using Golden Gate is directed by the unique overhangs generated during the restriction with the *BsaI* restriction enzyme (Fig. 20f). These overhangs must be carefully designed so that an unambiguous assembly of the individual sequences is possible in the desired order. Entry vectors were mixed with the acceptor plasmid and incubated together with the *BsaI* restriction enzyme and DNA ligase. Insertion of the assembled modules into pSG3651 destroys the *BsaI* restriction giving rise to a stable plasmid yielding viable ampicillin resistant colonies after transformation into *E. coli*. Using restriction analysis, clones with the correct inserts were identified for *BLM* and *FANCD2* and further validated by DNA sequencing (Fig. 20g-i).

In summary, a versatile modular cloning system has been established that allows to assemble CRISPR/Cas9 homology donors containing different combination of tags, fluorescent proteins and selection markers that can be targeted to any desirable genetic locus (Fig. 20j). One advantage of this cloning strategy is the PCR-free assembly of multiple fragments into a large homology doner. This strongly reduces the frequency of mutation during the assembly step, yielding error-free recombinants in most cases. In its current version, the cloning system only support c-terminal tagging of endogenous proteins.

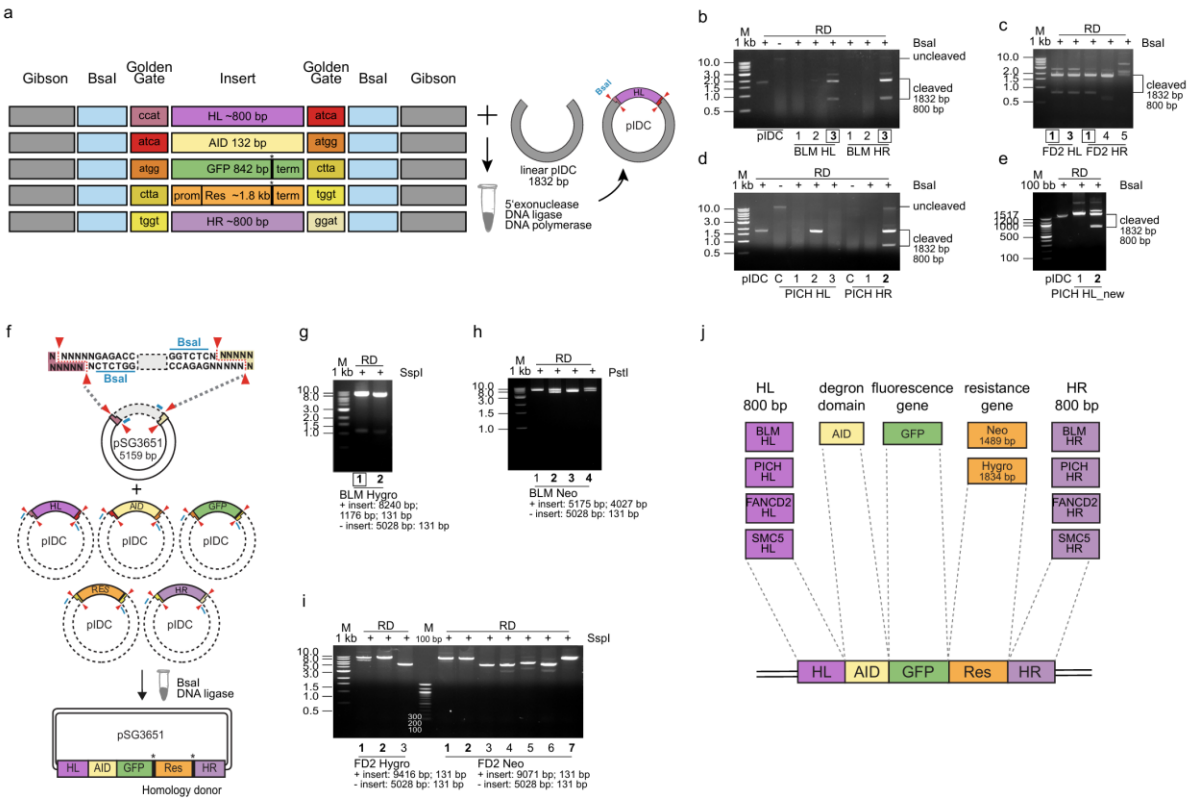

Figure 20|Modular cloning system facilitating assembly of long homology donors for gene editing. a, Schematic of the Gibson assembly. Following the design of individual inserts with specific overhangs, these fragments were individually incubated with the linearized pIDC plasmid serving as a backbone of Gibson entry clones. In a single-tube reaction with the addition of a 5'exonuclease, a DNA ligase and a DNA polymerase, the Gibson entry clones, each harboring another insert were generated. **b-e**, *BsaI* restriction digestion (RD) by gel electrophoresis to analyze incorporation of homology arms for BLM, PICH and FANCD2 into the pIDC vector. Positive clones with the expected cleavage products of 1832 bp and 800 bp are marked in bold and the ones

selected for further cloning steps surrounded by a box. **f**, Schematic depiction of Golden Gate cloning. Following the incubation of all entry clones to be combined together with the destination vector pSG3651 in a single-tube reaction supplemented with *BsaI* enzyme and DNA ligase, the final homology donor is assembled. **g-i**, Restriction digestion of homology donor plasmids was analyzed by gel electrophoresis. Positive clones for BLM Hygro, BLM Neo, FANCD2 Hygro and FANCD2 Neo are marked in bold. BLM Hygro clone 1 was selected for further transfection, marked with a surrounding box. **j**, Strategy of exchanging several components of a homology donor enabling a wide range of combinations easy to expand. Stop codons are marked with an asterisk. Cutting sites of restriction enzymes are marked with a red arrow. Data acquisition of b,d was performed together with Divya Reddy.

4.2 Validation of a cell line reveals endogenously tagged BLM gene with AID/GFP

The human colorectal cancer cell line HCT116 was selected as the parental cell line for following knock-in cell line generation harbouring an auxin inducible degron domain. Auxin inducible degradation of target proteins requires further the plant protein TIR1 serving as substrate adaptor protein to target endogenous SCF E3 ubiquitin ligase to the AID degron[206,207]. CRISPR/Cas9-based gene editing was already performed in HCT116 cells containing the insertion of a sequence for inducible TIR1 expression derived from *Oryza sativa* (OsTIR1) by a Tet-promoter at the safe-harbour AAVS1 locus (generated by Kanemaki et al.[206]). This parental cell line, designated HCT116 Tet-OsTIR1, was used for all subsequent gene editing to generate AID-mutant cell lines. In a first attempt, HCT116 Tet-OsTIR1 cells were transfected with RNP complexes targeting the *SMC5* gene locus together with two homology donors for C-terminal tagging with AID/GFP harbouring either a neomycin or hygromycin resistance gene. Exposing cells to low doses of neomycin and hygromycin simultaneously, a selection of cells with bi-allelic insertion of the two homology donors was expected. However, genotype analysis by gel electrophoresis revealed no positive AID-mutant clones (data not shown). Therefore, further transfections were also performed with a single homology donor plasmid targeting the *FANCD2* and *BLM* genes. From each transfection, several single-cell clones were grown and screened for correct insertion of the homology donor. However, of all the tested clones, no positive clones could be identified in attempts to target *FANCD2* (data not shown).

Subsequently, transfection was performed to target the *BLM* gene. The final homology donor, referred to as clone BLM Hygro clone 1 (Fig. 20g), contained the homology arms complementary to the cleavage site upstream of the stop codon for the C-terminal tag, the AID domain, the GFP sequence, and the hygromycin resistance cassette sequence, to generate BLM-AID/GFP cell lines (Fig. 21).

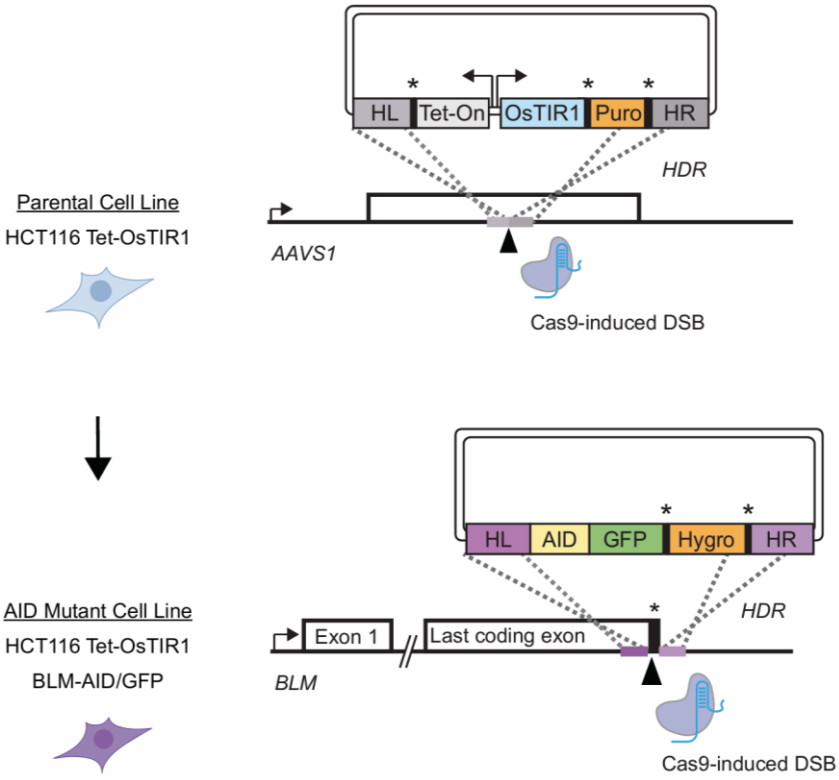

Figure 21|Strategy of endogenous AID/GFP-tagging of BLM. The parental cell line HCT116 Tet-OsTIR1 harbours already an insertion for OsTIR1 expression together with a puromycin (Puro) resistance cassette inserted at the safe-harbour AAVS1 locus generated by CRISPR/Cas9-based gene editing (Kanemaki et al.[206]). Transfection of the parental cell line with a homology donor is used for C-terminal tagging of *BLM* right before the STOP codon, selectable by hygromycin (Hygro) treatment. The asterisk indicates a stop codon.

The mutant BLM-AID/GFP cell lines were generated by transfection of the parental cell line HCT116 Tet-OsTIR1 (Fig. 22a). Among the tested clones, one clone with bi-allelic insertion and two clones with monoallelic insertion of the tagging cassette at the *BLM* locus were identified from co-transfection with the homology donor and pX330 vector, out of 7 clones screened. In comparison, none of the 5 tested clones generated by RNP delivery showed successful insertion (Fig. 22b). The successful tagging of the 3 clones could also be confirmed by western blotting, where homozygous tagging of the BLM protein caused a strong shift of the BLM protein consistent with a mass gain of about 26 kDa due to the fusion with GFP and the AID degron (Fig 22c). In contrast, in heterozygous tagged cells, two bands were recognized by the BLM antibodies, which run exactly as fast as the endogenous protein in the parental cells and the tagged BLM protein in the homozygously tagged cells. To independently confirm the expression of the GFP tagged BLM protein, the GFP signal was analyzed by flow cytometry (Fig. 22d). Compared to the untagged parental cell line, heterozygously tagged cell clone 5, as well as clone 6 (Suppl.Fig. 1a), showed a clear increase of the fluorescence intensity measured at 488 nm, that was even further shifted to higher intensity in the homozygously tagged cell clone 1. The modest increase in fluorescence intensity is likely due to the low expression levels of the endogenous BLM protein in asynchronous cells, which are mostly at G1 phase, in which BLM is least abundant[181]. Finally, the GFP tagged protein was also directly visualized by fluorescence microscopy, where the protein showed a characteristic focal pattern in interphase cells and was also found to be recruited to UFBs in mitotic cells (Fig. 22e). In conclusion, the results indicate that in the BLM cell clone 1 both alleles of the *BLM* gene were successfully edited to express a GFP-tagged BLM fusion protein, functional

to form interphase foci as well as BLM-positive UFBs. The homozygous cell clone B1 was hereafter referred to as BLM$^{AID/AID}$, and any of the heterozygous ones as BLM$^{AID/WT}$, respectively.

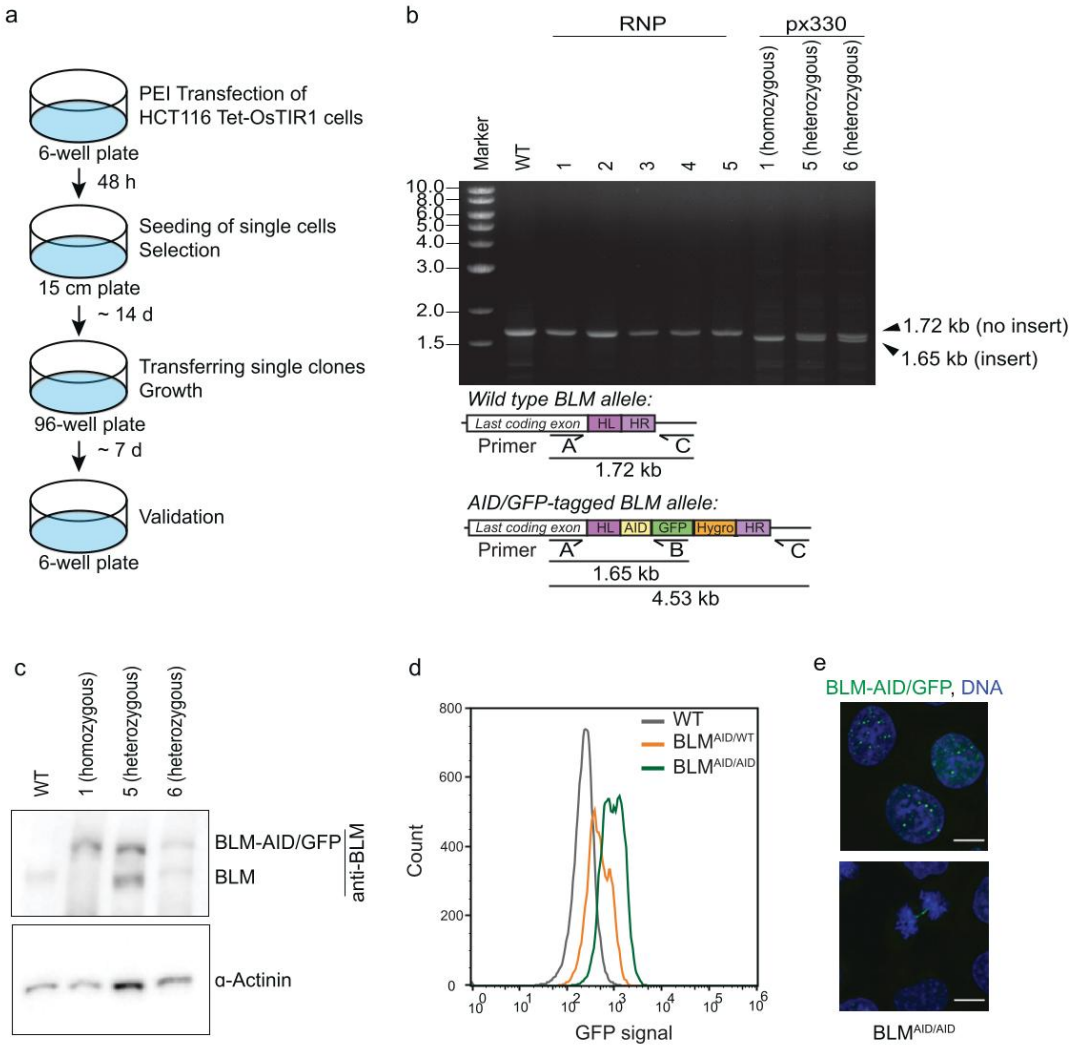

Figure 22|Validation of cell lines with BLM endogenously tagged with AID and GFP. a, Workflow showing transfection and selection of single cell clones with modified *BLM* loci. 48 h after transfection of the parental cell line HCT116 Tet-OsTIR1 using the PEI reagent, cell suspension from a 6-well plate was distributed on 2-4 of 15 cm plates to grow colonies from single cells. Individual colonies were transferred after drug selection for 14 d to 96-well plates until out growth and transferred to 6-well plates for further validation. **b**, Analysis by gel electrophoresis. This was done following co-delivery of the homology donor either with the RNP complex (Cas9 protein and sgRNA) or with the Cas9/sgRNA-expressing plasmid pX330. **c**, Protein levels of endogenous BLM tagged with AID and GFP (BLM-AID/GFP) were analyzed by Western Blot for clone 1, 5 and 6. **d**, GFP fluorescence signal was analyzed by flow cytometry at 488 nm wavelength for the homozygous clone 1, further referred to as BLM$^{AID/AID}$ and clone 5, further referred to as BLM$^{AID/WT}$. **e**, Representative fluorescence microscopy images of asynchronous BLM$^{AID/AID}$ cells with BLM-AID/GFP protein detected by fluorescence at 488 nm. BLM-AID/GFP foci in interphase cells are shown on top, a BLM-positive UFB is shown below. DNA was stained with DAPI. Scale bar, 10 µm.

4.3 The AID system enables inducible degradation of BLM

The functionality of the AID-tag on BLM was validated by auxin-induced BLM depletion in asynchronous HCT116 Tet-OsTIR1 BLM$^{AID/AID}$ cells. After 24 h of auxin treatment, BLM and GFP level were undetectable in the homozygous cell line. In the heterozygous cell line, remaining BLM level corresponded to the wild-type allele, confirming partial depletion only for the GFP/AID-tagged allele. The WT and the heterozygous cell line displayed BLM levels of the size of the untagged protein throughout the treatment, whereby the BLM signal was diminished upon auxin treatment (Fig. 23a).

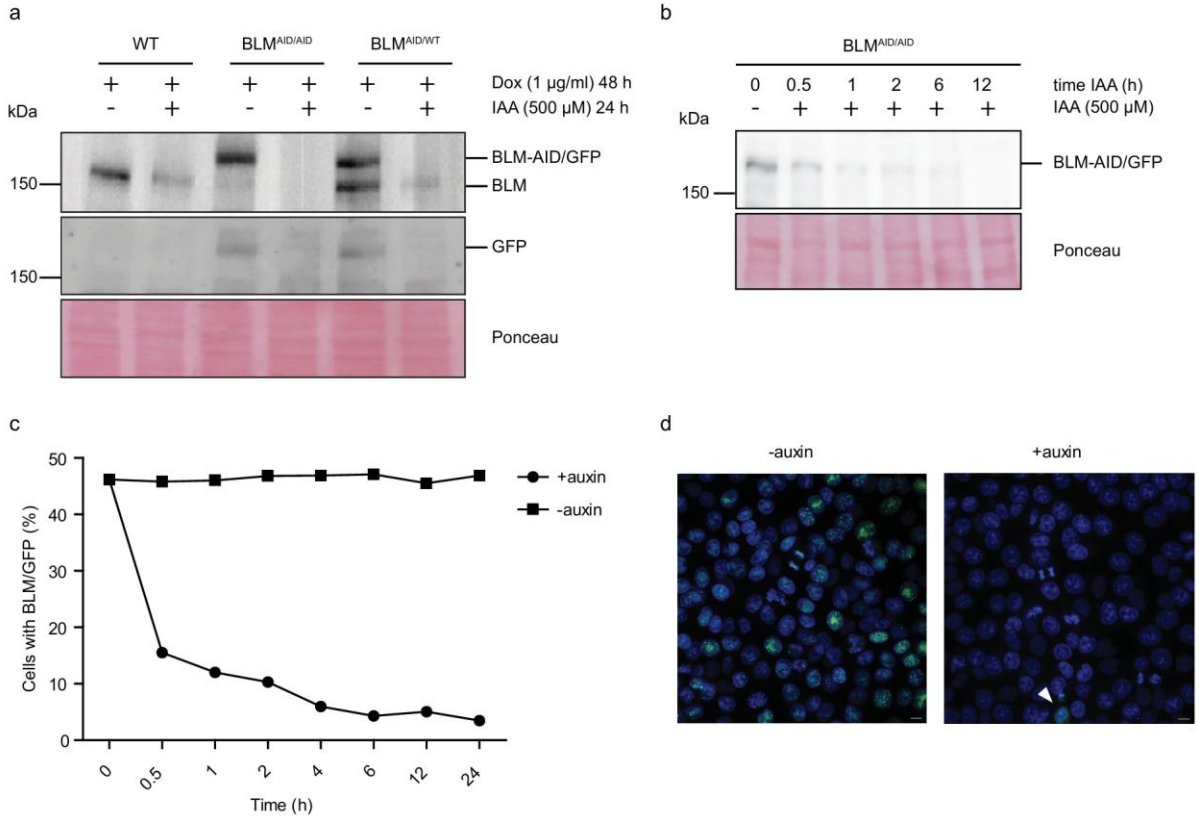

Figure 23|BLM degradation by auxin treatment. a, Protein detection of BLM degradation after 24 h of auxin treatment in homozygous and heterozygous BLM-AID/GFP cells. **b**, Protein detection of BLM degradation over time in homozygous BLM-AID cells. **c**, Flow cytometric analysis of BLM degradation over time in homozygous BLM-AID cells. **d**, Representative images from fluorescence microscopy, depicting the loss of BLM detection after 24 h of auxin treatment. White arrow indicates remaining BLM signal. BLM was detected via endogenous BLM-GFP signal, DNA was countestaining with DAPI. Scale bars, 10 µm.

Further analysis of the WT and the heterozygous cell lines confirmed that auxin does not deplete untagged BLM (Suppl. Fig. 1d,e). The observed decrease in BLM signal can be attributed to technical factors, particularly unequal protein transfer for higher molecular weight proteins. In a time-course treatment with auxin, BLM levels rapidly declined in the HCT116 Tet-OsTIR1 BLM$^{AID/AID}$ cell line, strongly declining within 30 min and became undetectable by 12 h (Fig. 23b). Flow cytometry corroborated the decline in GFP intensity within a time-course dependent auxin treatment with remaining GFP intensity of 7.5% after 24 h (Fig. 23c). Fluorescence microscopy confirmed a marked reduction in overall BLM-AID/GFP signal and in BLM-positive UFBs, with very few cells still exhibiting remaining BLM signal (Fig. 23d, white

arrow). The effects of auxin-induced degradation can be validated by excluding potential artifacts, as OsTIR1 expression was induced only upon Dox addition, and treatment with either EtOH solvent, Dox, or IAA alone did not result in BLM degradation (Suppl.Fig. 1b,c). These findings highlight the AID system's efficiency in depleting BLM protein rapidly and near-completely within a controlled timeframe. This precise depletion ensures that experimental results specifically reflect the impact of acute BLM depletion, providing a robust tool for investigating BLM-dependent processes. Additionally, it facilitates functional studies during targeted cell-cycle phases, enabling a deeper understanding of BLM's role in maintaining genomic stability and DNA repair dynamics.

4.4 Sister chromatid exchange

Loss of BLM protein is linked to elevated rates of SCE, a defining characteristic of BS[197]. To confirm this phenotype in the homozygous $BLM^{AID/AID}$ cells after auxin-induced depletion of functional BLM protein, SCE assays were performed[225,226] (Fig. 24a-d). SCE arises from the crossover events between sister chromatids, a process frequently linked to HR-mediated repair of DSBs[78,79]. In addition to the error-prone DSB repair mechanism mediated by NHEJ, HR becomes the favoured pathway during S and G2 phases of the cell cycle. During these phases, sister chromatids are available as templates for an error-free repair. HR encompasses mechanisms such as the SDSA pathway, which is preferentially utilized in mitotic-cycling cells and produces non-crossover outcomes[63]. Another HR mechanism, the dHJ repair pathway, is associated with meiotic repair but can also arise in mitotic-cycling cells, though at lower frequencies[79,81]. This pathway can result in either crossover or non-crossover events, with crossovers being more frequent during meiosis but rare during mitosis. BLM plays a crucial role in regulating HR by promoting the dissolution of dHJs into non-crossover products through the BTR complex (BLM-TOP3A-RMI1-RMI2), also referred to as the BLM dissolvasome[78,227]. In the absence of BLM, the dHJ repair mechanism shifts towards excessive crossover resolution events mediated by alternative HR resolvases. While these resolvases can generate both crossover and non-crossover products, the tendency towards crossover outcomes leads to an elevated frequency of SCE[142] (Fig. 24a). Consistently, the auxin-induced depletion of BLM in cells with homozygous AID/GFP-tagged BLM protein resulted in an approximately 5-fold increase in SCE events compared to its untreated control (Fig. 24d). The baseline SCE frequency observed in auxin-untreated cells with AID/GFP-tagged BLM was comparable to that of the untagged parental WT cell line. Interestingly, the baseline SCE levels without auxin addition, and wild-type levels with or without auxin, remained consistently below 10 SCE per metaphase, aligning with previously reported values. These findings demonstrate that the AID/GFP-tagged BLM protein does not impair its functionality by effectively limiting SCE and maintaining genomic stability. The observed increase in SCE rates upon BLM depletion is comparable to the elevated ratios seen in BS-derived fibroblasts (Suppl. Fig. 1f), underscoring its role in suppressing the formation of cross-over events. Depletion of BLM in heterozygous BLM-AID/GFP cells did not result in significantly increased SE rates (Suppl. Fig. 1f), aligning with the mild phenotypes seen in heterozygous carriers of BLM mutations demonstrating the necessity of homozygous BLM deficiency to fully replicate the autosomal recessive phenotype of Bloom syndrome.

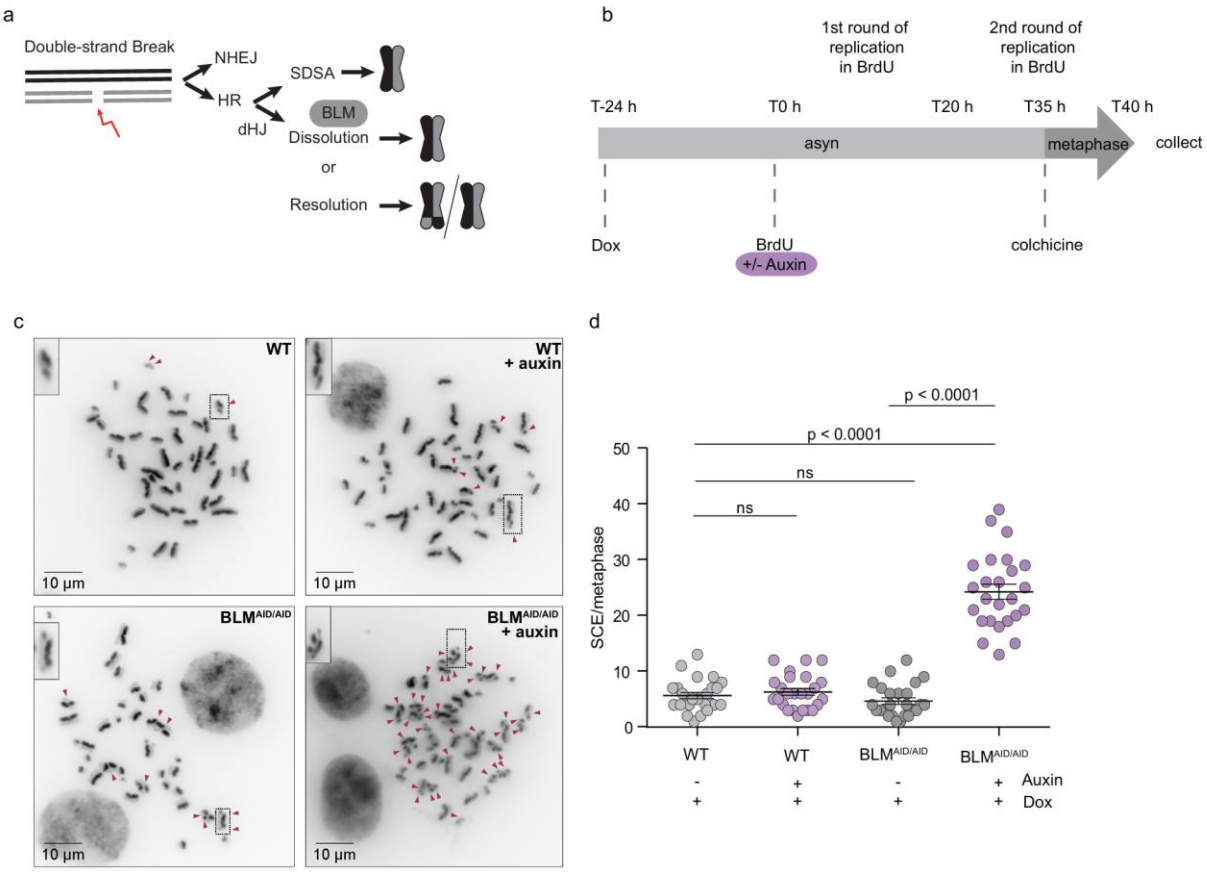

Figure 24|Sister chromatid exchange analysis in homozygous BLM-AID/GFP cells. a, Schematic of the DSB repair pathways by HR: dissolution of double Holliday junctions (dHJs) via the BTRR complex, avoiding cross-over events and resolution by HR resolvases, leading to non-crossover and crossover events in the absence of BLM. **b**, Workflow of SCE assay treatment. **c**, Representative fluorescence microscopy images of metaphase spreads from indicated conditions. **d**, Quantification of SCE per metaphase spread for the Tet-OsTIR1 HC116 WT cells and homozygous BLM-AID/GFP-tagged cells with and without auxin. Data represent mean ± S.E.M., statistical significance assessed by Student's t-test, 25 metaphases were analyzed, one experiment. Scale bars, 10 µm.

4.5 Loss of BLM function is associated with impaired cell proliferation and reduced colony formation

BLM plays a critical role in ensuring genome stability, particularly during the DNA replication process. By preventing replication fork stalling and resolving DNA lesions, it safeguards the integrity of DNA replication, especially under replication stress conditions. In the absence of BLM, cells experience replication fork stalling and accumulation of DNA lesions, potentially slowing proliferation. To evaluate the impact of BLM loss on cell proliferation and overall survival, AID/GFP-tagged BLM cells were treated with auxin to induce rapid degradation of BLM protein (Fig. 25a). Proliferation rates and colony formation were analyzed under normal and mild replication stress conditions. After three days of auxin treatment in AID/GFP-tagged BLM cells, proliferation proceeded for approximately two cell cycles before a significant decline in growth rate was observed, independent of mild replication stress conditions. This decrease contrasts with cells not exposed to auxin, which maintained consistent proliferation rates under both normal and mildly stressful replication conditions, similar to the unaltered WT cell line

(Fig. 25b,c). After 10 days of auxin treatment with 500 µM IAA, cells lacking functional BLM showed a marked decrease in both colony formation and colony size. This effect was further intensified under mild replication stress, where nearly all colony formation was abolished (Fig. 25d-f). Notably, while combined treatment with auxin and APH resulted in a markedly reduced number of colonies, yet without drastically decreasing in colony size compared to auxin alone. This suggests that while few colonies formed, those that did may have continued to grow robustly, potentially indicating malignant transformation, consistent with the strong cancer predisposition observed in BS patients[196]. These findings suggest that BLM is critical for maintaining replicative capacity and survival, particularly under stress conditions.

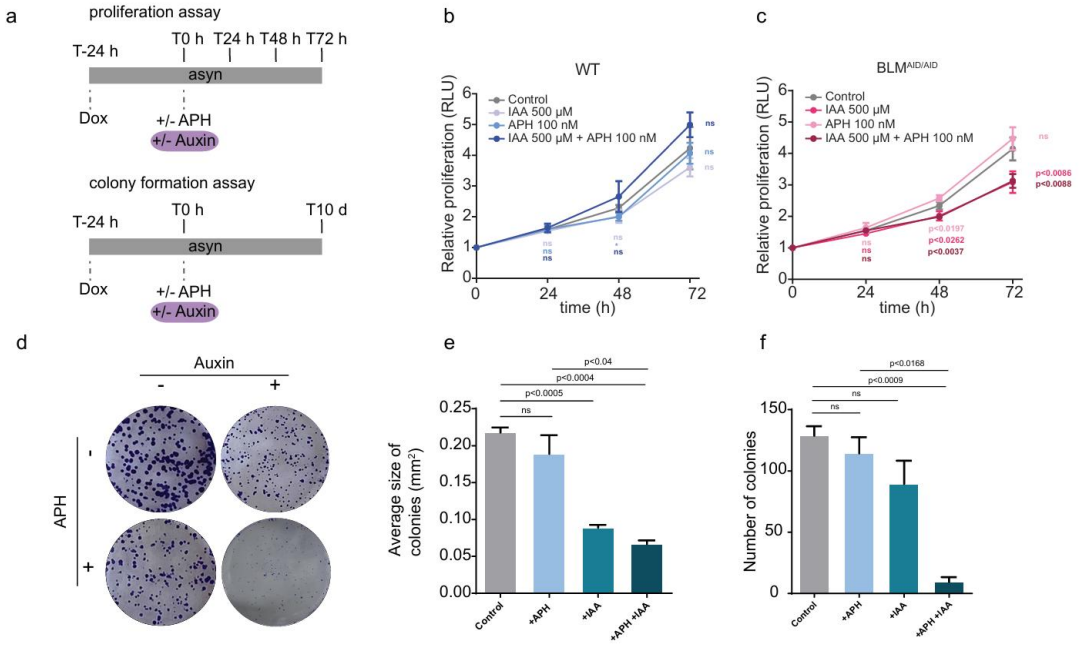

Figure 25|Proliferation and colony formation. a, Schematic of the workflow for proliferation assay (upper panel) and colony formation assay (lower panel). **b,** Proliferation assay in WT cells for 3 days in the presence or absence of auxin treatment and mild replication stress induction upon 100 nM aphidicolin treatment. **c,** Proliferation assay in homozygous AID/GFP-tagged BLM cells for 3 days in the presence or absence of auxin treatment and mild replication stress induction upon 100 nM aphidicolin treatment. **d,** representative images of colony formation assay in homozygous AID/GFP-tagged BLM cells. **e-f,** Quantifications of the colony formation ability estimated by the average size of the colonies **(e)** and the total number of colonies **(f)**. Data represent mean ± S.E.M., statistical significance assessed by Student's t-test, 3 technical replicates were performed per biological replicate for proliferation assay, all experiments were performed in 3 independent experiments.

4.6 Loss of BLM function is associated with elevated DNA damage and senescence

As demonstrated above, depletion of BLM in homozygous AID/GFP-tagged BLM cells leads to a significant increase in SCE rates (Fig. 24), which are believed to form as a result of excessive crossover events during HR. a critical repair pathway for DSBs and stalled or collapsed replication forks[79,228]. BLM acts as a suppressor of cross-over events during HR to prevent genomic rearrangements[79]. In line with this, BLM-deficient cells exhibit reduced proliferation rates and impaired colony-forming capacity, especially under mild replication stress conditions, such as treatment with 100 nM aphidicolin (Fig. 25). This suggests that the

impaired cellular fitness may arise from an accumulation of unresolved DNA damage due to defective processing of replication-associated lesions, ultimately hindering cell cycle progression and long-term viability. To investigate whether the loss of BLM leads to accumulation of DNA damage and replication stress, the formation of γH2AX foci, indicative of double-strand breaks and phosphorylated RPA at serine 33 (pRPA S33), a marker for replication-associated DNA damage, was analyzed (Fig. 26a-g). As expected from previous studies, mild replication stress induction by aphidicolin treatment alone led to a significant increase in both γH2AX and pRPA S33 foci per nucleus[18,229]. BLM depletion significantly increased the number of γH2AX and pRPA S33 foci per nucleus compared to DMSO-treated controls, highlighting a robust induction of DNA damage and replication stress (Fig. 26b-e). While previous studies have reported elevated γH2AX foci upon treatment with BLM inhibitors[230], this is a direct demonstration using genetic BLM depletion to show concurrent increases in both γH2AX and phosphorylated RPA S33. In BLM-deficient cells induced by auxin treatment, the number of γH2AX and pRPA S33 foci further increased upon the addition of aphidicolin in comparison to auxin treatment alone. Notably, combined auxin and aphidicolin treatment yielded a significantly higher γH2AX foci number per nucleus and an approximately 1.6-fold increase in mean γH2AX foci number/nucleus compared to aphidicolin alone, while pRPA S33 levels did not show a further rise beyond levels induced by aphidicolin alone. Co-localization analysis confirmed that BLM co-localizes with γH2AX and pRPA S33 in interphase, as demonstrated in previous studies[18,230,231]. Further, there was a significant increase in BLM and γH2AX foci co-localization in the presence of aphidicolin, indicating enhanced recruitment of BLM to sites of DNA damage. In contrast, no significant increase in co-localization was observed between BLM and pRPA S33 foci in the presence of aphidicolin. This is consistent with previous findings suggesting that, in contrast to BLM, phosphorylated RPA accumulation marks the progression of DNA resection rather than its initiation and may function as a negative feedback mechanism that limits further recruitment of BLM-EXO1 or BLM-DNA2 complexes, thereby regulating the extent of DNA end resection[28,29]. These observations suggest that while BLM is closely associated with the initial DNA damage response marked by γH2AX, it is functionally distinct from later-stage resection processes indicated by pRPA accumulation.

Flow cytometry analysis was used to assess the levels of GFP/AID-tagged BLM, γH2AX, and pRPA S33 in various treatment conditions (Fig. 26h-m). As expected, BLM expression was significantly reduced following auxin treatment, both alone and in combination with aphidicolin (Fig. 26h,i). Interestingly, while aphidicolin alone did not alter the fraction of BLM expressing cells, which is around 30% compared to control, HU treatment markedly increased the proportion of BLM-expressing cells, exceeding 80%. Investigation of DNA damage markers revealed that the fraction of γH2AX-positive cells reached 80% following HU treatment, consistent with its role in inducing replication stress (Fig. 26j,k). In contrast, aphidicolin and auxin alone caused only modest increases in γH2AX-positive cells, though a combined auxin and aphidicolin treatment resulted in an approximate 1.5-fold increase, indicating enhanced DNA damage accumulation under BLM-deficient and replication-stressed conditions, reaching a maximum of only around 40% of γH2AX-positive cells. Cells expressing pRPA S33 were the least abundant in all conditions (Fig. 26l,m). In control cells, only ~1% were positive for pRPA S33, and surprisingly, treatment with aphidicolin reduced this to approximately 0.8%, despite replication stress typically leading to ATR-mediated phosphorylation of RPA[18]. These findings suggest that a low dose of aphidicolin is insufficient to induce a global cell cycle arrest and does not robustly activate pRPA S33 signaling across the entire cell population. However, it may significantly increase pRPA S33 foci in a subset of cells that have already incurred DNA damage, as indicated in Fig. 26d. In contrast, HU treatment increased pRPA S33-positive cells

to around 9%, while auxin treatment alone raised it to 5%, and the combination of auxin and aphidicolin resulted in approximately 8%.

Additional microscopy analysis using HU as a positive control further demonstrated that mean γH2AX foci per nucleus were comparable between HU-treated cells and those treated with auxin or auxin with aphidicolin (Fig. 26n,o). Surprisingly, aphidicolin alone led to a decrease in γH2AX foci compared to control (Fig. 26o), which was not observed in earlier experiments (Fig. 26c), indicating potential variability between samples. Further, it was investigated whether the increased DNA damage induced by loss of BLM persists and might contribute to reduced proliferation and colony formation due to cell cycle arrest and the onset of senescence.

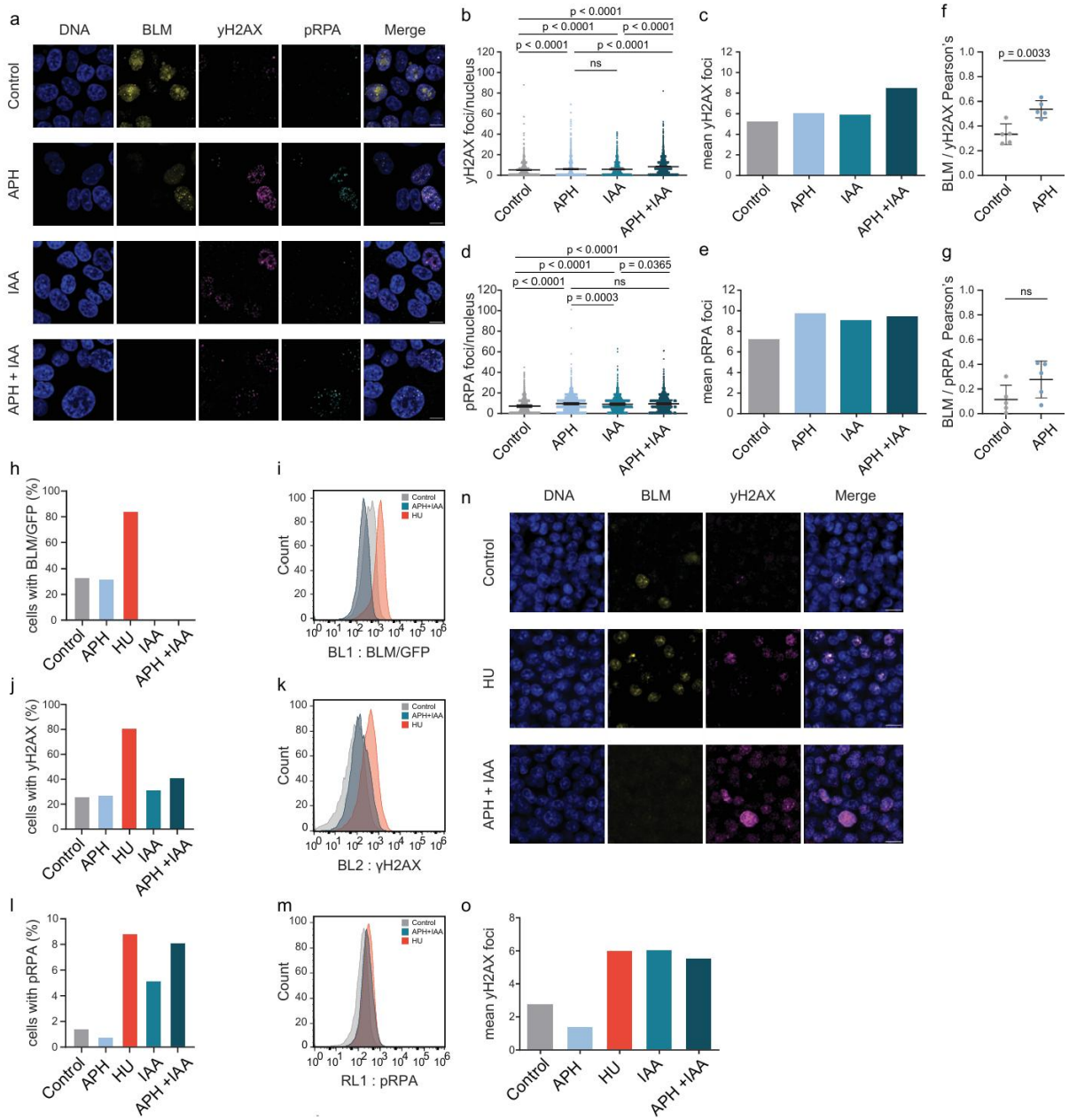

Figure 26|Loss of BLM function leads to accumulated DNA damage and senescence. a-o, Microscopy analysis of BLM, γH2AX, and pRPA S33 foci in asynchronous GFP/AID-tagged BLM cells following 24 h of treatment with 100 nM APH, 500 μM IAA, or the combination of APH and IAA. One experimental replicate, each condition > 1000 nuclei. **a,** Representative immunofluorescence images. **b-e,** Quantification of γH2AX and pRPA

S33 foci: distribution of foci numbers per nucleus (**b, d**) and mean number of foci per nucleus (**c, e**). **f-g**, Co-localization analysis of BLM with γH2AX (**f**) and pRPA S33 (**g**), shown by Pearson's correlation coefficient (r).**h-m,** Flow cytometry analysis of GFP-tagged BLM (**h–i**), γH2AX (**j–k**), and pRPA S33 (**l–m**) expression in asynchronous GFP/AID-tagged BLM cells under the indicated treatment conditions. **n-o,** Microscopy analysis of γH2AX foci formation in asynchronous GFP/AID-tagged BLM cells treated with 1 mM hydroxyurea (HU) with representative images (**n**) and quantification of mean γH2AX foci per nucleus (**o**). One experimental replicate per condition, >1000 nuclei analyzed for microscopic analysis. Pearson's=Pearson's correlation coefficient, HU=hydroxyurea, APH=aphidicolin, IAA=auxin. BLM was detected via endogenous BLM-GFP fluorescence, γH2AX and pRPA S33 were visualized using specific antibodies, DNA was counterstained with DAPI. Scale bars, 10 µm.

Senescence analysis using DDAOG-based flow cytometry revealed elevated levels of senescent cells in BLM-depleted populations under unstressed conditions following 24 h of auxin treatment and 4 days of recovery (Fig. 27a,b). Approximately 40% of cells exhibited DDAOG fluorescence in contrast to near 100% in the Doxo-treated positive control (Fig. 27a). Interestingly, neither mild replication stress alone nor combined BLM depletion with aphidicolin treatment induced a similar increase in senescence. Furthermore, no senescence was detected following continuous 4-day treatment with aphidicolin or auxin, suggesting more severe effects, such as cell death by apoptosis from auxin combined with aphidicolin treatment, consistent with previous studies showing that senescence depends on the amount of stress level[232,233]. BLM protein levels assessed after the recovery period confirmed re-expression of BLM in the 24 h treatment group, while BLM remained absent in most of the cells under continuous auxin exposure or auxin plus aphidicolin treatment, consistent with sustained depletion. Notably, cells treated with Doxo for 24 h followed by recovery exhibited BLM expression in nearly 80% of cells, with a part of cells showing even greater BLM intensity than untreated controls, suggesting stress-induced upregulation of BLM.

Additionally, X-gal staining[220] was visualized by light microscopy to detect β-galactosidase activity after 24 hours treatment of indicated conditions and 4 days of washout (Fig. 27e). X-gal staining is indicative of senescence, characterized by intense intracellular staining, as shown particularly in auxin treated cells (Fig. 27e). However, extracellular staining was also observed, potentially arising from the presence of dying or dead cells. Taken together, these findings suggest that while loss of BLM is not lethal under normal conditions, it increases cellular senescence in the absence of external stress. Under replication stress, induced by aphidicolin treatment, BLM-deficient cells fail to form colonies, likely due to the accumulation of unrepaired DNA damage that leads to cell death, for example by apoptosis rather than entering senescence, in line with reduced proliferation and viability (Fig. 25).

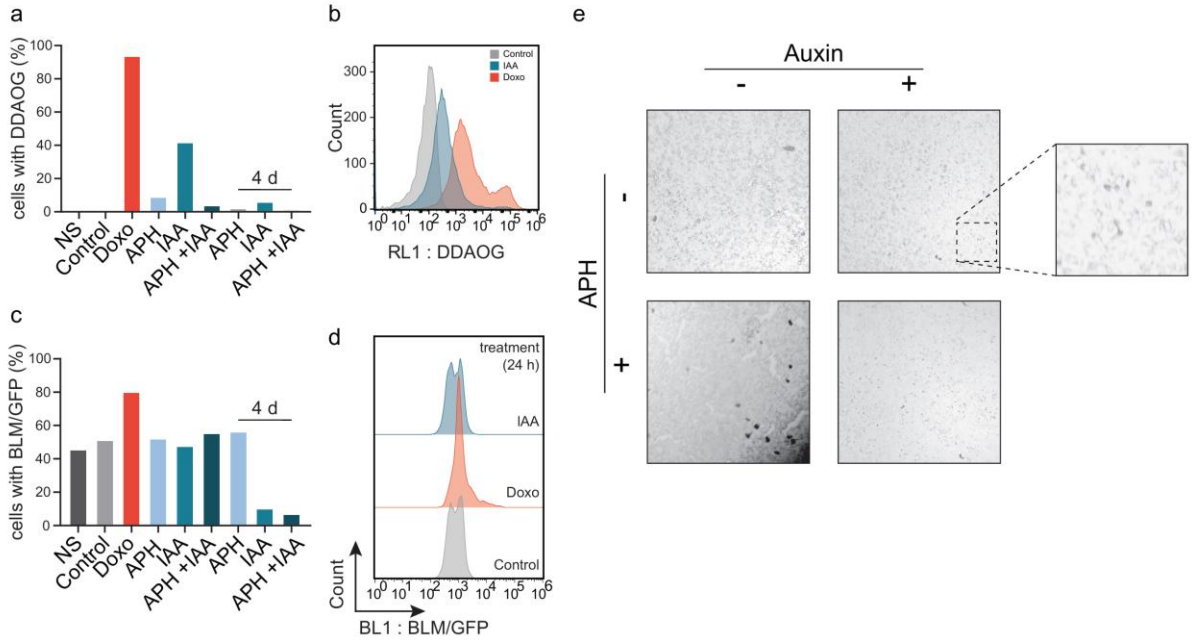

Figure 27|Loss of BLM leads to increased senescence. a-d, Flow cytometric analysis of DDAOG staining as β-galactosidase substrate to assess senescence and GFP/BLM expression following either 24 h treatment with a 4-day washout or continuous 4-day treatment with 1 μM Doxo, 100 nM APH, 500 μM IAA, or combined APH and IAA. **e,** Representative X-gal staining images showing senescence-associated β-galactosidase activity by light microscopy. One experimental replicate per condition. APH=aphidicolin, IAA=auxin, NS=no treatment, Doxo=doxorubicin.

4.7 Cell synchronization by single-thymidine block enables simultaneous proceeding through the cell cycle

To analyze BLM function in specific cell cycle phases and its effects on genomic stability following depletion, it is crucial to synchronize cells to ensure uniform progression through the cell cycle. Various synchronization methods were tested in HCT116 WT cells (data not shown), and the single-thymidine block was selected as the most effective and least stressful approach (Fig. 28a). This method involves temporarily halting the cell cycle in G1/S phase boundary by exposing cells to thymidine, a nucleotide analog that inhibits DNA replication. The single-thymidine block was preferred because stress-inducing synchronization methods can exacerbate replication stress, potentially confounding subsequent analyses. Stress indicators from alternative methods might serve as confounding variables when studying replication stress, particularly in response to treatments like aphidicolin, which inhibits DNA polymerase and induces replication stress. By minimizing stress during synchronization, the reliability of the subsequent analysis of BLM function and replication stress effects is improved. Flow cytometric analysis of cell cycle progression revealed that a single thymidine block was sufficient to arrest the majority of cells in S phase, with 78% of the population successfully synchronized (Fig. 28b,c). Upon removal of thymidine and replacement with fresh medium, cells promptly resumed cell cycle progression. Subsequently, the majority of cells reaching G2/M phase were observed at 6 h post-release and the first cells were detected in the next G1 phase approximately 8 h post-release (Fig. 28b, c). For comparison, asynchronous cells exhibited a heterogeneous distribution across the cell cycle: 16% in G1 phase, 28% in S

phase, and 2% in G2/M phase based on PI staining during flow cytometry (Data not shown). However, since G2 and M phase cells cannot be distinguished using PI alone, DAPI-stained cells were also analyzed by fluorescence microscopy (Fig. 28d). Mitotic cells emerged between 8 to 12 h post-release, confirming the flow cytometry findings and validating cell cycle progression. The fraction of anaphase cells peaked at 10.5 h post-release from the thymidine block, with approximately 15% of the cell population exhibiting mitotic phenotypes by manual counting. These findings emphasize the robustness of the synchronization method for studies requiring controlled cell cycle progression.

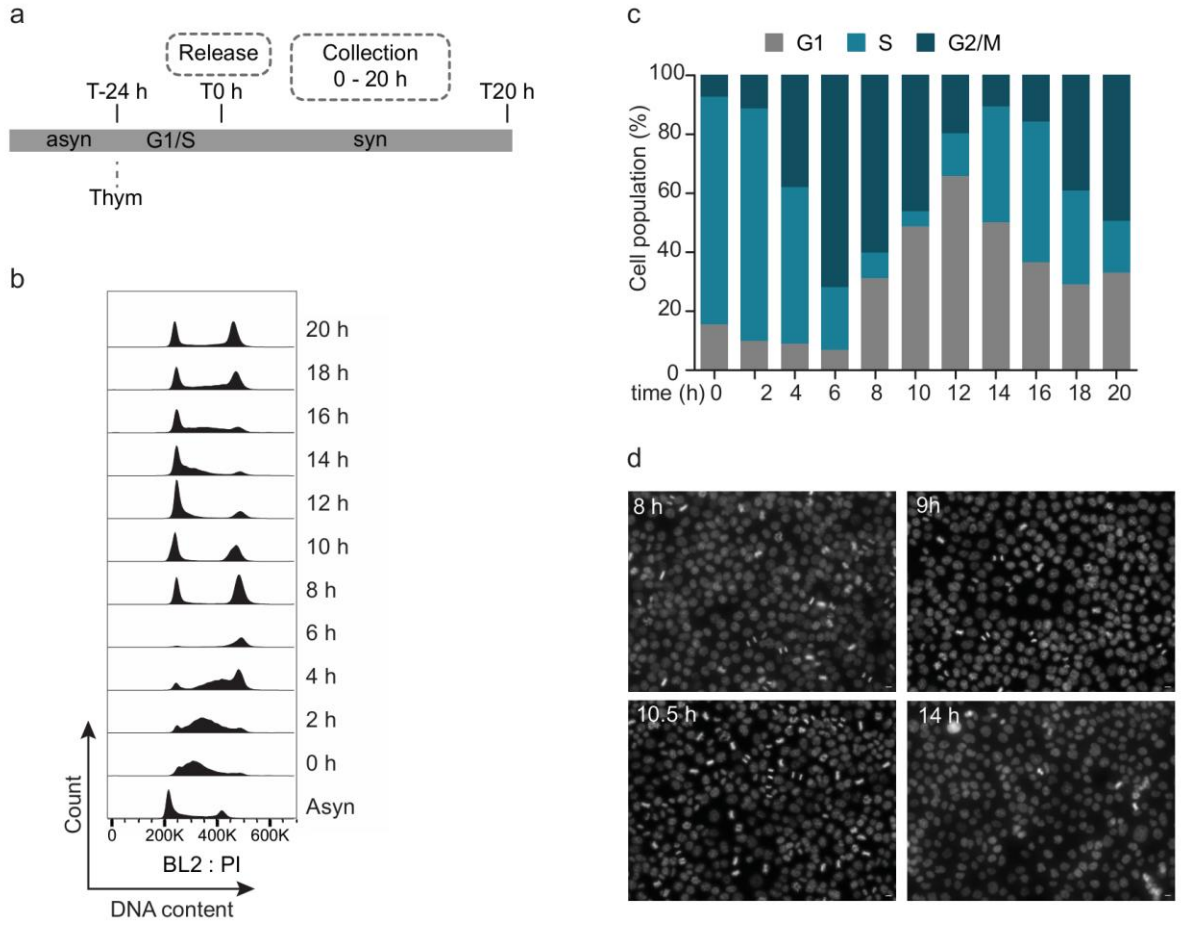

Figure 28|Cell cycle synchronization. a, Depiction of the synchronization work flow. Cells were arrested using a single-thymidine block and subsequently released into fresh medium to allow progression through the cell cycle. **b-c**, Flow cytometry analysis of synchronized HCT116 WT cells. Fixed cells were stained with propidium iodid (PI) at various time points after thymidine release. Histogram displaying DNA content, indicating progression through G1, S and G2/M phase **(b)**. Quantification of cell cycle phases with percentage of cells in G1, S and G2/M phase at each time point post-release **(c)**. **d,** Representative images of mitotic progression after thymidine release with a mitotic peak at 10.5 h after release. DNA was counterstained with DAPI. Scale bars, 10 µm. Experiments were performed together with Divya Reddy.

After successful synchronization of HCT116 WT cells using a single-thymidine block, which demonstrated efficient arrest at G1/S phase boundary and enrichment of mitotic cells at around 10 h post-release (Fig. 28), synchronization was extended to HCT116 Tet-OsTIR1 $BLM^{AID/AID}$ cells under various experimental conditions (Fig. 29). These conditions included BLM depletion via auxin treatment, mild replication stress induced by aphidicolin treatment, and both combined. The single-thymidine block effectively synchronized homozygous

AID/GFP-tagged BLM cells, similar to WT cells (see Fig. 28b, c) as demonstrated by cell cycle progression, analysed by flow cytometry (Fig. 29b). To induce BLM depletion, 500 µM IAA was added during thymidine treatment and after the release. To induce mild replication stress, cells were exposed additionally to 100 nM aphidicolin upon release into the cell cycle. At this low dose, aphidicolin only partially inhibits DNA polymerase α, inducing mild replication stress without causing cell cycle arrest, as demonstrated (see Fig. 25b,c), in line with previous studies whereby 100 nM APH can already reduce proliferation upon 4 days[234]. Despite reported slight delays in cell cycle progression compared to untreated cells, synchronization kinetics remained comparable, allowing cells to traverse the cell cycle under mild stress conditions (Fig. 29c-e). The majority of cells (approximately 60–70% across all conditions) accumulate at the G2/M phase peak around 8–10 h post-release and enter the subsequent G1 phase by 15 h. However, cells do not proceed synchronously through another round of the cell cycle within the 24h duration of analysis. This suggests that a single-thymidine block may not be sufficient to strongly synchronize a second round of cell cycle progression, possibly due to varying levels of DNA damage requiring different repair durations. Notably, IAA and APH+IAA treatments show clearly reduced S phase enrichment beyond 15 h, indicating a prolonged G1 phase, likely to accommodate repair of increased DNA damage resulting from BLM loss. This analysis confirmed that synchronization using a single-thymidine block is robust for evaluating loss of BLM during specific cell cycle phases during one round of cell cycle and enables detailed investigation into the consequences of BLM depletion and replication stress.

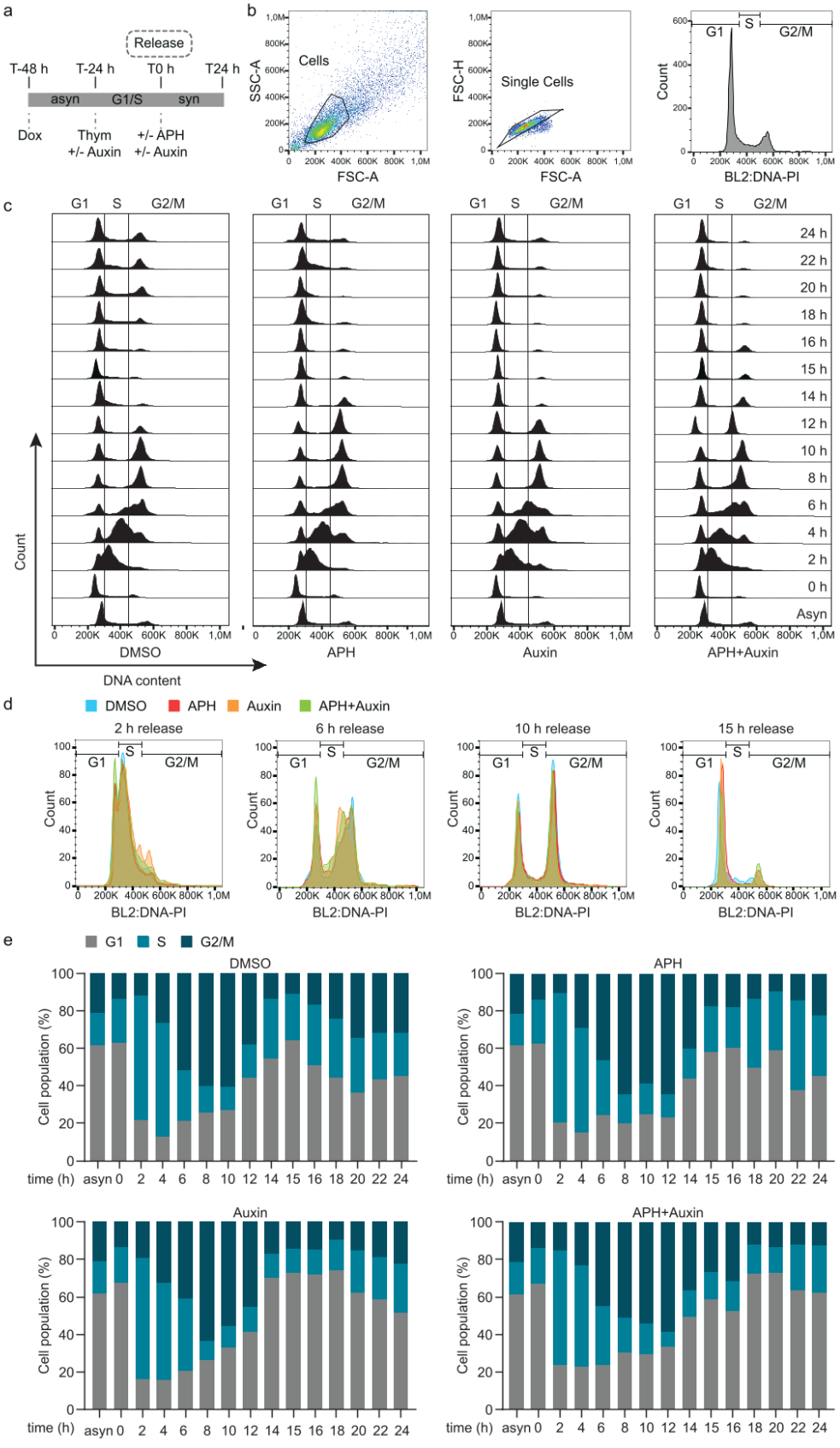
a
Release
T-48 h
T-24 h
T0 h
T24 h
asyn
G1/S
syn
Dox
Thym
+/- Auxin
+/- APH
+/- Auxin
b
Cells
SSC-A
FSC-A
Single Cells
FSC-H
FSC-A
G1
S
G2/M
Count
BL2:DNA-PI
c
G1
S
G2/M
24 h
22 h
20 h
18 h
16 h
15 h
14 h
12 h
10 h
8 h
6 h
4 h
2 h
0 h
Asyn
Count
DMSO
APH
Auxin
APH+Auxin
DNA content
d
DMSO
APH
Auxin
APH+Auxin
2 h release
6 h release
10 h release
15 h release
Count
BL2:DNA-PI
e
G1
S
G2/M
DMSO
APH
Auxin
APH+Auxin
Cell population (%)
time (h)
asyn 0 2 4 6 8 10 12 14 15 16 18 20 22 24

Figure 29|Cell synchronization in HCT116 Tet-OsTIR1 BLMAID/AID cells. a, Experimental workflow for cell cycle synchronization during BLM depletion and replication stress. Cells were pretreated with doxycycline (Dox) for 24 h to activate the tet promoter. Blockage at the G1/S phase boundary was induced by treatment with 2 nM thymidine (Thym) for additional 24 h. BLM depletion was induced by co-treating the cells with 500 µM auxin. Following washout of thymidine, cells were released into the cell cycle. To maintain BLM depletion, another 500 µM auxin treatment was added to the cells. Additionally, mild replication stress was induced with 100 nM aphidicolin (APH). Cells were collected every 2 h post-release and their cell cycle phases were analyzed by flow cytometry. **b,** Flow cytometry gating strategy. Cells were gated to exclude debris and apoptotic cells (1), doublets were removed (2) and G1, S and G2/M phases were defined based on DNA content profiles obtained by PI staining. **c,** DNA content was analysed in control (DMSO-treated), aphidicolin alone, auxin alone and in a combination of auxin and aphidicolin treated cells. Samples were collected at 2-hour intervals, as well as at the 15-hour mark post-release, over a total observation period of 24 hours to comprehensively monitor cell cycle progression. **d,** Overlay plots of DNA content were generated to compare DNA content across treatment conditions at timepoint 2, 6, 10 and 15 h post-thymidine washout. **e,** The fraction of cells in each phase of the cell cycle was quantified under the different treatment conditions.

4.8 Validation of the enrichment of mitotic and anaphase cells at T10.5 h

To confirm that synchronized homozygous AID/GFP-tagged BLM cells are enriched in mitosis at 10.5 h post-thymidine release and to validate this timepoint as appropriate for subsequent experiments in anaphase cells, as indicated for WT cells (see Fig. 28), Western blot, flow cytometry, and microscopy analyses were performed (Fig. 30). Western blot analysis revealed a substantial increase in cyclin B1 levels at 10.5 h, corroborating the enrichment of cells in the M phase (Fig. 30b). Furthermore, in auxin-treated cells, both BLM and GFP were undetectable at 0 hours and 10.5 h post-release, confirming efficient depletion of BLM protein at these timepoints. Flow cytometry analysis of asynchronous cells and synchronized cells collected at 0 h, 5 h, 9 h, and 10.5 h post-release revealed distinct patterns of cell cycle progression consistent with the expected cell cycle dynamics in this system (Fig. 30c). Asynchronous cells predominantly resided in the G1 phase, which is characteristic of a mixed population. Following synchronization, the G1 phase fraction decreased rapidly, with its lowest point observed at 9 h post-release. Meanwhile, the S phase, which ranged from 0 to 5 h post-release, steadily declined, reaching its minimum at 9 h and 10.5 h. These time points correspond to the peak of G2/M phase fractions (see Fig. 29e). The application of the MPM2 antibody, which specifically recognizes proteins phosphorylated during mitosis, allowed for the distinction between cells in G2 and M phases. This analysis demonstrated a 52% enrichment of M-phase cells at 10.5 h post-thymidine release, compared to only 6% M-phase cells at the 9h timepoint. While the mitotic fraction of cells is much higher than when it was manually counted from microscopy images of WT cells (Fig. 28d), suggesting loss of weakly attached mitotic cells during cell preparation for microscopic analysis.

Despite a more prominent overall G2/M peak at 9 h, these results indicate a strong progression into M-phase by 10.5 h, validating this timepoint as optimal for studying mitotic events. Next, microscopy analysis confirmed that anaphases and UFBs can be observed and analysed at 10.5 h post-release (Fig. 30d). In untreated cells, UFBs were successfully stained with BLM and PICH antibodies, demonstrating the presence of both proteins on the bridges. In contrast, cells treated with auxin for 24 h to deplete BLM showed only PICH-positive UFBs, confirming the absence of BLM from these structures and verifying its specific depletion. These results collectively validate that cells are synchronized effectively and enriched at the anaphase stage at 10.5 h post-release from thymidine block. These findings confirm robust synchronization and mitotic enrichment at 10.5 h also in homozygous AID/GFP-tagged cells, enabling the study of BLM function and UFB formation under conditions of auxin-induced depletion.

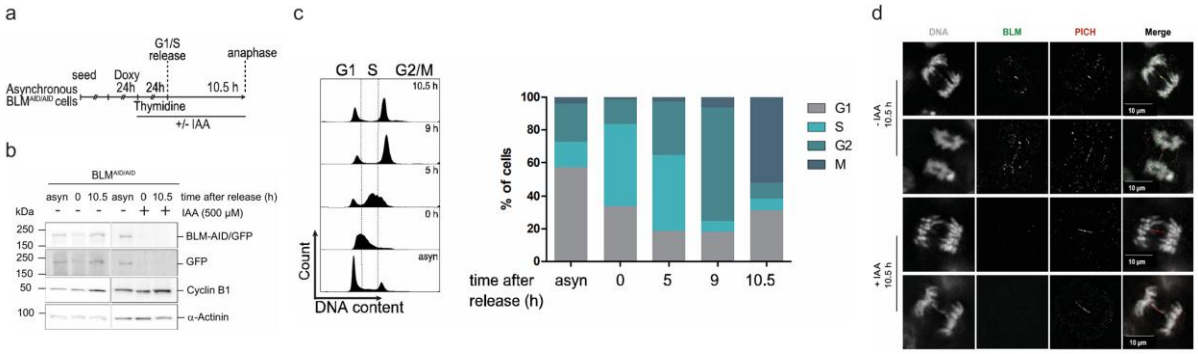

Figure 30|Enrichment of mitotic cells at 10.5 h after thymidine release. a, Depiction of the synchronization workflow used for homozygous HCT116 Tet-OsTIR1 BLM cells. Cells were synchronized by a single thymidine block and released into fresh medium, allowing progression through the cell cycle. **b,** Western Blot of synchronized cells treated with or without 24 h of auxin, showing increased levels of cyclin B1 at 10.5 h post-release, both in BLM-depleted and non-depleted conditions. **c,** Flow cytometry analysis of mitotic cells revealed a peak of 52 % mitotic cells observed at 10.5 h after release, confirmed by the mitotic marker MPM2. **d,** Representative fluorescence microscopy images of UFB-containing anaphase cells at 10.5 h after thymidine release. Cells were stained with anti-PICH antibody, BLM was directly detected by the fluorescence signal of the GFP tag. BLM signal was strongly reduced in most auxin-treated cells, resulting in PICH-positive but BLM-negative UFBs. BLM and PICH were visualized using specific antibodies, DNA was counterstained with DAPI. Scale bars, 10 µm.

4.9 Loss of BLM function during mitosis leads to genomic instability

Depletion of BLM in asynchronous HCT116 Tet-OsTIR1 BLM$^{AID/AID}$ cells results in elevated SCE rates (Fig. 24), reduced proliferation and colony formation ability (Fig. 25), as well as enhanced DNA damage response (Fig. 26) and senescence (Fig. 27). It has been widely hypothesized that the elevated SCE frequency is the primary driver of genomic instability and tumorigenesis observed in BS patients[79]. BLM, along with the BTRR complex, plays a crucial role in preventing crossovers between homologous chromosomes and, consequently, excessive SCE formation[79], which is associated with increased loss-of-heterozygosity (LOH) events[201,202]. However, LOH was shown to be relatively rare in BLM-deficient cells[235], suggesting that the loss of additional functions of BLM may contribute to the increased genomic instability observed in BS patients[236]. Beyond its role in crossover suppression, BLM is involved in multiple pathways, but its specific contributions at different cell cycle stages to maintaining genomic integrity remain unclear. To address this, phase-specific functions of BLM were separated by selectively depleting it at distinct cell cycle stages and analyzing the impact on mitotic aberrations as well as resulting abnormalities in the next G1 phase.

4.9.1 The cell cycle-specific BLM depletion enables distinct separation of BLM functions

The auxin-induced depletion of BLM during specific cell cycle phases allows for a precise assessment of the effects of phase-specific BLM loss. To achieve this, an auxin-inducible

degradation strategy (see chapter 4.3) was implemented to deplete BLM in synchronized HCT116 Tet-OsTIR1 BLM$^{AID/AID}$ cells (see chapters 4.7 and 4.8), which endogenously express BLM tagged with AID and GFP while co-expressing TIR1 induced by doxycycline addition (Fig. 31, grey cell). Cells were synchronized using a single-thymidine block, arresting them at the G1/S phase boundary before being released into the cell cycle to assess phase-specific BLM depletion. To ensure continuous BLM depletion throughout interphase and mitosis, auxin was applied during thymidine-induced cell cycle arrest and was reapplied immediately after thymidine wash-out to sustain BLM depletion throughout the entire cell cycle progression, further referred to as S+M phase depletion (Fig. 31, purple cell). To deplete BLM only during S phase, auxin was supplemented during thymidine-induced cell cycle arrest and reapplied until 6 h post-release. After 6 h of release from thymidine block, cells predominantly transitioned from late S phase into G2 (see Fig. 29d, e, timepoint 6 h post-release). At this point, the medium was exchanged to remove auxin, allowing BLM expression to resume. It was hypothesized that BLM levels fully recover, ensuring that its functions during S phase are abolished while potentially preserving its mitotic functions. This condition was designated as S-only depletion (Fig. 31, pink cell). Conversely, for M-only depletion, cells were treated with auxin starting at 6 h post-release, ensuring that BLM was fully functional during S-phase (Fig. 31, blue cell). As cells progressed into G2-phase, auxin treatment led to gradual BLM depletion over time, ideally with a substantial reduction in BLM levels starting already at 0.5 h of auxin treatment, as predicted from previous depletion kinetics (see Fig. 23b, c). This setup aimed to maintain BLM activity throughout S phase while selectively impairing its mitotic functions. For each condition, cells were collected at 10.5 h post-release to assess mitotic defects in anaphase cells, as well as aberrations arising in the next G1 phase, such as micronuclei formation and binucleation, that were evaluated at 15 h post-release.

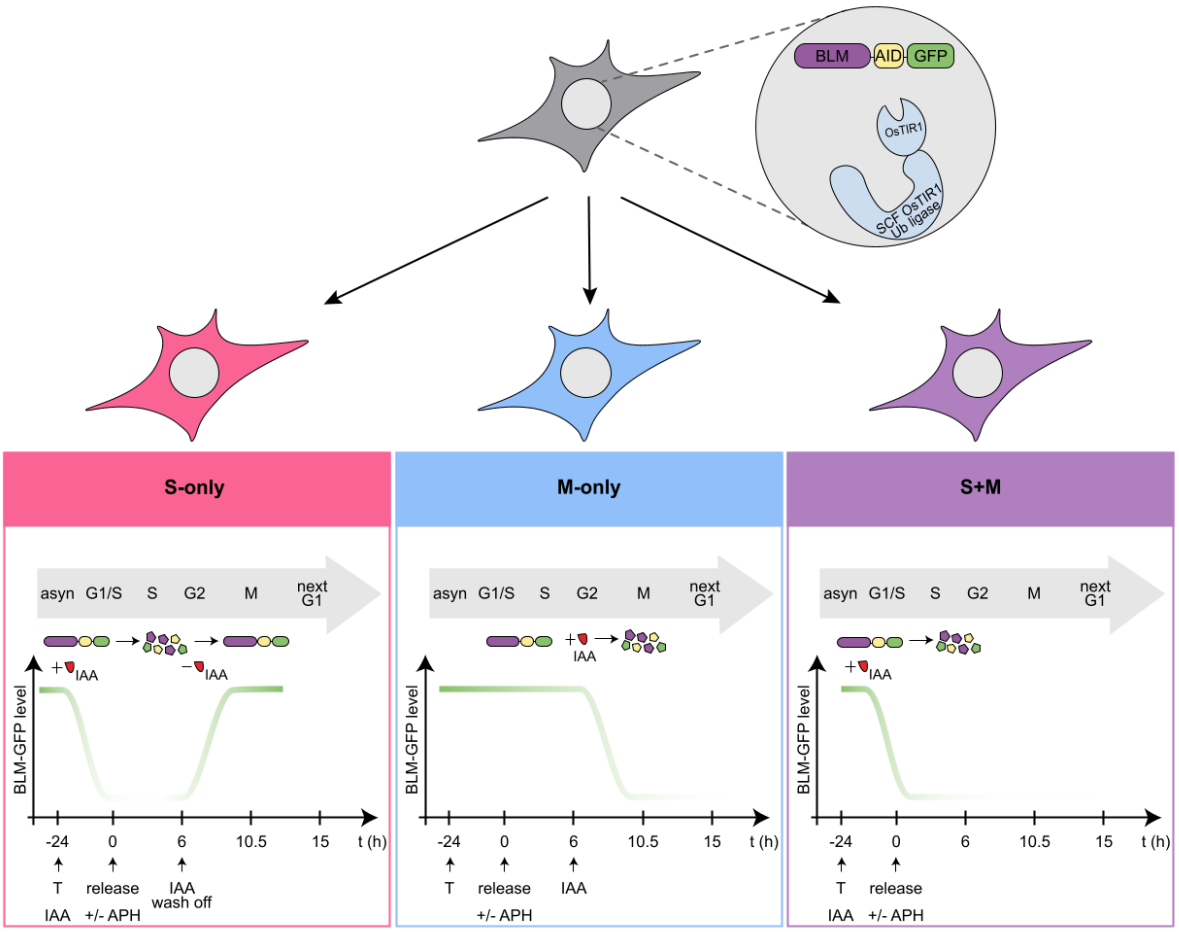

Figure 31|Cell-cycle specific depletion of BLM. Schematic representation of the experimental strategy for cell cycle-specific depletion of BLM in HCT116 Tet-OsTIR1 BLM$^{AID/AID}$ cells with hypothetical BLM expression levels. In these cells, endogenous BLM is tagged with AID and GFP, allowing for rapid degradation upon auxin addition due to the co-expression of TIR1 (grey cell). For S-phase-specific depletion, auxin is added concurrently with thymidine during G1/S arrest and removed 6 h post-release. This condition was designated as S-only (pink cell). For M-phase-specific depletion, auxin is applied at 6 h post-release, designated as M-only (blue cell). For S+M depletion, auxin is present throughout the entire cell cycle until the final cell harvesting, designed as S+M (purple cell). T means 2 mM thymidine treatment, IAA means 500 µM auxin treatment, APH means 100 nM aphidicolin treatment.

BLM protein levels were assessed under the conditions of S-only, M-only, and combined S+M phase depletion using Western blot analysis as well as microscopy analysis to determine BLM-positive UFB frequency (Fig. 32a-e). Homozygous BLM-AID/GFP cells with functional BLM protein were compared to cells that were treated with auxin. Samples were collected at multiple timepoints: 0 h post-thymidine release (representing G1/S-phase boundary), 10.5 h post-release (corresponding to the G2/M transition with an enrichment of mitotic cells, particularly in anaphase), and 15 h post-release (when cells progressed into the next G1 phase) (see Fig. 29) under mild replication stress induction by aphidicolin. In control cells, BLM was detected at all analyzed timepoints (0 h, 10.5 h, and 15 h). Notably, at 0 h post-release, when most of the cells were enriched at the G1/S phase boundary, BLM protein levels were reduced compared to other timepoints, consistent with a strong reduction of BLM in G1 phase due to BLM degradation in late mitosis[44] (Fig. 32b). Interestingly, BLM levels at 15 h post-release did not decline to levels comparable to the 0 h timepoint, indicating that not all cells had fully progressed into the subsequent G1 phase yet (Fig. 32b). This might be due to a potential delay induced by aphidicolin treatment (see Fig. 28). For S-only depletion, BLM

protein levels were undetectable at the time of cell release (0 h post-release), as expected and reappeared at 10.5 h and 15 h post-release. However, the signal was weaker compared to control conditions, suggesting BLM levels were not fully recovered within the analyzed timeframe. In the M-only depletion condition, BLM remained detectable at the time of auxin addition, as expected, and was not detectable at 15 h (Fig. 32b). However, residual BLM remained at 10.5 h, suggesting no full degradation yet, comparable with auxin depletion kinetics (see Fig. 23) and BLM-UFB analysis (Fig. 32d, e). Finally, in the S+M phase depletion condition, BLM was absent at all timepoints (0 h, 10.5 h, and 15 h post-release), as expected due to continuous auxin treatment throughout the experiment. Notably, absence of BLM levels at timepoints of 0 h showed a decrease in the Ponceau staining that served as loading control, most likely due to unequal protein loading (Fig. 32b). Analysis of BLM-positive UFBs revealed that they were detectable in anaphase at 10.5 h post-release under S-only depletion conditions, indicating successful recovery of BLM after auxin wash-out and further confirming that S phase functions of BLM are not required for the recruitment of BLM to UFBs during mitosis, consistent with previous studies demonstrating that PICH is promoting BLM recruitment to UFBs at anaphase onset[155,237] (Fig. 32c-e). There was no significant difference observed in either the percentage of anaphases with at least one BLM-positive UFB or the number of BLM-UFBs per cell in control conditions, regardless of aphidicolin treatment (Fig. 32d, e). This suggests that the presence of BLM is sufficient to suppress elevated UFB formation in response to mild replication stress, consistent with earlier findings reporting only an increase of BLM-UFBs, particularly FS-UFBs as indicated by FD2 foci, using 400 nM APH[127].

Strikingly, aphidicolin treatment in the context of S-only depletion significantly elevated both the frequency of anaphase cells with BLM-positive UFBs and the number of BLM-UFBs per cell compared to the control (Fig. 32d, e). These results further confirm that BLM activity during S phase is particularly critical under stress conditions in preventing the persistence of DNA junctions leading to UFB formation, as suggested for under-replicated regions after replication stress induction[127]. Notably, BLM-positive UFBs were rarely detectable when BLM was depleted during M-phase alone or throughout the entire cell cycle, regardless of whether mild replication stress was induced, confirming successful prevention of BLM-UFB formation during M-only and S+M depletion (Fig. 32d, e). A closer examination of the number of BLM-positive UFBs per anaphase further confirmed the efficiency of the BLM-depletion system across different cell cycle phases. In M-only and S+M phase depletion, the few detectable BLM-positive UFBs were limited to just one UFB per anaphase, except in a single instance (M-only condition without aphidicolin), where two BLM-positive UFBs were observed. In contrast, S-only depletion led to a maximum increase in BLM-positive UFBs, ranging from 3 per anaphase without aphidicolin to 6 per anaphase with aphidicolin (Fig. 32e).

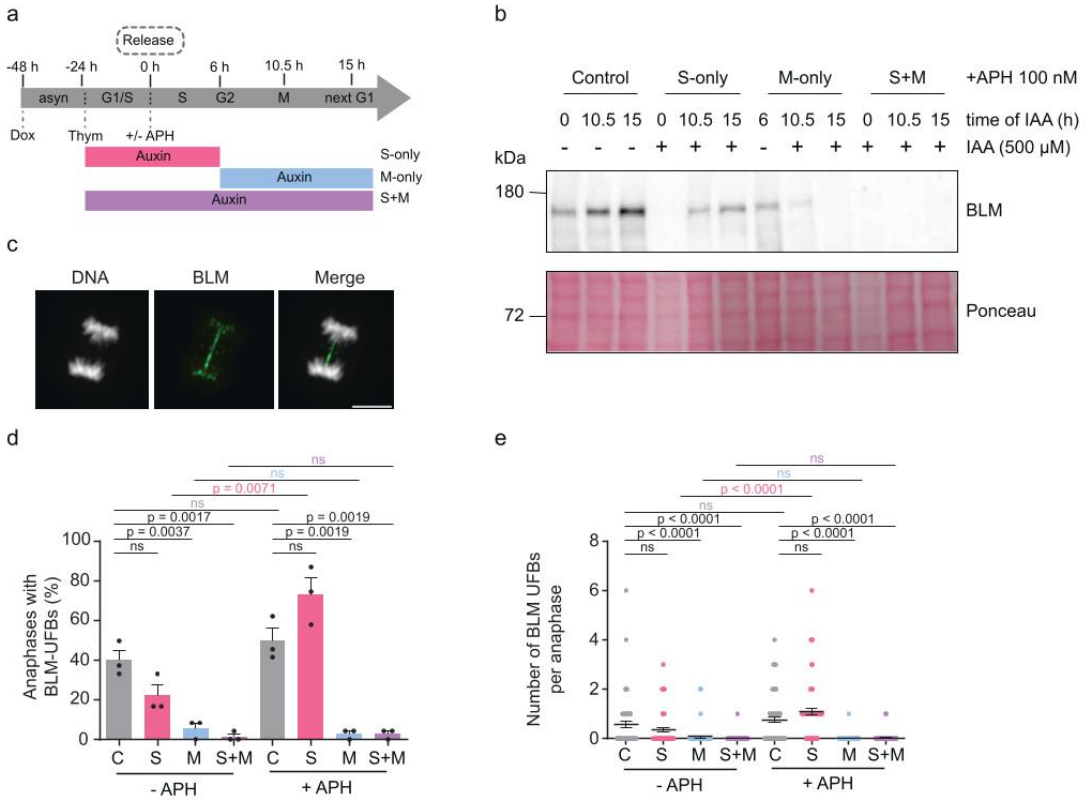

Figure 32|Cell-cycle specific depletion of BLM. a, Schematic representation of cell-cycle-specific BLM depletion. **b,** Western blot analysis of BLM levels under S-only, M-only, and S+M depletion conditions. Ponceau served as a loading control. **c,** Representative image of BLM-positive UFB. BLM was detected via endogenous BLM-GFP fluorescence, DNA was counterstained with DAPI. **d,** Quantification of the percentage of anaphases with at least one BLM-positive UFB. Data are mean ± S.E.M., statistical significance assessed by Student's t-test, 25 anaphases per replicate, 3 independent experiments. **e,** Quantification of the number of BLM-positive UFBs per anaphase cell. Data are mean ± S.E.M., statistical significance assessed by Student's t-test, 25 anaphases per replicate, 3 independent experiments. Scale bar, 10 µm.

BLM-GFP expression levels were compared across experimental conditions at 10.5 h post-release (Fig. 33). Both control and S-only depletion conditions showed that BLM-GFP signal was readily detectable, appearing as discrete foci and UFB-associated signal in mitosis and as diffuse signal and nuclear foci in interphase cells, regardless of aphidicolin treatment (Fig. 33, first two top rows). In contrast, M-only and S+M depletion conditions exhibited markedly reduced or absent BLM signals, including a lack of BLM-positive UFBs (Fig. 33, last two rows). Occasionally, rare cells displayed residual BLM signal or UFB staining, consistent with quantification of BLM-positive UFBs (see Fig. 32d, e). Notably, BLM intensity appeared slightly reduced in S-only conditions, consistent with Western blot analysis (see Fig. 32b), indicating that BLM recovery was incomplete in some cells at the time of analysis.

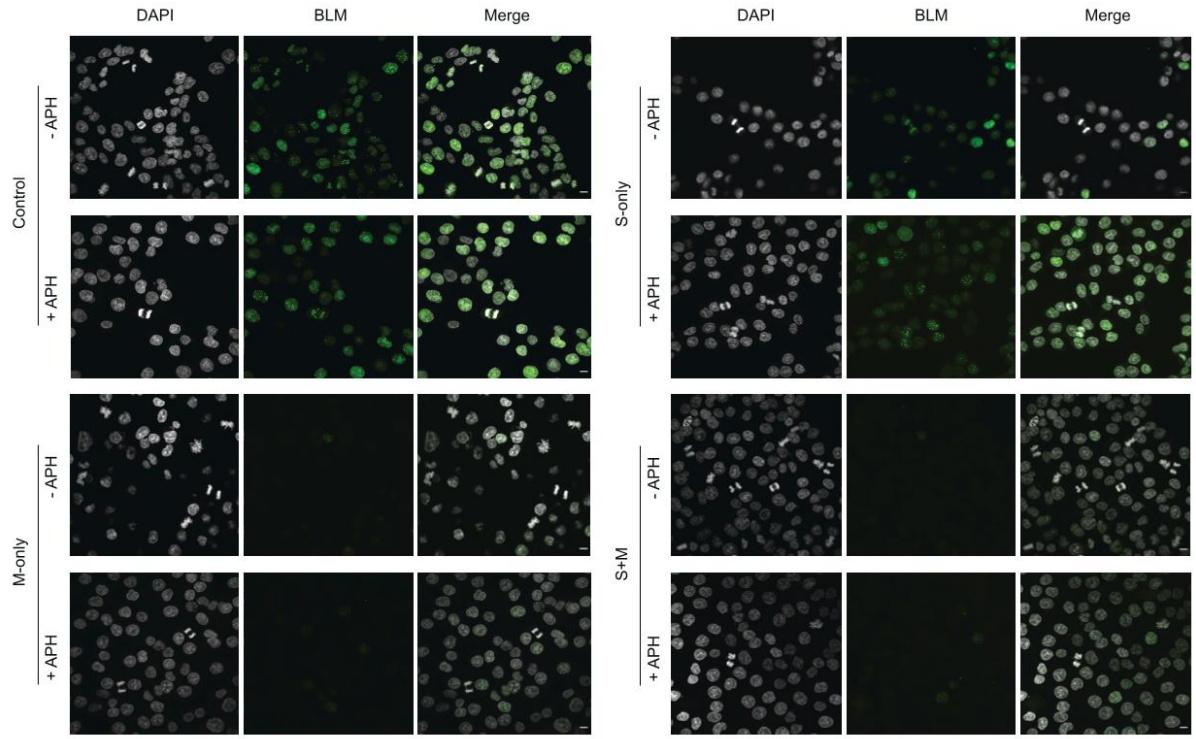

Figure 33|Successful recovery of BLM signal after S-phase specific BLM depletion. Representative images of BLM-GFP signal at 10.5 h post-release showing cells at different cell cycle stages with an increase of anaphase cells. In both control and S-only depletion conditions, BLM signal was observed in interphase and mitotic cells, with detectable BLM foci in anaphase and BLM-positive UFBs. In contrast, M-only and S+M depletion conditions showed a marked reduction or absence of BLM signal. BLM was detected via endogenous BLM-GFP fluorescence, DNA was counterstained with DAPI. Scale bars, 10 µm.

4.9.2 Assessment of the analysis of mitotic aberrations

To investigate miotic aberrations and chromosome segregation defects in anaphase cells at 10.5 h post-release, different mitotic stages, including prophase, prometaphase, metaphase, anaphase, and telophase, were visually determined to ensure the consistent identification of anaphase cells (Fig. 34).

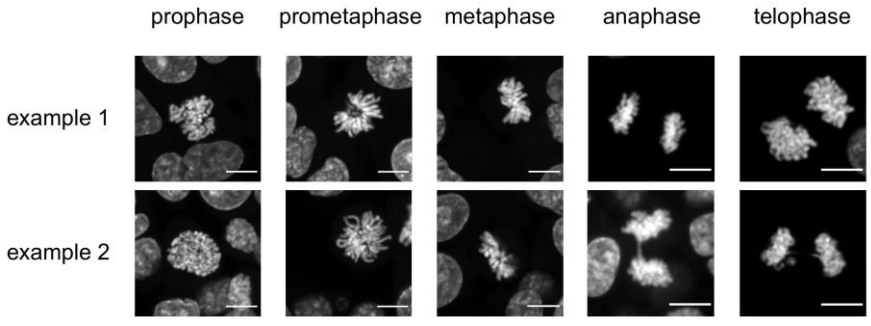

Figure 34|Distinguishing different mitotic phases. Different phases of mitosis were detected at T10.5 in synchronized HCT116 Tet-OsTIR1 BLM$^{AID/AID}$ cells. Scale bars, 10 µm.

4.9.3 BLM intensity in mitosis increases predominantly upon onset of anaphase

BLM, which is known to localize to PML bodies during interphase, is recruited to DNA damage sites where it forms distinct nuclear foci[162,163]. At the onset of mitosis, it is hypothesized that distinct BLM foci largely disappear, likely due to phosphorylation by kinases such as Plk1 to prevent centromere unwinding[125,155,170]. It is subsequently thought to be recruited to UFBs at the onset of anaphase, following the prior localization of PICH to these structures, whereby the mechanical tension on stretched DNA generated by spindle pole separation is proposed to facilitate the recruitment of PICH to UFBs[155,237,238]. However, key aspects of this process remain unclear, including the precise timing of BLM recruitment to mitotic chromatin and whether its localization to UFBs is strictly PICH-dependent. Interestingly, BLM foci and BLM-positive bridge-like structures were detected across different mitotic phases in BLM-AID/GFP cells across control and S-only conditions with and without APH (Fig. 35a-e), although BLM signal generally declined in early mitotic phases compared to interphase cells (data not shown). Nonetheless, BLM-positive foci and bridge-like structures were observed in some prometaphase and metaphase cells, suggesting that BLM may either persist at sites of DNA damage from S phase or be recruited to mitotic chromatin prior to anaphase onset under certain conditions. Further, PICH foci were found at prometaphase and metaphase chromatin consistent with previous studies showing that PICH foci are highly enriched at kinetochore-associated chromatin at metaphase centromeres and localize to mitotic chromatin from prometaphase[126], potentially initiating early BLM recruitment in a subset of cells (Fig. 35a). Interestingly, although PICH, and to a some extent RPA, were detected at analyzed prometaphase and metaphase cells, they did not exhibit bridge-like structures (Fig. 35a). Across different conditions, BLM foci were more frequently observed in prometaphase than in metaphase, suggesting that these represent early-stage repair foci that were likely newly recruited rather than persisting from S phase damage as indicated by the presence of BLM foci in prometaphase and metaphase cells under S-only depletion conditions (Fig. 35b, c). Notably, in the images analyzed, no metaphase cells were detected in the S-only condition with aphidicolin, and only two metaphase cells were found in the S-only condition without aphidicolin (Fig. 35c). BLM-positive bridge-like structures were also observed, particularly in metaphase cells of control conditions with or without aphidicolin, whereas in the S-only condition, they were only detectable during prometaphase (Fig. 34d). S-only depletion with aphidicolin seemed to show an increased number of both BLM foci and bridge-like structures rather in prometaphase than in metaphase, in contrast to the control, suggesting increased DNA damage in S phase and potentially reduced BLM phosphorylation, allowing BLM recruitment at earlier mitotic stages. Furthermore, BLM signal intensity increased markedly during metaphase and anaphase, both in the presence and absence of aphidicolin, suggesting that some cells categorized as metaphase may have already initiated the onset of anaphase, consistent with its essential role in UFB resolution during chromosome segregation, whereby in most of the metaphase cells analyzed, initiating of sister chromatid separation was not clearly detectable (Fig. 35a, last row). A significant reduction in BLM intensity was observed in telophase cells compared to metaphase and anaphase in control conditions without aphidicolin (Fig. 35e). Of note, no prophase and telophase cells were detected in control cells treated with aphidicolin among the analyzed images at timepoint 10.5 h post-release (Fig. 35e).

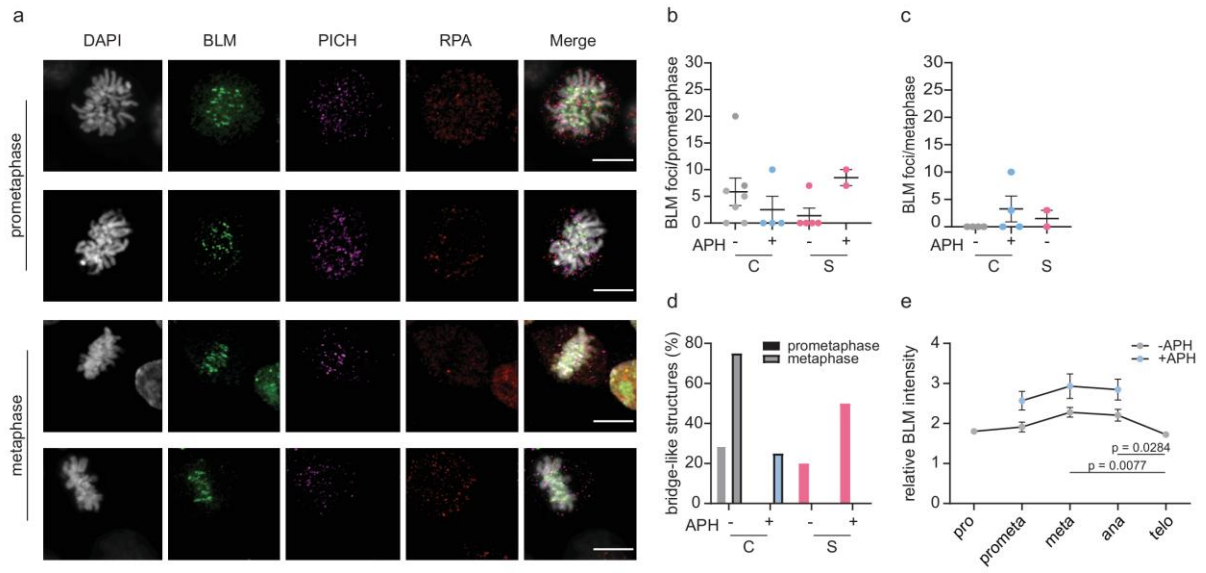

Figure 35|BLM localization dynamics during mitosis. a, Representative fluorescence images showing BLM-GFP localization in prometaphase and metaphase cells. BLM was detected via endogenous BLM-GFP fluorescence, PICH, RPA2 were visualized using specific antibodies, DNA was counterstained with DAPI. **b-c,** Quantification of the number of BLM foci per prometaphase (b) and metaphase (c). Data are mean ± S.E.M.; 5 images per condition were analyzed with 2-7 prometaphase and metaphase cells, one experiment. **d,** Quantification of mean percentage of mitotic cells displaying BLM-positive bridge-like structures at indicated conditions. Data are mean values; 5 images per condition were analyzed with 2-7 prometaphase and metaphase cells, one experiment. **e,** Relative BLM-GFP intensity across indicated mitotic phases, normalized to background. Data are mean ± S.E.M., statistical significance assessed by Student's t-test; 5 images per condition were analyzed with 2-7 prometaphase and metaphase cells, one experiment. Scale bars, 10 µm.

4.9.4 Loss of BLM increases early anaphases in the absence of mild replication stress

Although cells pass through anaphase in just about 4 min[239,240], this phase can still be further divided into early anaphase, characterized by the close association of condensed sister chromatids and the visible separation of chromosomes, and late anaphase, marked by two distinct DNA masses migrating toward opposite spindle poles as cells proceed towards telophase[125] (Fig. 36). Optical recognition of anaphase types was proved to be more efficient than measuring the distance between separating sister chromatids, as demonstrated by a comparison between an early anaphase cell with a larger distance of sister chromatid separation compared to a late anaphase cell positioned next to it (Fig. 36a). One reason might be that DNA masses of late anaphase cells are pulled back close to each other before abscission, as separating DNA masses of telophase cells were often found to be closely associated, in comparison to late anaphase cells (Fig. 36b, c).

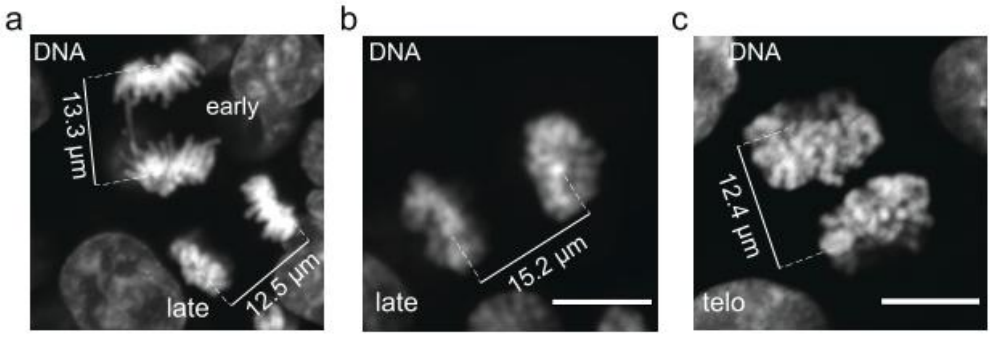

Figure 36|Distances of separating DNA masses in anaphase. a-c, Distance measurements between different anaphase cells by differentiating early **(a)** and late anaphase cells **(a, b)** and telophase cells **(c).** DNA was counterstained with DAPI. Scale bars, 10 µm.

Furthermore, cells in very early anaphase, characterized by closely associated DNA masses with no clear sister chromatid separation, as well as cells that were difficult to define, as they resemble anaphase due to separated DNA masses but were instead in telophase, late telophase/cytokinesis, or early G1 phase, were excluded from quantifications of mitotic aberrations in anaphase cells at 10.5 h post-release (Fig. 37a). The analysis of the frequency of early and late anaphase cells revealed that there were significantly more cells in late anaphase, consistent with previous findings[125] with an average difference of approximately 40%, suggesting that mitotic errors are potentially prolonging this phase until repair is completed (Fig. 37b, c). BLM depletion increased the frequency of early anaphase cells in the absence of mild replication stress, with a significant effect observed under S phase-specific depletion (Fig. 37b), whereby in the presence of mild replication stress, loss of BLM might rather increase the frequency of late anaphase cells. The absence of BLM during S phase may exacerbate DNA damage, resulting in delayed early anaphase progression as DNA repair proteins, potentially including BLM itself, are recruited to mitigate the damage.

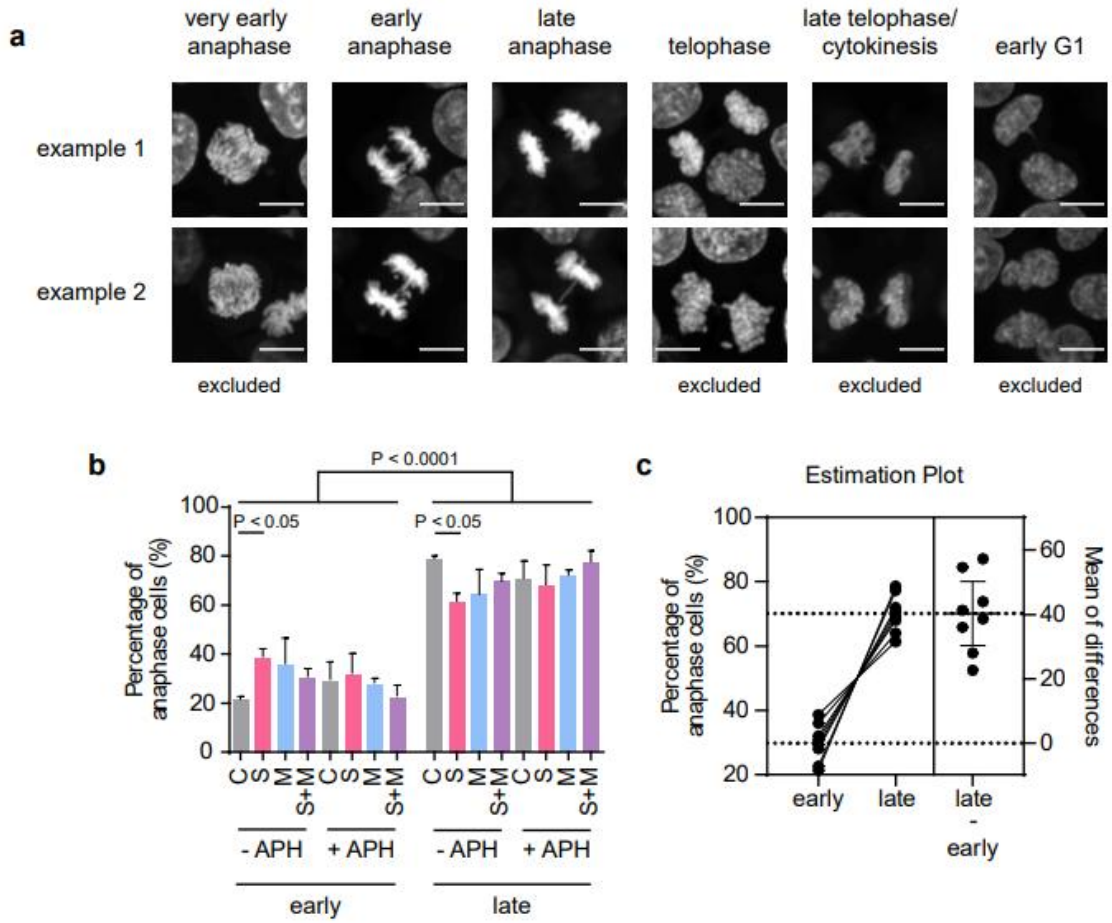

Figure 37| Loss of BLM during S phase increases the frequency of early anaphases in the absence of replication stress. a, Representative images of mitotic phases with separating DNA masses with exclusion of very early anaphase as well as telophase/cytokinesis and early G1 cells. DNA was counterstained with DAPI. **b,** Quantification of early and late anaphase cells in indicated conditions. Data represent mean ± S.E.M., statistical significance assessed by Student's t-test; 25 anaphases per replicate, 3 independent experiments. **c,** Estimation plot indicating the percentage of cells in early and late anaphase and the mean of difference between early and late anaphase cells. Data represent mean ± S.E.M., statistical significance assessed by Student's t-test; 25 anaphases per replicate, 3 independent experiments. Scale bars, 10 µm.

4.9.5 Loss of BLM function in mitosis increases lagging and misaligned chromosomes

To investigate the effects of BLM depletion on mitotic aberrations, lagging and misaligned chromosomes were analyzed in anaphase cells of BLM-AID/GFP cells, following BLM depletion at different cell cycle stages (Fig. 38). Both lagging and misaligned chromosomes that fail to be corrected before cell division frequently result in the formation of micronuclei and pose a risk of being mis-segregated into the wrong daughter cell which ultimately can contribute to chromosomal instability (CIN) and aneuploidy[59,241]. Previous studies have demonstrated that loss of BLM increases the frequency of lagging chromosomes[125], indicating potential chromosome mis-segregation during mitosis. Our data corroborate these findings, showing that in the absence of aphidicolin, approximately 20% of control cells exhibit lagging

and misaligned chromosomes, while there is a significant increase in BLM-depleted cells at any cell cycle stage, with more than 2-fold increase in S+M condition (Fig. 38b).

Additionally, mild replication stress induced by a low dose of aphidicolin alone increases this percentage almost 3-fold, consistent with previous reports linking replication perturbations to increased lagging chromatin[242]. Notably, BLM depletion exclusively in S-phase (S-only depletion) significantly increased lagging and misaligned chromosomes, even in the absence of aphidicolin, highlighting BLM's critical role in S-phase. Strikingly, and for the first time to our knowledge, we demonstrate that BLM depletion only in mitosis (M-only depletion) also leads to a significant increase in lagging and misaligned chromosomes, comparable to S-phase depletion (Fig. 38b). This suggests that BLM's mitotic function is equally crucial for ensuring proper chromosome segregation, reinforcing its dual role in both preventing replication stress-associated damage in S-phase and resolving abnormalities during mitosis. Interestingly, there is no significant difference between S-only depletion, M-only depletion, and S+M depletion in terms of lagging and misaligned chromosome formation. This suggests that the loss of BLM function during S and M phase may reach a saturation point that activates other repair pathways to compensate to some extent. This effect has been observed in the resolution of Holliday junctions, where resolvases such as GEN1, MUS81-EME1, and SLX1-SLX4 can act as a backup for the BTRR complex, whereby the depletion of these proteins also led to an increase of lagging chromosomes[139].

Notably, none of the BLM depletion conditions under unstressed conditions resulted in lagging and misaligned chromosome frequencies as high as those seen in aphidicolin-treated control cells (fig. 38b). Upon aphidicolin treatment, BLM depletion significantly increased lagging and misaligned chromosomes at M-only and S+M conditions compared to their non-aphidicolin-treated counterparts, though not beyond the level induced by aphidicolin alone in control cells. These findings suggest that BLM alone may not play a central role in preventing or resolving lagging and misaligned chromosomes, which aligns with the notion that such defects primarily arise from spindle assembly errors at the onset of mitosis[51], a stage during which BLM is largely absent as discussed in chapter 4.9.3. Still, the contribution of BLM remains critical, particularly under mild replication stress, as evidenced by a significant and approximately 20 % higher frequency of anaphases with lagging and misaligned chromosomes in BLM-depletion conditions in the presence of aphidicolin compared to their non-aphidicolin-treated counterparts.

Generally, it is important to note that this analysis only quantifies the percentage of anaphases with at least one lagging or misaligned chromosome. As shown in representative images, the number of lagging and misaligned chromosomes per cell appeared higher in aphidicolin-treated and BLM-depleted cells compared to control cells, but due to high variability in abnormal anaphases, it was not feasible to reliably count all individual laggards (Fig. 38a). Interestingly, the frequency of lagging and misaligned chromosomes in late anaphase slightly but not significantly increased under BLM depletion, particularly in the presence of aphidicolin. This observation is consistent with findings described in Chapter 4.9.4, supporting the notion that loss of BLM in the presence of APH might contribute to delayed progression through late anaphase (Fig. 38c). In addition, UFBs were occasionally observed connecting lagging or misaligned chromosomes to the main DNA mass, with an overall frequency of approximately 40% across all experimental conditions. Notably, this frequency was elevated, even though not significantly, in S+M depletion combined with aphidicolin, suggesting enhanced persistence of UFBs and/or lagging chromosomes. This may reflect accumulated DNA damage that BLM normally helps process (Fig. 38d).

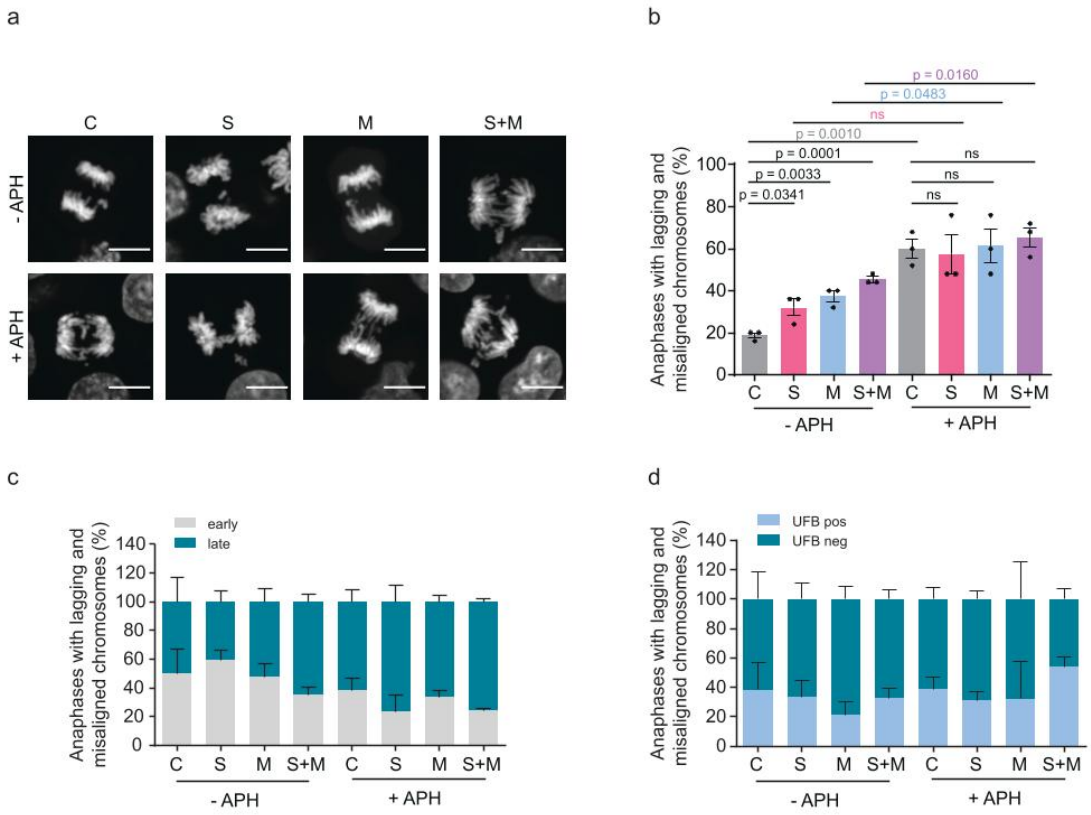

Figure 38|BLM depletion increases lagging and misaligned chromosome formation. a, Representative images of lagging and misaligned chromosomes at different mitotic stages. DNA was counterstained with DAPI. **b,** Quantification of the percentage of anaphase cells with lagging and misaligned chromosomes. Data represent mean ± S.E.M., 25 anaphases per replicate, 3 independent experiments. **c**, Quantification of the percentage of early and late anaphase cells with lagging and misaligned chromosomes. **d,** Quantification of the percentage of anaphase cells with lagging and misaligned chromosomes showing positive or negative co-staining with UFB markers (BLM, PICH or RPA2). Data represent mean ± S.E.M., statistical significance assessed by Student's t-test, 25 anaphases per replicate, 3 independent experiments. Scale bars, 10 μm.

4.9.6 Loss of BLM function in mitosis leads to increased chromatin bridges

In addition to lagging and misaligned chromosomes, DAPI-positive chromatin bridges were analyzed in anaphase cells of homozygous BLM-AID/GFP cells, following BLM depletion at different cell cycle stages (Fig. 39). DAPI-positive chromatin bridges were detected across various mitotic stages, even occasionally in early G1, where they persisted between daughter nuclei. However, as described in Chapter 4.9.4, the quantitative analysis focused only on anaphase cells (Fig. 39a). Comparing the frequency of early versus late anaphases with chromatin bridges revealed that the distribution was relatively consistent across conditions in the absence of aphidicolin, approximately 40% early and 60% late, although S+M depletion showed a higher proportion of late anaphase cells (Fig. 39b). Notably, BLM depletion under aphidicolin-induced mild replication stress further exacerbated bridge formation in late anaphase, particularly in M-only and S+M depletion conditions. This pronounced increase in late anaphase cells with chromatin bridges suggests that the loss of mitotic BLM impairs proper resolution of chromatin entanglements, further supporting the idea of delayed late anaphase progression in the absence of BLM, particularly under replication stress.

Previous studies showed that loss of BLM leads to an increased frequency of anaphases with chromatin bridges[125]. Similarly, S+M phase depletion of BLM resulted in a significant increase in anaphases with chromatin bridges (Fig. 39c, d). Interestingly, BLM depletion only during S-phase or M-phase alone did not induce a significant increase in chromatin bridges. This suggests that the presence of BLM in either phase is sufficient to prevent increased chromatin bridges. Furthermore, control cells did not show a significant increase in chromatin bridges upon aphidicolin treatment compared to untreated conditions, aligning with previous findings with 200 nM and 400 nM APH[242]. This suggests that the presence of BLM is sufficient to counteract replication stress-induced chromatin bridge formation. Strikingly, the induction of mild replication stress combined with BLM depletion, regardless of the specific cell cycle phase, led to a marked increase in anaphases with chromatin bridges and significantly elevated the number of chromatin bridges per anaphase compared to aphidicolin-treated control cells (Fig. 39d-f). Remarkably, there was no significant difference in chromatin bridge formation whether BLM was depleted only in S-phase or only in M-phase, reinforcing again its dual role in both preventing replication-associated damage in S-phase and resolving chromosome entanglements during mitosis.

In the absence of aphidicolin, S+M depletion led to an increase in anaphase cells exhibiting two or more chromatin bridges per cell (Fig. 39f). However, following aphidicolin treatment, a marked increase in anaphase cells with more than 2 chromatin bridges was observed, particularly M-only depletion condition. The proportion of chromatin bridges concurrently stained positive for the UFB marker proteins PICH, RPA2, and BLM remained consistently high at approximately 70% across all experimental conditions (Fig. 39g). This observation aligns with prior findings[125] and supports the notion of frequent co-occurrence of UFBs and chromatin bridges. A modest reduction in this co-localization was noted in BLM-depleted cells both with or without aphidicolin. Notably, under conditions of mild replication stress, there was an elevated frequency of chromatin bridges associated with UFBs compared to the aphidicolin-treated control, indicating prolonged persistence of UFBs when BLM is absent. However, neither BLM depletion nor aphidicolin treatment alone resulted in a global increase in the overall incidence of chromatin bridges co-localizing with UFBs.

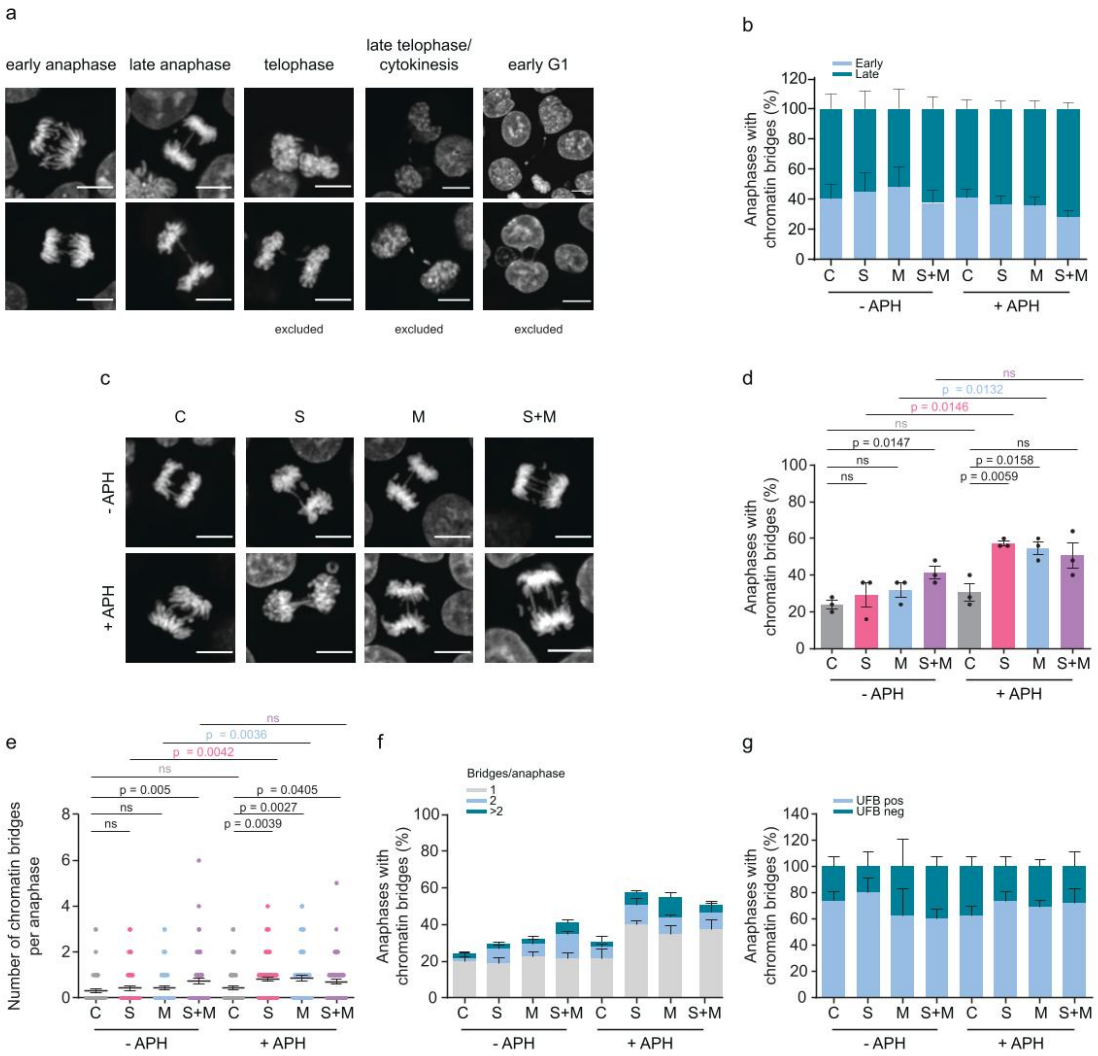

Figure 39|Mitotic BLM depletion increases chromatin bridge formation. a, Representative images of chromatin bridges at different mitotic stages. Only anaphase cells were included in the analysis. DNA was counterstained with DAPI. **b,** Quantification of early and late anaphase cells with chromatin bridges. Data represent mean ± S.E.M., 25 anaphases per replicate, 3 independent experiments. **c**, Representative images of chromatin bridges under different BLM depletion conditions. DNA was counterstained with DAPI. **d-g,** Quantification of the percentage of anaphase cells with chromatin bridges **(d)**, the number of chromatin bridges per anaphase cell **(e)**, the distribution of anaphase cells with 1, 2, or more than 2 chromatin bridges under each condition **(f)** and the percentage of anaphase cells with chromatin bridges showing positive or negative co-staining with UFB markers (BLM, PICH or RPA2) **(g)**. Data represent mean ± S.E.M., statistical significance assessed by Student's t-test, 25 anaphases per replicate, 3 independent experiments. Scale bars, 10 µm.

4.9.7 Loss of BLM function in mitosis increases PICH-UFBs and RPA-UFBs

Next, the frequency of anaphases with PICH-positive UFBs was analyzed (Fig. 40). Control cells treated with aphidicolin did not exhibit a significant increase in PICH-positive UFBs, consistent with previous studies[127] (Fig. 40a, b). This finding aligns with the idea that BLM plays a crucial role in both suppressing and resolving UFBs. In the absence of aphidicolin, BLM depletion did not significantly increase the number of anaphases with at least one PICH-positive UFB, regardless of the cell cycle phase in which BLM was depleted, consistent with

previous findings[125], but led to a significant increase in the number of PICH-UFBs per anaphase cell in S+M depletion condition (Fig. 40b, c). Upon replication stress, there is a significant increase in both the frequency of anaphase cells containing at least one PICH-positive UFB and the average number of PICH-UFBs per cell, regardless of the specific cell cycle phase during which BLM is depleted, compared to the control. Notably, BLM depletion restricted to mitosis was sufficient to increase PICH-UFB levels comparable to those observed with S-phase depletion. To our knowledge, this is the first evidence demonstrating that BLM functions exclusively during mitosis are important for reducing PICH-UFBs, suggesting BLM is involved in active UFB resolution and genome maintenance independently of its function in S phase. Strikingly, under replication stress, the average number of PICH-UFBs per cell was even higher in the M-only depletion condition than in S-only or combined S+M depletion conditions (Fig. 40c). Furthermore, while S-only depletion causes a modest increase in the number of PICH-UFBs, the more pronounced effect in M-only and S+M conditions suggests that BLM's mitotic function is not only essential for the resolution of PICH-UFBs, but may be even more critical than its role in preventing their formation.

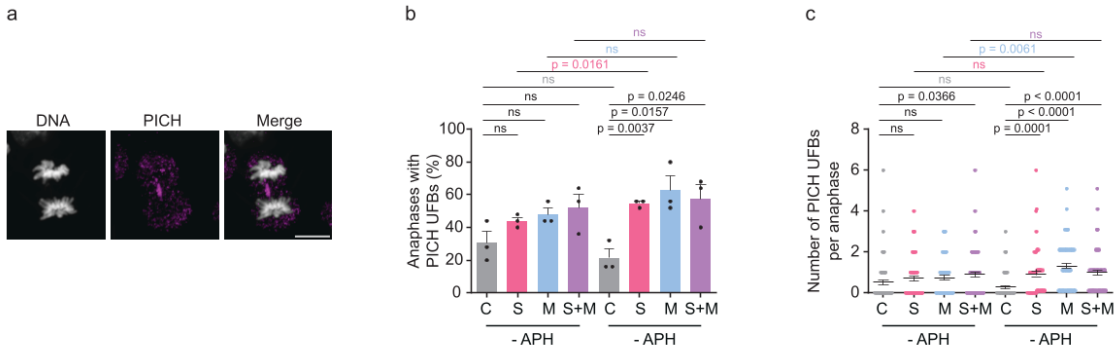

Figure 40|Mitotic BLM depletion increases PICH-UFB formation. a, Representative fluorescence image of PICH-positive UFB. PICH was visualized using a specific antibody, DNA was counterstained with DAPI. **b,** Quantification of the percentage of anaphases with at least one PICH-UFB. Data represent mean ± S.E.M., statistical significance assessed by Student's t-test, 25 anaphases per replicate, 3 independent experiments. **c,** Quantification of the number of PICH-positive UFBs per anaphase cell. Data represent mean ± S.E.M., 25 anaphases per replicate, 3 independent experiments, statistical significance assessed by Student's t-test. Scale bar, 10 µm.

Further, the frequency of anaphases with RPA-UFBs was analyzed (Fig. 41a-c). In the absence of aphidicolin, there was no significant change in either the percentage of anaphases exhibiting RPA-positive UFBs or the number of RPA-positive UFBs per cell (Fig. 41b, c). A modest reduction was observed specifically in the M-only and S+M depletion conditions, supporting the model that BLM mediates the formation of RPA-coated ssDNA at UFBs during mitosis[117]. Surprisingly, upon induction of replication stress, a significant increase in the percentage of anaphases containing RPA-positive UFBs was observed in the S+M BLM-depletion condition (Fig. 41b). Moreover, the number of RPA-positive UFBs per anaphase increased significantly under all BLM-depletion conditions compared to control cells in the presence of aphidicolin, with the most pronounced effect seen in the S+M condition (Fig. 41c). This increase did not occur in control cells exposed to mild replication stress, in agreement with previous findings demonstrating slightly elevated RPA-positive UFB formation only with 200 nM aphidicolin[117]. The observed variability among samples further supports the

hypothesis that RPA-positive UFBs are heterogeneous in origin, with only a subset being dependent on BLM.

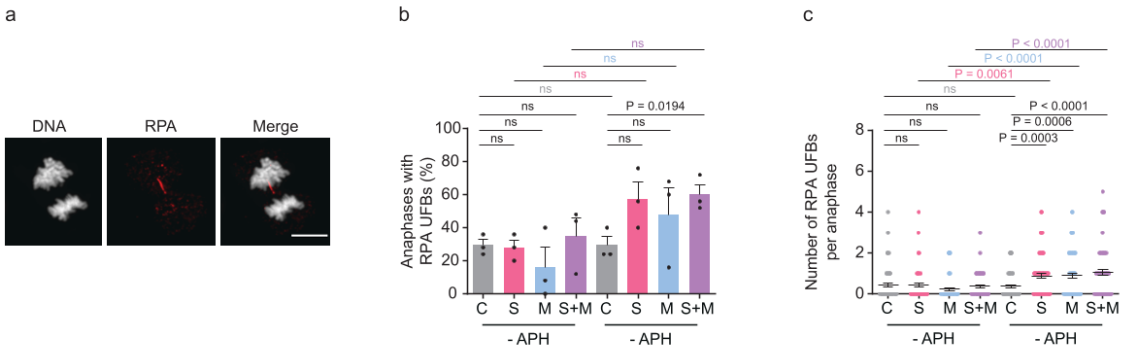

Figure 41|Loss of mitotic BLM is increasing RPA-UFBs. a, Representative fluorescence image of RPA-positive UFB. RPA2 was visualized using a specific antibody, DNA was counterstained with DAPI. **b,** Quantification of the percentage of anaphases with at least one RPA-UFB. Data represent mean ± S.E.M., statistical significance assessed by Student's t-test, 25 anaphases per replicate, 3 independent experiments. **c,** Quantification of the number of RPA-positive UFBs per anaphase cell. Data represent mean ± S.E.M., 25 anaphases per replicate, 3 independent experiments, statistical significance assessed by Student's t-test. Scale bar, 10 µm.

Next, the distribution of BLM-, PICH-, and RPA-positive UFBs was assessed under various conditions (Fig. 42a-c). BLM-positive UFBs were observed in approximately 80% of total UFBs in control cells, irrespective of aphidicolin treatment, underscoring the critical role of BLM in UFB processing (Fig. 42b). Upon APH treatment, the proportion of BLM-only UFBs increased, whereas UFBs co-stained with BLM and PICH decreased. Interestingly, this trend was reversed in S-phase-specific BLM-depleted cells, where BLM+PICH UFBs increased upon APH treatment. Although BLM+RPA UFBs were the least abundant overall, they exhibited a modest increase following APH treatment in both control and S-only depleted conditions. UFBs triple-positive for BLM, PICH, and RPA were most prevalent in unperturbed control cells, but were significantly reduced in S-only depleted and APH-treated cells. In contrast, RPA-only UFBs slightly increased in S-only depleted cells. These observations are consistent with previous findings showing that early anaphase UFBs are typically marked by PICH, BLM and RPA, whereas late anaphase or telophase UFBs are often exclusively RPA-coated, reflecting persistent unresolved DNA intermediates[117]. Together, these results support the notion that BLM, PICH, and RPA contribute dynamically to UFB recognition and processing at different stages of mitosis.

PICH-only UFBs, which were rare in control cells regardless of aphidicolin treatment, slightly increased in S-only conditions without aphidicolin as well as in M-only and S+M conditions with aphidicolin, but became the predominant UFB subtype in M-only and S+M BLM-depleted cells in the absence of aphidicolin (Fig. 42b). This is consistent with previous findings suggesting that particularly C-UFB resolution can also occur via a BLM-independent but RIF1- and TOP2A-dependent mechanism that involves decatenation without RPA recruitment, although PICH remains present[158], suggesting that RPA coating is not a hallmark of this subtype[156].

RPA-only UFBs primarily arise under BLM-depletion and aphidicolin treatment, while under S+M depletion combined with APH treatment, RPA-only UFBs became the most frequent,

followed by PICH-only and PICH+RPA UFBs (Fig. 42b). Notably, PICH+RPA UFBs were mostly absent in BLM-proficient cells, yet showed a marked increase upon BLM depletion. These UFBs are likely FS-UFBs, arising from under-replicated DNA regions that persist from S-phase into mitosis and recruit RPA independently of BLM. This interpretation aligns with previous findings showing that FANCD2 foci, often enclosing RPA-coated structures, originate during S-phase and later manifest as FS-UFBs during mitosis[127].

Furthermore, analysis of the distribution of anaphases containing 1, 2, or more than 2 of any type of UFB revealed a marked increase in the number of cells exhibiting 2 or more UFBs per anaphase, particularly under conditions of mild replication stress when BLM was depleted during mitosis (Fig. 42c). These findings highlight the critical role of BLM during mitosis in limiting the accumulation of UFBs and maintaining genome stability.

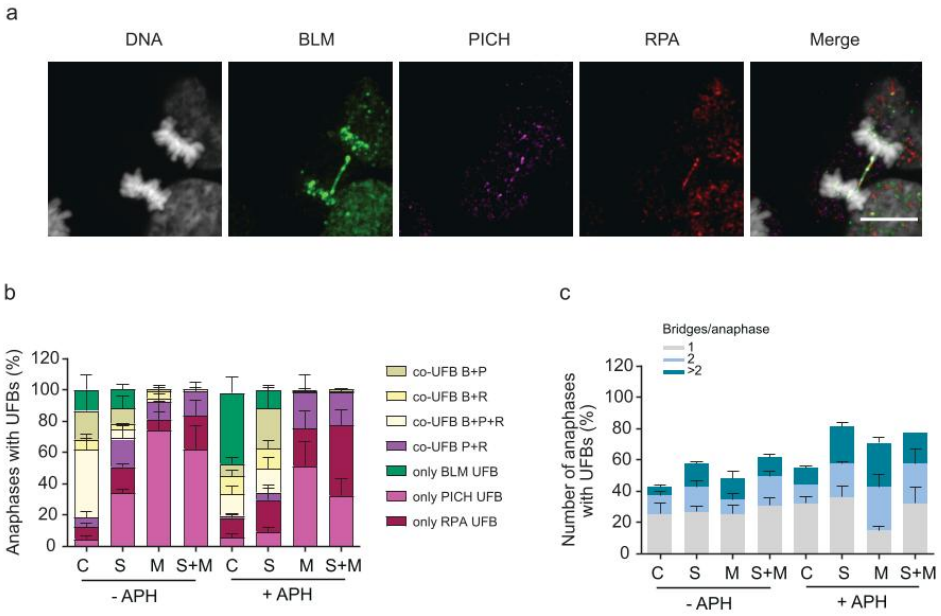

Figure 42|Loss of BLM in mitosis increases PICH-only and RPA-only UFBs. a, Representative fluorescence image of an anaphase with a UFB positive for BLM, PICH and RPA. BLM was detected by endogenous BLM/GFP fluorescence, PICH and RPA2 were detected using specific antibodies, DNA was counterstained with DAPI. **b,** Quantification of the percentage of anaphase cells with UFBs stained with BLM, PICH or RPA2. Data represent mean ± S.E.M., statistical significance assessed by Student's t-test, 25 anaphases per replicate, 3 independent experiments. **c,** Quantification of the distribution of anaphase cells with 1, 2, or more than 2 UFBs under each condition. Data represent mean ± S.E.M., statistical significance assessed by Student's t-test, 25 anaphases per replicate, 3 independent experiments. Scale bar, 10 μm.

4.9.8 Loss of BLM in mitosis leads to chromosome fragility

In addition to unresolved mitotic aberrations, such as lagging and misaligned chromosomes, chromatin bridges, and UFBs, which can contribute to chromosome mis-segregation and genomic instability observed in BS patients, CFSs might represent a major source of chromosomal instability and tumorigenesis[127]. These loci are inherently difficult to replicate and are particularly sensitive to replication stress, such as that induced by aphidicolin,

resulting in chromosomal breaks and gaps[28]. To assess the impact of BLM depletion on mitotic chromosome instability, chromosome breaks and gaps were quantified in metaphase spreads of BLM-AID/GFP cells following BLM depletion at distinct cell cycle stages (Fig. 43a, b). In the absence of aphidicolin, BLM loss led to an increased proportion of metaphases exhibiting chromosomal breaks and gaps across all depletion conditions compared to control, indicating a general role of BLM in preserving genome integrity (Fig. 43b).

As shown in previous studies, treatment with aphidicolin alone in control cells induced a ~3.5-fold increase in chromosomal aberrations[242] (Fig. 43b)). Strikingly, under aphidicolin-induced replication stress, M-only and S+M depletion of BLM resulted in a significant increase in metaphase breaks and gaps compared to their respective non-aphidicolin-treated counterparts. However, the extent of damage observed in these BLM-depleted, aphidicolin-treated conditions did not reach the levels seen in control cells treated with aphidicolin alone, implying the involvement of additional factors in suppressing CFS-associated chromosomal instability. Notably, the elevated levels of breaks and gaps after BLM depletion during mitosis, when replication should be completed, support the hypothesis that BLM participates in the resolution of late replication intermediates at CFSs during mitosis. Unexpectedly, S-only BLM depletion led to a significant increase in breaks and gaps in the absence of aphidicolin, but paradoxically resulted in a significant reduction of these aberrations in the presence of aphidicolin compared to aphidicolin-treated control. These results may indicate that BLM activity during S-phase contributes to preventing CFS expression under normal conditions, but under replication stress, compensatory mechanisms may be activated in the absence of BLM during S and G2 phases. In contrast, BLM loss during mitosis or throughout the cell cycle may compromise chromosome integrity to an extent that surpasses the capacity of compensatory pathways to resolve replication-associated damage.

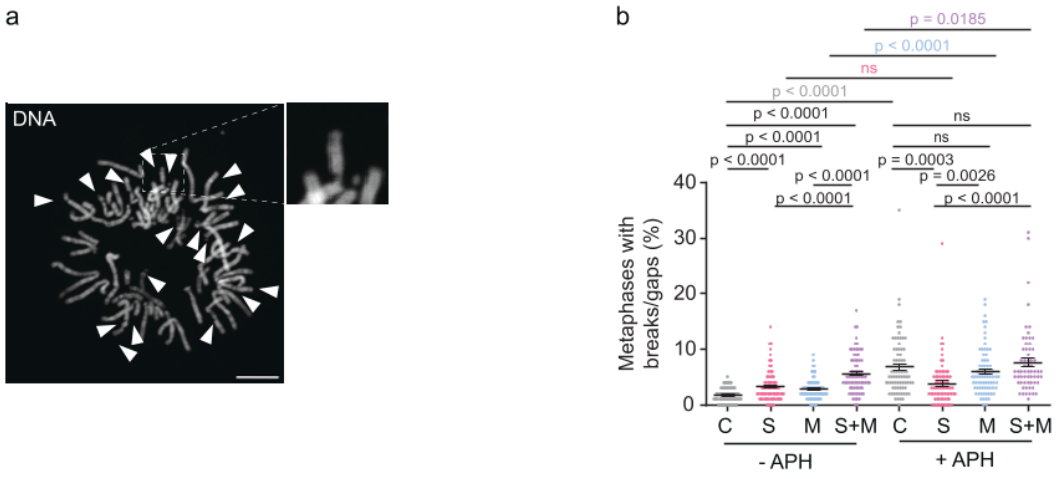

Figure 43|Loss of BLM in mitosis leads to metaphase gaps and breaks. a, Representative image showing a metaphase spread. Arrows indicate gaps and breaks. Zoom-in shows a chromosome arm with breaks/gaps. DNA was counterstained with DAPI. **b,** Quantification of the percentage of metaphases with breaks/gaps. Data represent mean ± S.E.M., statistical significance assessed by Student's t-test, 25 metaphases per replicate, 3 independent experiments. Scale bar, 10 µm.

4.9.9 Loss of functional BLM during mitosis leads to increased micronuclei formation

The accumulation of mitotic aberrations such as lagging and misaligned chromosomes, unresolved chromatin bridges, and UFBs can contribute to DNA breakage, potentially leading to DNA damage and chromosome mis-segregation in the following G1 phase.

To assess the impact of BLM function at distinct cell cycle phases on micronuclei formation, synchronized BLM-AID/GFP cells were analyzed at 15 h post-release following auxin-induced degradation of BLM at different cell cycle phases (Fig. 44). Consistent with previous studies, treatment with low-dose aphidicolin induced approximately a 2-fold increase in micronuclei formation compared to untreated controls[242,243] (Fig. 44b). Notably, S-only depletion of BLM did not result in a significant increase in micronuclei formation, regardless of aphidicolin treatment. This observation suggests that BLM activity during S-phase alone is not essential for preventing micronuclei formation, and correlates with the absence of a significant increase in lagging or misaligned chromosomes under these conditions (see Chapter 4.9.5). In contrast, BLM depletion restricted to mitosis (M-only) led to a significant increase in micronuclei formation both with and without aphidicolin treatment. Combined S- and M-phase (S+M) depletion resulted in the most pronounced effect, yielding a six- to sevenfold increase in micronuclei compared to untreated controls.

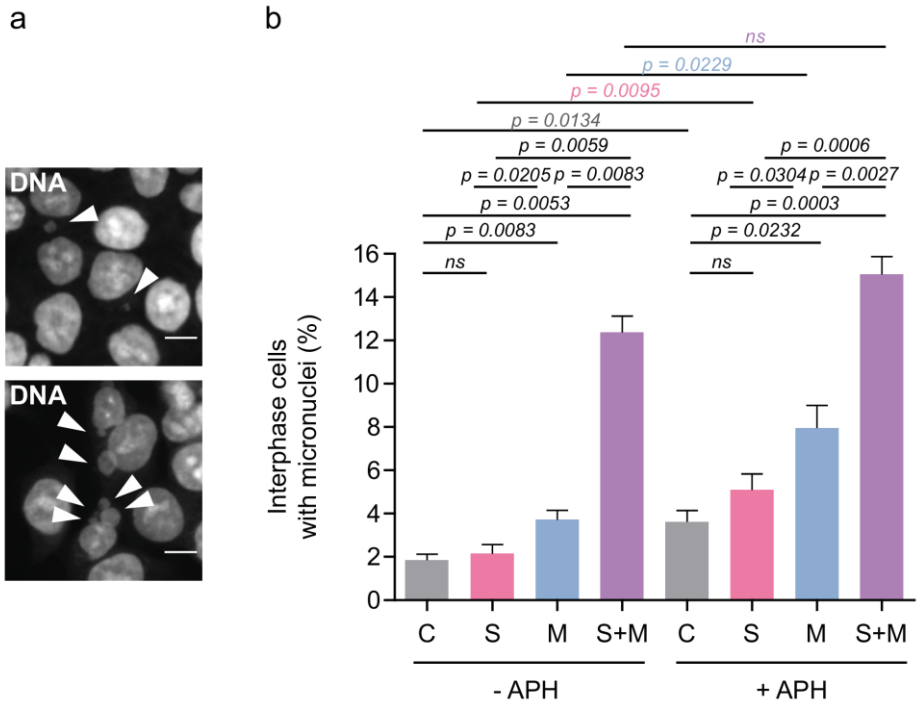

Figure 44|Loss of BLM in mitosis leads to increased micronuclei formation. a, Representative images showing micronuclei formation. Arrows are indicating micronuclei next to the daughter cell. DNA was counterstained with DAPI. **b,** Quantification of the percentage of interphase cells with micronuclei. Data represent mean ± S.E.M., statistical significance assessed by Student's t-test, ≥400 interphase cells per replicate, 3 independent experiments. Scale bars, 10 µm.

Interestingly, the extent of micronuclei formation was approximately threefold higher without and twofold higher with aphidicolin treatment, supporting the hypothesis that BLM plays a major role during mitosis in suppressing micronuclei formation. Nevertheless, BLM loss during

S-phase also contributes to micronuclei formation through alternative mechanisms, potentially via increased chromatin bridges and PICH-positive UFBs observed in anaphase, which may undergo breakage and contribute to chromosomal fragmentation. These fragments, along with metaphase breaks and gaps (see Chapters 4.9.6–4.9.8), may become encapsulated as micronuclei, further linking BLM function to genome integrity across cell cycle stages. Notably, all BLM depletion conditions exhibited a statistically significant increase in micronuclei formation compared to their respective non–aphidicolin-treated controls, underscoring the dual role of BLM in both S-phase and mitosis, with the most severe impact observed when BLM is depleted throughout the entire cell cycle.

4.9.10 Loss of functional BLM during mitosis leads to increased 53BP1 foci formation

To further investigate the phase-specific contribution of BLM to DNA damage repair, 53BP1 foci formation in the next G1 phase of homozygous BLM-AID/GFP cells following BLM depletion at different stages of the cell cycle was analyzed (Fig. 45). As expected, mild replication stress induced by aphidicolin treatment already significantly increased the number of 53BP1 foci per nucleus relative to untreated controls, consistent with previous findings[148]. In the absence of aphidicolin, S-only and S+M depletion of BLM resulted in a significant increase in 53BP1 foci per nucleus, particularly in cells exhibiting three or more foci, compared to untreated control cells, consistent with previous studies demonstrating that BLM depletion via siRNA leads to an increased number of cells harbouring more than three 53BP1 foci, indicative of elevated unrepaired DNA damage[148] (Fig. 45a, d). In the presence of aphidicolin, S-only and M-only depletion both led to an increase in the number of 53BP1 foci per nucleus, particularly to their non-aphidicolin-treated counterparts. However, only M-only depletion resulted in a statistically significant elevation in cells with 53BP1 foci, relative to aphidicolin-treated control cells, particularly with five or more 53BP1 foci (Fig. 45a, b, d, e). Interestingly, combined S+M depletion unexpectedly led to a significant reduction in the number of 53BP1 foci per cell and in the percentage of cells with more than ten 53BP1 foci under aphidicolin treatment (Fig. 45a, b). This reduction may reflect a delay in the cell cycle progression due to extensive DNA damage, potentially preventing severely damaged cells from entering or being captured in the subsequent G1 phase at the time of analysis, which was 15 h post-release.

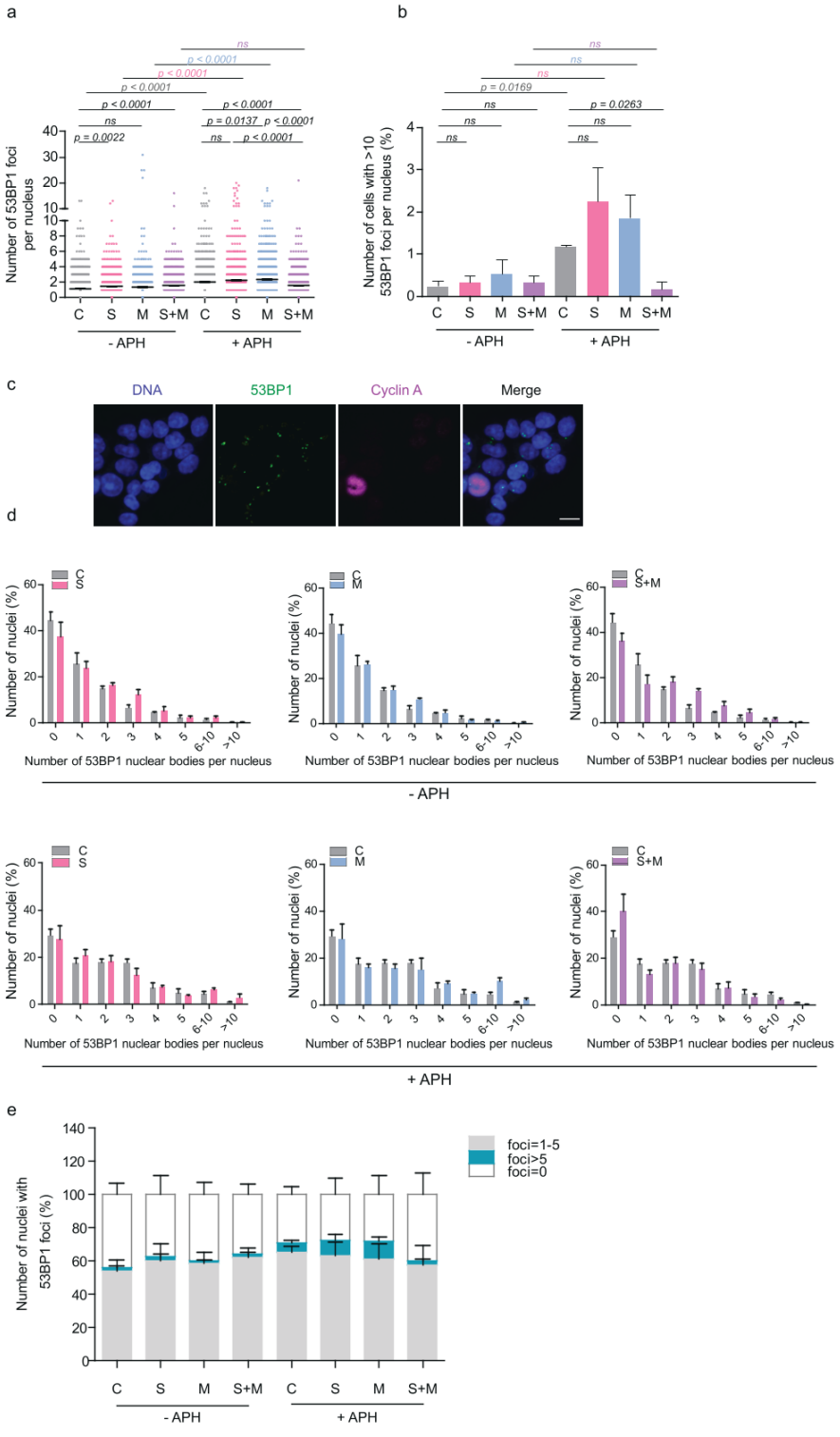

Figure 45|Loss of BLM in mitosis increases the number of 53BP1 foci. a, Number of 53BP1 foci per Cyclin A negative G1 nucleus. **b,** Percentage of cells displaying more than 10 53BP1 foci per Cyclin A negative G1 nucleus. **c,** Representative fluorescence image of 53BP1 foci formation in Cyclin A negative G1 cells. Cyclin A and 53BP1 were detected using specific antibodies, DNA was counterstained with DAPI. **d,** Percentage of interphase cells with different numbers of 53BP1 bodies per nucleus in comparison of each cell cycle phase-specific BLM depletion to its control (C). **e,** Percentage of nuclei with 53BP1 foci in comparison of 0, 1 to 5 or more than 5 53BP1 foci per nucleus. Data represent mean ± S.E.M., statistical significance assessed by Student's t-test, ≥200 interphase cells per replicate, 3 independent experiments. Scale bar, 10 μm.

4.9.11 Loss of functional BLM during mitosis leads to increased binucleated cell formation

To determine whether BLM depletion throughout the complete cell cycle alters cell cycle progression, the frequency of binucleated interphase cells, indicative of cytokinesis failure, was assessed (Fig. 46a, b). BLM depletion during S+M in the presence of aphidicolin resulted in a moderate increase in binucleated cells. In contrast, S-phase depletion alone led to a marked increase in binucleation both in the absence and presence of mild replication stress, suggesting a critical role for BLM during S phase in preventing cytokinesis failure, one that is not compensated by its function in mitosis. Notably, S+M depletion under replication stress did not reach the same level of binucleation observed with S-only depletion.

To explore whether mitotic arrest contributes to the observed differences in 53BP1 foci, the percentage of mitotic cells at 15 h post-release was analyzed (Fig. 46c, d). In the absence of aphidicolin, BLM depletion caused a modest increase in mitotic cells, with S-only depletion showing the strongest effect (~6-fold increase). Under replication stress, the frequency of mitotic cells was slightly increasing across all conditions. However, none of the BLM-depleted conditions showed a significant increase in mitotic cells compared to the control. Interestingly, S+M depletion resulted in the lowest frequency of mitotic cells, suggesting that mitotic arrest is unlikely to account for the reduced 53BP1 foci under these conditions.

To assess the possibility of G2 arrest contributing to this effect, Cyclin A-positive cells were quantified at T15 (Fig. 46e, f). S-phase BLM depletion led to a significant increase in Cyclin A-positive cells, both in the presence and absence of aphidicolin, indicating delayed G2 progression. In contrast, M-only and S+M depletion did not result in a significant increase in Cyclin A-positive populations, further suggesting that S+M depletion does not induce a substantial G2 arrest. To investigate whether the lower number of 53BP1 foci observed in S+M depletion was due to the presence of few but abnormally large foci, potentially reflecting clustered DNA lesions, cells were examined for very large 53BP1 foci (Fig. 46g). In the presence of aphidicolin, there was a significant increase in M-only and S+M depletion conditions with very large 53BP1 foci. However, no substantial increase in such foci was observed in the S+M condition compared to S- or M-only depletion. To verify effective BLM depletion across different cell cycle phases and to rule out inefficient protein degradation during S+M depletion, BLM foci were quantified in G1 phase cells (Fig. 46h). As expected, control cells showed low levels of BLM foci due to limited transcriptional activity during G1. Cells depleted of BLM in mitosis or during both S and M phases exhibited almost no detectable BLM foci. In contrast, S-only depletion led to elevated BLM foci levels, especially under aphidicolin treatment, likely due to increased DNA damage and compensatory recruitment of BLM. This may also relate to higher proportions of mitotic and Cyclin A-positive cells in S-only depletion, where BLM has not yet undergone degradation. Notably, even in aphidicolin-treated S-only depleted cells, elevated BLM foci were observed without corresponding increases in mitotic or Cyclin A-positive cells, suggesting acute damage-induced BLM recruitment independent of cell cycle status.

Finally, the colocalization of BLM and 53BP1 foci was assessed (Fig. 46i). In the absence of aphidicolin, BLM depletion led to a modest increase in overlapping foci, consistent with 53BP1-mediated recruitment of BLM to DNA lesions during late S phase. However, under mild replication stress, the overlap between BLM and 53BP1 foci was reduced in BLM-depleted cells compared to controls, potentially reflecting the absence of BLM-mediated recruitment to DNA lesions or altered cell cycle progression, the underlying mechanisms of which remain to be elucidated.

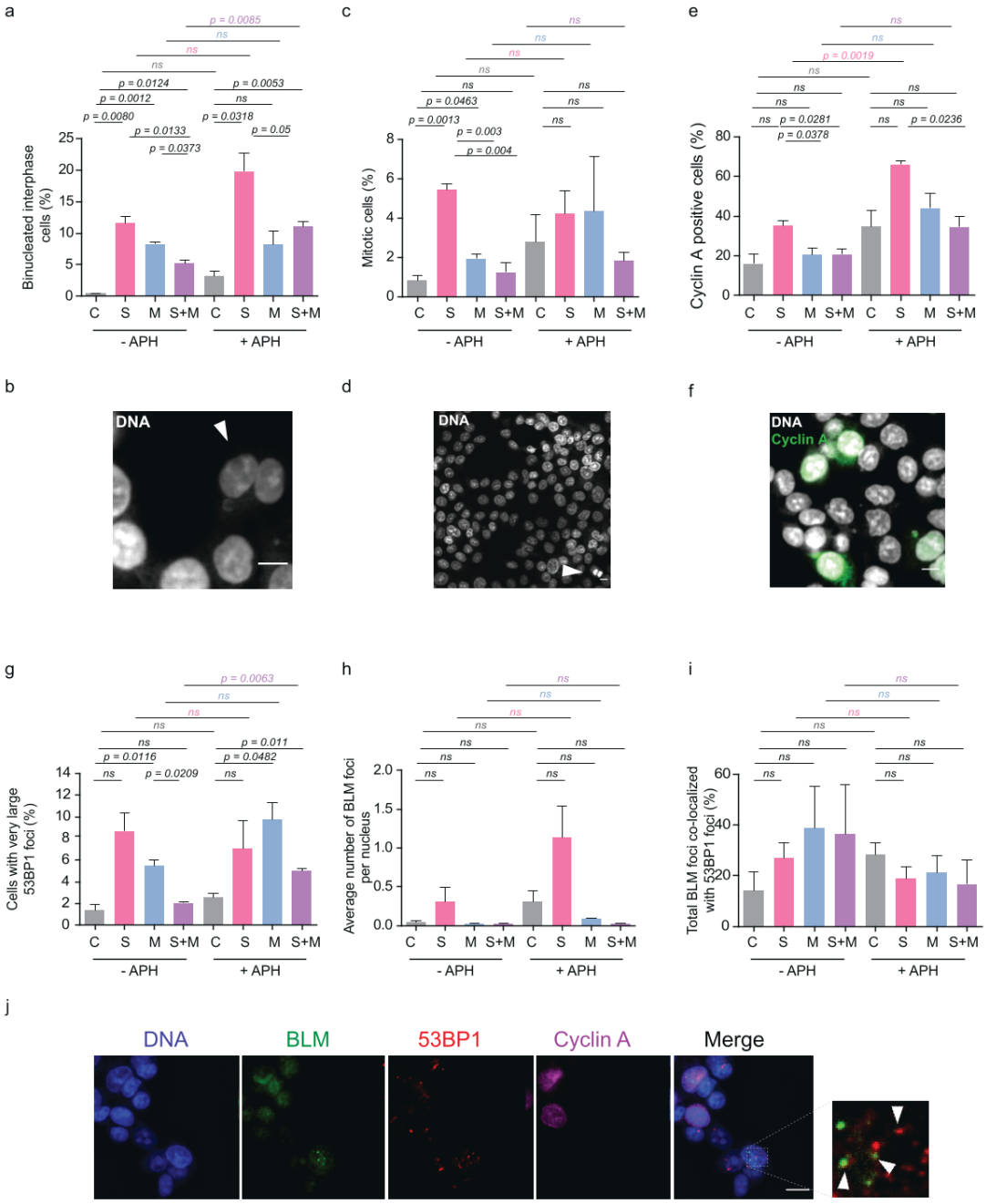

Figure 46|Loss of BLM in mitosis increases the frequency of binucleation. a, Percentage of binucleated interphase cells. **b**, Representative image of the formation of binucleated daughter interphase cells (white arrow). **c**, Percentage of mitotic cells. **d**, Representative image of a cell population at the following G1 phase displaying a fraction of mitotic cells (white arrow). **e**, Percentage of Cyclin A positive cells. **f**, Representative image of a cell population displaying a fraction of Cyclin A positive cells (green signal). **g**, Percentage of nuclei with very few (1 to 3) but extraordinarily big 53BP1 foci showing a circle as a fraction of accumulated 53BP1 cells. **h**, Average number of BLM foci in Cyclin A negative G1 cells. **i**, Percentage of 53BP1 foci overlapping with BLM foci. j, Representative image of BLM foci at cyclin A negative cells co-stained with 53BP1 or in very close proximity (indicated by white arrows). Data are mean ± s.e.m.; ≥200 interphase cells per replicate, 3 independent experiments. Scale bars, 10 μm.

4.10 Loss of BLM does not show increased chromosomal aberrations after one cell cycle

Analysis of mitotic aberrations and their consequences in the subsequent G1 phase revealed an increased frequency of MN formation, particularly when BLM was depleted for an entire cell cycle (Fig. 44). MN formation is known to increase the risk of chromosome breakage and fusion events, potentially triggering random shuffling of chromosomal fragments, hallmarks of chromothripsis and aneuploidy[57,115]. Notably, binucleation was observed upon BLM depletion, with the most pronounced increase occurring when BLM was specifically depleted during S phase (Fig. 46a). In this condition, the frequency of binucleation rose from approximately 11% (without aphidicolin, APH) to 18% (with APH), suggesting an elevated risk of aneuploidy if cells tolerate this form of whole-genome duplication.

To further assess genomic alterations, single-cell whole genome sequencing (scWGS) was conducted on cells subjected to BLM depletion either during mitosis (M-only) or during both S and M phases (S+M), 12 h post-release (Fig. 47a, b). At this time, more than 40% of untreated cells had entered G1, a trend also seen in auxin-treated cells (see Fig. 29e).

Surprisingly, while untreated cells with functional BLM displayed increased aneuploidy and genomic heterogeneity at 12 h post-release compared to time zero, cells depleted of BLM during mitosis or S+M phases did not show a comparable increase (Fig. 47c, d). However, increased genomic heterogeneity was observed specifically in S+M depleted cells relative to T0 controls (Fig. 47d). Intriguingly, structural variants were most abundant in untreated cells at T0, and their frequency declined when BLM was depleted from the G1/S boundary onward. This decline persisted through T12, although BLM-depleted cells still exhibited more structural variants at T12 compared to the untreated control at the same timepoint (Fig. 47e).

These observations suggest that cells, particularly those with severe chromosomal abnormalities, may not have reached the next G1 phase by 12 h post-release and were thus excluded from scWGS analysis, particularly at the relatively low number of cells analysed (Fig. 47b). This is supported by flow cytometry data showing that the majority of cells reach G1 around 15 h post-release, with G1 accumulation continuing even until 18 h post-release in the presence of APH and IAA (see Fig. 29e).

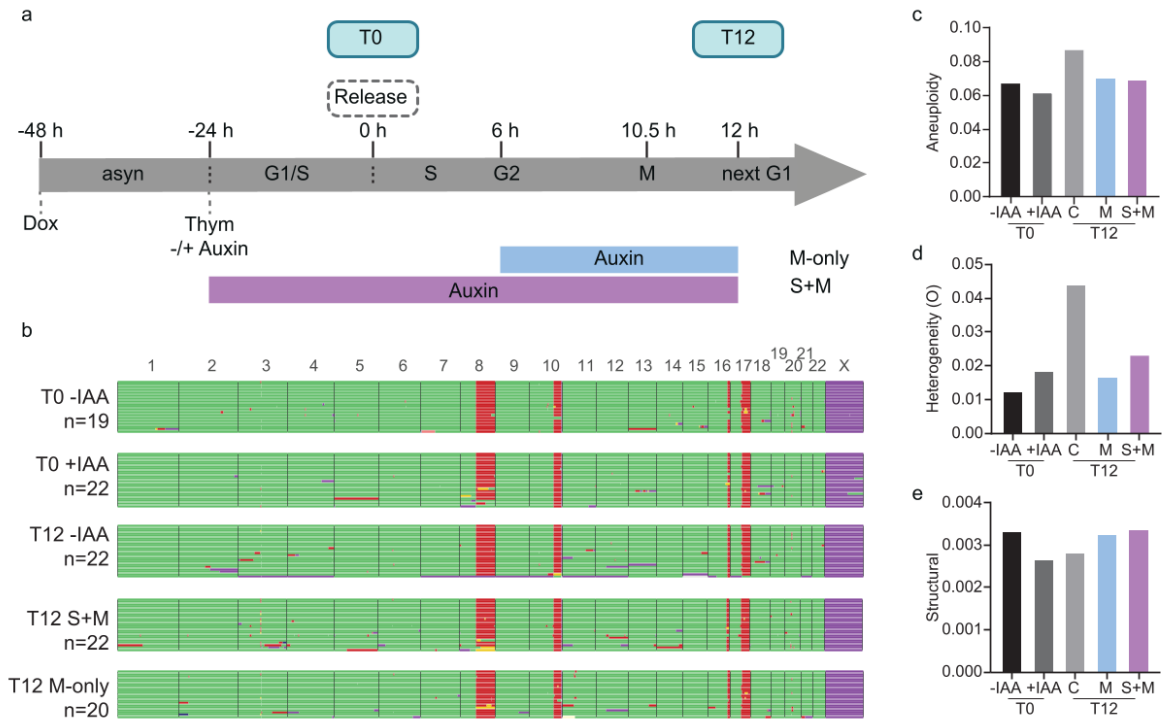

Figure 47|Single-cell whole genome sequencing following BLM depletion. a, Schematic illustrating the experimental design: homozygous BLM-AID/GFP cells were synchronized and collected either at 0 hours or 12 hours post-release for single-cell whole genome sequencing (scWGS). **b,** Heatmaps displaying chromosomal aberrations detected in individual cells. **c–e**, Quantification of genomic instability, including aneuploidy scores **(c)**, heterogeneity scores **(d)**, and structural variant scores, calculated as the average number of breakpoints per megabase **(e)** using the Aneufinder software. scWGS performance and subsequent Aneufinder analysis were conducted by Andrea Tijhuis and the laboratory of Prof. Floris Foijer, ERIBA, Groningen.

4.11 AID/GFP-tagging of BLM enables live-cell imaging

Fluorescent protein tagging offers a significant advantage, not only by facilitating detection via immunostaining techniques such as Western blotting or immunofluorescence, but also by enabling real-time monitoring of protein dynamics through live-cell imaging. While mitotic aberrations and subsequent G1 phase abnormalities in this study were assessed in fixed cells, live-cell imaging provides the opportunity to directly observe the fate of specific mitotic errors throughout several cell cycle phases.

In a first attempt of live-cell imaging, BLM-GFP signal was successfully detected in synchronized homozygous BLM-AID/GFP cells, which was performed from 8 h until 24 h post-release to analyse mitotic BLM functions (Fig. 48). While in the depicted cell the BLM-GFP level was initially detected at basal levels during metaphase, which started at around 10:05 h post-release, several BLM-positive UFBs became visible in early anaphase five minutes later, in line with previous studies observing a high rate of UFBs at the onset of anaphase even in unpertubed cells, before being resolved prior cell division[125]. At the established timepoint of 10.5 h post-release for anaphase cell analysis in this study, the analysed cell was in anaphase and showed a BLM-positive UFB (Fig. 48, top row, middle lane). Notably, discrete BLM-specific foci appeared at defined sites during anaphase, potentially marking DNA damage loci. The BLM-UFB detectable from 10:20 h post-release exhibited markedly increased signal

intensity compared to early anaphase UFBs, possibly representing newly formed UFB or increased recruitment of BLM to only a subset of UBs which might remain during late anaphase, and are representing increased DNA damage at these bridges (Fig. 48, white arrow). From approximately 10:30 h post-release, BLM no longer decorated the full length of the UFBs. Instead, the bridges became increasingly fragmented, leaving only a few BLM-rich remnants localized at the original UFB region. By the time cells progressed into interphase, no residual UFB structures were observed, suggesting complete resolution prior to cell division.

Interestingly, from around 10:25 h post-release, BLM- and DNA dye-positive fragments appeared to misalign from the main chromatin mass during mid-anaphase (Fig. 48, yellow arrow). These were not consistently observed, possibly due to temporary loss of focus during imaging. In the subsequent interphase, persistent BLM-positive DNA fragments were still detectable. This might indicate that these fragments are encapsulated by MN, raising the possibility that BLM remains associated with DNA in MN and may play a role in DNA repair within these structures. Further investigations are necessary to elucidate the full fate and function of mitotic BLM.

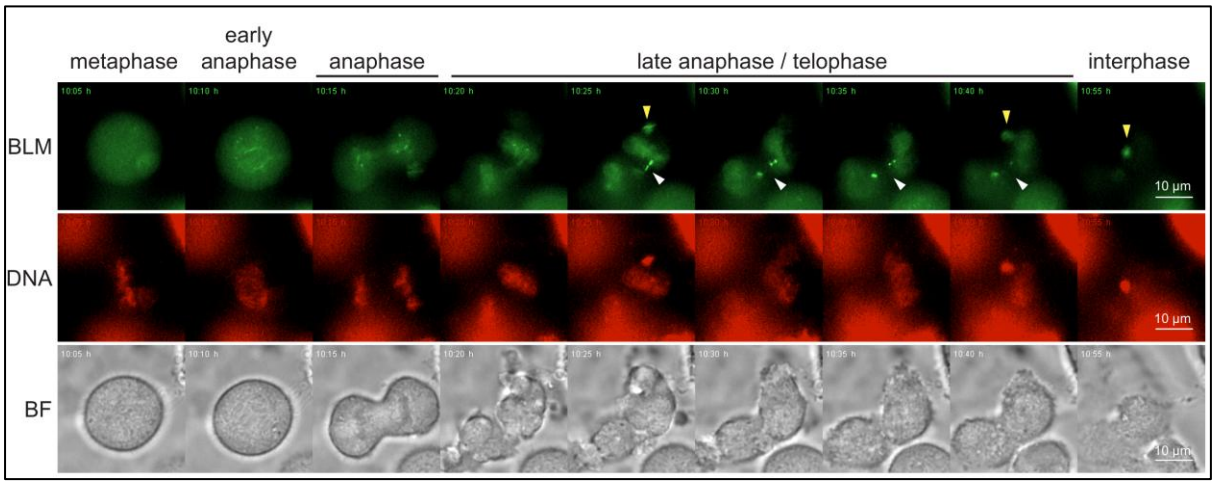

Figure 48|Live-cell imaging of BLM. Live-cell imaging of homozygous BLM-AID/GFP-tagged cells demonstrates successful visualization of the BLM-GFP signal. This system enables the study of ultrafine anaphase bridges (UFBs). A potential misaligned chromosome that may become encapsulated into a micronucleus during interphase is indicated by a yellow arrow, while BLM-associated UFBs are marked with white arrows. BLM was detected via endogenous BLM-GFP fluorescence, DNA was stained using NucSpot dye, and Bright field (BF) was used as cell surface visualization.

4.12 AID/GFP-tagging of BLM facilitates proteomic analysis of BLM interactors

While the AID/GFP tagging of homozygous BLM cells demonstrated a high potential for a variety of usage, evidenced by effective auxin-induced depletion (Fig. 23), detection of endogenous GFP signal for immunofluorescence (Fig. 32), and suitability for live-cell imaging

(Fig. 48), another key advantage of tagging a protein of interest is its application in affinity-based pulldown assays. This approach reduces costs of commercial antibodies, which can vary in consistency across experimental conditions. One of the objectives in generating these BLM-AID/GFP cell lines was to facilitate pulldown assays for interactome profiling. Proteomic analysis by mass spectrometry can utilized to identify novel UFB binding partners, such as from BLM, especially when cells are enriched in anaphase. Specifically, chromatin immunoprecipitation mass spectrometry (ChIP-MS) was chosen as a powerful technique for studying chromatin-bound protein complexes due to formaldehyde crosslinking[244,245].

Consistent with first attempts of ChIP-MS, using commercial antibodies to pull down BLM and FANCD2 (Fig. 49a, b), the use of GFP-Trap in BLM-AID/GFP cells successfully led to a strong enrichment of the bait BLM, along with a diverse set of associated proteins (Fig. 49c, e, f) . Many of these proteins were involved in DNA damage response and repair, RNA processing and RNA metabolism, and mitotic cell cycle regulation. Notably, several proteins, such as NONO, SFPQ, TRIM28, PARP1, and DDX39B, were frequently identified across independent ChIP-MS experiments and mostly were shared between the BLM-GFP and FANCD2 pulldown datasets (Fig. 49b-d). While NONO, DDX39B, and TRIM28 have been proposed to associate with PARP1[246–248], one of the earliest responders to DNA damage and initiators of DNA repair[249], several of these proteins, including NONO and DDX39B, are also implicated in RNA processing and R-loop regulation[246,247]. This suggests that BLM and FANCD2 may play roles in the recognition or resolution of R-loops, as supported by recent studies[184,250].

The comparison of the cells enriched at anaphase (10.5 h post-release) with cells enriched in S phase (6 h post-release) (Fig. 49e–g) revealed several proteins which were exclusively and strongly enriched during anaphase. These include APEX1, which is involved in BIR repair and telomere maintenance and is a component of the SET complex, along with TREX1[251–254], as well as ALYREF and U2AF1, which are involved in RNA export and splicing, respectively[255].

Interestingly, while FANCD2 pulldown confirmed its known heterodimeric partner FANCI, PICH was not detected in any pulldown and members of the BTRR complex were largely absent in BLM pulldowns. TOP3A was detected in only two instances (Fig. 49a, e), while RMI1 and RMI2 were never detected, suggesting that some interaction may be transient, cell cycle-dependent, or lost during the pulldown procedure. This further raises the possibility that BLM may act independently of the BTRR complex under certain conditions, particularly during anaphase. This is supported by previous studies, demonstrating that BLM-UFBs still form in TOP3A-deficient cells and TOP3A is associated at PICH-UFBs in BS cells[237]. To our knowledge, no BLM pulldown experiments using mass spectrometry have yet identified PICH[256]. While PICH immunoprecipitation followed by mass spectrometry has revealed the presence of BLM, it did not detect the components of the BTRR complex TOP3A, RMI1, or RMI2[155].

In summary, these results demonstrate that GFP-based pulldown of endogenously tagged BLM enables successful identification of known and potentially novel interaction partners. Comparative analyses with FANCD2 or BLM pulldowns across different cell cycle stages further enhance our understanding of protein networks involved in preventing mitotic aberrations and preserving genomic integrity.

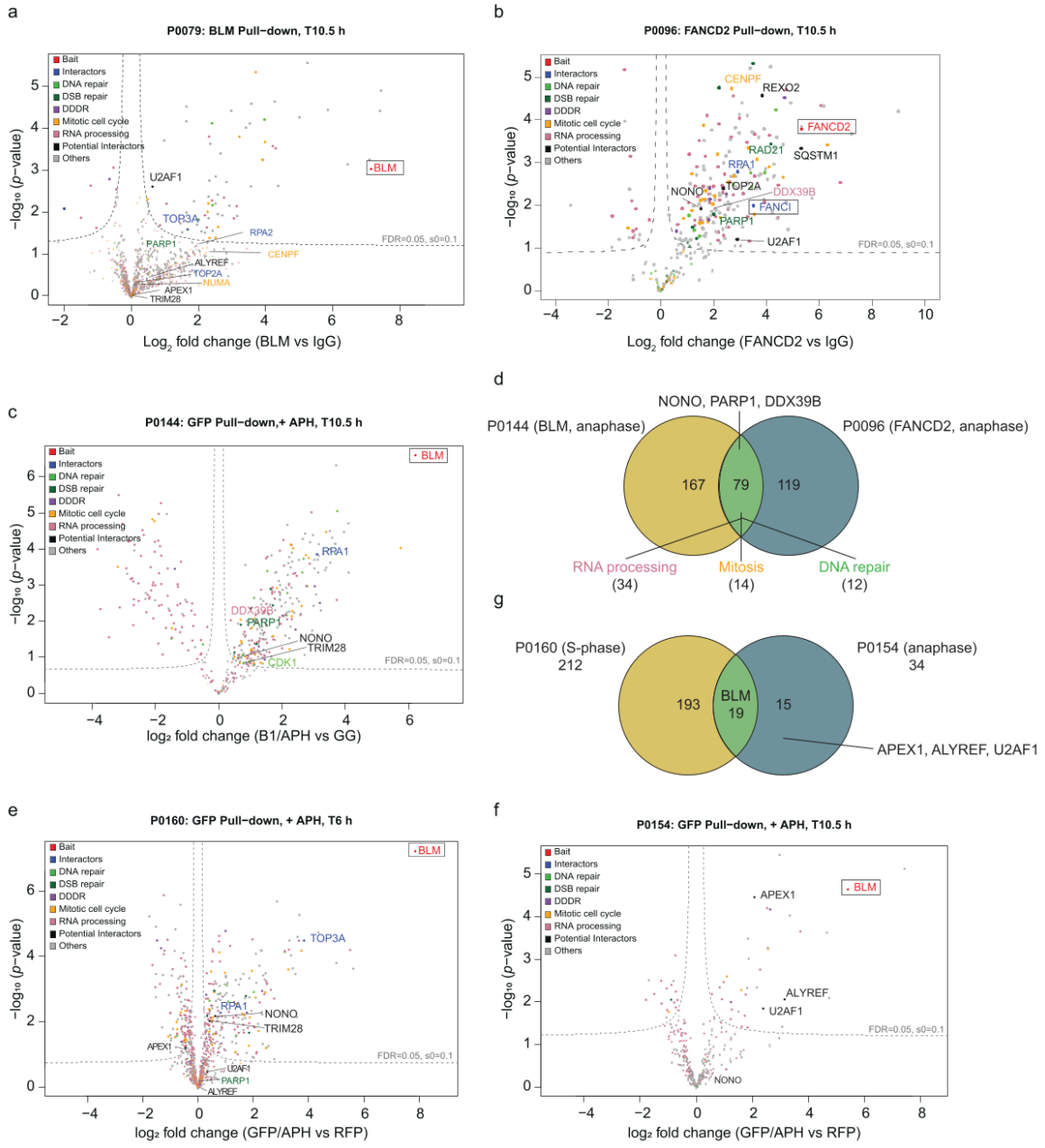

Figure 49|ChIP-MS Analysis of BLM and FANCD2 Interactomes. **a–b,** Chromatin immunoprecipitation followed by mass spectrometry (ChIP-MS) in synchronized HCT116 wild-type cells after 10.5 h post-release using commercial antibodies to pull down BLM (**a**) and FANCD2 (**b**). **c,** ChIP-MS of synchronized homozygous BLM-AID/GFP cells treated with 100 nM aphidicolin (APH), analyzed at 10.5 h post-release. GFP-tagged BLM was immunoprecipitated using a GFP-Trap. **d,** Venn diagram showing shared protein interactors between FANCD2 (**b**) and BLM (**c**) pull-downs, including NONO, TRIM28, PARP1, and DDX39B. **e–f,** ChIP-MS analysis of synchronized BLM-AID/GFP cells treated with 100 nM APH. Cells were harvested at 6 h (**e**, S-phase) and 10.5 h (**f**, anaphase) post-release. BLM was pulled down using GFP-Trap; RFP-Trap was used as a control. **g**, Venn diagram depicting proteins specifically enriched in the BLM pull-down during mitosis compared to S-phase, including APEX1, ALYREF, and U2AF1. ChIP-MS experiments and data acquisition were conducted together with Divya Reddy (**a, b**) and Farbod Mohseni (**c, e, f**).

5. Discussion

Genomic instability, broadly characterized by an elevated rate of genetic alterations across cell generations, is a fundamental feature of many cancers and contributes to tumor initiation, progression, and therapeutic resistance[84,257].

UFBs serve as key indicators and potentially mediators of unresolved DNA damage and genomic instability[125]. Although several proteins, such as PICH and BLM, have been identified to accumulate on UFBs, their precise hierarchy and functions often remain incompletely understood. Current research aims to deepen our understanding of the origin, classification, and resolution of UFBs, as new classes of UFBs continue to be described[117,125–129]. Further elucidation of the molecular machinery responsible for UFB resolution could uncover new targets for cancer therapy and provide new insights into the mechanisms that are essential to maintain genome stability.

5.1 The establishment of an auxin-inducible degradation system by an error-free modular cloning system

The development and refinement of gene editing technologies have revolutionized our ability to manipulate gene function and study protein dynamics in a highly controlled manner. Early genome engineering methods, such as zinc finger nucleases (ZFNs) and transcription activator-like effector nucleases (TALENs), although groundbreaking at their time, were often limited by technical complexity, low efficiency, and high costs[258–260]. The advent of the CRISPR/Cas9 system marked a transformative breakthrough in genome editing due to its simplicity, precision, and versatility. By guiding the Cas9 endonuclease to a specific genomic locus via a sgRNA, targeted DSBs can be introduced to facilitate site-specific genome modification[209].

In this study, CRISPR/Cas9 was harnessed to endogenously tag proteins of interest with both a minimal AID domain and a green fluorescent protein. This approach builds on the AID system originally characterized in plants and later adapted to mammalian cells, enabling rapid and reversible degradation of target proteins upon auxin addition[206–208]. This system was utilized for dissecting cell cycle–dependent functions of the BLM protein. In contrast to traditional RNAi-based knockdowns (e.g., siRNA or shRNA), which often result in incomplete depletion and off-target effects[261–264], the AID system provides a more acute and tuneable degradation mechanism[207]. However, challenges remain, including basal degradation in the absence of auxin and variability in degradation efficiency[206,265]. Improvements such as the AID2 system, which offers increased stability and reduced background degradation[265], were not applied in this study but remain promising for future work. Here, a dual cloning system was employed that integrates Gibson Assembly and Golden Gate Assembly (see Fig. 20). This modular and PCR-free strategy facilitates a rapid and highly efficient construction of tagging vectors with minimal cloning artifacts. Gibson Assembly was used to generate individual entry clones with specific overhangs, while Golden Gate Assembly facilitated the final combination of the AID tag, fluorescent marker, and an antibiotic resistance cassette into donor plasmids. This system provided the flexibility to rapidly generate constructs tailored to multiple gene targets with high fidelity with successful generation of entry vectors for *SMC5*, *BLM*, *PICH*, and *FANCD2* and

for the homology donors for *BLM* and *FANCD2* (Fig. 20b-j). The delivery of Cas9/sgRNA was provided by successfully generating RNP complexes as well as pX330 vectors for *BLM*, *PICH*, and *FANCD2* (Fig. 17-19). Despite theoretical advantages, co-transfection with two donor plasmids (each carrying a different resistance marker) and an RNP complex did not yield successful integration in this study. Instead, co-transfection of a single donor vector containing a hygromycin resistance cassette and a Cas9/sgRNA plasmid resulted in successful generation of heterozygous and homozygous BLM-tagged clones (Fig. 22). While RNP-based delivery of Cas9 has been shown to offer several advantages, including reduced off-target effects, higher editing precision, and greater suitability for hard-to-transfect cells[266,267], it did not yield successful integration in this study for the clones analyzed (Fig. 22b). This may be attributable to technical factors such as suboptimal delivery conditions.

Future efforts to generate degron-tagged cell lines for genes such as *SMC5*, *PICH*, and *FANCD2* may benefit from further optimization of RNP-mediated delivery or by applying the single-resistance vector strategy co-transfected with the pX330 plasmid that proved effective for BLM. Additionally, expanding the use of the dual selection approach, whereby one allele is targeted with a hygromycin resistance cassette and the other with neomycin, and screening a larger number of clones could enhance the efficiency of identifying biallelic integrations, as successfully demonstrated in previous studies[206]. An alternative strategy to efficiently screen for multiple clones without the need for long-term selection is fluorescence-activated cell sorting (FACS). This approach eliminates the need to insert large antibiotic resistance genes into the homology donor, which are often challenging to clone and limited in variety, an important advantage when aiming to analyze multiple tagged proteins within the same cell line. FACS has also been successfully used in this laboratory to isolate cells expressing AID/ fluorescent-tagged proteins (data not shown).

Overall, this study highlights the power and flexibility of combining CRISPR/Cas9-mediated genome editing with a modular cloning system to study cell cycle-specific functions of proteins in a temporally controlled manner.

5.2 New insights into the cell cycle-specific functions of BLM in maintaining genomic stability

The BLM helicase serves as a key genomic guardian through its diverse roles in DNA repair and genome maintenance. Its functions span a broad spectrum, including DNA end resection during HR, dissolution of recombination intermediates, restart of stalled replication forks, and the unwinding of problematic nucleic acid structures such as R-loops and G-quadruplexes. Additionally, BLM is associated with telomere fork progression and maintenance and is essential for resolving entangled chromosomes during mitosis, such as UFBs[161]. The wide-ranging nature of BLM's responsibilities highlights its central position in preserving genome integrity.

The BS disorder arises from biallelic mutations in the BLM gene and is characterized by a pronounced predisposition to early-onset cancers, with an average age of onset of about 30 years[196]. In line with the requirement for complete loss of BLM function in BS pathogenesis, our experiments using BLM-AID-tagged cell lines revealed that only cells with homozygous depletion of BLM displayed the characteristic increase in SCE (Fig. 24). Heterozygous clones, in contrast, maintained baseline SCE levels (Suppl. Fig. 1f). Nonetheless, some variability was

observed; one heterozygous cell line (B5) exhibited higher SCE rates under treated conditions compared to another (B6), though untreated data for B5 is lacking. This variability may reflect clonal differences or subtle impacts of reduced BLM dosage. Notably, while some studies report no evident phenotype in heterozygous BS carriers, others suggest that partial functional loss impairs repair capacity and increases tumorigenesis[197,268–270]. These model cell lines therefore provide a unique opportunity to assess whether partial BLM loss is sufficient to trigger the accumulation of DNA damage, senescence, or a cellular stress response under baseline or challenged conditions. Such experiments will reveal to what extent heterozygous mutations contribute to genome instability and altered cell fate.

BS has been associated with genomic instability, characterized by an elevated frequency of chromosomal breaks, translocations, and aberrant mitotic structures[193,197,204]. Although single-cell whole genome sequencing (scWGS) analysis of the BLM-depleted cell line did not reveal overt genomic alterations, this may reflect the non-lethal nature of acute BLM loss and the gradual buildup of DNA damage over time, in line with scWGS results in a PICH knockout cell line[271] (Fig. 47). Clinically, BS symptoms often worsen under stress conditions, such as UV exposure, suggesting that BLM-deficient cells struggle more when challenged[193]. Further, it has to be considered, that the analysis was performed at 12 h post-release which showed around 40-50% of cells reaching the next G1 phase while particularly under IAA or APH conditions, the peak of cells reaching the next G1 peaks to around 70% at 15-18 h post-release (Fig. 29). In light of this, future experiments should focus on longer recovery periods post-synchronization (e.g., 15 h post-release) to capture defects in mitotic exit and early G1, particularly under replication stress induced by agents such as APH. These approaches could help uncover delayed phenotypes linked to BLM loss, as seen in cell cycle dynamics (Fig. 28). Strikingly, in our recently submitted manuscript, scWGS was performed on cells at next G1 phase by entrapping cells using a CDK4/6 inhibitor, revealing that M-only or S+M BLM depletion in the presence of APH did not significantly affect the overall rate of aneuploidy or structural chromosomal aberrations in the next G1. However, it led to a moderate increase in cellular heterogeneity and accumulation of tetraploidy[272]. One explanation for the low rate of alterations might be that increased chromosomal aberrations, induced for instance, by the high fraction of MN formation, as seen in S+M depletion (Fig. 44) or breakage of UFBs, do not always correlate with strong abnormal phenotypes and therefore might escape the scWGS depth. Although low coverage can detect focal amplifications, it may fail to reveal more complex chromosomal rearrangements or the precise locations of chromosome breaks. Furthermore, since replication in MN is often delayed and may not initiate until later stages of the subsequent cell cycle, potentially leading to additional DNA breakage, as observed in BFB cycles, leading to catastrophic events such as chromothripsis, it may be more informative to analyze cells at later time points beyond the immediate next G1 phase, or to compare genomic alterations across multiple generations following BLM loss.

Given that BLM knockout is not embryonically lethal, it is plausible that cells can survive in its absence, though they experience increased stress under challenging conditions. This is supported by reduced proliferation and viability after several days, particularly under replication stress induced by APH treatment (Fig. 25). The essential role of BLM is further highlighted by developmental models: BS-affected human embryos exhibit intrauterine growth restriction[273], and notably, complete knockout of BLM in mice even led to embryonic lethality[274]. Thus, while BLM loss is not immediately cytotoxic, its absence gradually undermines the cell's ability to maintain genome stability and division competence.

In addition to APH, other replication-impairing agents, such as HU or DNA-damaging insults like UV irradiation, could offer further insight into how BLM-deficient cells respond to distinct forms of genotoxic stress. Applying these agents in future experiments, followed by genome-

wide sequencing, could help elucidate whether the spectrum or frequency of genetic alterations differs depending on the type of stress. This would extend our understanding of BLM's role in safeguarding genome integrity.

The functional assays performed in this study further support the notion that BLM-deficient cells are sensitive to APH-associated replication stress. Proliferation rate and colony formation capacity was significantly reduced upon APH treatment in BLM-depleted cells, correlating with a rise in replication stress markers, including γH2AX and pRPA S33 (Fig. 25, 26). Under normal conditions, BLM-deficient cells showed signs of senescence, which may reflect a DNA damage-induced growth arrest (Fig. 27). Although genomic instability is a hallmark of both BS and aging, there was so far no evidence reported that BS cells undergo replicative senescence more rapidly than healthy cells. Senescence, an irreversible state of cell cycle arrest characterized by the absence of replication, is strongly associated with telomere shortening and aging[275,276]. Interestingly, despite the high conservation among RecQ helicase family members, including strong homology in their helicase domains, only mutations in the *WRN* gene, causing Werner syndrome (WS), are clearly associated with features of premature aging such as early graying, cataracts, and osteoporosis[277,278]. In contrast, patients with BS or Rothmund-Thomson syndrome (RTS, caused by *RECQL4* mutations) do not typically show such age-related phenotypes[277]. Despite this fact, BLM-deficient cells do exhibit telomeric abnormalities, such as increased sister telomere loss and abnormal telomere associations, indicating a role for BLM in telomere maintenance[129]. However, when challenged with APH, these cells no longer showed an increase in senescence markers, but instead failed to form viable colonies. This suggests that, under replication stress, cells lacking BLM may undergo p53-induced apoptosis rather than enter senescence. These findings are consistent with recent studies that link BLM deficiency to enhanced apoptotic signaling and activation of the p53 pathway, particularly in response to genotoxic stress[279–281]. This further supports the idea that overexpressed BLM may act as an oncogene in certain tumors, potentially due to its role in reducing apoptosis, which could contribute to tumor progression[281]. Recent studies further support this hypothesis by demonstrating that *MYC* overexpression strongly enhances colony formation, which was otherwise abolished in non-cancerous cells lacking BLM as well as p53[282]. This also serves as evidence that the observed effects are not attributable to cancer cell line-specific phenomena.

Elevated SCE has been considered a central feature and a major driver of genomic instability observed in BS by LOH[197,201,202]. Although SCEs involve exchanges between identical sister chromatids, LOH may impair genomic diversity and contribute to tumorigenesis. Nevertheless, recent genome-wide studies have found relatively low LOH levels in BS patient genomes, suggesting that elevated SCE rates may not fully explain the genomic instability[235]. Instead, a broader disruption of DNA repair coordination and replication stress responses may play a more dominant role. Given the complexity of BLM's functions, a major challenge remains in determining how these activities are regulated across different stages of the cell cycle. To our knowledge, the separation of functions of BLM by cell cycle-specific depletion has not been performed to date and is demonstrated in our recently submitted and preprinted manuscript[272]. Using the AID system, this study enabled precise control of BLM protein levels at distinct cell cycle phases.

The S and G2 phases of the cell cycle are critical windows during which BLM helicase functions in DNA replication and DSB repair[175,185]. Consistent with these roles, selective depletion of BLM during S phase resulted in elevated chromatin bridges and increased metaphase chromosome gaps and breaks, potentially arising from unresolved replication stress, particularly at difficult-to-replicate genomic regions, chromosome breaks, and end-to-end fusions. However, an intriguing shift occurs under mild replication stress conditions by

APH treatment. Here, the frequency of metaphase gaps and breaks in S-only BLM-depleted cells unexpectedly decreased, suggesting that BLM may not play a central role in suppressing fragile site expression under stress-enhanced conditions. Alternatively, other compensatory or saturation-based mechanisms could be masking this outcome.

What stands out more prominently in the S phase depletion context under replication stress is the marked increase in binucleated cells (Fig. 46a). Given that BLM is present from mitosis in which it should successfully resolve UFBs, these binucleated cells, typically associated with cytokinesis failure, leading to WGD[283], likely originate from unresolved telomeric bridges that persist into mitosis, as described in recent studies[284,285]. Although BLM-depleted cells under APH treatment still exhibited elevated chromatin bridge frequency (Fig. 39d), there was no corresponding rise in MN (Fig. 44b), which could arise from broken anaphase bridges or from misaligned and lagging DNA fragments. These findings support the hypothesis that, unlike UFBs arising from recombination intermediates, under-replicated DNA, or catenanes, which are typically resolved by BLM during mitosis, unresolved DNA bridges, particularly telomeric bridges, may not primarily depend on BLM for resolution. Although BLM has been associated with T-UFBs, they are likely resolved by enzymatic processing via TREX1, ANKLE1, or mechanical breakage during cell division, as reported in previous studies[58,121,154] and discussed in chapter 1.3. Interestingly, APEX1 was identified in the BLM pull-down at 10.5 h post-release, which functions in the same complex as TREX1[253,254], whereby TREX1 itself was not identified (Fig. 49f). When cells experience a high burden of DNA damage, such as that induced by replication stress combined with BLM loss during S phase, this may result in exhaustion of cleavage mechanisms, such as by TREX1 or ANKLE1, shifting the balance toward division failure rather than fragmentation into MN (Fig. 50, upper row). This may explain the observed increase in binucleated cells, particularly under S phase-specific BLM depletion, although the frequency of binucleation does not exceed approximately 18% (Fig. 46a). This is consistent with previous findings showing that loss of BLM increases binucleation due to shortened abscission timing, an effect that was mitigated by ANKLE1 overexpression[282]. Alternatively, this could indicate that UFBs are rather resistant to processing by enzymes like TREX1 or ANKLE1, or that telomeric bridges overwhelm the repair machinery. This binucleation can have detrimental consequences. While many binucleated cells undergo senescence or apoptosis, some may tolerate this state, particularly transformed or pre-malignant cells[286,287]. Adaptation to binucleation and to WGD can promote aneuploidy and genomic instability, both hallmarks of tumor progression[96,283]. The sharp increase in binucleation following S phase BLM loss highlights a mechanism by which early genomic alterations, such as tetraploidy, could arise in a subset of surviving cells.

BLM's role in processing unresolved intermediates also extends into mitosis. When BLM was depleted exclusively during mitosis, cells exhibited increased misaligned and lagging chromosomes (Fig. 38), a notable rise in UFBs labeled with PICH, BLM, and RPA (Fig. 32, 40, and 41), and elevated metaphase gaps (Fig. 43). This effect was particularly enhanced under replication stress, suggesting that BLM is critical for resolving unresolved DNA structures that escape earlier repair. While certain mitotic UFBs, such as centromere-derived C-UFBs, can be resolved by RIF1, TOPBP1-recruited TOP2A, or, in the case of HR-UFBs, by specific endonucleases, UFBs originating from fragile sites (FS-UFBs) appear to lack such redundancy in repair mechanisms. Previous studies have proposed that endonucleases can partially resolve FS-UFBs through co-localization with FANCD2. However, while this prevents the persistence of UFBs, it comes at the cost of introducing breaks and gaps at fragile sites[32]. Therefore, it seems that FS-UFBs are heavily reliant on BLM activity for proper resolution. The absence of BLM in mitosis may therefore predispose FS-UFBs to breakage, leading to MN formation or to chromosomal rearrangements (Fig. 50, middle row). This is further supported by previous studies demonstrating that BLM is essential for preventing hyper-mitotic

recombination and chromosome breakage at CFSs[288], potentially through its role in resolving FS-UFBs during mitosis.

Furthermore, when BLM was depleted during both S and M phases, cells displayed a phenotype with substantial increases in MN formation (Fig. 44), persistent chromatin bridges (Fig. 39), and elevated PICH-positive UFBs (Fig. 40). These findings point to a scenario in which both S and M phase functions of BLM help cells to cope with DNA damage originating in S phase. The dual involvement of BLM in preventing the formation of sister chromatid linkages while also contributing to their resolution in mitosis may explain the strong impact of BLM loss on genome stability. If left unresolved, sister chromatid linkages may be processed via error-prone or incomplete repair pathways, such as cleavage by endonucleases like MUS81-EME1 and ANKLE1, by the exonuclease TREX1, or may undergo mechanical breakage. These processes increase the risk of chromosomal aberrations, particularly when chromosomes are broken and reshuffled at continued cell cycles, and severely compromise genomic stability (Fig. 50, lower row).

Interestingly, while BLM function is associated with the suppression of misaligned and lagging chromosomes[125] (Fig. 38b), these defects did not further increase beyond the level caused by APH alone when BLM was depleted. These observations suggest that BLM provides a buffering capacity against certain mitotic defects, but it is not solely responsible for their suppression, especially in cases related to spindle assembly failure, where BLM is unlikely to play a direct role. Consequently, lagging chromosomes that originate from acentric fragments are likely the primary contributors to the substantial increase in MN formation, as they originate from pre-mitotic defects, such as chromosome breakage at CFS, that cannot be accurately captured by the mitotic spindle. This increases their risk of mis-segregation and subsequent encapsulation into MN[55].

In summary, our findings indicate distinct but complementary roles for BLM throughout the cell cycle. During S-phase, BLM is thought to be essential for preventing replication-associated defects that can culminate in anaphase bridges, such as telomeric bridges, and binucleation (Fig. 46a). These outcomes are often incompatible with continued proliferation, resulting in senescence or cell death. However, in rare cases, such defects may be tolerated, potentially driving oncogenic processes via WGD and aneuploidy[283,286,287]. In contrast, mitotic BLM is indispensable for the resolution of persistent replication intermediates, such as UFBs, and thereby might induce increased MN formation. These structures can rupture, potentially resulting in chromothripsis, a catastrophic genome rearrangement process[115], and contribute to the extreme genomic instability, as observed in BS.

Outlook:

To further validate the proposed hypothesis that binucleated cells arise predominantly from unresolved telomere bridges, it will be essential to stain for telomeric associated proteins such as TRF2 and investigate the fate of these bridges in real time. Live-cell imaging approaches using fluorescently tagged histones or chromatin-associated proteins could provide critical insights into whether these bridges are rather DAPI-positive or negative bridges, if they persist, resolve, or break during late mitosis and cytokinesis. Such analysis would clarify whether these bridges are indeed a primary trigger for cytokinesis failure and subsequent binucleation. Moreover, it would be valuable to examine the involvement and activation of nucleases known to process telomeric and chromatin bridges, such as TREX1 and the recently implicated

ANKLE1, in the context of BLM loss. Assessing their recruitment and activity in BLM-depleted cells under replication stress could help elucidate whether failure in bridge resolution directly correlates with increased binucleation and whether these nucleases act in a BLM-dependent manner. Similarly, investigating actomyosin-associated mechanical rupture events and their frequency in BLM-depleted cells could offer additional mechanistic insights into how unresolved bridges are processed.

To further dissect the mitotic functions of BLM, distinguishing between the different classes of UFBs will be crucial. Experimentally enhancing C-UFBs, for example by inhibiting TOP2A, or selectively increasing FS-UFBs through depletion of an AID-tagged FANCD2 cell line or increasing HR-UFBs by depletion of homologous recombination proteins such as RAD51 or BRCA1, as demonstrated in previous studies[117], could help clarify which UFB types are most dependent on BLM for resolution. This would allow determination of whether BLM specifically protects against FS-UFB misprocessing and subsequent micronuclei formation, possibly through prevention of centromere-lacking chromosomal fragment generation.

Finally, to support the hypothesis that BLM is essential in preventing micronuclei formation through the resolution of FS-associated damage, it would be important to directly assess the centromere content of MN following FS-UFB enhancement and BLM depletion. The emerging evidence from our recently submitted manuscript, reporting a lack of centromeres in MN formed after a single-cell cycle loss of BLM, strongly supports this model[272]. Further investigation using centromere-specific FISH and live-cell imaging could solidify the link between improper FS-UFB resolution, acentric fragment formation, and MN generation.

As the investigation of BLM function in this study primarily relies on auxin-induced depletion at specific time points, determined based on flow cytometry analysis of cell cycle progression, it is important to note that at 10.5 h, only approximately 60% of cells were in G2/M, and by 15 h, a proportion of around 60 % had entered G1. Therefore, it remains possible that some of the observed effects arose due to BLM depletion at other cell cycle phases, and particularly those attributed to the subsequent G1 phase, may have occurred during other stages of the cell cycle. However, the fact that these cells are cyclin A-negative supports their classification as G1 phase cells. To strengthen these conclusions, further validation is necessary. This could include comparison with RO-3306-treated cells to ensure BLM depletion occurs exclusively during mitosis, and the use of live-cell imaging to accurately track individual cell fates over time.

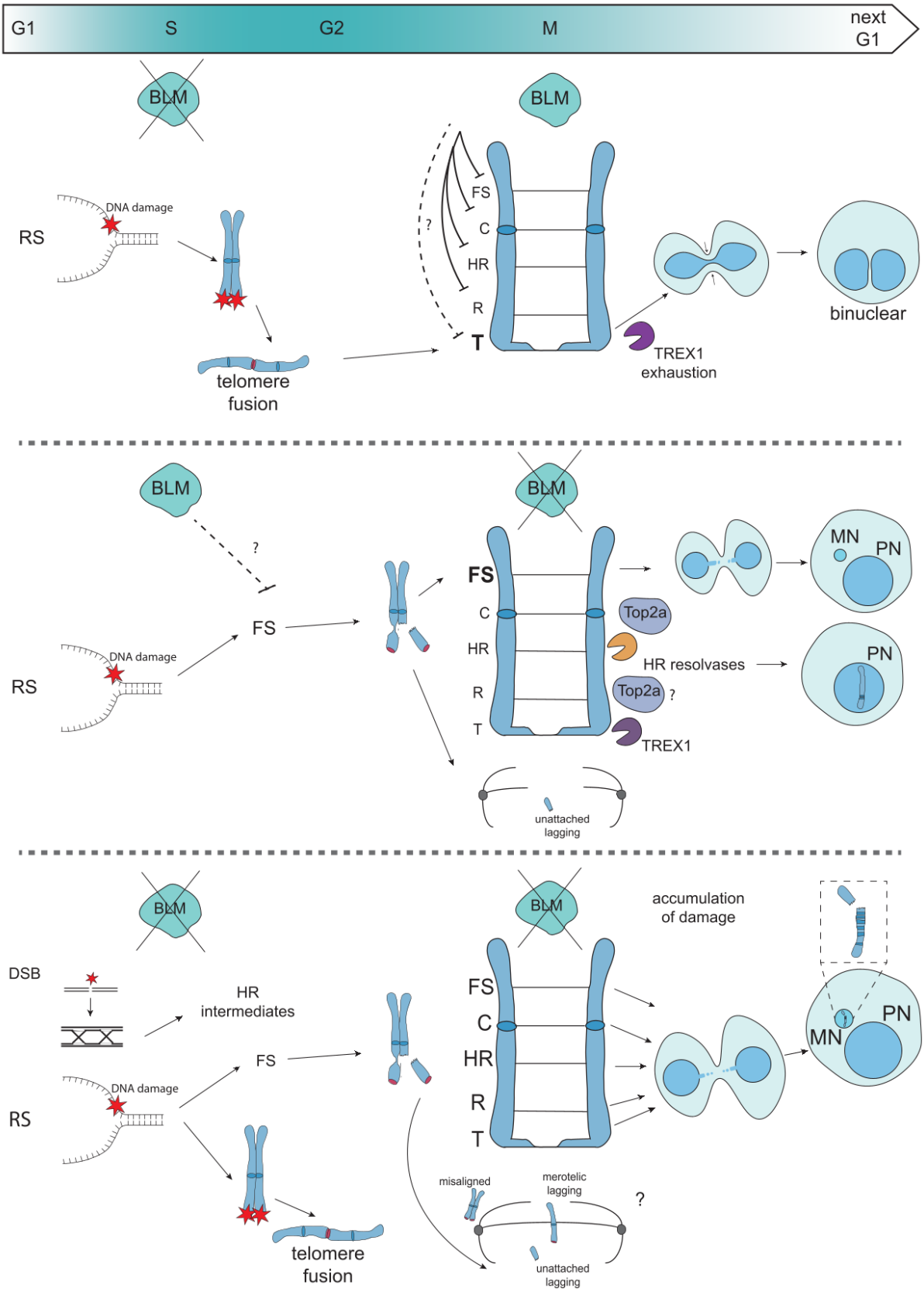

Figure 50|Hypothetical separation of BLM functions. S phase specific BLM functions (top) and M phase specific functions (center) compared to effects when BLM is lost during one complete cell cycle (bottom).

Supplementary

To validate the generation of heterozygous cell lines HCT116 Tet-OsTIR1 BLM$^{AID/WT}$ clone 5 and clone 6, flow cytometry analysis of BLM-GFP expression was performed (Suppl. Fig. 1a). These data, derived from the same dataset as shown in Fig. 22d, confirm that both heterozygous clones exhibit comparable BLM expression levels.

To exclude non-specific effects on protein degradation, HCT116 Tet-OsTIR1 WT cells were analyzed for OsTIR1 expression. As expected, OsTIR1 expression was only induced by Dox treatment for 24 h, and not by IAA or the IAA solvent (EtOH) alone (Suppl. Fig. 1b). Flow cytometry analysis of homozygous HCT116 Tet-OsTIR1 BLM$^{AID/AID}$ cells further demonstrated that neither EtOH nor IAA alone affected BLM expression, comparable to cells without treatment (NS), whereas combined Dox+IAA treatment for 24 h led to a strong reduction in BLM signal (Suppl. Fig. 1c).

Auxin-induced degradation of BLM after 24 h was confirmed in both heterozygous clones, consistent with the depletion seen in homozygous cells, while no depletion was observed in WT cells (Suppl. Fig. 1d). Furthermore, it can be confirmed that WT cells do not show auxin-induced BLM depletion, even though the levels after auxin addition appeared weaker in the first replicate (see Fig. 23a), suggesting unequal protein loading. A time-course analysis further confirmed that IAA treatment had no effect on BLM levels in WT cells. In contrast, both heterozygous clones exhibited a reduction in BLM-AID/GFP levels from 1 h of IAA treatment, with full loss of BLM detection by 12 h, comparable to the pattern observed in homozygous cells (see Fig. 23b). However, some variability in protein loading should be considered, especially in clone 5 (lane 6) and clone 6 (lane 3).

SE assays showed a significant increase in SCE levels in homozygous cells following 24 h of IAA treatment (same samples as shown in Fig. 24), whereas no significant increase was observed in the heterozygous clones. However, clone 5 displayed after IAA treatment a significantly higher SCE rate than clone 6. Missing data for clone 5 under untreated conditions need to be acquired to fully interpret this observation. Further, the SCE rates of homozygous cells after IAA treatment show similar trends to BLM-deficient cells of BS patient derived fibroblasts, confirmed that the SCE phenotype is comparable.

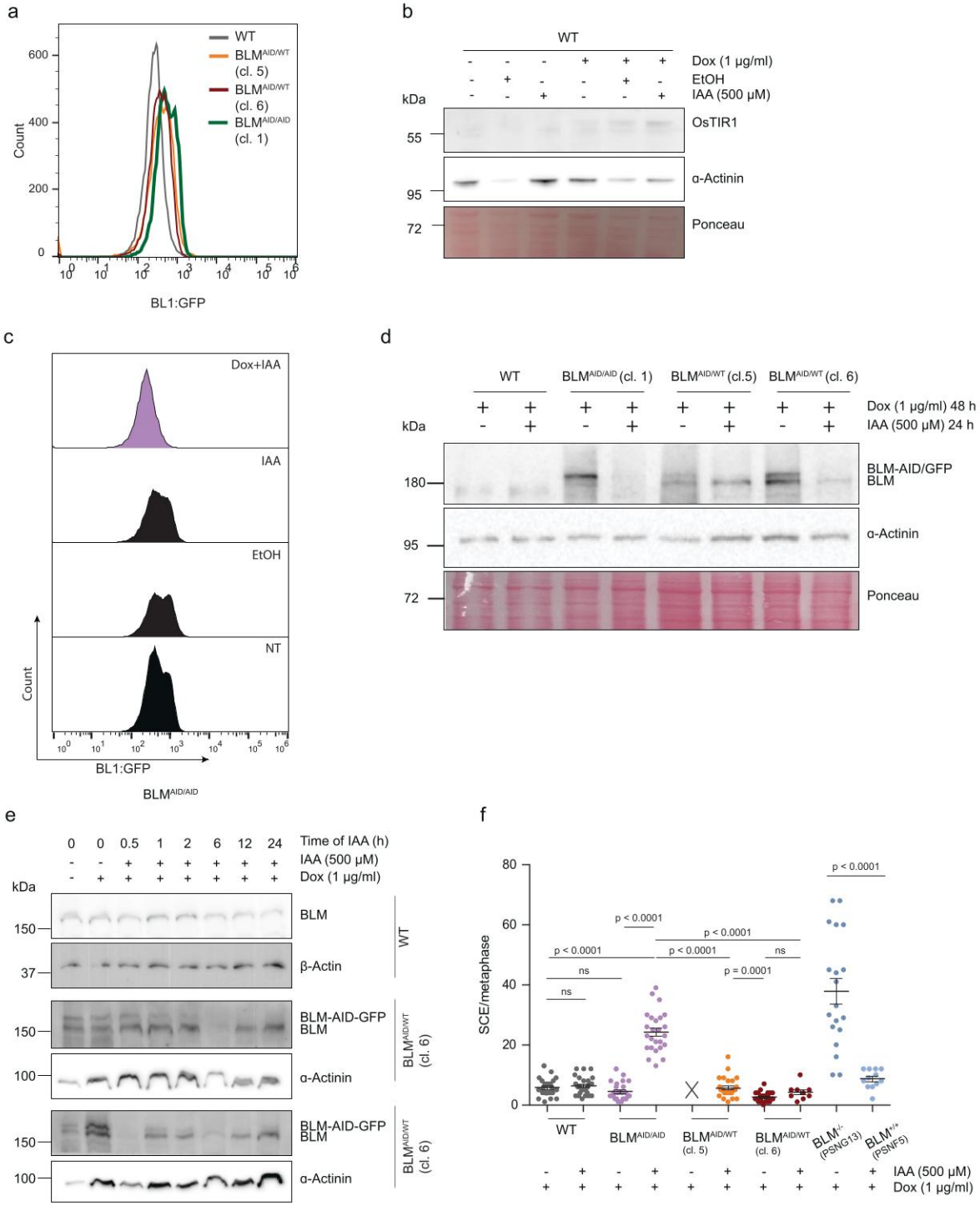

Suppl. Fig. 1|BLM depletion across different cell lines. a, Fow cytometry analysis of endogenous BLM GFP-signal of HCT116 Tet-OsTIR1 WT (grey), homozygous BLM$^{AID/AID}$ clone 1 (green), heterozygous BLM$^{AID/WT}$ clone 5 (orange), and heterozygous BLM$^{AID/WT}$ clone 6 (red), same experiment as in Fig. 22d, but depicting both heterozygous clones. **b-c,** Western blot analysis of the presence of OsTIR1 after doxycycline (Dox) induction in WT cells. d, Flow cytometry analysis of the effects of ethanol (EtOH), serving as the solvent of auxin (IAA), or Dox or IAA alone on IAA-induced depletion compared to no treatment (NT) in homozygous BLM-AID/GFP cells. **d,** IAA-induced BLM depletion of WT cells, clone 1, clone 5, and clone 6 after 24h. Corresponding to Fig. 23a. **e,** Western blot analysis of time course dependent auxin addition in WT and both heterozygous cell lines. **f,** Sister chromatid exchange (SCE) analysis of WT and homozygous cells (same samples as shown in Fig. 24), compared with both heterozygous clones as well as BLM-proficient and -deficient fibroblast cell lines as controls. No data were possible to acquire for the heterozygous clone 5 without auxin treatment during the time of this study.

List of Tables

List of Figures

Curriculum Vitae

Personal Information

Name:	Angela Vanessa Luisa Wieland
E-Mail:	awieland@bio.uni-kl.de

Work Experience and Academic Education

11/2023 – to date	**Biologist for diagnostics**
02/2019 – 12/2022	**PhD enrolment** Rhineland-Palatinate University of Technology Kaiserslautern-Landau, Germany Department: Molecular Genetics
07/2018 – 09/2018	**Scientific assistant** University Clinic Heidelberg, Germany Department: Molecular OncoSurgery
11/2016 – 02/2017	**Internship during Master enrolment** University Clinic Heidelberg, Germany Department: Molecular OncoSurgery
10/2015 – 03/2018	**Master of Science in Molecular Medicine** Albert-Ludwigs-University Freiburg, Germany Thesis title: “Identification of an amino acid motif diminishing protein expression”
10/2012 – 09/2015	**Bachelor of Science in Biology** Philipps-University Marburg, Germany Thesis title: “Establishment of a neuronal model system to identify molecular mechanisms of insulin resistance”

Conferences

09/2022	Mainz IMB/SFB 1361 Conference “Restore, Reorganise, Repurpose: The many faces of DNA repair” - audience
04/2022	Jena DGDR-KRUPP Symposium “DNA Repair and Human Disease” - Selected poster presentation, title: “Application of an inducible degradation system to study cell cycle-specific functions of the BLM helicase”
09/2021	CSHL conference “Eukaryotic DNA Replication & Genome Maintenance” – online audience
08/2021	Frankfurt Cancer Conference “From Molecular Research to Mechanism-based Cancer Therapy – online audience

Angela Wieland

Relevant Courses and Workshops

10/2022	Workshop: Career planning inside and outside the university
03/2022	Workshop: Coaching and leadership training “growing as a researcher – small group coaching for female scientists”
03/2022	Workshop: Self-confidence and assertive communication training
09/2021	Workshop: Project Management training for PhD students in the final phase
05/2021	Workshop: Successful self-presentation in talks
01/2016	FelasaB certificate
10/2015	Advanced training “Safety in Gene Technology §15 GenTSV”

Participations

02/2019 – 12/2022	FOR2800 DFG-funded Research Unit “Chromosomal Instability: Cross-talk of DNA replication stress and mitotic dysfunction” – regular progress reports, talks, retreats
12/2019 – 12/2022	Intralaboratory shared Instagram account for scientific communication *@guardians_of_the_genome*

Skills

Language	German (native), English (fluent), French (basic), Spanish (basic), Latin (small latinum)
Computational skills	Microsoft Office (Word, Excel, PowerPoint), Adobe Illustrator, GraphPad Prism, Fiji/ImageJ, FlowJo, Slidebook, R Programming, Perseus
Methods	Cell culture, blood isolation, transfection, transduction, western blotting, Gateway cloning, Gibson assembly, GoldenGate cloning, site-directed mutagenesis, CRISPR/Cas9-based genome editing, DNA/RNA isolation, PCR/RT-qPCR, Flow cytometry, proliferation assay, colony formation assay, ChIP-MS based proteomics

Angela Wieland

Acknowledgments

First and foremost, I would like to express my extraordinary gratitude to Prof. Dr. Zuzana Storchová, who enabled me to pursue my doctoral studies in her laboratory. Thank you for constantly driving the project forward, your continual accessibility for advice and for affording me the opportunity for professional development as a scientist.

My further unrestricted thanks go to Dr. Markus Räschle, who enabled me to work on his exciting project, which led to my unchallenged interest in ultra-fine anaphase bridges. Thank you for your mentorship throughout the project, your shared enthusiasm for each novel scientific revelation, and encouragement to explore alternative avenues of inquiry.

It was a great pleasure to work on this topic, about which so much is already known and so much is yet to be discovered. The project has awakened my curiosity to discover the big picture and work on becoming a better scientist.

I extend my gratitude to Prof. Dr. Jörg Fahrer for graciously accepting to serve as the second thesis examiner and Prof. Dr Tanja Maritzen for graciously accepting to serve as chair on my thesis committee.

I am deeply appreciative of the funding provided for this project through the research unit FOR2800. Thanks to all members for the enriching experience of collaborative engagement, where we shared insights from the latest findings during our regular progress reports and exchanged new research ideas. Being part of a group where all PhD students started around the same time and are studying in the same field has been incredibly beneficial. The exchange of knowledge among us, as well as with all supervisors throughout the years, has fostered growth and facilitated numerous collaborations. I extend special appreciation to Prof. Dr. Holger Bastians for being the speaker of this research unit, his collaborative efforts, and our joint manuscript, as well as for his kind gift of the HCT116 Tet-OsTIR1 cell lines. Thanks also to Xiaoxiao, Kristina, and Ipek for participating in various workshops together. Ipek, thank you for your visit to our lab and your continual support during the lengthy sister chromatid exchange experiments. Lastly, thanks to Ivan for your assistance with various protocol setups and R-loop discussions.

A special thanks goes to all my students, particularly Divya, Tamara, Nidhi, and Farbod. I am grateful for your unwavering commitment to driving the project forward, sustaining interest in its progression, and contributing to my growth as a research supervisor. I am truly thankful that, through this collaboration, we have also become great friends. Farbod, thank you for your continued involvement in the project after your master thesis, I am immensely proud of you. I also extend my appreciation to Andrea for joining the project as a postdoctoral researcher and to Tamara for your immense contributions to its progress.

Next, I would like to thank all members of this lab. It was a pleasure to work alongside each of you in this welcoming atmosphere, where meaningful friendships were forged. Su and Naren, you were there at the outset of my journey here. Thank you for making my start so easy and the great time we spent together. Karen, since you have joined the team, I could not have asked for a better office mate. Thank you for our daily breaks we shared together, for being my steadfast companion during sports activities, and for consistently lending me an open ear in every situation. Krissi, thank you for our writing sessions on the thesis and the moments of perseverance together. Assel and Anna, although our time together may have been brief, attending the data analysis course together and the daily lab life was truly enjoyable with you. Paul, thank you for being a great office mate during our time together and for your continuous

support with any programming. Jan, thanks for helping whenever I had any questions and creating outstanding box plots for me. Thanks to Leah, Devi (N.), Devi (B.), Petra, Anna (H.), Prince, Dastin, Stefan, Toni and Osmar, every day was so much fun because of you. Isabell, Robin and Ingeborg, thank you for managing administrative and lab-related tasks.

Chris, your steadfast support, unwavering encouragement, and attentive listening during challenging moments have been instrumental in my journey towards completing this PhD thesis. I am immensely grateful for your dedication, especially considering your own commitments towards completing your PhD. I am deeply thankful to have you by my side.

Finally, my gratitude extends to my whole family for your support and love, especially to my mum and Udo, for their extraordinary support and motivation in every situation, and for their constant encouragement towards every goal I have pursued throughout my entire life. You have played a fundamental role in shaping my journey to where I stand today.

References

1. Sender, R., Fuchs, S. & Milo, R. Revised Estimates for the Number of Human and Bacteria Cells in the Body. *PLoS Biol* **14**, e1002533 (2016).

2. Matthews, H. K., Bertoli, C. & de Bruin, R. A. M. Cell cycle control in cancer. *Nature Reviews Molecular Cell Biology* vol. 23 74–88 Preprint at https://doi.org/10.1038/s41580-021-00404-3 (2022).

3. HOWARD, A. & PELC, S. Nuclear incorporation of P as demonstrated by autoradiographs. *Exp Cell Res* **2**, 178–187 (1951).

4. Pennycook, B. R. & Barr, A. R. Restriction point regulation at the crossroads between quiescence and cell proliferation. *FEBS Lett* (2020) doi:10.1002/1873-3468.13867.

5. Rubin, S. M., Sage, J. & Skotheim, J. M. Integrating Old and New Paradigms of G1/S Control. *Mol Cell* **80**, 183–192 (2020).

6. Harper, J. W., Adami, G. R., Wei, N., Keyomarsi, K. & Elledge, S. J. The p21 Cdk-interacting protein Cip1 is a potent inhibitor of G1 cyclin-dependent kinases. *Cell* **75**, 805–16 (1993).

7. Polyak, K. *et al.* p27Kip1, a cyclin-Cdk inhibitor, links transforming growth factor-beta and contact inhibition to cell cycle arrest. *Genes Dev* **8**, 9–22 (1994).

8. Tanaka, S. & Araki, H. Helicase activation and establishment of replication forks at chromosomal origins of replication. *Cold Spring Harb Perspect Biol* **5**, a010371 (2013).

9. Bailis, J. M., Luche, D. D., Hunter, T. & Forsburg, S. L. Minichromosome Maintenance Proteins Interact with Checkpoint and Recombination Proteins To Promote S-Phase Genome Stability. *Mol Cell Biol* **28**, 1724–1738 (2008).

10. Aria, V. & Yeeles, J. T. P. Mechanism of Bidirectional Leading-Strand Synthesis Establishment at Eukaryotic DNA Replication Origins. *Mol Cell* **73**, 199-211.e10 (2019).

11. OKAZAKI, T. Days weaving the lagging strand synthesis of DNA — A personal recollection of the discovery of Okazaki fragments and studies on discontinuous replication mechanism —. *Proceedings of the Japan Academy, Series B* **93**, 322–338 (2017).

12. Song, H.-Y., Shen, R., Mahasin, H., Guo, Y.-N. & Wang, D.-G. DNA replication: Mechanisms and therapeutic interventions for diseases. *MedComm (Beijing)* **4**, e210 (2023).

13. Nurk, S. *et al.* The complete sequence of a human genome. *Science* **376**, 44–53 (2022).

14. Saxena, S. & Zou, L. Hallmarks of DNA replication stress. *Molecular Cell* vol. 82 2298–2314 Preprint at https://doi.org/10.1016/j.molcel.2022.05.004 (2022).

15. Zeman, M. K. & Cimprich, K. A. Causes and consequences of replication stress. *Nat Cell Biol* **16**, 2–9 (2014).

16. Koç, A., Wheeler, L. J., Mathews, C. K. & Merrill, G. F. Hydroxyurea arrests DNA replication by a mechanism that preserves basal dNTP pools. *J Biol Chem* **279**, 223–30 (2004).

17. Ikegami, S. *et al.* Aphidicolin prevents mitotic cell division by interfering with the activity of DNA polymerase-alpha. *Nature* **275**, 458–60 (1978).

18. Vassin, V. M., Anantha, R. W., Sokolova, E., Kanner, S. & Borowiec, J. A. Human RPA phosphorylation by ATR stimulates DNA synthesis and prevents ssDNA accumulation during DNA-replication stress. *J Cell Sci* **122**, 4070–4080 (2009).

19. Choi, J.-H. *et al.* Reconstitution of RPA-covered single-stranded DNA-activated ATR-Chk1 signaling. *Proc Natl Acad Sci U S A* **107**, 13660–5 (2010).

20. Cimprich, K. A., Shin, T. B., Keith, C. T. & Schreiber, S. L. cDNA cloning and gene mapping of a candidate human cell cycle checkpoint protein. *Proc Natl Acad Sci U S A* **93**, 2850–5 (1996).

21. Alexander, J. L. & Orr-Weaver, T. L. Replication fork instability and the consequences of fork collisions from rereplication. *Genes Dev* **30**, 2241–2252 (2016).

22. Keuper, K., Wieland, A., Räschle, M. & Storchova, Z. Processes shaping cancer genomes – From mitotic defects to chromosomal rearrangements. *DNA Repair (Amst)* **107**, (2021).

23. Lee, J. A., Carvalho, C. M. B. & Lupski, J. R. A DNA replication mechanism for generating nonrecurrent rearrangements associated with genomic disorders. *Cell* **131**, 1235–47 (2007).

24. Zhang, F. *et al.* The DNA replication FoSTeS/MMBIR mechanism can generate genomic, genic and exonic complex rearrangements in humans. *Nat Genet* **41**, 849–853 (2009).

25. Costantino, L. *et al.* Break-induced replication repair of damaged forks induces genomic duplications in human cells. *Science* **343**, 88–91 (2014).

26. Mankouri, H. W., Huttner, D. & Hickson, I. D. How unfinished business from S-phase affects mitosis and beyond. *EMBO J* **32**, 2661–71 (2013).

27. Kawabata, T. *et al.* Stalled fork rescue via dormant replication origins in unchallenged S phase promotes proper chromosome segregation and tumor suppression. *Mol Cell* **41**, 543–53 (2011).

28. Glover, T. W., Berger, C., Coyle, J. & Echo, B. DNA polymerase alpha inhibition by aphidicolin induces gaps and breaks at common fragile sites in human chromosomes. *Hum Genet* **67**, 136–42 (1984).

29. Le Beau, M. M. *et al.* Replication of a common fragile site, FRA3B, occurs late in S phase and is delayed further upon induction: implications for the mechanism of fragile site induction. *Hum Mol Genet* **7**, 755–61 (1998).

30. Helmrich, A., Ballarino, M. & Tora, L. Collisions between Replication and Transcription Complexes Cause Common Fragile Site Instability at the Longest Human Genes. *Mol Cell* **44**, 966–977 (2011).

31. Bhowmick, R., Minocherhomji, S. & Hickson, I. D. RAD52 Facilitates Mitotic DNA Synthesis Following Replication Stress. *Mol Cell* **64**, 1117–1126 (2016).

32. Naim, V., Wilhelm, T., Debatisse, M. & Rosselli, F. ERCC1 and MUS81-EME1 promote sister chromatid separation by processing late replication intermediates at common fragile sites during mitosis. *Nat Cell Biol* **15**, 1008–1015 (2013).

33. Palma, A. *et al.* Phosphorylation by CK2 regulates MUS81/EME1 in mitosis and after replication stress. *Nucleic Acids Res* **46**, 5109–5124 (2018).

34. Minocherhomji, S. *et al.* Replication stress activates DNA repair synthesis in mitosis. *Nature* **528**, 286–90 (2015).

35. Garribba, L. *et al.* Folate stress induces SLX1- and RAD51-dependent mitotic DNA synthesis at the fragile X locus in human cells. *Proc Natl Acad Sci U S A* **117**, 16527–16536 (2020).

36. Chappidi, N. *et al.* Fork Cleavage-Religation Cycle and Active Transcription Mediate Replication Restart after Fork Stalling at Co-transcriptional R-Loops. *Mol Cell* **77**, 528-541.e8 (2020).

37. Bhowmick, R., Hickson, I. D. & Liu, Y. Completing genome replication outside of S phase. *Molecular Cell* vol. 83 3596–3607 Preprint at https://doi.org/10.1016/j.molcel.2023.08.023 (2023).

38. Özer, Ö. & Hickson, I. D. Pathways for maintenance of telomeres and common fragile sites during DNA replication stress. *Open Biol* **8**, (2018).

39. McIntosh, J. R. Mitosis. *Cold Spring Harb Perspect Biol* **8**, (2016).

40. Murray, A. W. & Szostak, J. W. Chromosome Segregation in Mitosis and Meiosis. *Annu Rev Cell Biol* **1**, 289–315 (1985).

41. Musacchio, A. & Desai, A. A Molecular View of Kinetochore Assembly and Function. *Biology (Basel)* **6**, (2017).

42. Madian, N. & Jayanthi, K. B. Analysis of human chromosome classification using centromere position. *Measurement* **47**, 287–295 (2014).

43. Burke, D. J. & Stukenberg, P. T. Linking kinetochore-microtubule binding to the spindle checkpoint. *Dev Cell* **14**, 474–9 (2008).

44. Nilsson, J., Yekezare, M., Minshull, J. & Pines, J. The APC/C maintains the spindle assembly checkpoint by targeting Cdc20 for destruction. *Nat Cell Biol* **10**, 1411–20 (2008).

45. Devillers, R., dos Santos, A., Destombes, Q., Laplante, M. & Elowe, S. Recent insights into the causes and consequences of chromosome mis-segregation. *Oncogene* **43**, 3139–3150 (2024).

46. Basto, R. *et al.* Centrosome amplification can initiate tumorigenesis in flies. *Cell* **133**, 1032–42 (2008).

47. Maiato, H. & Logarinho, E. Mitotic spindle multipolarity without centrosome amplification. *Nat Cell Biol* **16**, 386–94 (2014).

48. Ganem, N. J., Godinho, S. A. & Pellman, D. A mechanism linking extra centrosomes to chromosomal instability. *Nature* **460**, 278–82 (2009).

49. Storchova, Z. & Pellman, D. From polyploidy to aneuploidy, genome instability and cancer. *Nat Rev Mol Cell Biol* **5**, 45–54 (2004).

50. Bakhoum, S. F., Thompson, S. L., Manning, A. L. & Compton, D. A. Genome stability is ensured by temporal control of kinetochore-microtubule dynamics. *Nat Cell Biol* **11**, 27–35 (2009).

51. Cimini, D., Fioravanti, D., Salmon, E. D. & Degrassi, F. Merotelic kinetochore orientation versus chromosome mono-orientation in the origin of lagging chromosomes in human primary cells. *J Cell Sci* **115**, 507–15 (2002).

52. Barber, T. D. *et al.* Chromatid cohesion defects may underlie chromosome instability in human colorectal cancers. *Proc Natl Acad Sci U S A* **105**, 3443–8 (2008).

53. Yost, S. *et al.* Biallelic TRIP13 mutations predispose to Wilms tumor and chromosome missegregation. *Nat Genet* **49**, 1148–1151 (2017).

54. Maciejowski, J., Li, Y., Bosco, N., Campbell, P. J. & de Lange, T. Chromothripsis and Kataegis Induced by Telomere Crisis. *Cell* **163**, 1641–54 (2015).

55. Burrell, R. A. *et al.* Replication stress links structural and numerical cancer chromosomal instability. *Nature* **494**, 492–496 (2013).

56. Thompson, S. L. & Compton, D. A. Chromosome missegregation in human cells arises through specific types of kinetochore-microtubule attachment errors. *Proc Natl Acad Sci U S A* **108**, 17974–17978 (2011).

57. Crasta, K. *et al.* DNA breaks and chromosome pulverization from errors in mitosis. *Nature* **482**, 53–8 (2012).

58. Umbreit, N. T. *et al.* Mechanisms generating cancer genome complexity from a single cell division error. *Science* **368**, (2020).

59. Ferrandiz, N., Downie, L., Starling, G. P. & Royle, S. J. Endomembranes promote chromosome missegregation by ensheathing misaligned chromosomes. *Journal of Cell Biology* **221**, (2022).

60. Gomes, A. M. *et al.* Micronuclei from misaligned chromosomes that satisfy the spindle assembly checkpoint in cancer cells. *Current Biology* **32**, 4240-4254.e5 (2022).

61. Tucker, J. B. *et al.* Misaligned Chromosomes are a Major Source of Chromosomal Instability in Breast Cancer. *Cancer Research Communications* **3**, 54–65 (2023).

62. Branzei, D. & Foiani, M. Regulation of DNA repair throughout the cell cycle. *Nat Rev Mol Cell Biol* **9**, 297–308 (2008).

63. Scully, R., Panday, A., Elango, R. & Willis, N. A. DNA double-strand break repair-pathway choice in somatic mammalian cells. *Nat Rev Mol Cell Biol* **20**, 698–714 (2019).

64. Savitsky, K. *et al.* A single ataxia telangiectasia gene with a product similar to PI-3 kinase. *Science* **268**, 1749–53 (1995).

65. Her, J., Ray, C., Altshuler, J., Zheng, H. & Bunting, S. F. 53BP1 Mediates ATR-Chk1 Signaling and Protects Replication Forks under Conditions of Replication Stress. *Mol Cell Biol* **38**, (2018).

66. Lee, J.-H. & Paull, T. T. ATM activation by DNA double-strand breaks through the Mre11-Rad50-Nbs1 complex. *Science* **308**, 551–4 (2005).

67. Kang, J. *et al.* Functional interaction of H2AX, NBS1, and p53 in ATM-dependent DNA damage responses and tumor suppression. *Mol Cell Biol* **25**, 661–70 (2005).

68. Chaturvedi, P. *et al.* Mammalian Chk2 is a downstream effector of the ATM-dependent DNA damage checkpoint pathway. *Oncogene* **18**, 4047–4054 (1999).

69. Zou, L. & Elledge, S. J. Sensing DNA damage through ATRIP recognition of RPA-ssDNA complexes. *Science* **300**, 1542–8 (2003).

70. Liu, Q. *et al.* Chk1 is an essential kinase that is regulated by Atr and required for the G(2)/M DNA damage checkpoint. *Genes Dev* **14**, 1448–59 (2000).

71. Lieber, M. R. The Mechanism of Human Nonhomologous DNA End Joining. *Journal of Biological Chemistry* **283**, 1–5 (2008).

72. Mao, Z., Bozzella, M., Seluanov, A. & Gorbunova, V. DNA repair by nonhomologous end joining and homologous recombination during cell cycle in human cells. *Cell Cycle* **7**, 2902–2906 (2008).

73. Li, Y. *et al.* Patterns of somatic structural variation in human cancer genomes. *Nature* **578**, 112–121 (2020).

74. Corneo, B. *et al.* Rag mutations reveal robust alternative end joining. *Nature* **449**, 483–6 (2007).

75. Takata, M. *et al.* Homologous recombination and non-homologous end-joining pathways of DNA double-strand break repair have overlapping roles in the maintenance of chromosomal integrity in vertebrate cells. *EMBO J* **17**, 5497–5508 (1998).

76. Nassif, N., Penney, J., Pal, S., Engels, W. R. & Gloor, G. B. Efficient copying of nonhomologous sequences from ectopic sites via P-element-induced gap repair. *Mol Cell Biol* **14**, 1613–25 (1994).

77. Fu, T.-J., Tse-Dinh, Y.-C. & Seeman, N. C. Holliday Junction Crossover Topology. *J Mol Biol* **236**, 91–105 (1994).

78. Raynard, S., Bussen, W. & Sung, P. A double Holliday junction dissolvasome comprising BLM, topoisomerase IIIalpha, and BLAP75. *J Biol Chem* **281**, 13861–4 (2006).

79. Wu, L. & Hickson, I. D. The Bloom's syndrome helicase suppresses crossing over during homologous recombination. *Nature* **426**, 870–4 (2003).

80. Chen, X. B. *et al.* Human Mus81-associated endonuclease cleaves Holliday junctions in vitro. *Mol Cell* **8**, 1117–27 (2001).

81. Bzymek, M., Thayer, N. H., Oh, S. D., Kleckner, N. & Hunter, N. Double holliday junctions are intermediates of DNA break repair. *Nature* **464**, 937–941 (2010).

82. Ivanov, E. L., Sugawara, N., Fishman-Lobell, J. & Haber, J. E. Genetic Requirements for the Single-Strand Annealing Pathway of Double-Strand Break Repair in *Saccharomyces cerevisiae*. *Genetics* **142**, 693–704 (1996).

83. Richardson, C. & Jasin, M. Frequent chromosomal translocations induced by DNA double-strand breaks. *Nature* **405**, 697–700 (2000).

84. Hanahan, D. & Weinberg, R. A. Hallmarks of cancer: the next generation. *Cell* **144**, 646–74 (2011).

85. Hadi, K. *et al.* Distinct Classes of Complex Structural Variation Uncovered across Thousands of Cancer Genome Graphs. *Cell* **183**, 197-210.e32 (2020).

86. ICGC/TCGA Pan-Cancer Analysis of Whole Genomes Consortium. Pan-cancer analysis of whole genomes. *Nature* **578**, 82–93 (2020).

87. Holland, A. J. & Cleveland, D. W. Boveri revisited: chromosomal instability, aneuploidy and tumorigenesis. *Nat Rev Mol Cell Biol* **10**, 478–87 (2009).

88. Zack, T. I. *et al.* Pan-cancer patterns of somatic copy number alteration. *Nat Genet* **45**, 1134–40 (2013).

89. McGranahan, N., Burrell, R. A., Endesfelder, D., Novelli, M. R. & Swanton, C. Cancer chromosomal instability: therapeutic and diagnostic challenges. *EMBO Rep* **13**, 528–38 (2012).

90. Knouse, K. A., Wu, J., Whittaker, C. A. & Amon, A. Single cell sequencing reveals low levels of aneuploidy across mammalian tissues. *Proc Natl Acad Sci U S A* **111**, 13409–14 (2014).

91. Stopsack, K. H. *et al.* Aneuploidy drives lethal progression in prostate cancer. *Proc Natl Acad Sci U S A* **116**, 11390–11395 (2019).

92. Taylor, A. M. *et al.* Genomic and Functional Approaches to Understanding Cancer Aneuploidy. *Cancer Cell* **33**, 676-689.e3 (2018).

93. Williams, B. R. *et al.* Aneuploidy affects proliferation and spontaneous immortalization in mammalian cells. *Science* **322**, 703–9 (2008).

94. Rutledge, S. D. *et al.* Selective advantage of trisomic human cells cultured in non-standard conditions. *Sci Rep* **6**, 22828 (2016).

95. Thompson, S. L., Bakhoum, S. F. & Compton, D. A. Mechanisms of chromosomal instability. *Curr Biol* **20**, R285-95 (2010).

96. Gemble, S. *et al.* Genetic instability from a single S phase after whole-genome duplication. *Nature* **604**, 146–151 (2022).

97. Sharma, R., Lewis, S. & Wlodarski, M. W. DNA Repair Syndromes and Cancer: Insights Into Genetics and Phenotype Patterns. *Front Pediatr* **8**, 570084 (2020).

98. Manthei, K. A. & Keck, J. L. The BLM dissolvasome in DNA replication and repair. *Cellular and Molecular Life Sciences* vol. 70 4067–4084 Preprint at https://doi.org/10.1007/s00018-013-1325-1 (2013).

99. Gönenc, I. I. *et al.* Phenotypic spectrum of BLM- and RMI1-related Bloom syndrome. *Clin Genet* **101**, 559–564 (2022).

100. Hudson, D. F. *et al.* Loss of RMI2 Increases Genome Instability and Causes a Bloom-Like Syndrome. *PLoS Genet* **12**, e1006483 (2016).

101. Moore, J. K. & Haber, J. E. Cell Cycle and Genetic Requirements of Two Pathways of Nonhomologous End-Joining Repair of Double-Strand Breaks in *Saccharomyces cerevisiae*. *Mol Cell Biol* **16**, 2164–2173 (1996).

102. Bartkova, J. *et al.* Oncogene-induced senescence is part of the tumorigenesis barrier imposed by DNA damage checkpoints. *Nature* **444**, 633–7 (2006).

103. Willis, N. A. *et al.* Mechanism of tandem duplication formation in BRCA1-mutant cells. *Nature* **551**, 590–595 (2017).

104. Wang, Y. *et al.* BASC, a super complex of BRCA1-associated proteins involved in the recognition and repair of aberrant DNA structures. *Genes Dev* **14**, 927–39 (2000).

105. Zhao, W., Wiese, C., Kwon, Y., Hromas, R. & Sung, P. The BRCA Tumor Suppressor Network in Chromosome Damage Repair by Homologous Recombination. *Annu Rev Biochem* **88**, 221–245 (2019).

106. Tsai, A. G. *et al.* Human chromosomal translocations at CpG sites and a theoretical basis for their lineage and stage specificity. *Cell* **135**, 1130–42 (2008).

107. Mitter, D. *et al.* Genotype-phenotype correlations in patients with retinoblastoma and interstitial 13q deletions. *Eur J Hum Genet* **19**, 947–58 (2011).

108. Groffen, J. *et al.* Philadelphia chromosomal breakpoints are clustered within a limited region, bcr, on chromosome 22. *Cell* **36**, 93–9 (1984).

109. Stephens, P. J. *et al.* Massive genomic rearrangement acquired in a single catastrophic event during cancer development. *Cell* **144**, 27–40 (2011).

110. Holland, A. J. & Cleveland, D. W. Chromoanagenesis and cancer: mechanisms and consequences of localized, complex chromosomal rearrangements. *Nat Med* **18**, 1630–8 (2012).

111. Baca, S. C. *et al.* Punctuated evolution of prostate cancer genomes. *Cell* **153**, 666–77 (2013).

112. Liu, P. *et al.* Chromosome catastrophes involve replication mechanisms generating complex genomic rearrangements. *Cell* **146**, 889–903 (2011).

113. Korbel, J. O. & Campbell, P. J. Criteria for inference of chromothripsis in cancer genomes. *Cell* **152**, 1226–36 (2013).

114. Cortés-Ciriano, I. *et al.* Comprehensive analysis of chromothripsis in 2,658 human cancers using whole-genome sequencing. *Nat Genet* **52**, 331–341 (2020).

115. Zhang, C.-Z. *et al.* Chromothripsis from DNA damage in micronuclei. *Nature* **522**, 179–84 (2015).

116. Mohr, L. *et al.* ER-directed TREX1 limits cGAS activation at micronuclei. *Mol Cell* **81**, 724-738.e9 (2021).

117. Chan, Y. W., Fugger, K. & West, S. C. Unresolved recombination intermediates lead to ultra-fine anaphase bridges, chromosome breaks and aberrations. *Nat Cell Biol* **20**, 92–103 (2018).

118. Janssen, A., van der Burg, M., Szuhai, K., Kops, G. J. P. L. & Medema, R. H. Chromosome segregation errors as a cause of DNA damage and structural chromosome aberrations. *Science* **333**, 1895–8 (2011).

119. McClintock, B. The Stability of Broken Ends of Chromosomes in Zea Mays. *Genetics* **26**, 234–82 (1941).

120. McClintock, B. The Fusion of Broken Ends of Chromosomes Following Nuclear Fusion. *Proc Natl Acad Sci U S A* **28**, 458–63 (1942).

121. Maciejowski, J. *et al.* APOBEC3-dependent kataegis and TREX1-driven chromothripsis during telomere crisis. *Nat Genet* **52**, 884–890 (2020).

122. Mendoza, M. *et al.* A mechanism for chromosome segregation sensing by the NoCut checkpoint. *Nat Cell Biol* **11**, 477–83 (2009).

123. Hong, Y. *et al.* LEM-3 is a midbody-tethered DNA nuclease that resolves chromatin bridges during late mitosis. *Nat Commun* **9**, 728 (2018).

124. Song, J., Freeman, A. D. J., Knebel, A., Gartner, A. & Lilley, D. M. J. Human ANKLE1 Is a Nuclease Specific for Branched DNA. *J Mol Biol* **432**, 5825–5834 (2020).

125. Chan, K. L., North, P. S. & Hickson, I. D. BLM is required for faithful chromosome segregation and its localization defines a class of ultrafine anaphase bridges. *EMBO Journal* **26**, 3397–3409 (2007).

126. Baumann, C., Körner, R., Hofmann, K. & Nigg, E. A. PICH, a Centromere-Associated SNF2 Family ATPase, Is Regulated by Plk1 and Required for the Spindle Checkpoint. *Cell* **128**, 101–114 (2007).

127. Chan, K. L., Palmai-Pallag, T., Ying, S. & Hickson, I. D. Replication stress induces sister-chromatid bridging at fragile site loci in mitosis. *Nat Cell Biol* **11**, 753–760 (2009).

128. Nielsen, C. F. & Hickson, I. D. PICH promotes mitotic chromosome segregation: Identification of a novel role in rDNA disjunction. *Cell Cycle* vol. 15 2704–2711 Preprint at https://doi.org/10.1080/15384101.2016.1222336 (2016).

129. Barefield, C. & Karlseder, J. The BLM helicase contributes to telomere maintenance through processing of late-replicating intermediate structures. *Nucleic Acids Res* **40**, 7358–7367 (2012).

130. Chan, Y. W. & West, S. C. A new class of ultrafine anaphase bridges generated by homologous recombination. *Cell Cycle* vol. 17 2101–2109 Preprint at https://doi.org/10.1080/15384101.2018.1515555 (2018).

131. Fernández-Casañas, M. & Chan, K. L. The unresolved problem of DNA bridging. *Genes* vol. 9 Preprint at https://doi.org/10.3390/genes9120623 (2018).

132. Wang, J. C. Cellular roles of DNA topoisomerases: a molecular perspective. *Nat Rev Mol Cell Biol* **3**, 430–40 (2002).

133. Spence, J. M. *et al.* Depletion of topoisomerase IIalpha leads to shortening of the metaphase interkinetochore distance and abnormal persistence of PICH-coated anaphase threads. *J Cell Sci* **120**, 3952–64 (2007).

134. Liu, Y., Nielsen, C. F., Yao, Q. & Hickson, I. D. The origins and processing of ultra fine anaphase DNA bridges. *Current Opinion in Genetics and Development* vol. 26 1–5 Preprint at https://doi.org/10.1016/j.gde.2014.03.003 (2014).

135. McFarlane, R. J. & Humphrey, T. C. A role for recombination in centromere function. *Trends Genet* **26**, 209–13 (2010).

136. Smogorzewska, A. *et al.* Identification of the FANCI protein, a monoubiquitinated FANCD2 paralog required for DNA repair. *Cell* **129**, 289–301 (2007).

137. Bergoglio, V. *et al.* DNA synthesis by Pol η promotes fragile site stability by preventing under-replicated DNA in mitosis. *J Cell Biol* **201**, 395–408 (2013).

138. Heyer, W.-D., Ehmsen, K. T. & Liu, J. Regulation of homologous recombination in eukaryotes. *Annu Rev Genet* **44**, 113–39 (2010).

139. Wyatt, H. D. M., Sarbajna, S., Matos, J. & West, S. C. Coordinated actions of SLX1-SLX4 and MUS81-EME1 for holliday junction resolution in human cells. *Mol Cell* **52**, 234–247 (2013).

140. Sarbajna, S., Davies, D. & West, S. C. Roles of SLX1-SLX4, MUS81-EME1, and GEN1 in avoiding genome instability and mitotic catastrophe. *Genes Dev* **28**, 1124–1136 (2014).

141. Garner, E., Kim, Y., Lach, F. P., Kottemann, M. C. & Smogorzewska, A. Human GEN1 and the SLX4-associated nucleases MUS81 and SLX1 are essential for the resolution of replication-induced Holliday junctions. *Cell Rep* **5**, 207–15 (2013).

142. Wechsler, T., Newman, S. & West, S. C. Aberrant chromosome morphology in human cells defective for Holliday junction resolution. *Nature* **471**, 642–646 (2011).

143. Matos, J., Blanco, M. G., Maslen, S., Skehel, J. M. & West, S. C. Regulatory control of the resolution of DNA recombination intermediates during meiosis and mitosis. *Cell* **147**, 158–172 (2011).

144. Tiwari, A., Addis Jones, O. & Chan, K.-L. 53BP1 can limit sister-chromatid rupture and rearrangements driven by a distinct ultrafine DNA bridging-breakage process. *Nat Commun* **9**, 677 (2018).

145. Ochs, F. *et al.* 53BP1 fosters fidelity of homology-directed DNA repair. *Nat Struct Mol Biol* **23**, 714–21 (2016).

146. Nielsen, C. F. *et al.* PICH promotes sister chromatid disjunction and co-operates with topoisomerase II in mitosis. *Nat Commun* **6**, (2015).

147. Voit, R., Seiler, J. & Grummt, I. Cooperative Action of Cdk1/cyclin B and SIRT1 Is Required for Mitotic Repression of rRNA Synthesis. *PLoS Genet* **11**, e1005246 (2015).

148. Lukas, C. *et al.* 53BP1 nuclear bodies form around DNA lesions generated by mitotic transmission of chromosomes under replication stress. *Nat Cell Biol* **13**, 243–253 (2011).

149. Baxter, J. & Aragón, L. A model for chromosome condensation based on the interplay between condensin and topoisomerase II. *Trends Genet* **28**, 110–7 (2012).

150. Nera, B., Huang, H.-S., Lai, T. & Xu, L. Elevated levels of TRF2 induce telomeric ultrafine anaphase bridges and rapid telomere deletions. *Nat Commun* **6**, 10132 (2015).

151. Ishikawa, F. Portrait of replication stress viewed from telomeres. *Cancer Sci* **104**, 790–4 (2013).

152. Palm, W. & de Lange, T. How shelterin protects mammalian telomeres. *Annu Rev Genet* **42**, 301–34 (2008).

153. Bennink, M. L. *et al.* Unfolding individual nucleosomes by stretching single chromatin fibers with optical tweezers. *Nat Struct Biol* **8**, 606–10 (2001).

154. Jiang, H., Kong, N., Liu, Z., West, S. C. & Chan, Y. W. Human Endonuclease ANKLE1 Localizes at the Midbody and Processes Chromatin Bridges to Prevent DNA Damage and cGAS-STING Activation. *Advanced Science* **10**, (2023).

155. Ke, Y. *et al.* PICH and BLM limit histone association with anaphase centromeric DNA threads and promote their resolution. *EMBO Journal* **30**, 3309–3321 (2011).

156. Broderick, R., Nieminuszczy, J., Blackford, A. N., Winczura, A. & Niedzwiedz, W. TOPBP1 recruits TOP2A to ultra-fine anaphase bridges to aid in their resolution. *Nat Commun* **6**, (2015).

157. Hengeveld, R. C. C. *et al.* Rif1 Is Required for Resolution of Ultrafine DNA Bridges in Anaphase to Ensure Genomic Stability. *Dev Cell* **34**, 466–474 (2015).

158. Kong, N., Liu, Z. & Chan, Y. W. RIF1 suppresses the formation of single-stranded ultrafine anaphase bridges via protein phosphatase 1. *Cell Rep* **42**, (2023).

159. German, J., Roe, A. M., Leppert, M. F. & Ellis, N. A. Bloom syndrome: an analysis of consanguineous families assigns the locus mutated to chromosome band 15q26.1. *Proc Natl Acad Sci U S A* **91**, 6669–73 (1994).

160. Karow, J. K., Chakraverty, R. K. & Hickson, I. D. The Bloom's syndrome gene product is a 3'-5' DNA helicase. *J Biol Chem* **272**, 30611–4 (1997).

161. Ababou, M. Bloom syndrome and the underlying causes of genetic instability. *Molecular Genetics and Metabolism* vol. 133 35–48 Preprint at https://doi.org/10.1016/j.ymgme.2021.03.003 (2021).

162. Yankiwski, V., Marciniak, R. A., Guarente, L. & Neff, N. F. Nuclear structure in normal and Bloom syndrome cells. *Proc Natl Acad Sci U S A* **97**, 5214–9 (2000).

163. Gharibyan, V. & Youssoufian, H. Localization of the Bloom syndrome helicase to punctate nuclear structures and the nuclear matrix and regulation during the cell cycle: comparison with the Werner's syndrome helicase. *Mol Carcinog* **26**, 261–73 (1999).

164. Beamish, H. *et al.* Functional Link between BLM Defective in Bloom's Syndrome and the Ataxia-telangiectasia-mutated Protein, ATM. *Journal of Biological Chemistry* **277**, 30515–30523 (2002).

165. Davies, S. L., North, P. S., Dart, A., Lakin, N. D. & Hickson, I. D. Phosphorylation of the Bloom's Syndrome Helicase and Its Role in Recovery from S-Phase Arrest. *Mol Cell Biol* **24**, 1279–1291 (2004).

166. Bayart, E. *et al.* The Bloom Syndrome Helicase is a Substrate of the Mitotic Cdc2 Kinase. *Cell Cycle* **5**, 1681–1686 (2006).

167. Leng, M. *et al.* MPS1-dependent mitotic BLM phosphorylation is important for chromosome stability. *Proceedings of the National Academy of Sciences* **103**, 11485–11490 (2006).

168. Leng, M., Besusso, D., Jung, S. Y., Wang, Y. & Qin, J. Targeting Plk1 to chromosome arms and regulating chromosome compaction by the PICH ATPase. *Cell Cycle* **7**, 1480–1489 (2008).

169. Addis Jones, O., Tiwari, A., Olukoga, T., Herbert, A. & Chan, K.-L. PLK1 facilitates chromosome biorientation by suppressing centromere disintegration driven by BLM-mediated unwinding and spindle pulling. *Nat Commun* **10**, 2861 (2019).

170. Fernández-Casañas, M. *et al.* Centromere protection requires strict mitotic inactivation of the Bloom syndrome helicase complex. Preprint at https://doi.org/10.1101/2024.05.21.595148 (2024).

171. Johnson, F. B. *et al.* Association of the Bloom syndrome protein with topoisomerase IIIalpha in somatic and meiotic cells. *Cancer Res* **60**, 1162–7 (2000).

172. Yin, J. *et al.* BLAP75, an essential component of Bloom's syndrome protein complexes that maintain genome integrity. *EMBO J* **24**, 1465–76 (2005).

173. Liu, Y. & West, S. C. More complexity to the Bloom's syndrome complex. *Genes Dev* **22**, 2737–42 (2008).

174. Wang, Y. *et al.* BASC, a super complex of BRCA1-associated proteins involved in the recognition and repair of aberrant DNA structures. *Genes Dev* **14**, 927–39 (2000).

175. Wu, L., Davies, S. L., Levitt, N. C. & Hickson, I. D. Potential role for the BLM helicase in recombinational repair via a conserved interaction with RAD51. *J Biol Chem* **276**, 19375–81 (2001).

176. Grierson, P. M., Acharya, S. & Groden, J. Collaborating functions of BLM and DNA topoisomerase I in regulating human rDNA transcription. *Mutat Res* **743–744**, 89–96 (2013).

177. Bhattacharyya, S. *et al.* Telomerase-associated protein 1, HSP90, and topoisomerase IIalpha associate directly with the BLM helicase in immortalized cells using ALT and modulate its helicase activity using telomeric DNA substrates. *J Biol Chem* **284**, 14966–77 (2009).

178. Pichierri, P., Franchitto, A. & Rosselli, F. BLM and the FANC proteins collaborate in a common pathway in response to stalled replication forks. *EMBO J* **23**, 3154–63 (2004).

179. Tripathi, V., Kaur, S. & Sengupta, S. Phosphorylation-dependent interactions of BLM and 53BP1 are required for their anti-recombinogenic roles during homologous recombination. *Carcinogenesis* **29**, 52–61 (2008).

180. Lillard-Wetherell, K. *et al.* Association and regulation of the BLM helicase by the telomere proteins TRF1 and TRF2. *Hum Mol Genet* **13**, 1919–32 (2004).

181. Dutertre, S. *et al.* Cell cycle regulation of the endogenous wild type Bloom's syndrome DNA helicase. *Oncogene* **19**, 2731–2738 (2000).

182. Huber, M. D., Duquette, M. L., Shiels, J. C. & Maizels, N. A conserved G4 DNA binding domain in RecQ family helicases. *J Mol Biol* **358**, 1071–80 (2006).

183. Machwe, A., Xiao, L., Groden, J. & Orren, D. K. The Werner and Bloom syndrome proteins catalyze regression of a model replication fork. *Biochemistry* **45**, 13939–46 (2006).

184. Tan, J., Wang, X., Phoon, L., Yang, H. & Lan, L. Resolution of ROS-induced G-quadruplexes and R-loops at transcriptionally active sites is dependent on BLM helicase. *FEBS Lett* **594**, 1359–1367 (2020).

185. Rao, V. A. *et al.* Endogenous gamma-H2AX-ATM-Chk2 checkpoint activation in Bloom's syndrome helicase deficient cells is related to DNA replication arrested forks. *Mol Cancer Res* **5**, 713–24 (2007).

186. Nimonkar, A. V *et al.* BLM-DNA2-RPA-MRN and EXO1-BLM-RPA-MRN constitute two DNA end resection machineries for human DNA break repair. *Genes Dev* **25**, 350–62 (2011).

187. Wang, W. *et al.* The absence of a functional relationship between ATM and BLM, the components of BASC, in DT40 cells. *Biochim Biophys Acta* **1688**, 137–44 (2004).

188. Adams, M. D., McVey, M. & Sekelsky, J. J. Drosophila BLM in double-strand break repair by synthesis-dependent strand annealing. *Science* **299**, 265–7 (2003).

189. Bachrati, C. Z. Mobile D-loops are a preferred substrate for the Bloom's syndrome helicase. *Nucleic Acids Res* **34**, 2269–2279 (2006).

190. Drosopoulos, W. C., Kosiyatrakul, S. T. & Schildkraut, C. L. BLM helicase facilitates telomere replication during leading strand synthesis of telomeres. *Journal of Cell Biology* **210**, 191–208 (2015).

191. Schawalder, J., Paric, E. & Neff, N. F. Telomere and ribosomal DNA repeats are chromosomal targets of the bloom syndrome DNA helicase. *BMC Cell Biol* **4**, 15 (2003).

192. Gratia, M. *et al.* Bloom syndrome protein restrains innate immune sensing of micronuclei by cGAS. *J Exp Med* **216**, 1199–1213 (2019).

193. German, J. Bloom's syndrome. I. Genetical and clinical observations in the first twenty-seven patients. *Am J Hum Genet* **21**, 196–227 (1969).

194. German, J. Bloom syndrome: a mendelian prototype of somatic mutational disease. *Medicine* **72**, 393–406 (1993).

195. Sugrañes, T. A. *et al.* Age of first cancer diagnosis and survival in Bloom syndrome. *Genetics in Medicine* **24**, 1476–1484 (2022).

196. German, J. Bloom's syndrome. XX. The first 100 cancers. *Cancer Genet Cytogenet* **93**, 100–6 (1997).

197. Chaganti, R. S. K., Schonberg, S. & German, J. *A Manyfold Increase in Sister Chromatid Exchanges in Bloom's Syndrome Lymphocytes (BrdU Substitution/Chromosome Rearrangement/Fanconi's Anemia/Ataxia Telangiectasia)*. vol. 71 (1974).

198. German, J., Schonberg, S., Louie, E. & Chaganti, R. S. Bloom's syndrome. IV. Sister-chromatid exchanges in lymphocytes. *Am J Hum Genet* **29**, 248–55 (1977).

199. Cunniff, C., Bassetti, J. A. & Ellis, N. A. Bloom's syndrome: Clinical spectrum, molecular pathogenesis, and cancer predisposition. *Molecular Syndromology* vol. 8 4–23 Preprint at https://doi.org/10.1159/000452082 (2017).

200. Martin, C.-A. *et al.* Mutations in TOP3A Cause a Bloom Syndrome-like Disorder. *Am J Hum Genet* **103**, 221–231 (2018).

201. Luo, G. *et al.* Cancer predisposition caused by elevated mitotic recombination Bloom mice. *Nat Genet* **26**, 424–429 (2000).

202. Groden, J., Nakamura, Y. & German, J. Molecular evidence that homologous recombination occurs in proliferating human somatic cells. *Proc Natl Acad Sci U S A* **87**, 4315–9 (1990).

203. Rosin, M. P. & German, J. Evidence for chromosome instability in vivo in bloom syndrome: Increased numbers of micronuclei in exfoliated cells. *Hum Genet* **71**, 187–191 (1985).

204. Yamanishi, A. *et al.* Enhancement of microhomology-mediated genomic rearrangements by transient loss of mouse Bloom syndrome helicase. *Genome Res* **23**, 1462–73 (2013).

205. Suzuki, T., Yasui, M. & Honma, M. Mutator Phenotype and DNA Double-Strand Break Repair in BLM Helicase-Deficient Human Cells. *Mol Cell Biol* **36**, 2877–2889 (2016).

206. Natsume, T., Kiyomitsu, T., Saga, Y. & Kanemaki, M. T. Rapid Protein Depletion in Human Cells by Auxin-Inducible Degron Tagging with Short Homology Donors. *Cell Rep* **15**, 210–218 (2016).

207. Nishimura, K., Fukagawa, T., Takisawa, H., Kakimoto, T. & Kanemaki, M. An auxin-based degron system for the rapid depletion of proteins in nonplant cells. *Nat Methods* **6**, 917–22 (2009).

208. Holland, A. J., Fachinetti, D., Han, J. S. & Cleveland, D. W. Inducible, reversible system for the rapid and complete degradation of proteins in mammalian cells. *Proc Natl Acad Sci U S A* **109**, E3350-7 (2012).

209. Jinek, M. *et al.* A programmable dual-RNA-guided DNA endonuclease in adaptive bacterial immunity. *Science* **337**, 816–21 (2012).

210. Hsu, P. D. *et al.* DNA targeting specificity of RNA-guided Cas9 nucleases. *Nat Biotechnol* **31**, 827–832 (2013).

211. Doench, J. G. *et al.* Rational design of highly active sgRNAs for CRISPR-Cas9–mediated gene inactivation. *Nat Biotechnol* **32**, 1262–1267 (2014).

212. Li, H. *et al.* Design and specificity of long ssDNA donors for CRISPR-based knock-in. Preprint at https://doi.org/10.1101/178905 (2017).

213. Cong, L. *et al.* Multiplex genome engineering using CRISPR/Cas systems. *Science* **339**, 819–23 (2013).

214. Ran, F. A. *et al.* Genome engineering using the CRISPR-Cas9 system. *Nat Protoc* **8**, 2281–2308 (2013).

215. Morawska, M. & Ulrich, H. D. An expanded tool kit for the auxin-inducible degron system in budding yeast. *Yeast* **30**, 341–51 (2013).

216. Gibson, D. G. *et al.* Enzymatic assembly of DNA molecules up to several hundred kilobases. *Nat Methods* **6**, 343–345 (2009).

217. Engler, C., Kandzia, R. & Marillonnet, S. A One Pot, One Step, Precision Cloning Method with High Throughput Capability. *PLoS One* **3**, e3647 (2008).

218. Braman, J., Papworth, C. & Greener, A. Site-Directed Mutagenesis Using Double-Stranded Plasmid DNA Templates. in *In Vitro Mutagenesis Protocols* 31–44 (Humana Press, New Jersey). doi:10.1385/0-89603-332-5:31.

219. Gaymes, T. J. *et al.* Increased error-prone non homologous DNA end-joining--a proposed mechanism of chromosomal instability in Bloom's syndrome. *Oncogene* **21**, 2525–33 (2002).

220. HORWITZ, J. P. *et al.* SUBSTRATES FOR CYTOCHEMICAL DEMONSTRATION OF ENZYME ACTIVITY. I. SOME SUBSTITUTED 3-INDOLYL-BETA-D-GLYCOPYRANOSIDES. *J Med Chem* **7**, 574–5 (1964).

221. BOLTE, S. & CORDELIÈRES, F. P. A guided tour into subcellular colocalization analysis in light microscopy. *J Microsc* **224**, 213–232 (2006).

222. Rappsilber, J., Mann, M. & Ishihama, Y. Protocol for micro-purification, enrichment, pre-fractionation and storage of peptides for proteomics using StageTips. *Nat Protoc* **2**, 1896–906 (2007).

223. Bakker, B. *et al.* Single-cell sequencing reveals karyotype heterogeneity in murine and human malignancies. *Genome Biol* **17**, 115 (2016).

224. Venegas, A. B., Natsume, T., Kanemaki, M. & Hickson, I. D. Inducible Degradation of the Human SMC5/6 Complex Reveals an Essential Role Only during Interphase. *Cell Rep* **31**, (2020).

225. Latt, S. A. Microfluorometric Detection of Deoxyribonucleic Acid Replication in Human Metaphase Chromosomes. *Proceedings of the National Academy of Sciences* **70**, 3395–3399 (1973).

226. PERRY, P. & WOLFF, S. New Giemsa method for the differential staining of sister chromatids. *Nature* **251**, 156–158 (1974).

227. Xu, D. *et al.* RMI, a new OB-fold complex essential for Bloom syndrome protein to maintain genome stability. *Genes Dev* **22**, 2843–2855 (2008).

228. Spies, J., Polasek-Sedlackova, H., Lukas, J. & Somyajit, K. Homologous Recombination as a Fundamental Genome Surveillance Mechanism during DNA Replication. *Genes (Basel)* **12**, 1960 (2021).

229. Schwartz, M. *et al.* Homologous recombination and nonhomologous end-joining repair pathways regulate fragile site stability. *Genes Dev* **19**, 2715–2726 (2005).

230. Ma, X.-Y. *et al.* ML216-Induced BLM Helicase Inhibition Sensitizes PCa Cells to the DNA-Crosslinking Agent Cisplatin. *Molecules* **27**, 8790 (2022).

231. Eladad, S. *et al.* Intra-nuclear trafficking of the BLM helicase to DNA damage-induced foci is regulated by SUMO modification. *Hum Mol Genet* **14**, 1351–1365 (2005).

232. Song, Y. S., Lee, B. Y. & Hwang, E. S. Dinstinct ROS and biochemical profiles in cells undergoing DNA damage-induced senescence and apoptosis. *Mech Ageing Dev* **126**, 580–590 (2005).

233. Childs, B. G., Baker, D. J., Kirkland, J. L., Campisi, J. & van Deursen, J. M. Senescence and apoptosis: dueling or complementary cell fates? *EMBO Rep* **15**, 1139–1153 (2014).

234. Böhly, N., Kistner, M. & Bastians, H. Mild replication stress causes aneuploidy by deregulating microtubule dynamics in mitosis. *Cell Cycle* **18**, 2770–2783 (2019).

235. Van Wietmarschen, N. *et al.* BLM helicase suppresses recombination at G-quadruplex motifs in transcribed genes. *Nat Commun* **9**, (2018).

236. Shorrocks, A. M. K. *et al.* The Bloom syndrome complex senses RPA-coated single-stranded DNA to restart stalled replication forks. *Nat Commun* **12**, (2021).

237. Sarlós, K. *et al.* Reconstitution of anaphase DNA bridge recognition and disjunction. *Nat Struct Mol Biol* **25**, 868–876 (2018).

238. Biebricher, A. *et al.* PICH: A DNA Translocase Specially Adapted for Processing Anaphase Bridge DNA. *Mol Cell* **51**, 691–701 (2013).

239. Lewis, W. H. & Lewis, M. R. The duration of the various phases of mitosis in the mesen chyme cells of tissue cultures. *Anat Rec* **13**, 359–367 (1917).

240. El-Alfy, M. & Leblond, C. P. Long duration of mitosis and consequences for the cell cycle concept, as seen in the isthmal cells of the mouse pyloric antrum. II. Duration of mitotic phases and cycle stages, and their relation to one another. *Cell Prolif* **20**, 215–226 (1987).

241. Thompson, S. L. & Compton, D. A. Examining the link between chromosomal instability and aneuploidy in human cells. *J Cell Biol* **180**, 665–672 (2008).

242. Wilhelm, T. *et al.* Mild replication stress causes chromosome mis-segregation via premature centriole disengagement. *Nat Commun* **10**, (2019).

243. Shaikh, N. *et al.* Replication stress generates distinctive landscapes of DNA copy number alterations and chromosome scale losses. *Genome Biol* **23**, (2022).

244. Wang, C. I. *et al.* Chromatin proteins captured by ChIP–mass spectrometry are linked to dosage compensation in Drosophila. *Nat Struct Mol Biol* **20**, 202–209 (2013).

245. Wierer, M. & Mann, M. Proteomics to study DNA-bound and chromatin-associated gene regulatory complexes. *Hum Mol Genet* **25**, R106–R114 (2016).

246. Krietsch, J. *et al.* PARP activation regulates the RNA-binding protein NONO in the DNA damage response to DNA double-strand breaks. *Nucleic Acids Res* **40**, 10287–10301 (2012).

247. Mosler, T. *et al.* PARP1 proximity proteomics reveals interaction partners at stressed replication forks. *Nucleic Acids Res* **50**, 11600–11618 (2022).

248. Yang, Y. *et al.* HIF-1 Interacts with TRIM28 and DNA-PK to release paused RNA polymerase II and activate target gene transcription in response to hypoxia. *Nat Commun* **13**, 316 (2022).

249. Ray Chaudhuri, A. & Nussenzweig, A. The multifaceted roles of PARP1 in DNA repair and chromatin remodelling. *Nat Rev Mol Cell Biol* **18**, 610–621 (2017).

250. Olazabal-Herrero, A. *et al.* The FANCI/FANCD2 complex links DNA damage response to R-loop regulation through SRSF1-mediated mRNA export. *Cell Rep* **43**, 113610 (2024).

251. Bennett, R. A. O., Wilson, D. M., Wong, D. & Demple, B. Interaction of human apurinic endonuclease and DNA polymerase β in the base excision repair pathway. *Proceedings of the National Academy of Sciences* **94**, 7166–7169 (1997).

252. Li, M., Völker, J., Breslauer, K. J. & Wilson, D. M. APE1 Incision Activity at Abasic Sites in Tandem Repeat Sequences. *J Mol Biol* **426**, 2183–2198 (2014).

253. Fan, Z., Beresford, P. J., Zhang, D. & Lieberman, J. HMG2 Interacts with the Nucleosome Assembly Protein SET and Is a Target of the Cytotoxic T-Lymphocyte Protease Granzyme A. *Mol Cell Biol* **22**, 2810–2820 (2002).

254. Chowdhury, D. *et al.* The Exonuclease TREX1 Is in the SET Complex and Acts in Concert with NM23-H1 to Degrade DNA during Granzyme A-Mediated Cell Death. *Mol Cell* **23**, 133–142 (2006).

255. Du, J. *et al.* LncRNA Pnky Positively Regulates Neural Stem Cell Migration by Modulating mRNA Splicing and Export of Target Genes. *Cell Mol Neurobiol* **43**, 1199–1218 (2023).

256. Rodemoyer, B., Kariyawasam, G., Subramanian, V. & Schmidt, K. Condensin II interacts with BLM helicase in S phase to maintain genome stability. *Commun Biol* **8**, (2025).

257. Sharma, S. V *et al.* A chromatin-mediated reversible drug-tolerant state in cancer cell subpopulations. *Cell* **141**, 69–80 (2010).

258. Khan, S. H. Genome-Editing Technologies: Concept, Pros, and Cons of Various Genome-Editing Techniques and Bioethical Concerns for Clinical Application. *Mol Ther Nucleic Acids* **16**, 326–334 (2019).

259. Christian, M. *et al.* Targeting DNA Double-Strand Breaks with TAL Effector Nucleases. *Genetics* **186**, 757–761 (2010).

260. Klug, A. & Rhodes, D. Zinc Fingers: A Novel Protein Fold for Nucleic Acid Recognition. *Cold Spring Harb Symp Quant Biol* **52**, 473–482 (1987).

261. Fire, A. *et al.* Potent and specific genetic interference by double-stranded RNA in Caenorhabditis elegans. *Nature* **391**, 806–811 (1998).

262. Paddison, P. J., Caudy, A. A., Bernstein, E., Hannon, G. J. & Conklin, D. S. Short hairpin RNAs (shRNAs) induce sequence-specific silencing in mammalian cells. *Genes Dev* **16**, 948–58 (2002).

263. McAnuff, M. A., Rettig, G. R. & Rice, K. G. Potency of siRNA versus shRNA mediated knockdown in vivo. *J Pharm Sci* **96**, 2922–30 (2007).

264. McBride, J. L. *et al.* Artificial miRNAs mitigate shRNA-mediated toxicity in the brain: implications for the therapeutic development of RNAi. *Proc Natl Acad Sci U S A* **105**, 5868–73 (2008).

265. Yesbolatova, A. *et al.* The auxin-inducible degron 2 technology provides sharp degradation control in yeast, mammalian cells, and mice. *Nat Commun* **11**, 5701 (2020).

266. Zhang, S., Shen, J., Li, D. & Cheng, Y. Strategies in the delivery of Cas9 ribonucleoprotein for CRISPR/Cas9 genome editing. *Theranostics* **11**, 614–648 (2021).

267. Zoppo, M., Okoniewski, N., Pantelyushin, S., Vom Berg, J. & Schirmer, K. A ribonucleoprotein transfection strategy for CRISPR/Cas9-mediated gene editing and single cell cloning in rainbow trout cells. *Cell Biosci* **11**, 103 (2021).

268. Li, L., Eng, C., Desnick, R. J., German, J. & Ellis, N. A. Carrier Frequency of the Bloom SyndromeblmAshMutation in the Ashkenazi Jewish Population. *Mol Genet Metab* **64**, 286–290 (1998).

269. Gruber, S. B. *et al.* BLM heterozygosity and the risk of colorectal cancer. *Science* **297**, 2013 (2002).

270. Goss, K. H. *et al.* Enhanced tumor formation in mice heterozygous for Blm mutation. *Science* **297**, 2051–3 (2002).

271. Stok, C. *et al.* FIRRM/C1orf112 is synthetic lethal with PICH and mediates RAD51 dynamics. *Cell Rep* **42**, 112668 (2023).

272. Hamann, T. E. *et al.* Mitotic BLM functions are required to maintain genomic stability. Preprint at https://doi.org/10.1101/2025.06.16.659902 (2025).

273. Keller, C., Keller, K. R., Shew, S. B. & Plon, S. E. Growth deficiency and malnutrition in Bloom syndrome. *J Pediatr* **134**, 472–479 (1999).

274. Chester, N., Kuo, F., Kozak, C., O'Hara, C. D. & Leder, P. Stage-specific apoptosis, developmental delay, and embryonic lethality in mice homozygous for a targeted disruption in the murine Bloom's syndrome gene. *Genes Dev* **12**, 3382–3393 (1998).

275. Hayflick, L. & Moorhead, P. S. The serial cultivation of human diploid cell strains. *Exp Cell Res* **25**, 585–621 (1961).

276. Rossiello, F., Jurk, D., Passos, J. F. & d'Adda di Fagagna, F. Telomere dysfunction in ageing and age-related diseases. *Nat Cell Biol* **24**, 135–147 (2022).

277. Monnat, Jr. , R. J. & Sidorova, J. Human RECQ helicases: roles in cancer, aging, and inherited disease. *Adv Genomics Genet* 19 (2014) doi:10.2147/AGG.S54078.

278. Yu, C.-E. *et al.* Positional Cloning of the Werner's Syndrome Gene. *Science (1979)* **272**, 258–262 (1996).

279. Davalos, A. R. & Campisi, J. Bloom syndrome cells undergo p53-dependent apoptosis and delayed assembly of BRCA1 and NBS1 repair complexes at stalled replication forks. *J Cell Biol* **162**, 1197–209 (2003).

280. Chen, Y. *et al.* miR-27b-3p and miR-607 cooperatively regulate BLM gene expression by directly targeting the 3'-UTR in PC3 cells. *Mol Med Rep* (2019) doi:10.3892/mmr.2019.10135.

281. Qian, X. *et al.* RecQ helicase BLM regulates prostate cancer cell proliferation and apoptosis. *Oncol Lett* **14**, 4206–4212 (2017).

282. Singh, M. I. *et al.* Mechanistic insight into anaphase bridge signaling to the abscission checkpoint. *EMBO J* (2025) doi:10.1038/s44318-025-00453-w.

283. Fujiwara, T. *et al.* Cytokinesis failure generating tetraploids promotes tumorigenesis in p53-null cells. *Nature* **437**, 1043–1047 (2005).

284. Pampalona, J., Frías, C., Genescà, A. & Tusell, L. Progressive Telomere Dysfunction Causes Cytokinesis Failure and Leads to the Accumulation of Polyploid Cells. *PLoS Genet* **8**, e1002679 (2012).

285. Steigemann, P. *et al.* Aurora B-Mediated Abscission Checkpoint Protects against Tetraploidization. *Cell* **136**, 473–484 (2009).

286. Margolis, R. L., Lohez, O. D. & Andreassen, P. R. G1 tetraploidy checkpoint and the suppression of tumorigenesis. *J Cell Biochem* **88**, 673–683 (2003).

287. Bizard, A. H. & Hickson, I. D. Anaphase: a fortune-teller of genomic instability. *Curr Opin Cell Biol* **52**, 112–119 (2018).

288. Wang, H. *et al.* BLM prevents instability of structure-forming DNA sequences at common fragile sites. *PLoS Genet* **14**, (2018).